DISSERTATION

AEROSOL EFFECTS ON CLOUD-PRECIPITATION AND LAND-SURFACE PROCESSES

Submitted by

Toshihisa Matsui

Department of Atmospheric Science

In partial fulfillment of the requirements

For the Degree of Doctor of Philosophy

Colorado State University

Fort Collins, Colorado

Spring 2007

COLORADO STATE UNIVERSITY

November 20, 2006

WE HEREBY RECOMMEND THAT THE DISSERTATION PREPARED UNDER OUR SUPERVISION BY TOSHIHISA MATSUI ENTITLED AEROSOL EFFECTS ON CLOUD-PRECIPITATION AND LAND-SURFACE PROCESSES BE ACCEPTED AS FULFILLING IN PART REQUIREMENTS FOR THE DEGREE OF DOCTOR OF PHILOSOPHY.

Committee on Graduate Work

Adviser

Department Head

ABSTRACT OF DISSERTATION

AEROSOL EFFECTS ON CLOUD-PRECIPITATION AND LAND-SURFACE PROCESSES

Aerosols not only directly scatter and absorb solar radiation (denoted as the aerosol direct effects), but also modulate cloud properties by acting as cloud condensation nuclei (CCN) to form cloud droplets (denoted as the aerosol indirect effects). High concentrations of aerosols can overseed cloud droplets to reduce the mean size of cloud droplets, which is hypothesized to increase cloud albedo for the constant cloud liquid water path thereby slowing the warm-rain processes. The first part of this dissertation examines the sensitivity of the aerosol indirect effect to different thermodynamic environments over the tropical ocean. The variability of marine warm cloud properties is derived from satellite multiple sensors, and is normalized by the variability of satellite-derived aerosol index (AI) and reanalysis-derived lower-tropospheric stability (LTS). Global statistics show that increases in AI (polluted air) are associated with reductions in the cloud droplet effective radius (R_e), supporting the hypothesis of the aerosol indirect effect. Increase in LTS (strong lower-troposphere stability) is also associated with reductions in the R_e, indicating that the stronger inversion prevents dynamical growth of cloud droplets. Marine warm rain processes are

estimated from the comparison between cloud-top and column R_e, and the global statistics indicate that the warm-rain processes are minimized regardless of the air pollution under a strong temperature inversion, while they are inhibited due to air pollution under unstable thermodynamic conditions. The cloud liquid water path (CLWP) tends to be decreased for higher AI, which does not support the assumption of constant CLW associated with the reduction of R_e. Global variability of corrected cloud albedo (CCA: the product of cloud optical depth and cloud fraction) is better explained by the variability of the LTS than by AI. CCA appear to be highest under the strong-inversion regions, and is the first-order property that controls the radiation budget. Local variability of these cloud properties is explained by a combination of AI and LTS better than by either AI or LTS alone. Finally, the spatial mean and the spatial gradient of the aerosol direct and indirect radiative forcing are estimated and compared with the forcing attributed to well-mixed greenhouse gases (GHG) over the tropical ocean.

The aerosol direct effect not only reduces global irradiance but also increases diffuse radiation. Diffuse radiation is more homogeneously absorbed by the plant canopy and more efficiently utilized for the plant photosynthesis process than direct radiation. Thus, aerosol loading is expected to increase plant productivity (the aerosol diffuse-radiation effect). The second part of this dissertation examines the spatio-temoporal variability of the aerosol diffuse-radiation effect over the eastern U.S., using a sun-shade canopy model. First, satellite and model aerosol optical depth (AOD) products are assimilated via an optimal interpolation technique, and a comparison against the ground-based observations shows that the satellite-model assimilated AOD product is superior to either a satellite or model product. Second, surface albedo, surface radiative temperature,

CO_2 flux, and sensible/latent heat fluxes in a sun-shade canopy model (Unified Land Model: ULM) are compared with corresponding satellite and ground-based observations. Tuning parameters in ULM are constrained by reducing model-observation discrepancies via the Gauss-Maquardt-Levemberg automatic optimization algorithm. Third, the well-calibrated ULM is run in an off-line model for the warm seasons in 2000 and 2001. Downwelling shortwave radiation is computed with (a control experiment) and without (a potential experiment) assimilated daily AOD in all-sky conditions. The sensitivity experiments (control-potential) show that aerosol loading increases plant productivity in mixed forests and deciduous broadleaf forests in the southeastern U.S., while plant productivity is decreased over the croplands and grasslands. The spatio-temporal variability of aerosol diffuse-radiation effect is well explained by the variability of LAI, cloud optical depth, near-surface atmospheric temperature, and diurnal cycles. Due to the combination of the positive and negative effects, the aerosol diffuse-radiation effect increases plant productivity by only +0.5% in 2001 and –0.09% in 2000 from the potential experiment over the eastern U.S.

Toshihisa Matsui
Atmospheric Science Department
Colorado State University
Fort Collins, CO 80523
Spring 2007

Table of Contents

List of Tables

List of Figures

Acknowledgements

This entire Ph.D. work is funded by NASA-CSU CEAS fellowship (NAG512105), NASA Radiation (NNG04GB87G), and NASA Interdisciplinary Sciences (NNG04GL61G). My special thanks go to my family, Miwa and Schunta Matsui, for their unconditional love and enduring support; my advisors, Roger A. Pielke and Wei-Kuo Tao, for their great mentorship and funding support; my Ph.D. committees and collaborators, Dev Niyogi, Sonia Kreidenweis, Michael Coughenour, and A. Scott Denning, for their excellent academic and research guidance; Pielke's research groups, , Adriana Beltrán-Przekurat, Chris Castro, Glen Liston, John Lin, Chris Hiemistra, Giovanni Leoncini, Ji-Wang Wang, John Strack, Curtis Marshall, David Stokowski, and Dallas Staley, for spending wonderful research time; department staffs including Melissa Tucker, Jen Weingardt, and Marilyn Hanson, for their assistance with my administrative processes; department colleagues, Tak Yamaguchi, K.D. Corbin, Derek Posselt, Ian Baker, Lixing Lu, Gustavo Carío, Sue Van Den Heever, Hong-Li Jiang, Kevin Schaefer, for useful discussion in diverse research topics; department professors, Bill Cotton, Chris Kummerow, Wayne Schubert and Graeme Stephens for their academic classes and useful discussions; NASA GSFC's colleagues, Mian Chin, Allen Chu, Steve Lang, Hongbin Yu, Eric Moody, Brian Cosgrove, Kristi Arsenault, Jim Geyger and Sujay Kumar, for their cutting-edge research skill and collaborations; computer system administrators: Tony

Arcieri, Sloan Johnson and Michael Aumock for their patience of teaching computer skill to me. In addition, the first half of this dissertation (aerosol-cloud interactions) was strongly inspired by Yoram Kaufman at NASA GSFC, who was unexpectedly passed away in spring 2006, and Hirohiko Masunaga, a former CSU scientist and a new professor in Nagoya University.

Chapter 1

INTRODUCTION

1.1 Overview of Aerosol Effects on Climate

Atmospheric aerosols, suspended atmospheric particles, derive from many sources, and are characterized by different compositions, sizes, and shapes. Atmospheric particulate matter is often broadly categorized as arising from either natural sources or from anthropogenic sources. Natural sources include biogenic emissions, sea salt, volcanic ash and aerosol precursor gases, smoke and precursor gases from natural forest fires, and soil minerals. Anthropogenic sources include aerosol precursor gases from industries, home heating, and traffic, and smoke and precursor gases from agricultural practices [e.g., *Jaenicke* 1993]. Industrial aerosols are present only since the era of the industrial revolution, while biomass burning-derived aerosols have been emitted since the beginning of these agricultural practices in the tropics. In the last century, increases in world population have drastically increased the amount of aerosol emissions from anthropogenic sources [*IPCC* 2001].

Aerosols are expected to modify the atmosphere by i) directly scattering and absorbing solar radiation (denoted as the *aerosol direct effect* [*Harshvardhan* 1993; *Haywood and Boucher* 2000; *Yu et al.* 2005]) and by ii) modulating cloud properties and

formation by serving as cloud condensation nuclei in supersaturated environments (denoted as the *aerosol indirect effect* [*Hobbs* 1993; *Haywood and Boucher* 2000; *Lohmann and Feichter* 2005]). For example, for most aerosol constituents (excepting black carbon) the single scattering albedo is greater than 0.9, and they effectively scatter shortwave radiation. Thus, the presence of aerosols enhances the backscatter of solar radiation (*aerosol direct effect*). Higher concentrations of sub-micron aerosols are expected to reduce the average size of cloud droplets (*aerosol indirect effect*), in turn increasing the cloud albedo under the assumption of constant liquid water content [*Twomey et al.* 1984], and could enhance the cloud liquid water path by inhibiting the precipitation initiation process [*Albrecht* 1989].

Both aerosol direct and indirect effects can modulate atmospheric temperature and moisture profiles, vertical and horizontal motions of the air, formation of clouds, and surface energy and mass fluxes. Aerosols and their effects on climate have received increased attention from the science community, because of their proposed counter impact against the warming effect (trapping of the earth's longwave emission) of anthropogenic greenhouse gases (GHGs) [*Anderson et al.* 2003]. Namely, on the global scale, aerosol radiative forcing is expected to have a cooling effect on the earth by increasing the planetary (top-of-atmosphere: TOA) albedo.

While aerosol radiative forcing is often discussed on the global scale, the characteristics and concentration of aerosols are heterogeneous in time and space. Unlike gases that may have residence time of years, aerosols typically have a residence time of about a week. This is because aerosols are heterogeneously distributed in the global atmosphere according to varying source regions, transported by atmospheric motions, and

removed by dry/wet deposition. *NACIP* [2002] states that the regional change in radiative flux due to aerosols could be 2 to 4 times larger than without the forcing and the seasonal mean surface flux changes could be 10 times larger. This creates a strong gradient in radiative forcing that could dynamically modulate atmosphere and ocean circulations on the long-time scale, which could have much a greater forcing on the regional climate than those either from the direct or indirect effect on the short-time scale (denoted as the *aerosol dynamic effect* [*Rotstayn and Lohmann* 2002; *Menon et al.* 2002; *Lau et al.* 2006; *Takemura et al.* 2006]).

The effects of aerosols on surface carbon sinks have been addressed recently [*Roderick et al.* 2001; *Gu et al.* 2003; *Niyogi et al.* 2004]. Enhanced diffuse components of solar radiation due to aerosols could increase total photosynthetically active radiation (PAR) reaching the shaded canopy without saturating PAR, while a slight reduction of direct radiation does not lower the sunlit-canopy photosynthesis due to the saturated direct PAR in sunlit leaf. Thus, enhanced diffuse radiation is expected to increase total photosynthesis and canopy stomatal conductance [*Goudriaan* 1977]. Following the massive 1991 eruption of Mt. Pinatubo, globally distributed sulphate aerosols scattered solar radiation, enhancing the global carbon sink [*Gu et al.* 2003]. *Niyogi et al.* [2004] also show that aerosol-driven increases in diffuse radiation enhance the observed carbon sink over the forest in the eastern U.S. This is denoted as the *aerosol diffuse-radiation effect*.

The *aerosol direct*, *indirect*, *dynamic*, and *diffuse-radiation effects* must interact with each other in a nonlinear manner though the earth's climate variability. The

magnitude and variability of those effects are some of the largest uncertainties in accurately describing the future projection of earth's climate [*NRC* 2005; *IPCC* 2001].

1.2. Motivations and Overviews of Chapters

Aerosols climatic effects are complex issues as explained in the previous section. While this dissertation examines different proposed aerosol effects, it particularly focuses on the *aerosol indirect effect* and the *aerosol diffuse-radiation effect*. This is because, the *aerosol indirect effect* is the largest uncertainty in estimated anthropogenic forcing of climate, and the *aerosol diffuse-radiation effect* has not been recognized in the science community [*IPCC* 2001]. Here is a motivation and brief overview of each chapter.

Chapter 1 (this chapter) introduces the uncertainties in aerosol effects on climate, including brief descriptions of the *aerosol direct, indirect, dynamic and diffuse-radiation effects*. This chapter provides a motivation and overview of each chapter in this dissertation.

Chapters 2, 3, and 4 examine the *aerosol indirect effect* over the tropical ocean using multiple satellite datasets. An examination of this *aerosol indirect effect* is difficult due to the intrinsic complexity of cloud dynamics and properties, which are essentially affected by both the aerosols and background thermodynamics [*Houze* 1993]. However, previous studies examined either aerosol or thermodynamic aspects in their analyses [e.g.,, *Twomey et al.* 1984; *Klein and Hartmann,* 1993], and a rationalization of the *aerosol indirect effect* is needed in different thermodynamic environments. Thus, chapter 2 asks the following question.

- *How are mean size of cloud droplet and precipitation distributed and related to aerosol concentrations as well as thermodynamics?*

In order to answer the question, this study focuses on the measurement-based assessment using space-born remote sensing. Tropical Ocean is the ideal region for this study, since it is covered by varying concentrations of aerosols under different thermodynamic environments; and ii) it has different forms (e.g., fog, trade cumuli, cumulus congestus, and etc.) of marine low clouds. Chapter 2 uses a combination of cloud-top and columnar droplet sizes derived from the multiple Tropical Rainfall Measurement Mission (TRMM) sensors, as linked to the satellite-derived aerosol index (AI) and reanalysis-derived lower-tropospheric stability (LTS). A combination of cloud-top and columnar droplet sizes reveals the geographic distribution of warm rain process over the tropical ocean. A statistical correlation indicates that the warm rain process is prevented regardless of the aerosol concentrations under high static stability such as when a strong temperature inversion exists, while a high aerosol concentration suppresses the warm rain formulation under low static stability [*Matsui et al.* 2004a].

Chapter 3 is the extended study of chapter 2, and examines variability in marine low cloud properties (including cloud liquid water path and cloud fraction in addition to cloud droplet sizes), as linked to LTS, AI, and diurnal cycle. Particularly, this chapter asks the following questions.

- *Which factor (either aerosols or thermodynamics) is more important to describe variability of marine low cloud properties?*
- *How do diurnal cycles of cloud properties vary in different aerosol and thermodynamic environment?*

In order to answer the question, variability of marine low cloud properties, LTS and AI are quantified based on the probability density functions from the 1-year sampling. These statistics show that high cloud droplet size is better correlated with AI than it is with LTS. Global variability in corrected cloud albedo (CCA), the product of cloud optical depth and cloud fraction, is very well explained by LTS, while both AI and LTS are needed to explain local variability in CCA. Most of the local correlations between AI and cloud properties are similar to the results from the global statistics, while weak anomalous aerosol-cloud correlations appear locally in the regions where simultaneous high (low) AI and low (high) LTS compensate each other. Daytime diurnal cycles explain additional variability in cloud properties. CCA has the largest diurnal cycle in high-LTS regions. Cloud droplet size and CLWP have weak diurnal cycles that differ between clean and polluted environments [*Matsui et al.* 2006a].

Unlike GHG, aerosols have much greater spatial heterogeneity in their radiative forcing. The heterogeneous diabatic heating can modulate the gradient in horizontal pressure field and atmospheric circulations, thus altering the regional climate. Whereas the science community tends to quantify the aerosol radiative forcing as the global averaged top-of-atmosphere (TOA) value [*Anderson et al.* 2003], another metric is required for the heterogeneous radiative forcing. Chapter 4 seeks a following question.

- *How can heterogeneous radiative forcing be effectively quantified and linked to atmospheric circulation and regional climate?*

Chapter 4 diagnoses the spatial mean and the spatial gradient of the aerosol radiative forcing in comparison with the forcing attributed to well-mixed greenhouse gases (GHG) over the tropical ocean. Aerosol direct radiative forcing is estimated from the satellite-

based aerosol optical depths (AODs), model-based aerosol composition and vertical profile, and the Optical Properties of Aerosol and Cloud (OPAC) dataset. Aerosol indirect radiative forcing is estimated from the empirical relationship between satellite-derived aerosol and cloud properties in chapter 3. To describe the potential effect of heterogeneous radiative forcing, the *Normalized Gradient of Radiative Forcing* (*NGoRF*) is proposed and defined as a fraction of the present global heterogeneous insolation attributed to human activity. Although the GHG has a larger forcing (+1.7 Wm^{-2}) as measured than those of aerosol direct (-1.59 Wm^{-2}) and possible indirect effect (-1.38 Wm^{-2}) in terms of a spatially averaged TOA value, the aerosol direct and indirect effects have far greater *NGoRF* values (~0.18) than that of GHG (~0.003). This large *NGORF* indicates that aerosol direct and indirect effects must have stronger contributions to the atmospheric heating and resultant pressure gradient that induces various atmospheric circulations [*Matsui and Pielke* 2006].

Chapters 5, 6, and 7 examine the *aerosol diffuse-radiation effect* over the eastern U.S. In comparison with the *aerosol direct* and *indirect effect*, *aerosol diffuse-radiation effect* has been examined only in limited studies [*Roderick et al.* 2001; *Gu et al.* 2003; *Niyogi et al.* 2004]. While the previous studies have shown the observational evidence of aerosol diffuse-radiation effects on the local scale, there is a need to include *aerosol diffuse-radiation effect* in climate models for examining the effect on the regional to global scale. This requires development of a regional simulation framework, including a construction of regional-scale AOD map and development of a robust sun-shade canopy scheme in the land-surface model that accounts for the aerosol diffuse-radiation effect. Chapters 5, 6, and 7 focus particularly on the conterminous U.S. (CONUS) or eastern

U.S., which features high concentrations of anthropogenic aerosols (sulfate and its precursor gases) over a dense forest and agricultural crops. In addition, this region has high concentrations of ground-based observation sites that support developing a modeling framework. Thus, these factors suggest the eastern U.S. as an ideal region to examine the *aerosol diffuse-radiation effect* [*Niyogi et al.* 2004].

Chapter 5 evaluates aerosol optical depths (AOD) products from the Moderate Resolution Imaging Spectroradiometer (MODIS) and the Goddard Chemistry Aerosol Radiation and Transport (GOCART) model and their integrated products, and examines which product agrees best with ground measurements across the eastern U.S. from March 1, 2000 to December 31, 2001. The result shows that the Terra MODIS Level-3 (collection 4) AOD at 0.55 μm has better correlation with the observations, but consistently overestimates the AODs from the Aerosol Robotic Network (AERONET) measurements. GOCART has small biases of AODs for a 22-month integration, and slight positive biases of AODs appear for the cold season. These results are also supported by comparison with the IMPROVE (Interagency Monitoring of Protected Visual Environments) light extinction index. Optimal interpolation of MODIS and GOCART products improves the daily-scale RMSE of AODs from either MODIS or GOCART alone in warm seasons, while it does not improve the AOD due to the positive biases of MODIS and GOCART products in cold season. This suggests that the regional biases in the aerosol products constitute a major constraint in the optimal estimate of AODs [*Matsui et al.* 2004a].

A framework is needed to assess and calibrate the complex sun-shade scheme in a land-surface model on the regional scale. Chapters 6 and 7 are aimed at a continental-

scale comprehensive calibration and assessment of the sophisticated sun-shade canopy scheme in the land-surface model, denoted as Colorado State University Unified Land Model (ULM). This calibration frame work is composed of the sophisticated off-line LSM simulation system (NASA GSFC LIS), the unbiased regional-scale meteorological forcing from the North American Land Data Assimilation (NLDAS), and Parameter Estimation (PEST) model. First (chapter 6), the vegetation and soil optical parameters are calibrated in different land-cover classes by comparing model-predicted surface albedo with those derived from the Moderate Resolution Imaging Spectroradiometer (MODIS) (including black- and white-sky albedo for visible and near infrared band). The sum of squared deviations (Ψ) between model- and MODIS-derived albedo is iteratively reduced via the Gauss-Marquardt-Levenberg (GML) algorithm. The calibration process (i) reduced Ψ by about 80% for non-calibrated as well as calibrated seasons and years, (ii) revealed the functional biases related to diffuse-radiation upscattering parameters in two-stream canopy radiation scheme (which was fixed before the second calibration), and (iii) shows that the some of the parameters cannot be tuned [*Matsui et al.* 2006b].

Second (chapter 7), parameters related to aerodynamic resistances, soil-moisture stress function, and photosynthesis capacity in the ULM are calibrated against the surface eddy-covariance measurements of sensible/latent heat flux and CO_2 fluxes as well as satellite-derived land surface temperature (LST). Canopy roughness length in ULM has been decreased significantly in order to raise the daytime radiative temperature in the ULM. Optimum level of soil moisture is also added in the function of soil moisture stress on the photosynthetic capacity, because canopy photosynthesis overly reacts to the initial soil-moisture-stress function. Within-canopy profiles of photosynthesis capacity were

diagnosed based on the monthly means values of CO_2 flux and leaf area index (LAI). Although i) there are relatively small biases of LST; and ii) uncertainties in surface flux for some land-cover classes (particularly croplands), most of the significant biases in ULM were removed after the calibrations on the regional scale [*Matsui et al.* 2006c].

By using the well-calibrated sun-shade canopy model, the remainder of chapter 7 seeks to address the following question.

- *What is the effect of the routine aerosol loading on the terrestrial carbon and energy fluxes over the eastern U.S.?*

As examined in chapter 5, aerosols are heterogeneously concentrated in time and space over the eastern U.S. In addition, the eastern U.S. comprises different land-cover classes, LAI and soil types. Thus, a simulation study must be conducted to examine the *aerosol diffuse radiation effect*. The well-calibrated ULM is run in off-line mode over the similar period to the model calibration, but also including 2001 to examine the sensitivity in different synoptic weather (especially cloud cover and surface air temperature) conditions. Shortwave radiation is perturbed in with- and without-aerosol conditions by using the MODIS-GOCART assimilated AOD. Analyses examine the spatio-temporal variability of the *aerosol diffuse radiation effect*, focusing on the mechanical response of the parameterized sun-shade canopy to variability of diffuse radiation under various environmental factors, such as LAI, cloud cover, land-cover types, and temperatures. Downwelling shortwave radiation is computed with (a control experiment) and without (a potential experiment) assimilated daily AOD in all-sky conditions. The sensitivity experiments (control-potential) show that aerosol loading increases plant productivity in mixed forests and deciduous broadleaf forests in the southeastern U.S., while plant

productivity is decreased over the croplands and grasslands. The spatio-temporal variability of the aerosol diffuse-radiation effect is well explained by the variability of LAI, cloud optical depth, near-surface atmospheric temperature, and diurnal cycles. Due to the combination of the positive and negative effects, the aerosol diffuse-radiation effect increases plant productivity by only +0.5% in 2001 and –0.09% in 2000 from the potential experiment over the eastern U.S.

Chapter 8 addresses summaries and further discussion of each chapter and proposes future research directions to address remaining uncertainties.

References

Anderson, T. L., R. J. Charlson, S. E. Schwartz, R. Knutti, O. Boucher, H. Rodhe, and J. Heintzenberg (2003), Climate forcings by aerosols—A hazy picture. *Science.,* 300, 1103–1104.

Goudriaan, J. (1977), *Crop Micrometeorology: A Simulation Study.* Center for Agricultural Publication and Documents, Wageningen, 249 pp.

Gu, L., Dennis D. Baldocchi, Steve C. Wofsy, J. William Munger, Joseph J. Michalsky, Shawn P. Urbanski, and Thomas A. Boden (2003), Response of a Deciduous Forest to the Mount Pinatubo Eruption: Enhanced Photosynthesis, *Science*, 299, 2035-2038.

Harshvardhan, R. (1993), Chapter 3: Aerosol-climate interactions. *Aerosol–Cloud–Climate Interactions,* P. V. Hobbs, Ed., Academic Press, 76–93.

Haywood, J., and O. Boucher (2000), Estimates of the direct and indirect radiative forcing due to tropospheric aerosols: A review. *Rev. Geophys.,* 38, 513–543.

Hobbs, P.V. (1993), Chapter 2: Aerosol-cloud interactions. Tropospheric aerosols. *Aerosol–Cloud–Climate Interactions,* P. V. Hobbs, Ed., Academic Press, 33–69.

Houze, R. A. Jr, 1993: *Cloud Dynamics*. Academic Press, 573 pp.

IPCC Third Assessment Report (2001), *Climate change 2001: The scientific basis*. J.T. Houghton et al., Eds.,Cambridge Univ. Press, Cambridge, 994 pp.

Jaenicke, R. (1993), Chapter 1: Tropospheric aerosols. *Aerosol–Cloud–Climate Interactions,* P. V. Hobbs, Ed., Academic Press, 1–31.

Lau, K.-M., M.-K. Kim, and K.-M. Kim (2006), Aerosol induced anomalies in the Asian summer monsoon – the role of the Tibetan Plateau. *Climate Dynamics*, in press.

Lohmann, U., and J. Feichter (2005), Global indirect aerosol effects: A review. *Atmos. Chem. Phys.,* 5, 715–737.

Roderick M.L., G.D. Farquhar, S.L. Berry, and I.R. Noble (2001), On the direct effect of clouds and atmospheric particles on the productivity and structure of vegetation. *Oecologia*, 129(1), 21-30.

Rotstayn, L. D., and U. Lohmann (2002), Tropical rainfall trends and the indirect aerosol effect. *J. Climate.,* 15, 2103–2116.

Matsui, T., H. Masunaga, R. A. Pielke Sr., and W.-K. Tao (2004a), Impact of aerosols and atmospheric thermodynamics on cloud properties within the climate system. *Geophys. Res. Lett.* 31, L06109, 10.1029/2003GL019287.

Matsui, T., S. M. Kreidenweis, R.A. Pielke Sr., B. Schichtel, H. Yu, M. Chin, D.A. Chu, and D. Niyogi (2004b), Regional comparison and assimilation of GOCART and MODIS aerosol optical depth across the eastern U.S. *Geophys. Res. Letts.*, 31, L21101, doi:10.1029/2004GL021017.

Matsui, T. H. Masunaga, S.M.Kreidenweis, R.A.Pielke, Sr, W.-K. Tao, M. Chin, Y. Kaufman (2006a), Satellite-based assessment of global warm cloud properties associated with aerosols, atmospheric stability, and diurnal cycle, *J. Geophys. Res.* 111, D17204, doi:10.1029/2005JD006097

Matsui, T. and R.A. Pielke Sr. (2006b), Satellite-based estimation of spatial gradient of aerosol radiative forcing, *Geophys. Res. Letts.* 33, L11813, doi:10.1029/2006GL025974.

Matsui, T., A. Beltrán-Przekurat, R. A. Pielke Sr., D. Niyogi, and M. B. Coughenour (2006c), Continental-scale multi-observation calibration and assessment of Colorado State University Unified Land Mode by Application of MODIS surface albedo, *J. Geophys. Res.* (Accepted)

Matsui, T., A. Beltrán-Przekurat, R. A. Pielke Sr., D. Niyogi, S. A. Denning, M. Coughenour, and Z. Wan (2006d), Mechanical Response of Plant Productivity and Surface Energy Budget to the Aerosol Direct Effect over Eastern U.S., Using A Well-Calibrated Sun-Shade Canopy Model, (in preparation)

Menon, S, J Hansen, L Nazarenko, and Y. F Lua (2002), Climate effects of black carbon aerosols in China and India. *Science,* 297, 2250–2253.

National Research Council (2005), *Radiative forcing of climate change: Expanding the concept and addressing uncertainties.* The National Academies Press, Washington, D.C.

NACIP, National Aerosol-Climate Interaction Program (NACIP) White Paper, May 21, 2002, http://www-nacip.ucsd.edu/NACIPWhitePaperMay2102.pdf

Niyogi, D., H.-I. Chang, V.K. Saxena, T. Holt, K. Alapaty, F. Booker, F. Chen, K.J. Davis, B. Holben, T. Matsui, T. Meyers, W.C. Oechel, R.A. Pielke Sr., R. Wells, K. Wilson, and Y. Xue (2004), Direct observations of the effects of aerosol loading on the net ecosystem CO_2 exchanges over different landscapes. *Geophys. Res. Letts.*, 31, L20506, doi:10.1029/2004GL020915.

Twomey, S., M. Piepgrass, and T. L. Wolfe (1984), An assessment of the impact of pollution on global cloud albedo. *Tellus,* 36B, 356-366.

Yu, H., et al. (2005), A review of measurement-based assessment of aerosol direct radiative effect and forcing. *Atmos. Chem . Phys. Discuss.*, 5, 7647-7768.

Chapter 2

SATELLITE-BASED ASSESSMENT OF IMPACT OF AEROSOLS AND ATMOSPHERIC THERMODYNAMICS ON WARM RAIN PROCESS

2.1. Introduction

Maritime low clouds, denoted hereafter as stratus, reduce the Earth's energy budget by approximately 15W/m^2 in an annual average through an imbalance between the longwave emission and the reflection of solar radiation [*Hartmann et al.,* 1992]. Variability in Maritime low clouds modulates the warm rain rate, which is estimated to account for 31% of the total surface precipitation over the tropics [*Lau and Wu* 2004]. This large impact of stratus to the Earth's radiation budget and water cycle has motivated studies to examine the factors governing the microphysical properties of stratus.

Stratus amount is, in particular, positively correlated with *lower-tropospheric stability* (LTS), defined as the potential temperature difference between the surface and the 700mb pressure level [*Klein and Hartmann,* 1993]. *Klein and Hartmann* [1993] demonstrate that high LTS represents a strong temperature inversion at the top of the atmospheric boundary layer, and the regional observations show that the stratus cloud is confined to the boundary layer in high LTS, while extending their horizontal areal

coverage.

Aerosols also control stratus properties by acting as cloud condensation nuclei (CCN) to form cloud droplets. A high concentration of the aerosols overseed cloud droplets to generate highly concentrated, narrowly distributed cloud droplet spectra, which is expected to increase the cloud albedo up to 30% [*Twomey et al.,* 1984]. Narrowly distributed cloud droplet spectra prevent the formulation of precipitation. This climatic impact of aerosols on cloud properties is called the aerosol indirect effect, which is one of the largest uncertainties in accurately describing the sensitivity of climate to changes in aerosol concentrations in the future.

Figure 2.1 exhibits a global distribution of seasonally-averaged LTS (color contours) derived from the NCEP/NCAR Reanalysis [*Kalnay et al.,* 1996] and seasonally-averaged aerosol index derived from the MODerate resolution Imaging Spectroradiometer (MODIS) (dark shaded) [*Tanré et al.,* 1997]. The aerosol index is better correlated than aerosol optical depths with the column aerosol concentrations under some assumptions [*Nakajima et al.,* 2001], and was derived from the aerosol optical

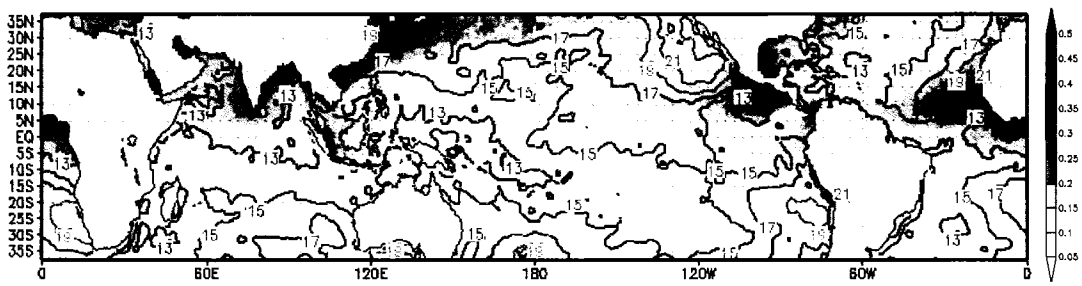

Figure 2.1. Global distribution of aerosol index (dark shaded) from the MODIS measurements and lower-tropospheric static stability (LTSS) (K) (colored contour) derived from the NCEP/NCAR Reanalysis averaged through March-May 2000.

thickness at 0.55μm and Ångstrom exponent computed from 0.55 and 0.865μm. Different contributions from these two factors across the globe possibly influence the cloud microstructure. This paper examines the sensitivity of the aerosol effect to the cloud properties on a global scale due to the background atmospheric thermodynamic structure.

2.2. TRMM-Derived Cloud Properties

Masunaga et al. [2002a] proposed a new algorithm that simultaneously derives different cloud properties through a combined use of data from the TRMM Microwave Imager (TMI) and Visible/Infrared Radiance Imager (VIRS). First, VIRS radiances at 0.63 micron, 3.7 micron, and 10.8 micron are used to derive low-cloud optical depths, cloud-top droplet effective radius (Re(top)), and cloud-top temperature [*GTR* 1.0 package from T.Y. Nakajima, personal communication, 2002]. Second, TMI brightness temperatures at 10.65GHz, 19.35GHz, and 37.0GHz yield the column water vapor and cloud liquid water path (CLWP) for the VIRS-derived cloud-top temperatures and cloud fractions. The look-up table used by the microwave algorithm was updated so that it allows realistic variability of the water vapor and temperature profiles to improve the products obtained by *Masunaga et al.* [2002a]. The TMI-derived CLWP ($CLWP_{TMI}$) with the VIRS-derived optical thickness (τ_{VIRS}) provide the cloud droplet effective radius (Re) via

$$\mathrm{Re}(column) = \frac{1.5\ CLWP_{TMI}}{\rho_w \tau_{VIRS}},$$

where ρ_w represents water density. Re(*column*) represents column-integrated Re, since microwave brightness temperature and visible radiance do not suffer from saturation within any cloud thickness of marine low clouds (see the details of the algorithm in *Masunaga et al.* [2002a]).

This new algorithm provides the vertical structure of warm cloud (cloud top temperature > 273K) microstructure by investigating two types of droplet effective radius (Re): shortwave-derived droplet size (Re (top)) and microwave-derived droplet size (Re (column)). This is because a VIRS-derived Re tends to be biased toward a cloud-top value due to strong absorption of the near-infrared band, whereas a TMI-derived Re is expected to be close to the value averaged over the cloud layer since microwave can detect cloud droplets and rain drops without suffering from saturation within low maritime clouds. Partial cloudiness in a large TMI footprint is corrected by VIRS-derived cloud fraction [*Masunaga et al.,* 2002a].

Figure 2.2 shows the relationship between seasonally averaged (March – May) Re (top) and Re (column) at each grid between 37°N and 37°S. Re (top) generally ranges from 10 to 21μm, whereas Re (column) broadly ranges up to 50μm. Re (top) is generally larger than that derived from the *Bréon et al.* [2002], since optically thin, broken clouds (less than 30 % of TMI footprint) were omitted from the analysis in order to reduce the error associated with the surface emissivity in microwave analysis. Figure 2.2 can be used to judge different cloud modes due to the fact that clouds are likely to exhibit significant droplet growth when Re exceeds 15μm (see *Masunaga et al.,* [2002b] and references therein). A cloud with both Re (top) and Re (column) < 15μm in the zone-I is assigned as *non-precipitating*, since the cloud is not drizzling with Re (column) < Re

(top); i.e., cloud droplet sizes increase toward the cloud top. Clouds with Re (top) > 15μm and Re (column) < 15μm in the zone-II are assigned as *transitional*, since the droplets increase in size toward the cloud top where drizzle drops have begun to form. Clouds with Re (top) > 15 (μm) and Re (column) > 15 (μm) in the zone-III are assigned as *precipitating*, since the cloud is drizzling with Re (column) > Re (top); i.e., droplet sizes increase toward the cloud base, indicating the presence of larger precipitation-size droplets in that area. In a small number of clouds, Re (column) is greater than the Re (top), although Re (top) does not exceed the drizzle threshold. Clouds in zone-IV are assigned as *uncertain*.

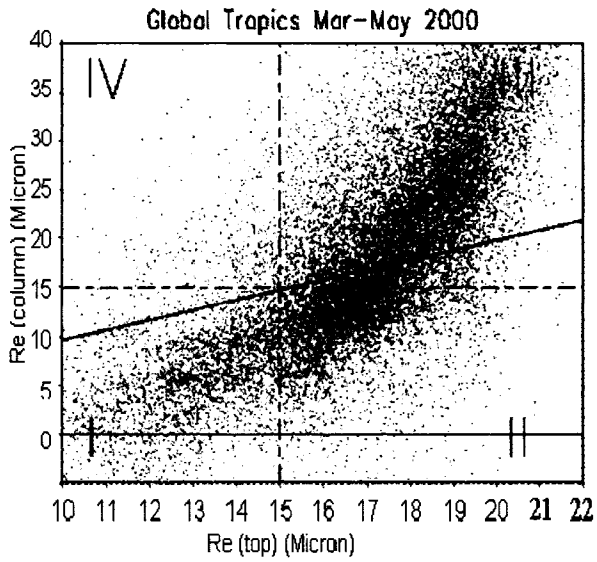

Figure 2.2. Seasonally averaged Re (top) and Re (column) at each grid box are compared. Dash lines represent 15-micron drizzle threshold. Solid line shows the 1:1 ratio between Re (top) and Re (Column). Re (column) is greater than the Re (top) when clouds are located above the solid line.

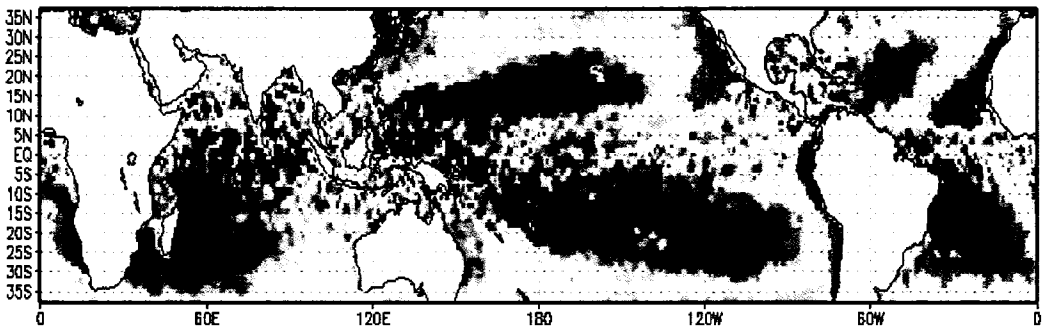

a)

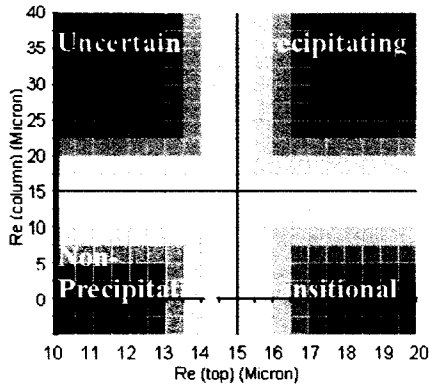

b)

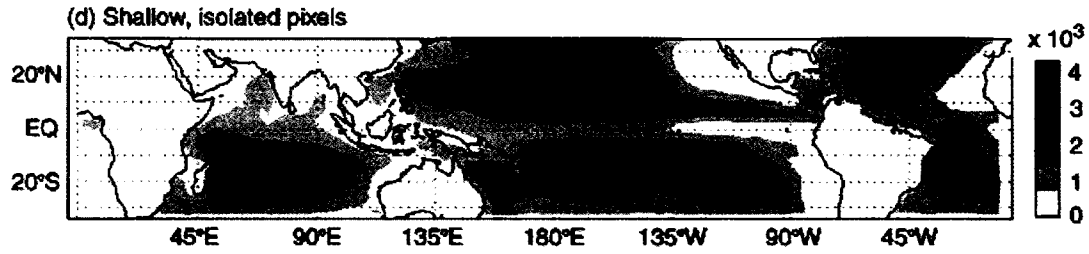

c)

Figure 2.3. a) Global distribution of non-precipitating (red), transitional (green) and precipitating (blue) modes of warm cloud averaged through March-May 2000. b) Color coordination based on the warm cloud modes. c) Counts of shallow, isolated pixels observed by TRMM Precipitation Rader (PR) by *Schumacher and Houze* [2003] (copy right from AMS).

Figure 2.3a shows a global map of four cloud modes by overlaying the global distribution of Re (column) and Re (top) with a color coordination to represent the degree

of the cloud mode (Figure 2.3b). Non-precipitating stratus (red) exists downwind of continents. Those regions are generally characterized with polluted (a high aerosol index) and/or stable atmosphere (high LTSS) (Figure 2.1). The stratus in the rest of the subtropical regions characterized with relatively polluted and moderately stable atmosphere is in the transitional mode (green). Transitional stratus is also found in the Inter Tropical Convergence Zone and the Pacific Warm Pool where deep cumulus convection (cold-rain process) promotes a subsidence in the surrounding warm clouds.

Precipitating stratus (blue) is found in the outer fringes of the tropical rain area. These regions, compared to the regions with non-precipitating stratus, are generally characterized with pristine and/or less stable atmosphere (Figure 2.1). The areas with precipitating clouds correspond to the warm rain regions observed by the TRMM Precipitation Radar [*Schumacher and Houze,* 2003] (Figure 2.3c). Uncertain stratus (black) is present in a small portion of the north Indian Ocean and Caribbean Sea.

2.3. Sensitivity of the Aerosol-Cloud Interaction

Since it is difficult to quantify the relationship from the seasonal mean values, a statistical analysis is performed for the individual estimates of stratus, aerosol index, and LTS. The three individual datasets are not precisely concurrent in time and space. The daily 1° MODIS aerosol index, 0.25° TRMM cloud properties, and 2.5° LTS from the NCEP/NCAR reanalysis are directly related each other without spatial interpolation. The maximum difference in overpass timing between the TRMM and the MODIS is set to be 3 hours, minimizing the error associated with the different satellite overpasses. The LTS from the NCEP/NCAR Reanalysis is linearly interpolated for the TRMM overpass timing.

The total sampling number of the quasi-coincident observations was 462,289; 287,007 of the total were observed in the subtropical region (25°-37°N and 25°-37°S), while 170,304 of the total were observed in the tropical region (25°S – 25°N).

The means of Re (top) and Re (column) were derived with a given aerosol index (bins of 0.02) and LTS (bins of 0.4 K) (Figure 2.4). The three-dimensional slope shows that high aerosol index and/or high LTS leads to the smaller droplet size in both Re (column) and Re (top); i.e., a larger temperature inversion and higher concentrations of aerosols inhibit cloud droplet growth. On the other hand, cloud droplet sizes are maximized in the pristine and less stable atmosphere.

For a fixed liquid water path, the relationship between *Re* and aerosol index is expressed as [e.g., *Bréon et al.*, 2002]

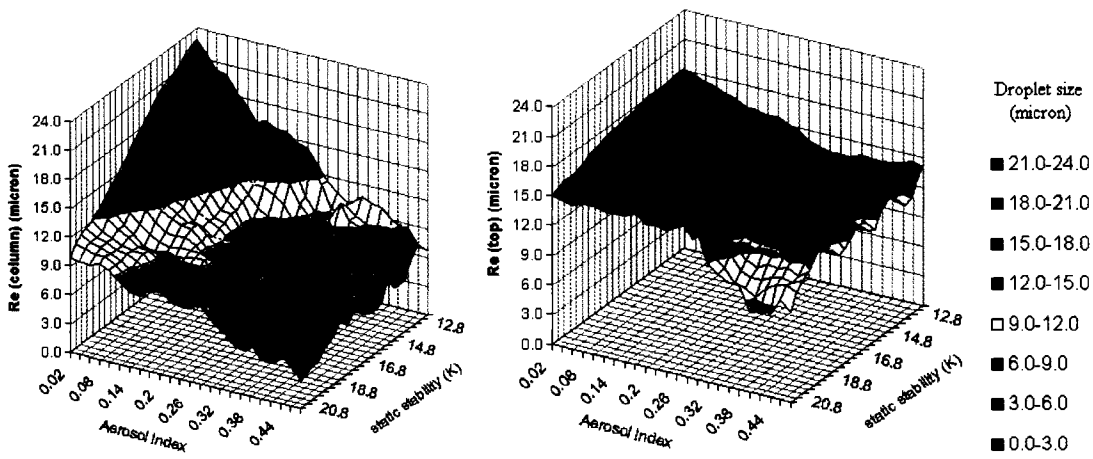

Figure 2.4. The mean of Re (top) and Re (column) were derived for sets with a given aerosol index (bins of 0.01) and low-atmosphere static stability (bins of 0.4 K) from May to March.

$$\frac{d\log(\mathrm{Re})}{d\log(AI)} = \frac{\alpha}{3}, \qquad (1)$$

where AI is aerosol index, and α approximately relates the aerosol index to the number of cloud droplets (N_c) via $N_c \approx (AI)^{\alpha}$. The slope (α/3) is a parameter that simply quantifies the magnitude of the aerosol indirect effect. Since the standard errors ($\sigma/\sqrt{n-2}$, where n and σ are the number of quasi-coincident measurements for each bin and is standard deviation, respectively) are generally larger for the bins of higher aerosol index due to the lack of the sample number, the slopes for an aerosol index > 0.25 are derived. Although the sampling and statistical processes are different from the previous studies in a strict manner, the slope of Re (top) averaged over a full range of LTS (0.069) is close to that derived from *Bréon et al.* [2002] (0.085) and less than 50% of that derived from *Nakajima et al.* [2001] (0.16). The slope of Re (column) is 0.222, which is three times larger than that of Re (top), and is close to that using a characteristic value, α= 0.7 [*Charlson et al.,* 1992]. Finally, Figure 2.5 provides the distribution of the cloud modes as functions of the aerosol index and the LTSS with the color coordination in Figure 2.3b. Precipitating stratus (blue) exists when the aerosol index and LTS are less than approximately 0.08 and 16.8, respectively. Note that the absence of dark blue, which dominates the tropical region in Figure 2.3, is due to the sampling biases mentioned above. Therefore, Figure 2.5 should be considered to mainly represent cloud-aerosol interaction in the subtropical region. Non-precipitating stratus (red) exists with a high aerosol index (~0.24). Transitional stratus (green) lies between the non-precipitating and precipitating stratus. The boundaries of three cloud modes are tilted toward the higher LTSS. Figure 2.5 clearly shows that a high aerosol concentration suppresses the cloud

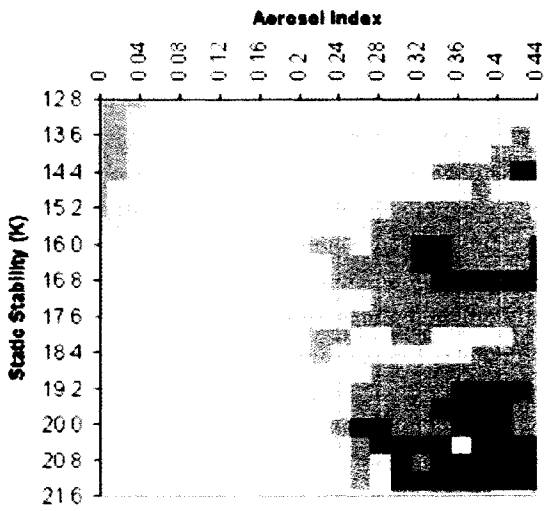

Figure 2.5. Re (column) and Re (top) are overlaid and colored based on the Figure 2.3b.

droplet growth and warm rain process under low static stability; nevertheless, the warm rain process is prevented regardless of aerosol concentration under a high static stability where a strong temperature inversion exists.

2.4. Summary and Perspectives

This study demonstrates an important sensitivity of the aerosol effect on the cloud-precipitation process to the different static stability regimes through a simultaneous examination of the cloud-top and columnar droplet effective radius. A combination of cloud-top and columnar droplet sizes derived from the multi Tropical Rainfall Measurement Mission (TRMM) sensors reveals the sensitivity of the aerosols effect on cloud-precipitation processes due to environmental vertical thermodynamic structure. First, the magnitude of aerosol indirect effect could be larger with the analysis of columnar droplet sizes than that derived from the cloud-top droplet sizes since column-

droplet size can account for the broader droplet spectra in the cloud layers. Second, a combination of cloud-top and columnar droplet sizes reveals that the warm rain process is prevented regardless of the aerosols concentration under high static stability such as when a strong temperature inversion exists, while a high aerosol concentration suppresses the warm rain formulation under low static stability. The cloud-aerosol interaction is clearly identified except where LTS is so high that the cloud droplet growth is dynamically suppressed.

A further analysis is required for a more quantitative assessment. This study does not account for the vertical distribution of the aerosol concentration. A possible solution is to combine the aerosol dataset from MODIS and a global chemical transport model to distinguish the aerosols above the warm cloud, such as the dust aerosols from the Gobi and Sahara desert [*Ginoux et al.,* 2001]. Indeed, multi-seasonal and multi-year datasets will provide a sufficient sampling number to derive a statistically significant relationship in the specific regions where the chemical compositions of aerosols strongly differ.

REFERENCES

Bréon, F.-M., D. Tanré, and S. Generoso (2002), Aerosol effect on cloud droplet size monitored from satellite, *Science,* **295**, 834-838.

Charlson R. J., S. E. Schwartz, J. M. Hales, R. D. Cess, J. A. Coakley Jr., J. E. Hansen, and D. J. Hofmann (1992), Climate forcing by anthropogenic aerosols, *Science,* **255**, 423-430.

Feingold, G., W. L. Eberhard, D. E. Veron, and M. Previdi (2003), First measurements of the Twomey indirect effect using ground-based remote sensors, *Geophys. Res. Lett.*. **30**(6), doi:0.029/2003GL017967.

Ginoux, P., M. Chin, I. Tegen, J. Prospero, B. Holben, O. Dubovik, and S.-J. Lin (2001), Sources and global distributions of dust aerosols simulated with the GOCART model, *J. Geophys. Res.*, **106**, 20,255-20,273.

Hartmann, D. L., M. E. Ockert-Bell, and M. L. Michelsen (1992), The effect of cloud type on earth's energy balance: Global analysis. *J. Clim.*, **5,** 1281-1304.

Kalnay *et al.* (1996), The NCEP/NCAR 40-year reanalysis project. *Bull. Amer. Meteor. Soc.*, **77**, 437-471.

Klein, S. A., and D. L. Hartmann (1993), The seasonal cycle of low stratiform clouds., *J. Clim.*, **6**, 1587-1606.

Masunaga, H., T. Y. Nakajima, T. Nakajima, M. Kachi, R. Oki, and S. Kuroda (2002a), Physical properties of maritime low clouds as retrieved by combined use of Tropical Rainfall Measurement Mission Microwave Imager and Visible/Infrared Scanner: Algorithm, *J. Geophys. Res.* **107**(10), doi:10.1029/2001JD000743.

Masunaga, H., T. Y. Nakajima, T. Nakajima, M. Kachi, K. Suzuki (2002b), Physical properties of maritime low clouds as retrieved by combined use of Tropical Rainfall Measurement Mission Microwave Imager and Visible/Infrared Scanner 2. Climatology of warm clouds and rain, *J. Geophys. Res.* **107**(19), doi:10.1029/2001JD001269.

Nakajima, T., A. Higurashi, K. Kawamoto, and J. E. Penner (2001), A possible correlation between satellite-derived cloud and aerosol microphysical parameters, *Geophys. Res. Lett.*, **28**, 1171-1174.

Rosenfeld, D., and G. Feingold (2003), Explanation of discrepancies among satellite observations of the aerosol indirect effect, *Geophys. Res. Lett.* **30**(14), doi;10.029/2003GL017684.

Schumacher, C., and R. A. Houze Jr. (2003), The TRMM Precipitation Radar's View of Shallow, Isolated Rain. *J. Appl. Meteorol.*, **42**, 1519-1524.

Tanré, D., Y. J. Kaufman, M. Herman, and S. Mattoo (1997), Remote sensing of aerosol properties over oceans using the MODIS/EOS spectral radiance. *J. Geophys. Res.*, **102**, 16,971-16,988.

Chapter 3

SATELLITE-BASED ASSESSMENT OF MARIN LOW CLOUD VARIABILITY ASSOCIATED WITH AEROSOL, ATMOSPHERIC THERMODYNAMICS, AND THE DIURNAL CYCLE

3.1. Introduction

Global low cloud properties critically control the Earth's radiation budget and hydrological cycle. Marine low clouds have been extensively observed in the descending branch of the Hadley Circulation, where large-scale subsidence occurs [*Klein and Hartmann* 1993]. Marine low clouds have an annually- and globally-averaged net cooling effect of -15 (W/m^2) [*Hartmann et al.* 1992]. A four-percent increase in low cloud cover could offset the anthropogenic greenhouse gas warming due to a doubling of CO_2 [*Slingo* 1990]. The *National Research Council (NRC)* [2005] highlighted the importance of cloud radiative effects within the climate system. This large effect on the Earth's climate prompts scientists to examine the variability of low cloud properties as linked to various meteorological parameters, such as sea surface temperature (SST), relative humidity (RH) near cloud layers, and lower-tropospheric stability (LTS) [e.g., *Weare* 1994; *Klein and Hartmann* 1993; *Park and Leovy* 2004; *Klein* 1997]. Comparisons of different parameters used in cloud models show that no single meteorological parameter explains more than

13% of the variance in low-cloud amounts, and that multiple regressions using a combination of different parameters do not increase the explained variance [*Klein* 1997].

Marine low clouds have a strong diurnal cycle due to radiation-driven turbulence in the cloud-capped marine boundary layer [e.g., *Driedonks and Dynkerke* 1989]. In the early morning, solar radiation starts heating the sub-cloud layer, while longwave emission cools the cloud top. The combination of longwave cooling and shortwave heating drives turbulent mixing that i) destabilizes the cloud layer separately from the rest of the boundary layer, and ii) induces entrainment of dry air that thins the cloud layer in a complex manner. The isolated layer progressively thins the cloud during the late morning and into the afternoon [see the review in *Driedonks and Duynkerke* 1989]. This diurnal cloud cycle was captured in the Atlantic Stratocumulus Transition Experiment (ASTEX) [*Ciesielski et al.* 2001], in the First International Satellite Cloud Climatology Project Regional Experiment (FIRE) [*Hignett* 1991], and in observations from the California coastal region [*Betts* 1990]. *Wood et al.* [2002] showed the semi-global-scale diurnal cycle of the cloud liquid water path (CLWP) using a two-year dataset from the Tropical Rainfall Measuring Mission (TRMM) satellite. They demonstrated that the diurnal cycle generally peaked early in the morning, but that the timing of those peaks varied slightly in different geographic regions.

In recent decades, advanced space-borne satellites and global modeling systems investigated the global distribution of aerosol concentrations [*Kaufman et al.* 2002]. Hygroscopic aerosol particles serve as cloud condensation nuclei (CCN) that initiate the formation of cloud droplets. Higher concentrations of sub-micron aerosols are expected to reduce the average size of cloud droplets, in turn increasing the cloud albedo under the

assumption of constant liquid water content [*Twomey et al.* 1984], and could enhance the cloud liquid water path by inhibiting the precipitation initiation process [*Albrecht* 1989]. These aerosol-cloud-climate linkages are called the *aerosol indirect effects*. Many studies show a reduction of cloud droplet size associated with high aerosol concentrations observed in ground-based experiments [e.g., *Feingold et al.* 2003; *Penner et al.* 2004] as well as in satellite imagery [e.g., *Kaufman and Fraser* 1997; *Nakajima et al.* 2001; *Bréon et al.* 2002; *Matsui et al.* 2004a; *Kaufman et al.* 2005]. Some of the studies capture rainfall inhibition due to air pollution [*Rosenfeld* 1999; *Matsui et al.* 2004a]. Although many researchers show links between small cloud droplets and high aerosol concentrations in the ambient air, they do not consistently find a dramatic increase in cloud albedo as initially hypothesized, probably due to the complicated feedbacks involving thermodynamics and below-cloud turbulent mixing processes [*Jiang et al.* 2002].

Another important aspect of the aerosol effect is that aerosol particles absorb and scatter radiation, which is denoted as the *aerosol direct effect*. Absorbing aerosols, such as black carbon and mineral dust, could contribute to high diabatic heating in the atmosphere that often enhances cloud evaporation (the *semidirect effect*) [*Ackerman et al.* 2000; *Koren et al.* 2004; *Kruger and Graßl* 2004]. Atmospheric diabatic heating could strengthen inversions, which could inhibit the cyclogenesis process and consequently constrain hurricane tracks [*Dunion and Velden* 2004]. *Ramanathan et al.* [2001] suggested that a combination of the aerosol direct and indirect effects could weaken the hydrological cycle, which could be a major environmental issue in this century.

To summarize, the large-scale thermodynamic field, the radiation-driven diurnal cycle, and aerosol-cloud interactions are all critical in understanding the variability of global marine low cloud properties. This study attempts to incorporate these aspects together to arrive at a deeper understanding of marine low cloud variability. This study extends the analysis by *Matsui et al.* [2004a] to an annual cycle (section 2), includes different aerosol datasets (section 2.1), examines not only cloud droplet size but also cloud liquid water path and cloud albedo (section 2.3), statistically quantifies the relationship on the global scale (section 3.1) and local scale (section 3.2), and examines the diurnal cycle in regions with different thermodynamic environments and aerosol concentrations (section 3.3).

3.2. Datasets and Method

3.2.1. Lower-Tropospheric Stability (LTS) from the NCEP Reanalysis

A large amount of latent heat release over the warm sea surface drives upward motion in the equatorial regions and large-scale subsidence in the sub-tropics. The large-scale subsidence over cold sea surface temperatures (SST) creates a strong inversion in the lower troposphere. Consequently, cool, moist air below the inversion layer supports an increase in the relative humidity (RH) and, thus, frequent cloudiness. The magnitude of the inversion strength can be measured as the potential temperature difference between the atmosphere at the 700-mb level and the surface, denoted as lower-tropospheric stability (LTS) [*Klein and Hartmann* 1993].

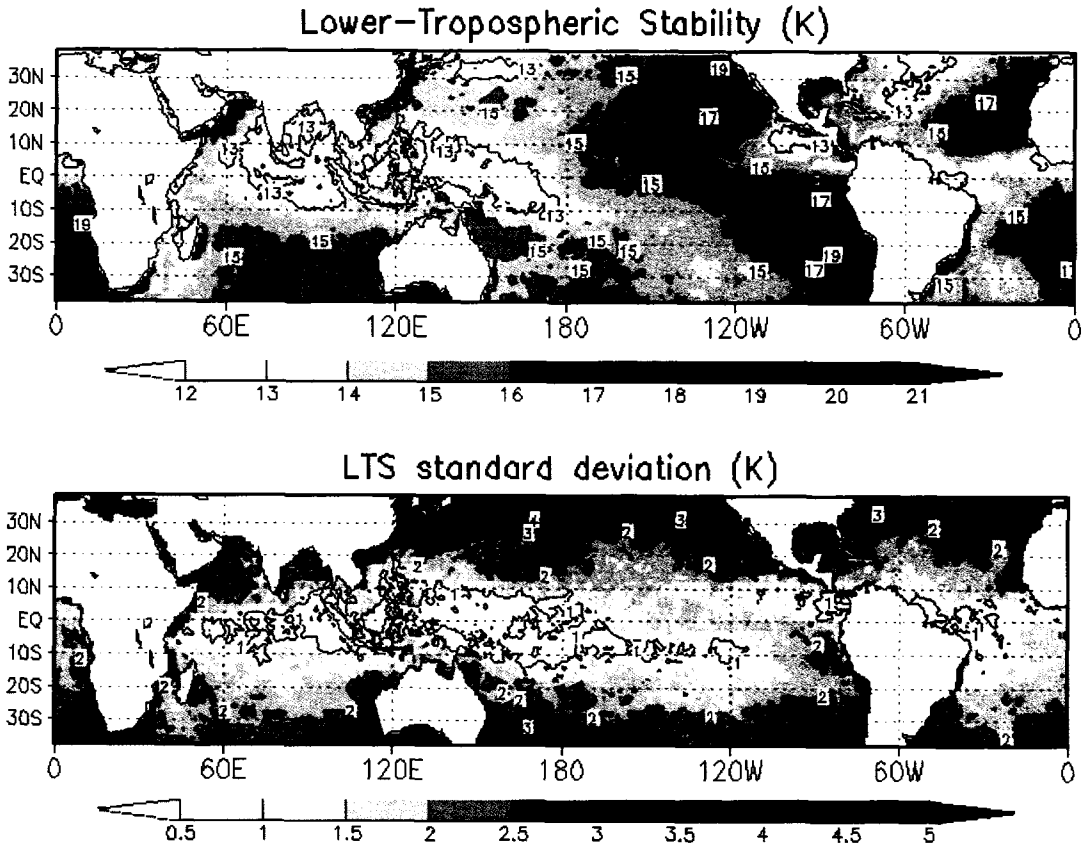

Figure 3.1. Annual mean (above) and standard deviation (below) of lower-tropospheric stability (LTS), sampled from March 2000 to February 2001. High LTS (strong inversion) regions are located in the eastern parts of major oceans.

Klein [1997] found that LTS is highly correlated with cloud amount, although other parameters such as lower-tropospheric relative humidity are important as well. This study focuses on LTS as an indicator of the thermodynamic environment, as was done in the previous study [*Matsui et al.,* 2004a], where low-cloud properties were investigated in terms of aerosols and LTS. While the role of other parameters is certainly important, their impact on low clouds is not considered in the present paper, as I wanted to focus specifically on LTS. LTS is also more readily derived from remote sensing soundings or objective analyses, in comparison with subgrid parameters, such as cloud updraft velocity

or turbulent kinetic energy. In this study, LTS is derived from the NCEP/NCAR reanalysis dataset (2.5° × 2.5° grid space) [*Kalnay et al.* 1996]. Although LTS can be correlated with aerosols on the regional scale, these correlations tend to be canceled out on the global scale. For example, global linear correlations between AI and LTS are -0.016 and 0.024 for the MODIS and GOCART cases. respectively. These values are significant at .05 level, but are very small. Regional correlations of LTS with AI can account for regional anomalies in the dependence of cloud properties on AI and LTS, as discussed later.

Figure 3.1 shows the annual mean and standard deviation of the global distribution of LTS sampled from March 2000 to February 2001 at the same sampling rate as that of the cloud dataset. LTS varies season-by-season and year-by-year. Regions with high LTS (strong inversions) are frequently observed off the coast of California, Namibia, and Chile. Those areas are located in the eastern parts of major oceans (Figure 3.1). Low-LTS regions are found in the tropics over warm SSTs, where surface energy flux and mass convergence create strong vertical mixing in the boundary layer. LTS exhibits large standard deviations in mid-latitude regions, in comparison to those in seen in the tropics (Figure 3.1), due to propagating synoptic fronts and seasonal shifts of the Hadley cell.

3.2.2. Aerosol Index from MODIS and GOCART

In this study, aerosol concentration is represented by the Aerosol Index (AI), which is the product of aerosol optical depth (AOD) and the Ångstrom exponent. AI is better correlated with column aerosol concentrations and cloud properties than is AOD

alone [*Nakajima et al.* 2001; *Bréon et al.* 2003]. Global aerosol distributions from satellite retrievals and global chemistry transport model calculations are used in this study, since both data have different advantages and disadvantages [*Yu et al.* 2003; *Chin et al.* 2004; *Matsui et al.* 2004b]. The satellite dataset used to compute AI is the Moderate Resolution Imaging Spectroradiometer (Terra MODIS) Level-3 (collection 4) instantaneous AOD at 0.55 μm and Ångstrom exponent between 0.55 μm and 0.87μm, which are archived on a global 1° × 1° latitude-longitude grid. A comprehensive description of the algorithm, sensor specification, validation, and datasets is summarized in *Remer et al.* [2005]. The other dataset used to compute AI is from the Goddard Chemistry Aerosol Radiation and Transportation (GOCART) model, which is a global chemical-aerosol-transport model driven by the Goddard Earth Observing System Data Assimilation System (GEOS DAS) global analysis (2° × 2.5° grid space). It prognoses a global distribution of sulfate and its precursors, organic carbon, black carbon, mineral dust, and sea salt (see details in *Chin et al.* [2002] and *Chin et al.* [2004]). This study computes AI from GOCART predictions of daily AOD at 0.55 μm and Ångstrom exponent between 0.55 μm and 0.90 μm. The Ångstrom exponent ($-\frac{d\log AOD}{d\log \lambda}$, where λ is the wavelength at which AOD is determined) is an indicator of the size distribution of aerosols; e.g., fine-mode particulate matter, such as sulfate and organic carbon, tend to be associated with high Ångstrom exponents, whereas the size distributions of coarse-mode particles, such as large sea salt and dust, tend to have low (near-zero) Ångstrom exponents.

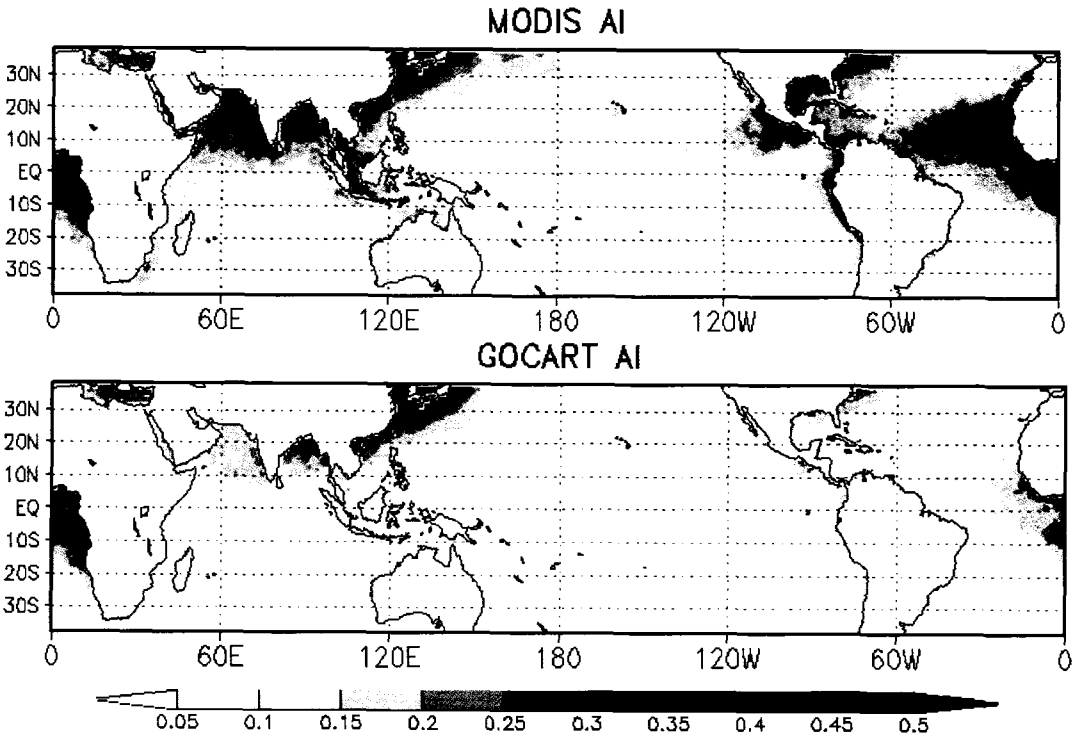

a)

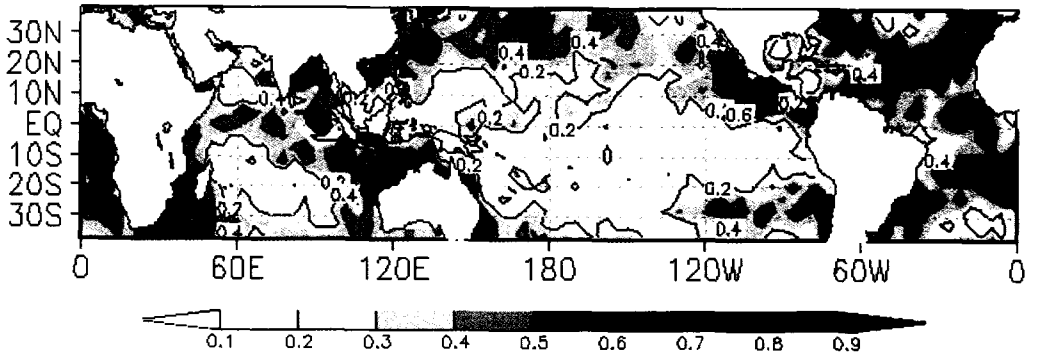

b)

Figure 3.2. a) Annual average of MODIS and GOCART AI. b) Local linear correlation coefficient (in 4° × 4° grid boxes) between daily GOCART AI and MODIS AI. All data are sampled from March 2000 to February 2001.

While satellite estimates of AOD are based on the measured instantaneous top-of-atmosphere (TOA) radiance, estimates of AOD from global chemistry transport models are calculated based on aerosol and precursor emissions inventories, atmospheric objective analysis, and simulated aerosol optical and microphysical properties.

Intercomparison of AOD at 0.55 μm between MODIS retrievals and GOCART simulations has been reported for global and regional scales [*Yu et al.* 2003; *Chin et al.* 2004; *Matsui et al.* 2004b]. Figure 3.2a shows the global distribution of GOCART and MODIS AI integrated from 1 March 2000 to 28 February 2001, whenever MODIS retrievals and GOCART outputs are simultaneously available. MODIS and GOCART AI exhibit high spatial coherence on global scales (correlation: 0.83). High values of AI appear along the coastlines of Asia, India, eastern U.S., and West Africa. Very small values of AI appear in the remote Indian and Pacific Oceans. However, local correlations (daily correlation in 4° × 4° grid boxes) are highly variable in different regions (Figure 3.2b). Remote oceans, particularly the southern portions of the Indian and Pacific Oceans, have correlations less than 0.2 between MODIS and GOCART AI, probably due to the low, and therefore more uncertain, AI values.

The GOCART model explicitly simulates different aerosol species in 4-dimensional fields. When the GOCART-predicted AOD is converted to AI, the summation of the contributions of sulfate, organic carbon, and black carbon represents approximately 97% of the total AI. Dust and sea salt together represent about 3% of the total AI, because the Ångstrom exponents of the assumed size distributions for those species are close to zero. Large particles of sea salt and sulfate-coated dust serve as giant cloud condensation nuclei (GCCN). GCCN potentially enhance the cloud drizzle process in environments characterized by high CCN concentrations, but probably have little effect in low-CCN-concentration environments where drizzle is active regardless of the presence of GCCN [*Feingold et al.* 1999]. However, it is not possible using AI to explicitly investigate the potential role of GCCN, as investigated by *Feingold et al.*

[1999]. Emissions of sulfate and sulfate precursors and of organic carbon are primarily from industrial and agricultural activities. Therefore, AI derived from multi-spectral AOD can be lined to the anthropogenic aerosol impact on marine low cloud. Although the size distributions assumed in the MODIS retrievals are slightly different from those used in GOCART, the correspondence between aerosol types and concentrations and MODIS AI can be similarly interpreted.

The vertical distribution of AI remains uncertain in satellite-based aerosol-cloud interaction studies [*Matsui et al.* 2004a, *Bréon et al.* 2002, *Nakajima et al.* 2001, *Sekiguchi et al.* 2003]. More accurate assessments will be available when the multi-satellite A-Train platform is established [*Stephens et al.* 2002; *Kaufman et al.* 2003].

3.2.3 Marine Low Cloud Properties from the TRMM Satellite

Masunaga et al. [2002a] proposed a new algorithm that simultaneously derives different cloud properties through a combined use of data from the TRMM Microwave Imager (TMI) and Visible/Infrared Radiance Imager (VIRS). First, VIRS radiances at 0.63 micron, 3.7 micron, and 10.8 micron are used to derive low-cloud optical depths, cloud-top droplet effective radius (Re(top)), and cloud-top temperature [*Kawamoto et al,.* 2001; GTR 1.0 package from T.Y. Nakajima, personal communication 2003]. Second, TMI brightness temperatures at 10.65GHz, 19.35GHz, and 37.0GHz yield the column water vapor and cloud liquid water path (CLWP) for the VIRS-derived cloud-top temperatures and cloud fractions. The look-up table used by the microwave algorithm was updated so that it allows realistic variability of the water vapor and temperature profiles to improve the products obtained by *Masunaga et al.* [2002a] and *Matsui et al.*

[2004a]. The TMI-derived CLWP ($CLWP_{TMI}$) with the VIRS-derived optical thickness (τ_{VIRS}) provide the cloud droplet effective radius (Re) via

$$\mathrm{Re}(column) = \frac{1.5\ CLWP_{TMI}}{\rho_w \tau_{VIRS}},$$

where ρ_w represents water density. Re(*column*) represents column-integrated Re, since microwave brightness temperature and visible radiance do not suffer from saturation within any cloud thickness of marine low clouds (see the details of the algorithm in *Masunaga et al.* [2002a]). Simultaneous analysis of Re(*top*) and Re(*column*) provides more information to examine warm rain processes [*Masunaga et al.* 2002b; *Matsui et al.* 2004a].

Klein and Hartmann [1993] showed that the low-cloud fraction is the primary parameter controlling the surface cooling effect. While many studies focus on the change in cloud optical depth and cloud fraction separately, this study uses cloud amount defined by the corrected cloud albedo, *CCA*:

$$CCA = A_{cloud} * CF,$$

where *CF* is the low cloud fraction in a 1 × 1 degree box derived from VIRS 2km-footprint pixels, and A_{cloud} is the cloud albedo, which is expressed for a plane-parallel cloud in a two-stream radiative transfer model [*Hobbs* 1993] as,

$$A_{cloud} = \frac{\tau_{VIRS}}{\tau_{VIRS} + 6.7}.$$

CCA accounts for cloud radiative forcing as the combined effect of the cloud optical depth and cloud fraction.

To define a VIRS 2km-footprint pixel that is overcast, the following criteria must be satisfied simultaneously [Kawamoto et al. 2001]. 1) radiances in channel 1 (λ=0.623μm), channel 2 (λ=1.610μm), and channel 3 (λ=3.784μm) are all positive; 2) solar zenith angle must be within 0 ~ 60°; 3) reflectance in channel 1 is greater than the sum of 0.1 and the ocean albedo value; 4) brightness temperature of channel 4 (λ=10.826μm) is less than the sea surface temperature; 5) brightness temperature of channel 4 (λ=10.826μm) is greater than brightness temperature of channel 5 (λ=12.028μm); 6) 3×3-window standard deviations of channel 1 is less than 100 $Wm^{-2}ster^{-1}\mu m^{-1}$, and 3×3-window standard deviations of brightness temperature of channel 5 is also less than 100 K, indicating a horizontally homogeneous pixel. Cloud pixels with high ambient aerosols were removed from the analysis by taking the 95% of the total PDF (Figure 3.3). These data screening procedures should ensure separation between cloudy pixels and pixels with very high aerosol concentrations.

3.2.4 Method of Analysis

This section describes the various statistical method and results. The sampling and statistical methods are as follows.

1. Sample the TRMM-derived low cloud properties, MODIS AI, GOCART AI, and NCEP LTS, only when they are simultaneously available. Note that the NCEP LTS is temporally interpolated to coincide with the TRMM satellite overpasses. MODIS AI values are instantaneous values at approximately 10:30 am local time, and GOCART AI values are daily averages. Although a time lag up to ± 5 hour exists between the

MODIS and TRMM overpasses, temporal autocorrelations of aerosol extinction are still very high in this range [*Anderson et al.* 2003].

2. Generate the probability density function (PDF) of MODIS AI, GOCART AI and NCEP LTS from the total samples (Figure 3.3).

3. Select 95% of the most frequent ranges from the total PDF by removing ± 2.5% of the smallest and largest values for MODIS AI, GOCART AI and NCEP LTS. For a normal distribution, 95% of the total PDF is equivalent to the range of four standard deviations (4σ). These ranges are represented as $dAI_{95\%}$ (0.41 for MODIS; 0.26 for GOCART) and $dLTS_{95\%}$ (10.5K), respectively (Figure 3.3).

4. Similarly, select 95% of the most frequent ranges for Re(*column*), CLWP, and CCA. These ranges are represented as $dRe(column)_{95\%}$ (50.0 μm), $dCLWP_{95\%}$ (188.0 g/m^2), and $dCCA_{95\%}$ (0.37) (Figure 3.3). These values are used to examine how well AI and LTS can explain the variability of cloud properties.

5. Select the sampling bins for MODIS AI, GOCART AI and NCEP LTS as 10 % of $dAI_{95\%}$ and $dLTS_{95\%}$, respectively. These are represented as dAI_{bin} (0.04 for MODIS; 0.026 for GOCART) and $dLTS_{bin}$ (1.05 K).

6. Compute mean values of Re(column), CLWP, and CCA for each bin (dAI_{bin} and $dLTS_{bin}$) of the MODIS AI, GOCART AI and NCEP LTS. Mean values are represented as $\overline{Re(column)}$, $\overline{CLWP}$, and $\overline{CCA}$.

The above symbols and variables are summarized in the Appendix. The TRMM overpasses include the annual cycle from March 2000 – February 2001. Sampling is significantly concentrated in the subtropics due to the large amount of marine low cloud in those regions and the unique overpass pattern of the TRMM satellite (Figure 3.4). The

sampling weights are identical between the GOCART and MODIS cases. Sampling was restricted to low clouds, defined as those which have a cloud-top temperature above 273 K.

It is worthwhile to note that Re(top) is generally larger than Re(column) for non-precipitating clouds, while Re(top) can be smaller than Re(column) for precipitating clouds [*Masunaga et al.* 2002a; *Matsui et al.* 2004a]. Figure 3.3b show the mode of Re(column) appear to be greater than the Re(top). This is possibly explained by the sampling biases in precipitating clouds and/or algorithm biases. Re(column)-Re(top)

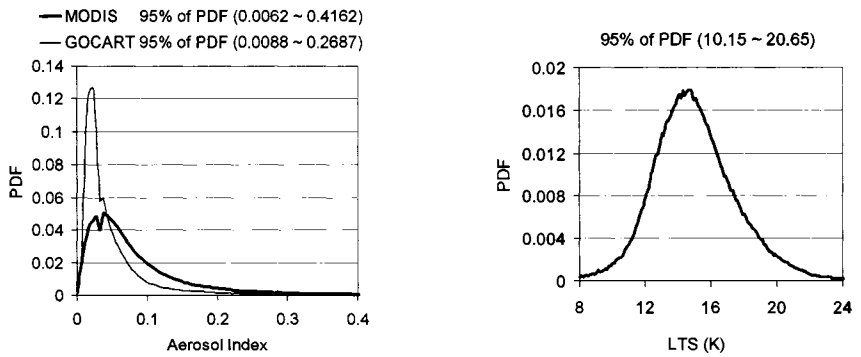

a)

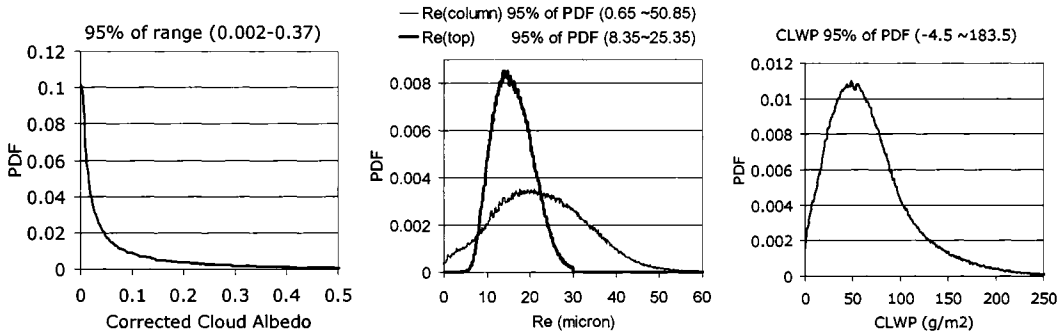

b)

Figure 3.3. Probability density function (PDF) of AI and LTS (a) and cloud properties (b). Variability of 95% of the total PDF is shown for each variable.

relationship and algorithm must be re-examined for different types of clouds in different climatological regions, when the global-scale vertical profile of cloud properties become available [*Stephens et al.* 2002]. Nevertheless, this uncertainty fundamentally does not affect the analysis, since this study does not focus on the comparison between Re(top) and Re(column).

3.3. Results

3.3.1. Global Statistics Among Cloud Properties, LTS and AI

Figure 3.5a shows the variability of $\overline{\mathrm{Re}(column)}$ as a function of *LTS* and *AI*. Clean (low-AI) environments in regions with low LTS tend to have the largest $\overline{\mathrm{Re}(column)}$, while polluted (high-AI) environments with high LTS tend to have the smallest $\overline{\mathrm{Re}(column)}$. Table 3.1 shows the changes in cloud properties for $\mathrm{d}AI_{95\%}$ and $\mathrm{d}LTS_{95\%}$. For example, $d\overline{\mathrm{Re}(column)}_{95\%}$ for $\mathrm{d}AI_{95\%}$ and $\mathrm{d}LTS_{95\%}$ are defined as

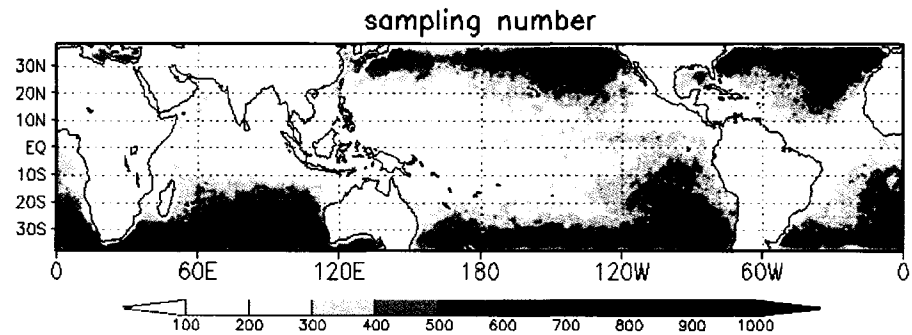

Figure 3.4. Global distribution of sampling number. Sampling numbers are significantly concentrated in the subtropics due to the large amount of marine low cloud and the unique overpass pattern of the TRMM satellite.

$$d\overline{\mathrm{Re}(column)}_{95\%} = \begin{cases} \dfrac{\sum_{LTSbin}\left(\overline{\mathrm{Re}(column)}_{low\_AIbin} - \overline{\mathrm{Re}(column)}_{high\_AIbin}\right) * sampling\#_{LTSbin}}{\sum_{LTSbin} sampling\#_{LTSbin}} \\ \dfrac{\sum_{AIbin}\left(\overline{\mathrm{Re}(column)}_{low\_LTSbin} - \overline{\mathrm{Re}(column)}_{high\_LTSbin}\right) * sampling\#_{AIbin}}{\sum_{AIbin} sampling\#_{AIbin}} \end{cases} \quad (1)$$

where $\overline{\mathrm{Re}(column)}_{low\_AIbin}$ is the $\overline{\mathrm{Re}(column)}$ in the lowest bin of AI, $\overline{\mathrm{Re}(column)}_{high\_AIbin}$ is the $\overline{\mathrm{Re}(column)}$ in the highest bin of AI, $\overline{\mathrm{Re}(column)}_{low\_LTSbin}$ is the $\overline{\mathrm{Re}(column)}$ in the lowest bin of LTS, and $\overline{\mathrm{Re}(column)}_{high\_LTSbin}$ is the $\overline{\mathrm{Re}(column)}$ in the highest bin of LTS. Similar definitions are applied to CLWP and CCA.

This result shows that an increase in $dAI_{95\%}$ corresponds to a reduction of 12.24 μm in $\overline{\mathrm{Re}(column)}$ in the MODIS case and 12.19 μm in the GOCART case, explaining 24.4% and 24.3% respectively of $dRe(column)_{95\%}$ (50.0 μm) (Table 3.1). Similarly, an increase in $dLTS_{95\%}$ corresponds to a reduction of 8.77 μm in $\overline{\mathrm{Re}(column)}$ in the MODIS case and 8.35 μm in the GOCART case, explaining 17.5% and 16.6% respectively of $dRe(column)_{95\%}$ (50.0 μm) (Table 3.1). Note that relationships between LTS and cloud properties appear to be slightly different between the MODIS and GOCART cases, although LTS is independent of AI in the global sampling. This is because differences in global distribution of AI between MODIS and GOCART cause slightly different sampling of background LTS. In both cases, however, the global distribution of cloud droplet size is correlated better with AI than it is with LTS. This result can be applied to the warm rain process, since the process can be diagnosed by the droplet effective size [*Matsui et al.* 2004a].

Figure 3.5a shows that the relationships between Re(*column*) and AI are nonlinear, whereas the Re-LTS slopes are approximately linear. For example, $\overline{\mathrm{Re}(column)}$ appears to decline more rapidly with increases in AI for small AI, whereas increases in AI at high AI do not reduce the cloud droplet size effectively. This trend for small AI is important, because small values of AI are much more frequent than high values (Figure 3.3a). Thus, I additionally define changes in $\overline{\mathrm{Re}(column)}$ between neighboring bins (dAI_{bin} and $dLTS_{\mathrm{bin}}$), weighted by the frequency distribution of the sampling number, which is strongly peaked near the mean value of the LTS PDF and low AI values (Figure 3.3a):

$$d\overline{\mathrm{Re}(column)}_{freq} = \frac{\sum_{LTS\,bin}\sum_{AI\,bin} d\overline{\mathrm{Re}(column)} * sampling\#_{bin}}{\sum_{LTS\,bin}\sum_{AI\,bin} sampling\#_{bin}} \qquad (2)$$

The similar definition is applied to CLWP and CCA. This value represents the frequency weighted mean values of the change in clouds properties over the globe. Table 3.2 shows $d\overline{\mathrm{Re}(column)}_{freq}$ (-1.80 and -0.94, respectively) as a function of dAI_{bin} and $dLTS_{\mathrm{bin}}$. dAI_{bin} explains twice the variability in $\overline{\mathrm{Re}(column)}$ that is attributed to $dLTS_{\mathrm{bin}}$ for both the MODIS and GOCART cases, showing consistently that cloud droplet size is correlated better with AI than it is with LTS by using the definition (1) and (2).

Figure 3.5b shows the variability of $\overline{CLWP}$ as a function of NCEP LTS and AI. While higher LTS corresponds to slightly lower CLWP for all AI bins, it is clear that AI is more strongly correlated with CLWP. An increase in $dAI_{95\%}$ corresponds to a reduction of 39.2 g/m^2 of $\overline{CLWP}$ in the MODIS AI case and 43.56 g/m^2 in the GOCART case, explaining 20.8% and 22.6% of $dCLWP_{95\%}$ (188.0 g/m^2) (Table 3.1). On the other hand,

an increase in $dLTS_{95\%}$ corresponds to a reduction of 8.51 g/m^2 of $\overline{CLWP}$ in the MODIS case and 5.04 g/m^2 in the GOCART case, which explains only 4.5% and 2.6% of $dCLWP_{95\%}$ (188.0 g/m^2), respectively (Table 3.1). Table 3.2 also shows that $\overline{CLWP}$ is more strongly correlated with the AI than it is with LTS by using the definition (2). Note that the VIRS-derived CLWP are tested, and found similar results (not shown here). *Han et al.* [1998] examined data from the Advanced Very High Resolution Radiometer (AVHRR) with the same 273 K cloud-top temperature threshold for low cloud sampling, and also found that the liquid water path decreases with decreasing cloud droplet size. On the other hand, *Sekiguchi et al.* [2003] examined AVHRR data corresponding to a different low cloud-top temperature threshold (below 257 K), and found that the liquid water path increases with decreasing cloud droplet size. These different results suggest that different sampling criteria in terms of cloud-top temperature could be a key issue leading to qualitative differences in the relationships between liquid water path and cloud droplet size.

Twomey et al. [1984] assumed that liquid water path remained constant as aerosol concentrations increased, while *Albrecht* [1989] hypothesized that high aerosol concentrations could increase CLWP via a less efficient precipitation process. Originally both hypotheses were built assuming that only microphysical processes affect cloud properties. The aerosol semidirect effect [*Ackerman et al.* 2000; *Koren et al.* 2004; *Kruger and Graßl* 2004] is one possible reason for the low CLWP with high aerosol concentrations observed in this analysis. Some model studies proposed micro-scale dynamic processes that qualitatively explain this result. For example, *Jiang et al.* [2002], using a non-hydrostatic two-dimensional eddy–resolving model with an explicit

microphysics parameterization, found that drizzle inhibition due to air pollution results in a stable boundary layer below cloud, which reduces the moisture supply and leads to low CLWP. In the clean environment, enhanced drizzle evaporation below the cloud destabilizes the boundary layer, which results in penetrating cumuli, leading to high CLWP. These relationships must be further tested with different observations and a number of simulation studies.

Finally, Figure 3.5c shows variations in $\overline{CCA}$ with LTS and AI. There is a strong, linear correlation with LTS. An increase in $dLTS_{95\%}$ corresponds to an increase of $\overline{CCA}$ by 0.115 in the MODIS case and by 0.117 in the GOCART case, which explains 31.2% and 31.8% respectively of $dCCA_{95\%}$ (0.37) (Table 3.1). On the other hand, the AI-CCA relationship appears to be nonlinear and different between the MODIS and the GOCART cases. An increase in $dAI_{95\%}$ corresponds to a very slight increase of $\overline{CCA}$ (about 0.039 in the MODIS case and 0.026 in the GOCART case), and explains 10.6% and 7.1% respectively of $dCCA_{95\%}$ (0.37) (Table 3.1). For high-AI bins, CCA-AI correlation slopes are nearly zero and/or slightly negative, while positive CCA-AI correlation slopes exist for low-AI bins. Although CCA is used instead of cloud optical depth in this study, this result is similar to that inferred from satellite measurements of cloud optical depth over the Amazon basin [*Kaufman and Fraser* 1997]. By using the definition (2), the correlation slope of MODIS AI with CCA is comparable to the correlation of LTS with CCA (Table 3.2), suggesting that the aerosol-CCA correlation can be captured frequently over the globe. However, this is not captured in the GOCART case; i.e., AI has a weak correlation with the CCA by using both the definition (1) and (2). Further tests of these relationships will be tested on a local scale in the next section.

Note that partially cloudy VIRS pixels could result in biases in the retrieved cloud properties. Cloud optical depth and cloud-top temperature could have a negative bias, while cloud droplet radius can be overestimated, from a partially cloudy VIRS pixel. Variation of AI in a partially cloudy pixel can affect the values of estimated cloud properties to some degree that has not yet been quantified.

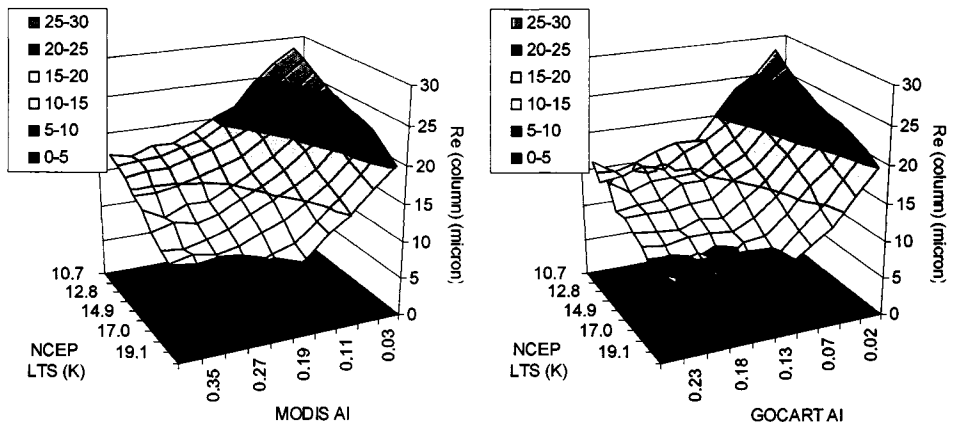

a. Column cloud droplet effective radius

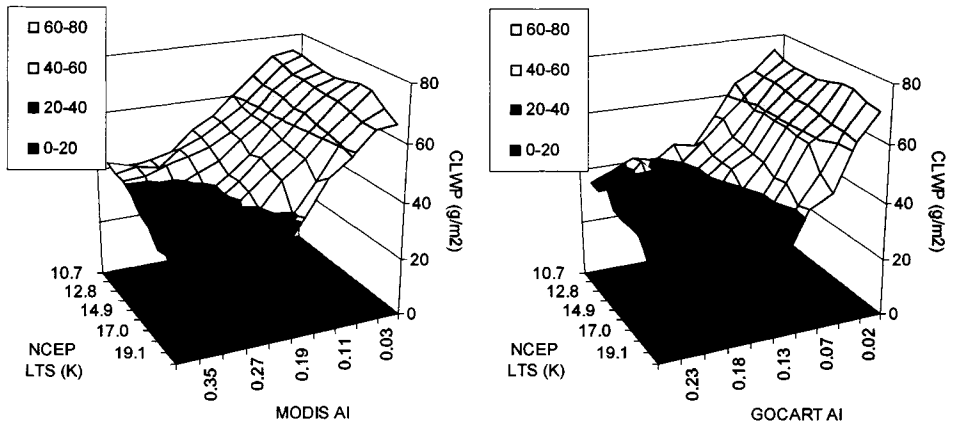

b Cloud liquid water path

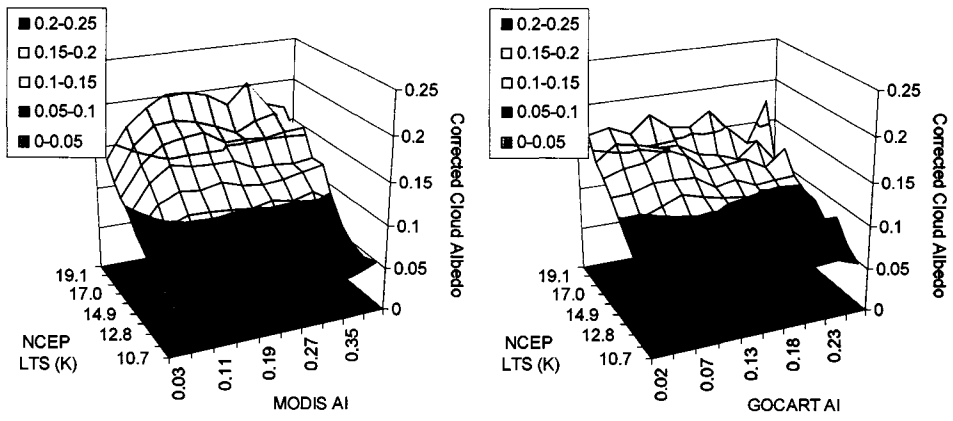

c Corrected cloud albedo (cloud amount)

Figure 3.5. Global statistics of mean warm cloud properties as functions of LTS and AI.

	$d\overline{\mathrm{Re}(column)}_{95\%}$ [μm] $\left(\frac{\lvert d\overline{\mathrm{Re}(colum)}\rvert}{d\,\mathrm{Re}(column)_{95\%}}*100\right)$		$d\overline{CLWP}_{95\%}$ [g/m^2] $\left(\frac{\lvert d\overline{CLWP}\rvert}{dCLWP_{95\%}}*100\right)$		$d\overline{CCA}_{95\%}$ $\left(\frac{\lvert d\overline{CCA}\rvert}{dCCA_{95\%}}*100\right)$	
Forcing	**MODIS**	**GOCART**	**MODIS**	**GOCART**	**MODIS**	**GOCART**
d$AI_{95\%}$	-12.24 (24.4%)	-12.19 (24.3%)	-39.24 (20.8%)	-42.56 (22.6%)	0.039 (10.6%)	0.026 (7.1%)
d$LTS_{95\%}$	-8.77 (17.5%)	-8.35 (16.6%)	-8.51 (4.5%)	-5.04 (2.6%)	0.115 (31.2%)	0.117 (31.8%)

Table 3.1. Mean changes in cloud properties with increases in d$AI_{95\%}$ and d$LTS_{95\%}$

	$d\overline{\mathrm{Re}(column)}_{freq}$ [μm]		$d\overline{CLWP}_{freq}$ [g/m^2]		$d\overline{CCA}_{freq}$	
Forcing	**MODIS**	**GOCART**	**MODIS**	**GOCART**	**MODIS**	**GOCART**
dAI_{bin}	-1.80	-1.58	-3.85	-5.04	0.0136	0.0016
dLTS_{bin}	-0.94	-0.85	-0.62	-0.37	0.0135	0.0133

Table 3.2. Frequency weighted mean values of the change in cloud properties with increases in dAI_{bin} and dLTS_{bin} over the globe. Changes in cloud properties are weighted by the sampling number as described in the text.

3.3.2. Local Statistics Between Cloud Properties, AI and LTS

In the previous section, strong relationships between cloud properties, AI, and LTS are found on the global scale, and the correlation slopes are quantified by the definition (1) and (2). In this section, those relationships are examined in different geographical regions. *Sekiguchi et al.* [2003] examined local correlations using the AVHRR and the POLarization and Directionality of the Earth's Reflectances (POLDER) instrument, and showed that strong correlation between aerosols and cloud properties exist along coastlines where continental air masses meet maritime clean air. The linear correlation coefficients are derived in each 4-degree box on a global grid for the same annual sampling period used in the previous section. The variability of local positive or

negative correlation reported by *Sekigushi et al.* [2003] is seen in this study to depend on both aerosol and thermodynamic variability. Positive (negative) correlations are showed in red (blue) shades, and statistically insignificant correlations (approximately, $|r| < 0.05$) with t-distribution critical level set to 0.05 are shown in white (Figure 3.6).

Figure 3.6a shows the correlation map between Re(*column*) and MODIS AI (left), GOCART AI (center), and NCEP LTS (right). Strong negative correlations (blue) appear in the subtropics in the Northern Pacific Ocean, in the Indian Ocean, and in most of the Atlantic Ocean. Correlation maps for the MODIS and GOCART cases show general agreement with the global statistics discussed in section 3.1. Weak correlations (white) and slightly positive correlations (red) appear in the remote Southern Pacific Ocean in the MODIS case, in the middle of the Pacific Ocean in the GOCART case, and off the west coast of Africa. In the remote ocean, the correlation coefficient may be very small due to the small variability in AI and the low sampling number. Overall correlations are negative, which was captured in the global statistics (section 3.1). The LTS-Re(*column*) correlation also appears to be highly positive in the subtropics and weak or slightly negative in the Pacific Ocean. This is because, in subtropical regions, LTS varies substantially due to propagating mid-latitude fronts and the seasonal shift of the large-scale circulation (Figure 3.1). These considerations also explain the weak correlation in the equatorial regions, where LTS does not change substantially throughout the year (Figure 3.1).

Figure 3.6b shows the local correlation map between CLWP and MODIS AI (left), GOCART AI (center), and NCEP LTS (right). Negative correlations (blue) in the MODIS case appear in the northern subtropics in the Pacific Ocean, in the coastal zones

around the Indian Ocean and South Africa, and for the northern part of the Atlantic Ocean. The GOCART case has a slightly larger area of negative correlations than the MODIS case, which is consistent with the result discussed in the previous section. The geographical locations of the negative correlations are, apparently, coherent with those of Re(column) (Figure 3.6a). This suggests that a reduction in cloud droplet size and cloud liquid water associated with high concentrations of aerosols occurs simultaneously on a local scale over the ocean.

Figure 3.6c shows the local correlation map between CCA and MODIS AI (left), GOCART AI (center), and NCEP LTS (right). The MODIS case shows positive correlations over almost the entire domain; i.e., the aerosol indirect effect exists over almost the entire ocean. The GOCART case shows positive correlations in the northern part of the Pacific Ocean and off the east coast of North America, while negative correlations appear off the east coast of Australia and Africa and in some remote ocean areas. This result is consistent with the global statistics; the MODIS case shows stronger correlation between AI and the CCA than the GOCART case does (section 3a). Both the MODIS and the GOCART cases show that the strongest positive correlation appears in the Northern Pacific, where a combination of industrial and dust aerosols from East Asia advect over the ocean. LTS also has a consistently positive correlation with CCA over the global ocean.

In section 3.1, increases in AI as well as LTS are appear to be accompanied by decreases in cloud droplet size, decreases in liquid water path, and increases in CCA. However, in a marine environment, if AI becomes high, but LTS becomes low, changes in cloud properties can be offset or very small due to the competition between AI and

LTS. *Jiang et al.* [2002] and *Takemura et al.* [2005] also found that a change in simulated CLWP could depend upon the large-scale thermodynamic feedback. In section 1, AI and LTS are not strongly correlated on the global scale. In contrast, they are usually correlated either positively or negatively on a local scale (Figure 3.7). In the MODIS case, negative correlations appear in a large portion of the southern Pacific Ocean, and positive and negative correlations appear in the Atlantic Ocean. In the GOCART case, negative and positive correlations also appear in different regions. Positive AI-LTS correlations mean that high (low) AI appears with high (low) LTS. For positively-correlated regions, both factors tend to reduce Re(column) and CLWP, while increasing CCA (Figure 3.6). On the other hand, negative AI-LTS correlations mean that high (low) AI appears with low (high) LTS, which has the opposite effect on cloud properties (Figure 3.6). Comparing Figure 3.6 and Figure 3.7, the regions with negative AI-LTS correlations are coherent with the regions with weak AI-cloud properties correlation in Figure 3.6, such as the southern Pacific Ocean and off the west coast of West Africa. This implies that the global distribution of local aerosol-cloud relationship could be modulated by feedback from the large-scale thermodynamic field. The importance of the large-scale feedback on aerosol direct and indirect effects is investigated and discussed in the global modeling study presented in *Takemura et al.* [2005].

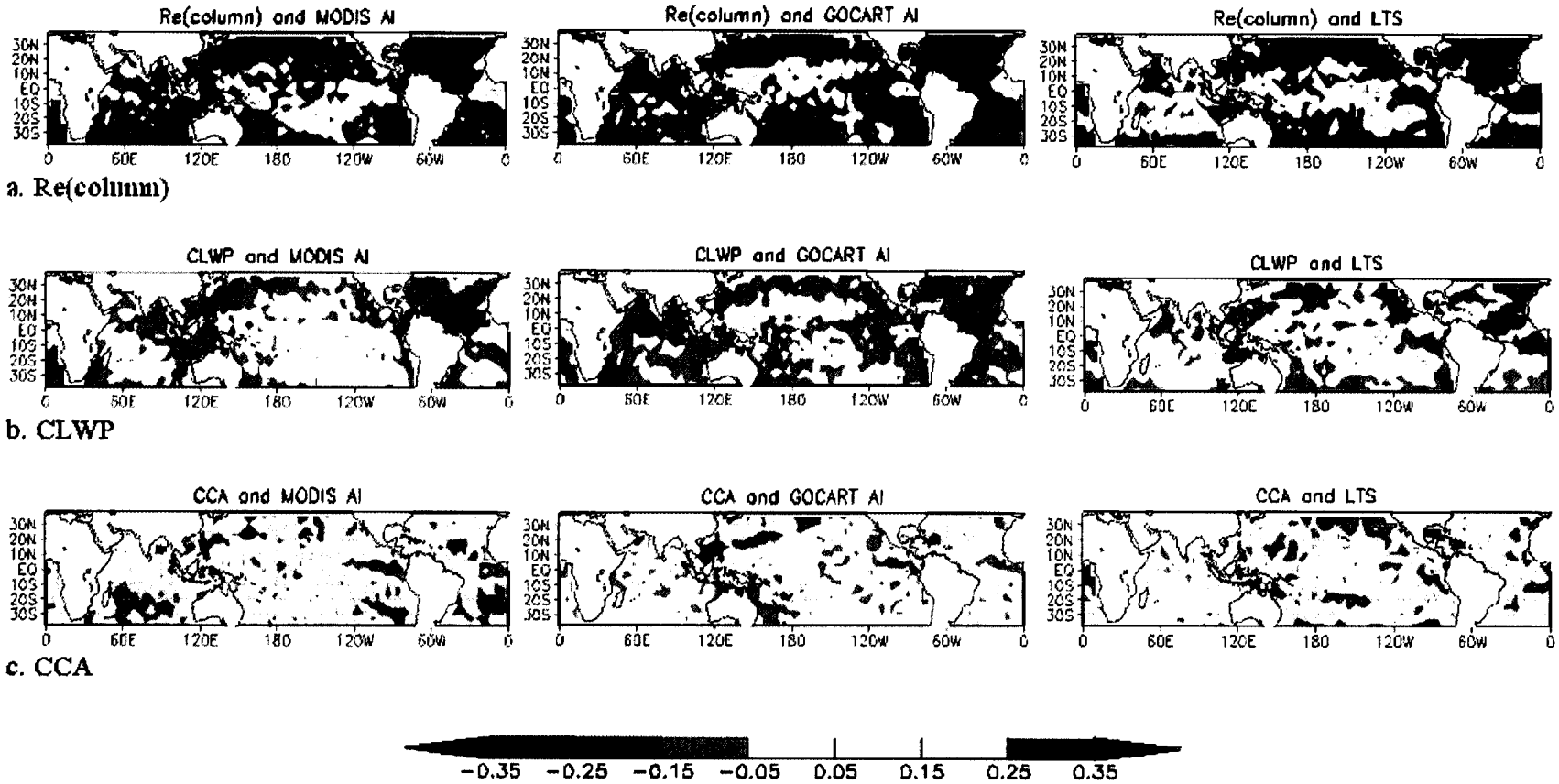

Figure 3.6. Linear correlation coefficient in each 4-degree box on a global grid for the same annual sampling period as in Figures 3.1 and 3.2. Non-sampled grids (over land) and statistically insignificant correlations (approximately, $|t| < 0.05$) with the t-distribution critical level set to 0.05 are shown in white.

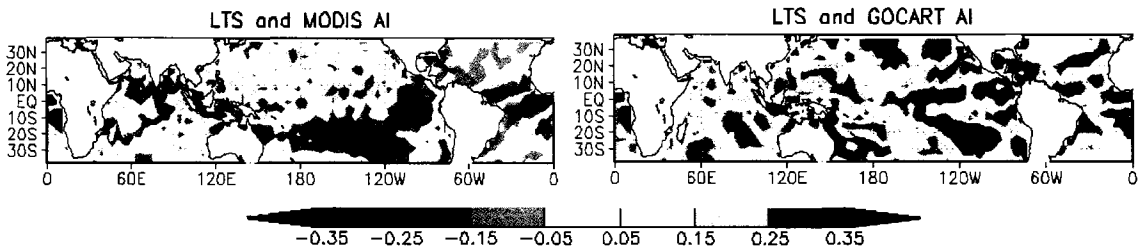

Figure 3.7. Linear correlation coefficient between AI and LTS in each 4-degree box on a global grid for the same annual sampling period as in Figure 3.6. Positive AI-LTS (red) correlations mean that high AI appears with high LTS, while negative AI-LTS correlations mean that high AI appears with low LTS, which has opposite effect on cloud properties. Therefore, negative-correlation regions appear to be coherent with the weak-correlation regions in Figure 3.6.

3.3.3. Diurnal Cycle of Cloud Properties in Different LTS and AI Regions

As introduced in section 1, marine low clouds have radiation-driven strong diurnal variability [e.g., *Driedonks and Duynkerke* 1989]. The TRMM sun-asynchronous orbit enables to examine the daytime diurnal cycle of $\overline{\mathrm{Re}(column)}$, $\overline{CLWP}$, and $\overline{CCA}$ in regions with different LTS and AI. For clarity, LTS and AI bins are assigned to be twice as large as those in the previous sections. The LTS and AI contours in the figures are labeled by the mean value of each LTS and AI bin, respectively.

Figure 3.8a shows the daytime diurnal cycle of various cloud properties in different LTS bins. $\overline{\mathrm{Re}(column)}$ appears to be higher in lower-LTS bins, while $\overline{CCA}$ appears to be larger in higher-LTS bins over most of the diurnal cycle. $\overline{\mathrm{Re}(column)}$ reaches its maximum from 10 am to 1 pm and decreases towards evening, with consistent behavior for any LTS. The largest LTS regions (19.6) exhibit a slightly different pattern in $\overline{CLWP}$ from the other regions. $\overline{CLWP}$ stays at its maximum from 7 am to 12 pm and then rapidly decreases in the afternoon. In particular, times of peak $\overline{CLWP}$ in high-LTS bins (highest three bins of LTS) appear to be in the early morning between 7 am and 9 am,

while peak times in the lowest two LTS bins are in the late morning between 9 am and 1 pm. The diurnal cycles of cloud-top height varies with LTS, but generally decline (~ a few hundred meters) from the morning to the evening. These patterns are similar to observations from the FIRE intensive observation period [*Hignett* 1991]. The diurnal cycle of $\overline{CCA}$ depicts a strong contrast between daytime diurnal variability in high- and low-LTS regions. Higher-LTS bins tend to have larger morning/evening peaks and the largest diurnal variability. In the highest LTS (19.6 K) regions, $\overline{CCA}$ declines about 50% from its peak value in the morning. For all LTS bins, except the lowest (=11.2), the diurnal minima appear to be at noon. Morning maxima are slightly larger than those in the evening.

Figure 3.8b shows the daytime cloud diurnal cycle for different AI. $\overline{\mathrm{Re}(column)}$ and $\overline{CLWP}$ are generally higher for lower AI (clean) environments over most of the diurnal cycle. Note that the sampling is unbiased with the background LTS values. Both the MODIS and GOCART relationships show distinctly different diurnal cycles between high and low AI bins. In the polluted-environment cases (the highest three bins of AI), $\overline{\mathrm{Re}(column)}$ and $\overline{CLWP}$ have sharp rises in the early morning between 7 am and 9 am in the MODIS case, and between 7 am and 12 pm in the GOCART case. On the other hand, the clean environmental cases (lowest two bins of AI) show consistently high values of $\overline{\mathrm{Re}(column)}$ and $\overline{CLWP}$ between 7 am and 1 pm. In all the cases, $\overline{\mathrm{Re}(column)}$ and $\overline{CLWP}$ show a rapid decrease in the late afternoon. Cloud-top height gradually declines from the morning to mid-afternoon, and slightly increases between 3 pm and 5 pm. The diurnal cycle of cloud-top height exhibits substantial diversity between the high and low

AI regions in the GOCART case, but this feature is not seen in the MODIS case. $\overline{CCA}$ has a strong diurnal cycle, but does not have any discernible variation with AI.

While data from the TRMM satellite showed the daytime diurnal cycle of $\overline{\mathrm{Re}(column)}$, $\overline{CLWP}$, and $\overline{CCA}$, the exact mechanism that drives different daytime diurnal cycles is still unknown. One possible explanation could be solar heating. As explained in section 1, absorption of solar radiation in the middle of the cloud layer and longwave cooling at cloud-top drive turbulent mixing in the cloud layer [e.g., *Driedonks and Duynkerke* 1989]. The degree of solar heating may change for different droplet size spectra. Water clouds could absorb up to 15-20% of the incident solar radiation, with the largest values arising from the thickest clouds with large cloud droplets [*King et al.* 1990]. On the other hand, small, narrowly concentrated cloud droplet spectra tend to have less absorption of solar radiation. Therefore, thin clouds with smaller droplet size forming in polluted environments could reduce evaporation due to solar heating in the morning, supporting increases the cloud droplet size and liquid water that persist later in the morning as compared with thicker clouds having larger mean droplet sizes. However, this discussion is only speculative. More intensive measurements will be required to establish the mechanisms involved.

An important implication of the daytime diurnal cycle is that satellite-based assessments of the aerosol indirect effect could appear to be slightly different depending on the local time of satellite overpass. Unlike the TRMM satellite, all of the polar orbiting environmental satellites (POES) have a constant local time of satellite overpass. Differences in $\overline{\mathrm{Re}(column)}$ and $\overline{CLWP}$ between the highest-AI bin and the lowest-AI bin are largest in the early morning (Figure 3.8b). If one measures $\overline{\mathrm{Re}(column)}$ and

$\overline{CLWP}$ early in the morning, the correlation slope between aerosols and cloud properties could be larger than the daily mean, whereas the correlation could be smaller around noon. Moreover, the CCA-LTS correlation slope could become much larger for morning/evening-time sampling, and vice versa for noontime sampling. This daytime diurnal cycle must be incorporated into the estimation of cloud radiative forcing and the aerosol indirect effect estimated from the POES.

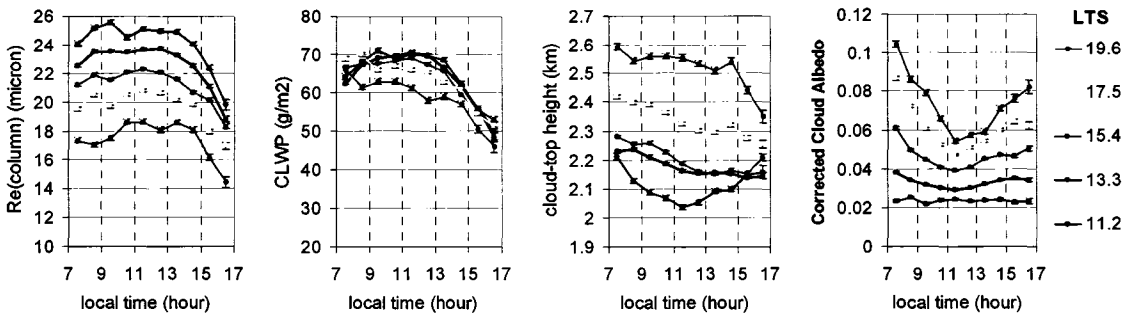

a. Diurnal cycle of cloud properties in different LTS (K) regions

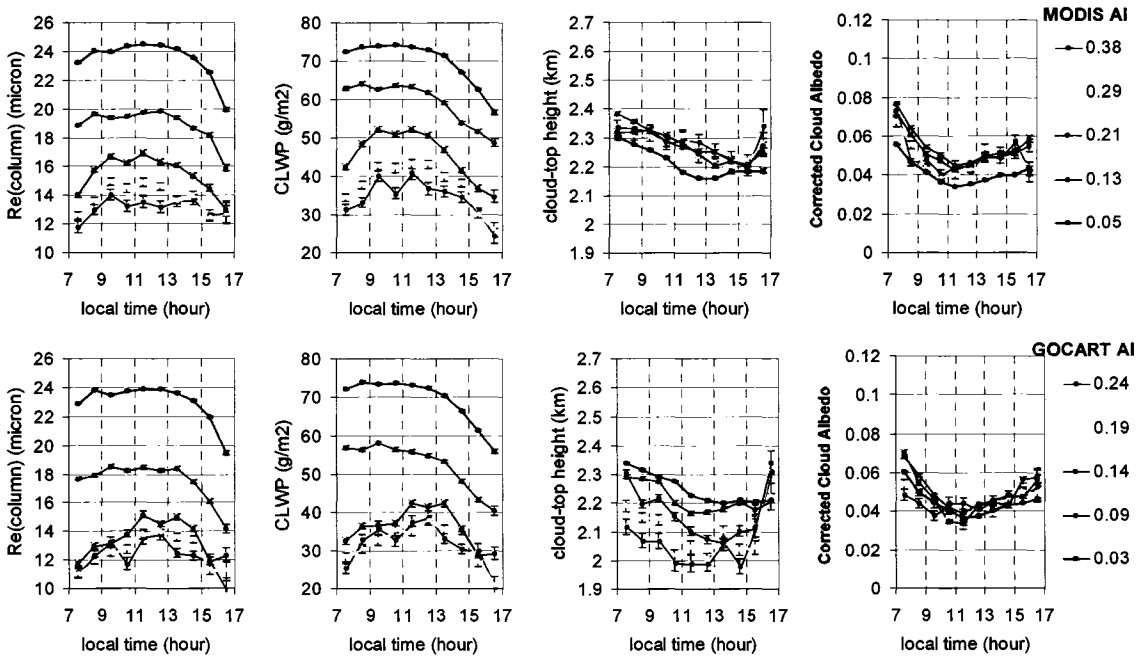

b. Diurnal cycle of cloud properties in different AI regions

Figure 3.8. Diurnal cycles of cloud properties in different LTS (a) and AI (b) regions. Contours of LTS and AI represent the mean values of the LTS and AI bins, respectively. Error bars represent standard errors ($\sigma / \sqrt{n-2}$, where n and σ are the number of quasi-coincident measurements for each bin and standard deviation, respectively).

3.4. Summary

This study examines links between variability in marine low cloud properties derived from the TRMM satellite, MODIS/GOCART-derived aerosol index (AI), and lower-tropospheric stability (LTS) derived from the NCEP/NCAR reanalysis. AI and LTS are used to represent column-integrated aerosol concentrations and background thermodynamic environments, respectively. Results are summarized as follows.

- Cloud droplet sizes tend to be smallest in polluted and strong-inversion environments. Cloud droplet size decreases linearly with increasing LTS, while AI has even stronger anti-correlations with cloud droplet size, especially in clean environments. Statistical quantification shows that twice as much variability in cloud droplet size is explained by AI than by LTS.

- Higher values of AI tend to be associated with significantly lower cloud liquid water path (CLWP), while higher LTS is linked with a slightly lower CLWP. Statistical quantification showed that the global variability of CLWP is more strongly correlated with AI than it is with LTS. These results do not support the hypotheses or assumption of constant or increased LWP of warm clouds associated with high aerosol concentrations [*Twomey et al.* 1984; *Albrecht* 1993].

- High LTS, i.e., strong inversions, result in extensive cloud cover and high regional albedo. LTS is linearly correlated with the corrected cloud albedo (CCA: product of cloud optical depth and cloud fraction), while the AI-CCA relationship is nonlinear

and is different for the MODIS AI and the GOCART AI cases. In clean environments, small increases in AI can enhance CCA; however, this enhancement was not observed in already-polluted (high-AI) environments. For the MODIS dataset, statistical quantification suggests that global variability in CCA is well explained by LTS, while both AI and LTS are needed to explain local variability of CCA.

- Most of the local correlations between AI and cloud properties agree with the results from the global statistics; i.e., higher AI or higher LTS is associated with smaller cloud droplet size and lower CLWP, and higher CCA. On the other hand, weak local aerosol-cloud correlations appear in the regions where high (low) AI and low (high) LTS occur simultaneously, thereby offsetting each other.

- Daytime diurnal cycles can explain additional variability in cloud properties; none of the cloud properties is constant through the daytime. CCA has the largest diurnal cycle in high-LTS regions, such as off the coasts of California, Namibia, and Chile. Cloud droplet size and CLWP have slightly different diurnal cycles between clean and polluted environments. Reasons for this behavior remain uncertain. This daytime diurnal cycle should be incorporated into the estimation of cloud solar radiative forcing and aerosol indirect effects produced using data from Polar Orbiting Environmental Satellites (POES).

These findings should be tested with data from different satellite platforms and with various numerical modeling experiments. Remaining uncertainties and proposed future directions for analyses are summarized as follows.

- The statistical quantification may vary for a different choice of thermodynamic (e.g., turbulent kinetic energy or updraft velocity) and aerosol parameters (e.g., AOD and the Ångstrom exponent derived at different wavelengths).
- Our statistical sampling and analysis is limited to warm clouds with cloud-top temperatures greater than 273 K. Analyses must be extended to ice and mixed-phase clouds in future work. Such studies [e.g., *Koren et al.* 2005; *Lin et al.* 2005] have shown different relationships for cloud-aerosol interactions than were seen in this work.
- Observations of the vertical distribution of AI are required on a global scale. *Kaufman et al.* [2003] proposed multi-sensor satellite retrievals of coarse- and fine-mode aerosol optical depth and vertical distribution by utilizing space-born LIDAR measurements in addition to MODIS radiances in the inversion. These techniques and datasets will be available in the near future.
- The role of GCCN is largely ignored by the use of AI as the aerosol variable. A study examining the role of GCCN more explicitly is possible by investigating the relative roles of the fine- and coarse-mode aerosol fractions available in the MODIS aerosol products.
- The VIRS footprint size may be too coarse to resolve the properties of highly broken clouds, leading to unknown biases in the quantitative analysis. The TMI-VIRS combined algorithm used in this study can be applied to the combination of

the Advanced Microwave Scanning Radiometer (AMSR) and MODIS sensors on the Aqua satellite platform. MODIS has a much smaller footprint than VIRS, while AMSR has microwave channels similar to those of TMI.

Symbols and Terminology

AI	Aerosol index: the product of aerosol optical depth and the Ångstrom exponent
$dAI_{95\%}$	95% of the most frequent AI out of total probability density function (0.41 for MODIS; 0.26 for GOCART)
dAI_{bin}	Size of sampling bin: 10% of $dAI_{95\%}$ (0.04 for MODIS, 0.026 for GOCART)
LTS	Lower-tropospheric stability (or inversion strength): potential temperature at 700 mb - surface potential temperature
$dLTS_{95\%}$	95% of the most frequent LTS out of total probability density function (10.5 K)
$dLTS_{bin}$	Size of sampling LTS bin: 10% of $dLTS_{95\%}$ (1.05 K).
Re(*column*)	Column integrated cloud droplet effective radius (μm)
$dRe(column)_{95\%}$	A range of 95% of the most frequent (≈ 4σ) Re(*column*) out of total probability density function (50.0 μm)
$\overline{\text{Re}(column)}$	Re(*column*) averaged for each bin (dAI_{bin} and $dLTS_{bin}$)
$d\overline{\text{Re}(colum)}_{95\%}$	Mean change in $\overline{\text{Re}(column)}$ with increase in $dAI_{95\%}$ and $dLTS_{95\%}$
$d\overline{\text{Re}(colum)}_{freq}$	Frequency weighted mean values of the change in $\overline{\text{Re}(column)}$ with increase in dAI_{bin} and $dLTS_{bin}$ over the globe
CLWP	Cloud liquid water path (g/m^2)
$dCLWP_{95\%}$	A range of 95% of the most frequent (≈ 4σ) CLWP values out of total probability density function (188.0 g/m^2)

$\overline{CLWP}$	CLWP averaged for each bin (dAI_{bin} and $dLTS_{bin}$)
$d\overline{CLWP}_{95\%}$	Mean change in $\overline{CLWP}$ with increase in $dAI_{95\%}$ and $dLTS_{95\%}$.
$d\overline{CLWP}_{freq}$	Frequency weighted mean values of the change in $\overline{CLWP}$ with increase in dAI_{bin} and $dLTS_{bin}$ over the globe
CCA	Corrected cloud albedo: the product of cloud optical depth and cloud fraction in 1-degree box
$dCCA_{95\%}$	A range of 95% of the most frequent ($\approx 4\sigma$) CCA out of total probability density function (0.37)
$\overline{CCA}$	CCA averaged for each bin (dAI_{bin} and $dLTS_{bin}$)
$d\overline{CCA}_{95\%}$	Mean change in $\overline{CCA}$ with increase in $dAI_{95\%}$ and $dLTS_{95\%}$
$d\overline{CCA}_{freq}$	Frequency weighted mean values of the change in $\overline{CCA}$ with increase in dAI_{bin} and $dLTS_{bin}$ over the globe.

References

Ackerman A.S., O.B. Toon, D.E. Stevens, A.J. Heymsfield, V. Ramanathan, E.J. Welton (2000), Reduction of tropical cloudiness by soot. *Science*, **288**, 1042 – 1047.

Albrecht, B.A. (1989), Aerosols, cloud microphysics, and fractional cloudiness, *Science,* **245**, 1227-1230.

Anderson, T.L., R.J. Charlson, D.M. Winker, J.A. Ogren and K. Holmén (2003), Mesoscale variations of tropospheric aerosols, *J. Atmos. Sci.,* **60**(1), 119–136.

Betts, A.K. (1990), Diurnal variation of California coastal stratocumulus from two days of boundary layer soundings, *Tellus*, **42A**, 302-304.

Bréon, F.-M., D. Tanré, and S. Generoso (2002), Aerosol effect on cloud droplet size monitored from satellite, *Science*, **295**, 834-838.

Chin, M., P. Ginoux, S. Kinne, O. Torres, B. N. Holben, B. N. Duncan, R. V. Martin, J. A. Logan, A. Higurashi, and T. Nakajima (2002), Tropospheric aerosol optical thickness from the GOCART model and comparisons with satellite and sunphotometer measurements, *J. Atmos. Sci.,* **59**, 461-483.

Chin, M., D. A. Chu, R. Levy, L. A. Remer, Y.J. Kaufman, B. N. Holben, T. Eck, and P. Ginoux (2004), Aerosol distribution in the northern hemisphere during ACE-Asia: Results from global model, satellite observations, and sunphotometer measurements, *J. Geophys. Res.*, **109**, D23S90, doi:10.1029/2004JD004829.

Cieselski, P.E., W.H. Schubert, and R. H. Johnson (2001), Diurnal variability of the marine boundary layer during ASTEX. *J. Atmos. Sci.*, **58**(16), 2355–2376.

Driedonks, A. G. M., and P. G. Duynkerke (1989), Current problems in the stratocumulus-topped atmospheric boundary layer. *Bound.-Layer Meteor.* **46,** 275–303.

Dunion, J. P. and C. S. Velden (2004), The impact of the Saharan air layer on Atlantic tropical cyclone activity. *Bull. Amer. Meteor. Soc.* **85**(3), 353–365.

Feingold, G., W. L. Eberhard, D. E. Veron, and M. Previdi (2003), First measurements of the Twomey indirect effect using ground-based remote sensors, *Geophys. Res. Lett.* **30**(6), doi:0.029/2003GL017967.

Feingold, G., W. R. Cotton, S. M. Kreidenweis, and J. T. Davis (1999), The impact of giant cloud condensation nuclei on drizzle formation in stratocumulus: implications for cloud radiative properties. *J. Atmos. Sci.*, **56**(24), 4100–4117.

Han, Q., W. B. Rossow, J. Chou, and R. Welch (1998), Global survey of the relationship of cloud albedo and liquid water path with droplet size using ISCCP, *J. Climate*, **11**, 1516-1528.

Hartmann, D. L., M.E. Ockert-Bell, and M. L. Michelsen (1992), The effect of cloud type on Earth's energy balance: Global analysis, *J. Climate*, **5**, 1281 – 1304.

Hignett, P. (1991), Observations of diurnal variation in a cloud-capped marine boundary layer. *J. Atmos. Sci.* **48**(12), 1474–1482.

Hobbs, P.V. (1993), *Aerosol-Cloud Interactions*, Elsevier Science & Technology Books Series: International Geophysics Series, 235 pp

Jiang, H., G. Feingold, and W.R. Cotton (2002), Simulations of aerosol-cloud-dynamical feedbacks resulting from entrainment of aerosol into the marine boundary layer during the Atlantic Stratocumulus Transition Experiment. *J. Geophys. Res.* **107**, doi: 10.1029/200JD001502.

Kalnay, E., M. *et al.* (1996), The NCEP/NCAR 40-year reanalysis project. *Bull. Amer. Meteor. Soc.*, **77**, 437-471.

Kaufman, Y.J, and R.S. Fraser (1997), The effect of smoke particles on clouds and climate forcing *Science*, **277**, 1636-1639.

Kaufman, Y.J., D. Tanré, and O. Boucher (2002), A satellite view of aerosols in the climate system. *Nature*, **419,** 215-223.

Kaufman, Y.J., D. Tanré, J.-F. Léon, and J. Pelon (2003), Retrievals of profiles of fine and coarse aerosols using lidar and radiometric space measurements. *IEEE Trans. Geosci. Remote Sens.*, **41** (8), 1743-1754.

Kaufman, Y. J., I. Koren, L. A. Remer, D. Rosenfeld, and Y. Rudich (2005), The effect of smoke, dust and pollution aerosol on shallow cloud development over the Atlantic Ocean. *Proceedings of the National Academy of Sciences*, **102**(32), 11207-11212.

Kawamoto, K., T. Nakajima, and T. Y. Nakajima (2001), A global determination of cloud microphysics with AVHRR remote sensing, *J. Climate*, **14**, 2054-2068.

King, M. D., L. F. Radke, and P. V. Hobbs (1990), Determination of the spectral absorption of solar radiation by marine stratocumulus clouds from airborne measurements within clouds, *J. Atmos. Sci.,* **47**(7), 894 – 907.

Klein, S. A. (1997), Synoptic variability of low-cloud properties and meteorological parameters in the subtropical trade wind boundary layer. *J. Climate,* **10**(8), 2018-2039.

Klein, S. A., and D. L. Hartmann (1993), The seasonal cycle of low stratiform clouds. *J. Climate,* **6**, 1587-1606.

Kruger, O., and H. Graßl (2004), Albedo reduction by absorbing aerosols over China, *Geophys. Res. Lett.* **3**, doi: 0.029/2003GL01911.

Koren I., Y. J. Kaufman, L. A. Remer, J. V. Martins (2004), Measurement of the Effect of Amazon Smoke on Inhibition of Cloud Formation. *Science,* **303**, 1342 – 1345.

Koren, I., Y. J. Kaufman, D. Rosenfeld, L. A. Remer, and Y. Rudich (2005), Aerosol invigoration and restructuring of Atlantic convective clouds. *Geophys. Res. Lett.*, **32**, doi: 10.1029/2005GL023187.

Lau K. M., H. T. Wu (2004), Warm rain processes over tropical oceans and climate implications, *Geophys. Res. Lett.,* **30**(24), 2290, doi:10.1029/2003GL018567.

Lin, J.C., T. Matsui, R.A. Pielke Sr., and C. Kummerow (2006), Effects of biomass burning-derived aerosols on precipitation and clouds in the Amazon Basin: A satellite-based empirical study. *J. Geophys. Res.* (in press)

Nakajima, T., A. Higurashi, K. Kawamoto, and J. E. Penner (2001), A possible correlation between satellite-derived cloud and aerosol microphysical parameters, *Geophys. Res. Lett.*, **28**, 1171-1174.

National Research Council (NRC) (2005), Radiative forcing of climate change: Expanding the concept and addressing uncertainties. Washington, D.C., The National Academies Press.

Masunaga, H., T. Y. Nakajima, T. Nakajima, M. Kachi, R. Oki, and S. Kuroda (2002a), Physical properties of maritime low clouds as retrieved by combined use of TRMM Microwave Imager and Visible/Infrared Scanner. Algorithm, *J. Geophys. Res.,* **107**, 4083, doi:10.1029/2001JD000743.

Masunaga, H., T. Y. Nakajima, T. Nakajima, M. Kachi, and K. Suzuki (2002), Physical properties of maritime low clouds as retrieved by combined use of TRMM Microwave Imager and Visible/Infrared Scanner. II. Climatology of warm clouds and rain, *J. Geophys. Res.* **107**, doi:10.1029/2001JD001269.

Matsui, T., H. Masunaga, R. A. Pielke Sr., and W.-K. Tao (2004a), Impact of aerosols and atmospheric thermodynamics on cloud properties within the climate system. *Geophys. Res. Lett.* **31** (6), L06109, doi: 10.1029/2003GL019287.

Matsui, T., S. M. Kreidenweis, R. A. Pielke Sr., B. Schichtel, H. Yu, M. Chin, D. A. Chu, and D. Niyogi (2004b), Regional comparison and assimilation of GOCART and MODIS aerosol optical depth across the eastern U.S. *Geophys. Res. Lett.,* **31**, L21101, doi:10.1029/2004GL021017.

Park, S. and C. B. Leovy (2004), Marine low-cloud anomalies associated with ENSO, *J. Climate* **17**, 3448 – 3469.

Penner, J. E. X Dong and Y. Chen., Y. (2004), Observational evidence of a change in radiative forcing due to the indirect aerosol effect, *Nature*, **427**, 231-234.

Ramanathan, V., P. J. Crutzen, J. T. Kiehl and D. Rosenfeld (2001), Aerosols, climate, and the hydrological cycle, *Science*, **294**, 2119-2124.

Remer, L. A., Y. J. Kaufman, D. Tanre, S. Mattoo, D. A. Chu, J. V. Martins, R.-R. Li, C. Ichoku, R. C. Levy, R. G. Kleidman, T. F. Eck, E. Vermote, and B. N. Holben (2005), The MODIS aerosol algorithm, products and validation. *J. Atmos. Sci.* **62**, 947–973.

Rosenfeld, D. (1999), TRMM observed first direct evidence of smoke from forest fire inhibiting rainfall. *Geophys. Res. Lett.*, **26**, 3105-3108.

Sekiguchi, M., T. Nakajima, K. Suzuki, K. Kawamoto, A. Higurashi, D. Rosenfeld, I. Sano, and S. Mukai (2003), A study of the direct and indirect effects of aerosols using global satellite data sets of aerosol and cloud parameters, *J. Geophys. Res.*, **108**, 4699, doi:10.1029/2002JD003359.

Slingo, A. J. (1990), Sensitivity of the Earth's radiation budget to changes in low clouds. *Nature,* **343**, 49 – 50.

Stephens, G. L., et al. (2002), The CloudSat mission and the A-train: A new dimension of space-based observations of clouds and precipitation. *Bull. Amer. Meteor. Soc.*, **83**, 1771-1790, doi:10.1175/BAMS-83-12-1771.

Takemura, T., T. Nozawa, S. Emori, T. Y. Nakajima, and T. Nakajima (2005), Simulation of climate response to aerosol direct and indirect effects with aerosol transport-radiation model. *J. Geophys. Res.*, **110**, D02202, doi:10.1029/2004JD005029.

Twomey, S., M. Piepgrass, and T. L. Wolfe (1984), An assessment of the impact of pollution on global cloud albedo. *Tellus,* **36B**, 356-366.

Weare, B.C. (1994), Interrelationships between cloud properties and sea surface temperatures on seasonal and interannual time scales. *J. Climate,* 7(2), 248-260.

Wood, R., C. S. Bretherton, and D. L. Hartmann (2002), Diurnal cycle of liquid water path over the subtropical and tropical oceans. *Geophys. Res. Lett.*, **29**, 2092, doi:10.1029/2002GL015371.

Yu, H., R. Dickinson, M. Chin, Y. J. Kaufman, B. N. Holben, I. V. Geogdzhayer, and M. I. Mishchenko (2003), Annual cycle of global distributions of aerosol optical depth from integration of MODIS retrievals and GOCART model simulations, *J. Geophys. Res.*, **108**, 4128, doi:10.1029/2002JD02717.

Chapter 4

MESUREMENT-BASED ESTIMATION OF THE SPATIAL MEAN AND GRADIENT OF AEROSOL RADIATIVE FORCING

4.1. Introduction

Aerosol radiative forcing (ARF) is one of the largest uncertainties with respect to anthropogenic forcing on the present climate system [*NRC* 2005]. ARF is composed of direct radiative forcing (ADRF: direct scattering/absorbing of radiation) and indirect radiative forcing (AIRF: scattering/absorbing of radiation due to the modulation of cloud properties by serving as cloud condensation nuclei or ice nuclei).

Advanced satellite instruments can distinguish the small- (submicron) and coarse-mode (supermicron) aerosol optical depths that can be used to estimate the anthropogenic component of aerosol optical depth (AOD) and radiative forcing [*Kaufman et al.* 2005a]. Combined use of satellite data and chemical-transportation models is also a practical method to estimate ADRF [*Yu et al.* 2004]. A variety of measurement-based estimations of ADRF is reviewed in *Yu et al.* [2005].

The difficulty of estimating AIRF is linked to the intrinsic complexity of cloud dynamics and microphysics processes. Satellite instruments can measure the relationship between clouds and ambient aerosols on the large scale, and the AIRF can be possibly

estimated from the measured correlation. However, a satellite-based estimation has certain limitations. First, it is difficult to distinguish the cloud-aerosol correlation from a variety of thermodynamic effects on clouds [*Sekigushi et al.* 2003], although it is possible to reduce such effects by measuring the aerosol-cloud relationship in specific meteorological conditions [*Koren et al.* 2004; *Matsui et al.* 2005]. Second, the measured aerosol-cloud correlation does not imply physical causality; i.e., it is uncertain whether aerosols affect clouds (via nucleation or the semi-direct effect) or clouds affect aerosols (via wet deposition) [*Kaufman et al.* 2005b].

The ARF is typically discussed and compared as a global-scale spatial mean top-of-atmosphere (TOA) radiative forcing. Unlike greenhouse gases (GHG), however, aerosols have a much greater heterogeneity of their radiative forcing in time and space. This forcing can modulate mesoscale and large-scale circulations, which have potential impacts on the regional climate through dynamical feedback [*Menon et al.* 2002; *Lau* 2006, *Takemura et al.* 2004]. The spatial mean TOA radiative forcing may be ineffective in representing such effects [*NRC* 2005].

This paper evaluates the mean and spatial gradient of aerosol radiative forcing in comparison with that of the well-mixed GHG. The appropriate metric to assess the importance of the gradient of diabatic heating is the resulting gradients in the horizontal pressure field that fundamentally drives the atmospheric circulation [*Gill* 1982]. This study does not aim to compare methods or assess the detailed uncertainties in estimating the global mean ARF among different studies.

4.2. Methodology

The estimation of ARF in this paper is limited to the shortwave radiation and over tropical oceans between 37°N to 37°S for the period starting from 1st March 2000 to 28th February 2001, since i) the energy budget in the tropics is a critical factor for the global atmospheric circulation; and ii) the cloud and aerosol properties were compiled in this period and correspond to the domain in the previous study [*Matsui et al.* 2005]. The atmospheric radiative transfer was computed by the NASA Langley-version of the Fu-Liou code, which updated several components of the original four-stream correlated-k radiative transfer code [*Fu and Liou* 1993; *Charlock and Rose: personal communication*]. The vertical profile of atmospheric temperature, water vapor mixing ratio, and ozone mixing ratio are derived from the climatological values of sounding [*McClatchey et al.* 1972]. The spectral ocean surface albedo is computed from an empirical look-up table [*Jin et al.* 2002].

ADRF is estimated from the difference in the shortwave radiative heating rate between the current AOD and the potential AOD in clear sky conditions. The current AOD is obtained by the Moderate Resolution Imaging Spectroradiometer (Terra MODIS) Level-3 (collection 4) instantaneous AOD at 0.55 μm and 0.865μm, which are archived on a global 1° × 1° latitude-longitude grid. Total column AOD is subdivided into dust, sea salt, organic carbon, black carbon and sulfate components for each vertical atmospheric layer based on the co-located daily product of the chemical transportation model [*Chin et al.* 2004]. Potential AOD is estimated from the sum of estimated sea salt and dust AOD, although the potential AOD can be also estimated from the small-mode fraction of MODIS AOD [*Kaufman et al.* 2005a]. Aerosol optical properties are based on the Optical Properties of Aerosol and Cloud (OPAC) values [*Hess et al.* 1998].

Matsui et al. [2005] found relationships between marine low cloud properties and ambient thermodynamics and aerosols. For AIRF, potential low cloud properties (column cloud effective radius, liquid water path, and cloud fraction) are estimated as a function of ambient aerosol index (AI: AOD multiplied by the Ångstrom exponent) as well as lower-tropospheric stability (LTS: potential temperature difference between 700 mb and the surface), by using the correlation in *Matsui et al.* [2005]. The estimation of AIRF accounts for low liquid clouds with cloud top temperatures greater than 273 K. The approach is to perturb the observed *current* cloud properties for the *potential* cloud properties by using the empirical relationship between the ambient AI and cloud properties for a given LTS. Although this method helps to resolve the effect of aerosols and thermodynamics on cloud properties to some degree, physical causality is still uncertain. Thus, the estimated radiative forcing could be interpreted as the *possible* AIRF. The current and potential AIs are derived from the identical AOD to those used in the estimation of ADRF. The ADRF is not included in the estimation of AIRF.

4.3. Results

4.3.1. Aerosol Direct Radiative Forcing (ADRF)

Figure 4.1 shows the annually averaged ADRF over tropical oceans. The mean values of ADRF for the study area (37°S to 37°N) are –1.59 and –5.12 W m^{-2} at the TOA and the surface level. The large gap between the TOA and surface ADRF is explained by the strong atmospheric heating rate (3.53 W m^{-2}) due to presence of absorbing aerosols. These values are slightly higher than those in *Yu et al.* [2004], since this study focuses on tropical oceans where annual incoming solar radiation is high. The ADRF is quite

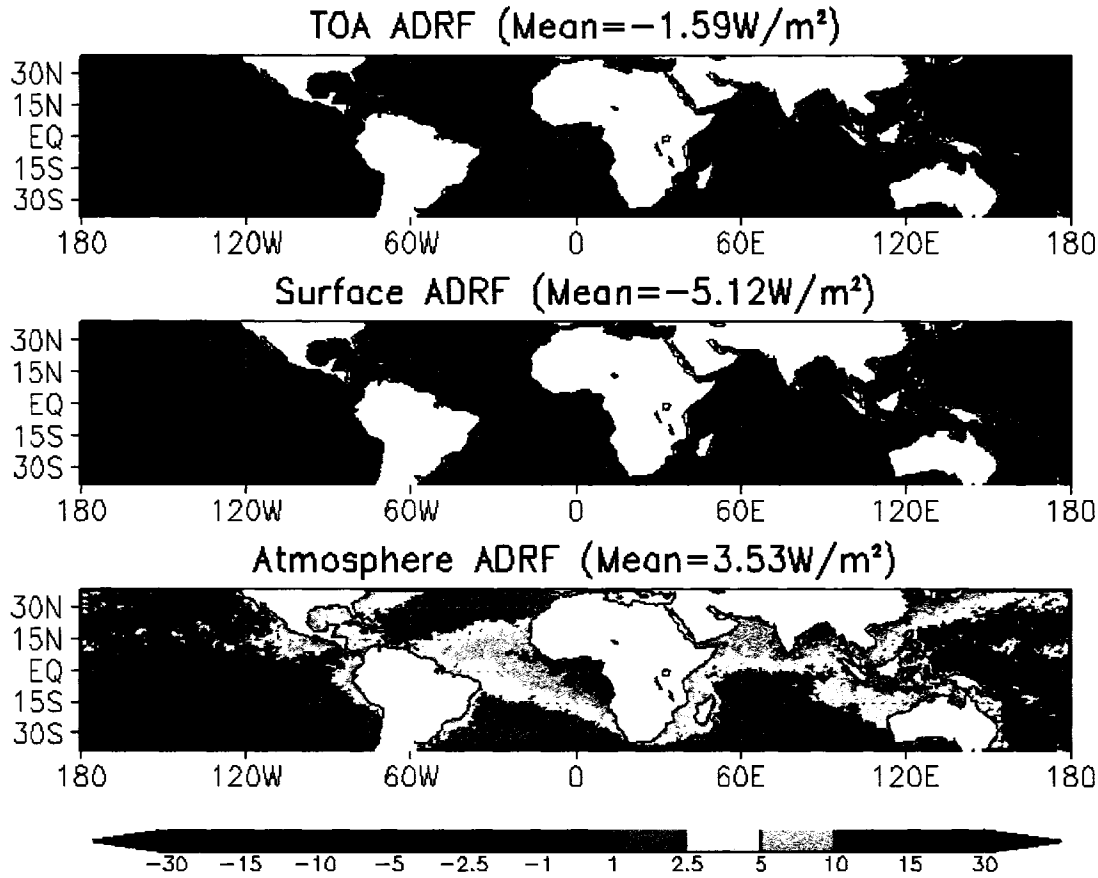

Figure 4.1. Shortwave aerosol direct radiative forcing (ADRF) for top-of atmosphere (TOA), surface, and atmosphere.

heterogeneous in space, ranging from 0 to –30 W m^{-2} at the surface level. Large ADRF at the surface and in the atmosphere exists off the west coast of Africa and the coastal zone along the South to East Asia. Althrough different assumptions of single scatting albedo of absorbing aerosols could change the mean radiative forcing [*Yu et al.* 2004], it does not change the annual spatial pattern of ADRF to a great extent.

Figure 4.2 shows the vertical profile of atmospheric heating rate due to shortwave ADRF at latitudes of 35°N, 15°N, and 5°S. At the latitude of 35°N, there is weak

boundary layer heating off the east coast of U.S. and across the Mediterranean Sea. The largest heating appears off the east coast of China, with the heating concentrated in the lower atmospheric layer. At the latitude of 15°N, strong boundary layer heating exists off the west coast of the Yucatan Peninsula due to the smoke emitted from biomass burning, and the strong peak over the Bay of Bengal is due to a relatively high concentration of soot [*Ramanathan et al.* 2001]. This South Asian brown haze induces atmospheric heating up to 0.5 K day^{-1} (about 20Wm^{-2}) in the bottom atmospheric layer. *Menon et al.* [2002] showed that the presence of the ADRF of black carbon modulates the general circulation and static stability fields elsewhere in the globe. *Lau et al.* [2006] found that ADRF over Tibetan Plateau can modulate the Asian Monsoon through the "elevated heat pumping" mechanism. At the latitude of 5°S, strong atmospheric heating extends up to the 600 mb pressure level off the west coast of Africa, where biomass burning frequently occurs due to agricultural practices. These vertical profiles and magnitudes of heating could be different for different seasons comparatively, and they must have unrevealed, dynamical interactions between the ADRF and regional climate.

4.3.2. Aerosol Indirect Radiative Forcing (AIRF)

Figure 4.3 shows the shortwave AIRF over the tropical ocean. The domain averaged AIRF is –1.38 W m^{-2} at the TOA level. It is slightly higher than the estimate (-0.6 to -1.2 W m^{-2}) in *Sekiguchi et al.* [2003]. The estimated AIRF is also heterogeneous in space, ranging from 0 to –30 W m^{-2} at the surface level. The strongest AIRF exists off the west coast of California, Chile, and Namibia, where strong temperature inversions (high LTS) exist. Over the Atlantic Ocean, the spatial pattern of AIRF reasonably agrees to the result

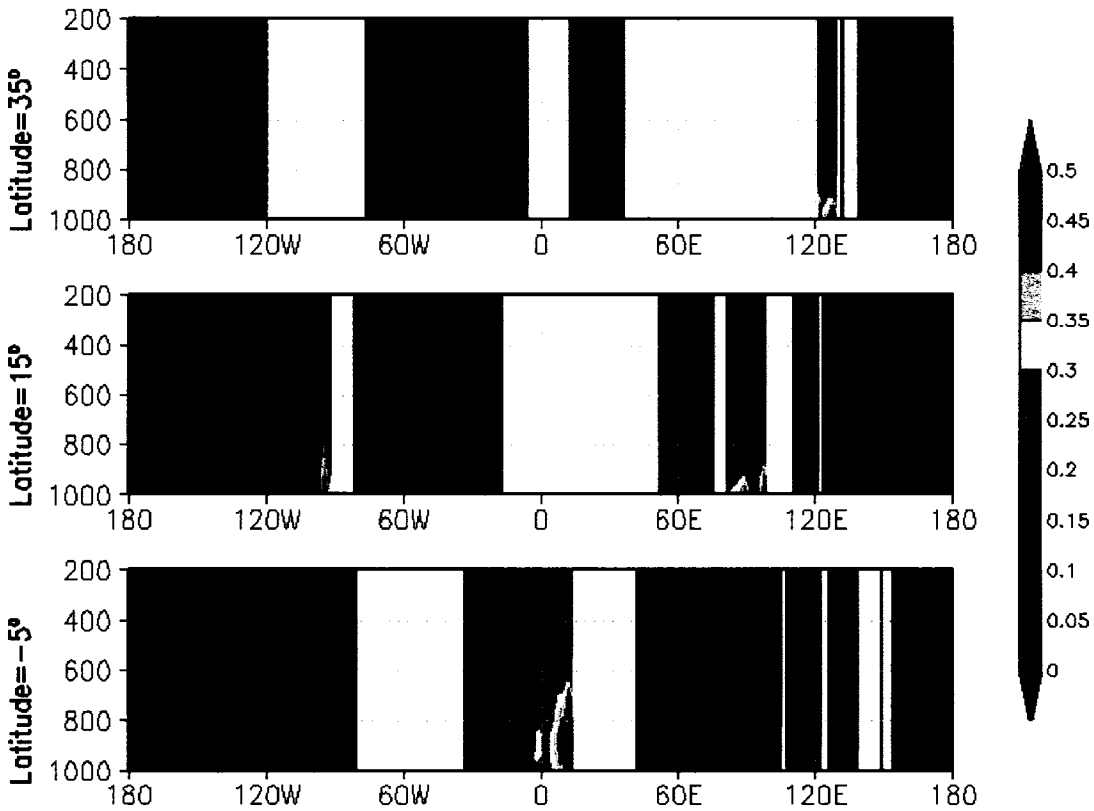

Figure 4.2. Vertical profile of atmospheric heating rate (K day^{-1}) due to shortwave ADRF. Vertical coordinate is pressure level (mb).

in *Kaufman et al.* [2005b]. In high LTS regions, the measured correlation in *Matsui et al.* [2005] tends to increase the cloud fraction for high AI, which strongly contributed to the large values of AIRF. *Sekiguchi et al.* [2003] also show that large AIRF exist over the downwind of continents. The peak ADRF regions appear to be associated with very weak or positive AIRF, possibly because the high ADRF enhances the evaporation of low clouds [*Koren et al.* 2004]. The estimation of AIRF could be significantly different, in terms of the spatial mean and the spatial pattern, if cold cloud-aerosol interaction is included [*Lin et al.* 2005].

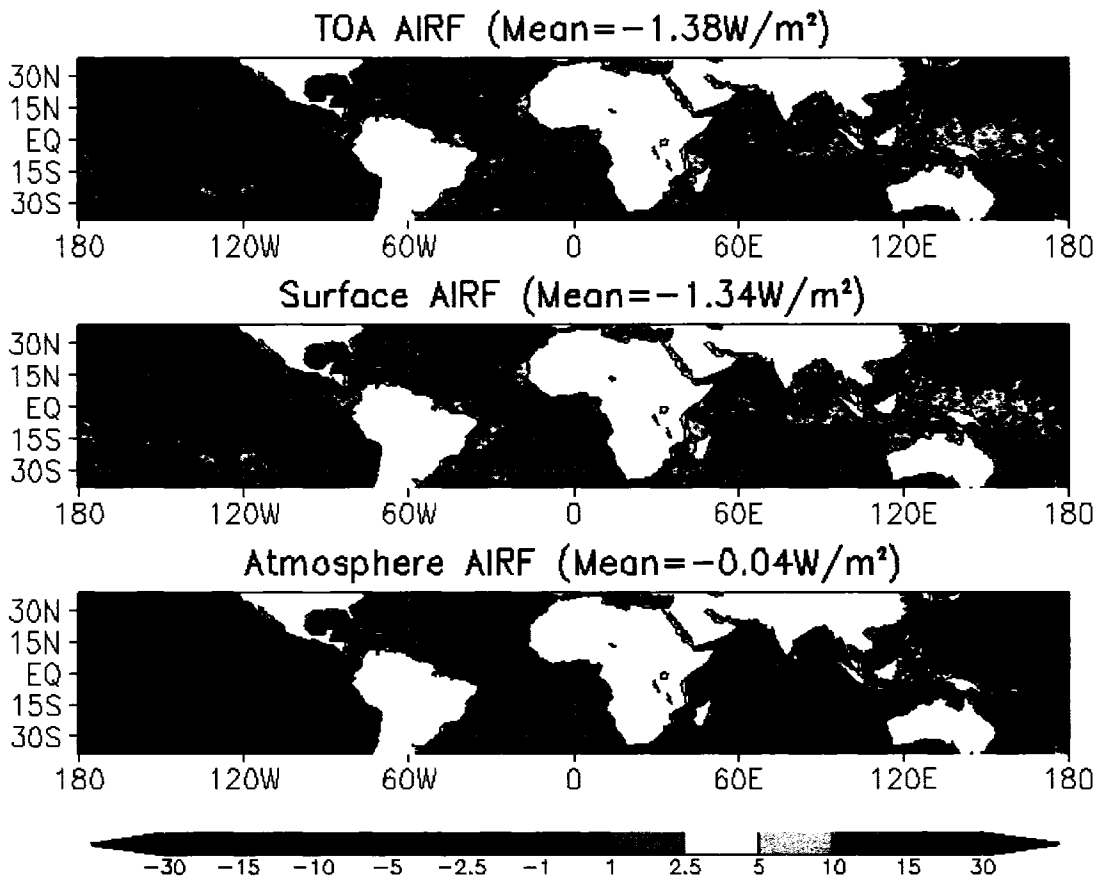

Figure 4.3. Shortwave aerosol indirect radiative forcing (AIRF) for top-of atmosphere (TOA), surface, and atmosphere.

4.4. Spatial Mean Radiative Forcing

Anthropogenic radiative forcing is currently expressed as the spatial (often on global scale) mean TOA radiative forcing in climate assessment reports or journals. This metric is useful for the energy budget of the entire Earth as a closed system, and for intercomparison among different studies and different forcing.

Figure 4.4 compares the tropical-ocean averaged radiative forcing between the GHG effect, aerosol direct effect, and aerosol indirect effect. GHG radiative forcing (GRF) was

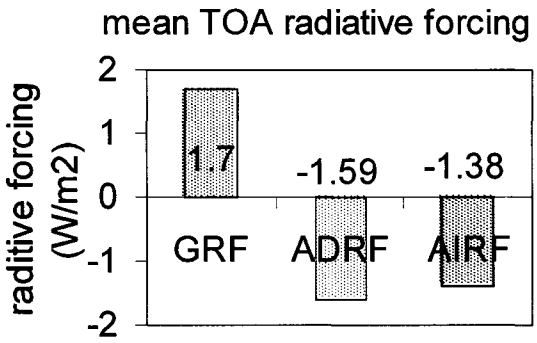

Figure 4.4. Comparison of Mean TOA radiative forcing between infrared GRF, shortwave ADRF, and shortwave AIRF.

estimated from the difference in infrared radiative cooling between pre-industrial and current levels of CO_2 (285.43 and 336.77 ppmv), N_2O (0.28 and 0.32 ppmv), CH_4 (0.86 and 1.79 ppmv), CFC-11 (0.0 and $268.\times10^{-6}$ ppmv), CFC-12 (0.0 and $503.\times10^{-6}$ppmv), and CFC-113 (0.0 and $105.\times10^{-6}$ ppmv), respectively. Note that shortwave ADRF is estimated in the clear sky, and shortwave AIRF is estimated without ADRF. Therefore, i) total aerosol radiative forcing is not equivalent to the sum of ADRF and AIRF; ii) ADRF and AIRF could be overestimated by neglecting cold clouds in the tropics.

In the spatial mean radiative forcing, GHG has the largest positive forcing (+1.7 Wm^{-2}), and aerosols appear to have an equivalent negative forcing (-1.59 and -1.38 Wm^{-2}) (Figure 4.4). However, this comparison may not be useful to discuss the effect on the climate, because the global climate is often suitably described as a combination of regional climates. Heterogeneous radiative forcing potentially induces a much greater impact on the regional climate by modulating atmospheric circulations [*Menon et al.* 2002; *Lau* 2006] and ocean circulation [*Takemura et al.* 2004].

4.5. Spatial Gradient of Radiative Forcing

In order to account for radiative forcing on the atmospheric motion, the spatial gradient of radiative forcing (*GoRF*) is defined. This is because fluid motion works to reduce the temperature gradient given by the heterogeneous insolation, as influenced by the Earth's rotation, friction, and other dynamical processes [e.g., *Gill* 1982; *Emanuel* 1995]. The types of circulation depend on the horizontal and vertical scale of the gradient and the latitude, ranging from mesoscale to planetary-scale circulations; thus, the gradient was computed for different spatial scales (e.g., in this study, horizontal distance from 1° to 20°). In addition, the anthropogenic component of *GoRF* is normalized with respect to the total component of *GoRF* for each spatial scale. The derived normalized gradient of radiative forcing (*NGoRF*) essentially means the fraction of the present Earth's heterogeneous insolation attributed to human activity on different horizontal scales. *NGoRF* for the meridional component is mathematically represented as

$$NGoRF = \frac{GoRF_{anthro}}{GoRF_{total}}$$

where

$$GoRF_{total} = \overline{\frac{\partial R_{total}}{\partial \lambda}}$$

$$GoRF_{anthro} = \overline{\frac{\partial R_{anthro}}{\partial \lambda}}$$

where $R_{total} = R_{total}(\lambda, \varphi)$ represents the present-time total radiative forcing at the surface level or in the atmosphere, $R_{anthro} = R_{anthro}(\lambda, \varphi)$ represent the anthropogenic component (GRF, ADRF, and AIRF in this study) of radiative forcing, λ represents longitude, φ represents latitude, over-bar means the spatial averaging. The zonal component of *NGoRF* can be described in a similar manner. In this study, R_{total} is limited to the observed (1st March 2000 to 28th February 2001) aerosols, marine low cloud, GHGs, and sea surface temperature. For this, I 1) derived the total and anthropogenic component of *GoRF* for the each neighboring pixels, and averaged over the entire domain to compute the *NGoRF*; and 2) aggregated the R_{total} and R_{anthro} map on different horizontal scales (λ=1°, 2, ··· 20°) to re-do the process 1) for computing the multi-scale *NGoRF*.

Figure 4.5 shows the multi-scale *NGoRF* in the atmosphere and at the surface level of shortwave ADRF, shortwave AIRF, and infrared GRF. *NGoRF* in the atmosphere on the spatial scale of less than a few degrees of latitude/longitude are associated with mesoscale circulations. *NGoRF* in the atmosphere on larger scales (up to 20°) is associated synoptic features such as the Hadley Circulation or the Walker Circulation in the tropics. Both are associated with meridional and zonal baroclinic atmospheric processes.

Figure 4.5 shows that ADRF exhibits the highest *NGoRF* (~0.18) for all horizontal scales. This means that the ADRF contributes up to 18% with respect to the meridional gradient of insolation in the current atmosphere. At the surface level, *NGoRF* on the large horizontal scale would be linked to the ocean insolation patterning. Figure 4.5 indicates that ADRF and AIRF show large contributions to the current ocean insolation patterning. *Takemura et al.* [2004] showed that the ADRF and AIRF have strong feedbacks to the

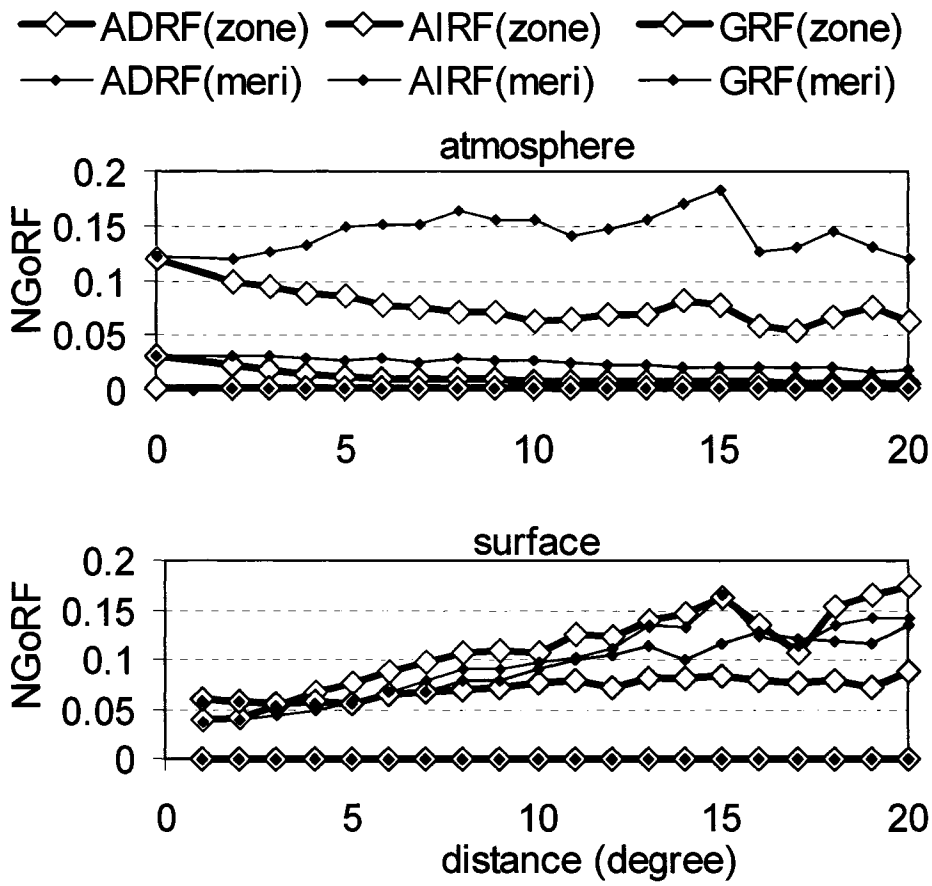

Figure 4.5. Comparison of the meridional and the zonal component of *NGoRF* between infrared GRF, shortwave ADRF, and shortwave AIRF for atmosphere and surface.

simulated general circulation, when the global atmospheric model is coupled with the ocean circulation model.

Although the TOA radiative forcing of GRF is the largest (Figure 4.4), the *NGoRF* of the GRF is almost negligible (~0.003) in comparison with AIRF (~0.14) and ADRF (~0.18). This study did not measure the interaction between the homogenous GRF and the heterogeneous ARF and how it affects the general circulation and regional climate. However, basic atmospheric dynamics requires that atmospheric diabatic heating

anomalies necessarily result in wind circulation anomalies. Thus, the aerosols have the potential to have a major effect on the weather and climate patterns in regions with a high aerosol gradient.

4.6. Summary

This study present a measurement-based estimation of the spatial gradient of aerosol radiative forcing. The *NGoRF* is introduced to represent the potential effect of the heterogeneous radiative forcing on the general circulation and regional climate. At present, there is no single metric of radiative forcing that can represent the complex interactions of atmospheric circulation. While the spatially resolved *NGoRF* could add to the ability to quantify regional climate forcing, this study encourage the community to test and develop the *NGoRF* for different years, seasons, over land, and patterns of sea surface temperature (SST) via numerical models or analytic solutions.

References

Emanuel, K.A. (1995), On thermally direct circulations in moist atmospheres. *J. Atmos. Sci.*, **52**, 1529-1534.

Fu, Q., and K.-N. Liou (1993), Parameterization of the radiative properties of cirrus clouds. *J. Atmos. Sci.,* 50, 2008-2025.

Gill, A. (1982), *Atmosphere-Ocean Dynamics*. Academic Press, New York, 662 pp.

Hess, M., P. Koepke, and I. Schult (1998), Optical Properties of Aerosols and clouds: The software package OPAC, *Bull. Amer. Meteor. Soc.,* 79, 831-844.

Jin, Z., T. Charlock, W. Smith Jr., and K. Rutledge (2004), A parameterization of ocean surface albedo. *Geophys. Res. Lett.*, 31, L22301, doi:10.1029/2004GL021180

Kaufman, Y. J., O. Boucher, D. Tanre, M. Chin, L. A. Remer, and T. Takemura (2005a), Aerosol anthropogenic component estimated from satellite data. *Geophys. Res. Lett.* **32**, L17804, doi:10/1029/2005GL023125.

Kaufman, Y. J., I. Koren, L. A. Remer, D. Rosenfeld, and Y. Rudich (2005b), The Effect of Smoke, Dust and Pollution Aerosol on Shallow Cloud Development Over the

Atlantic Ocean. *Proceedings of the National Academy of Sciences*, Vol 102 (32), pp 11207-11212.

Koren I., Y. J. Kaufman, L. A. Remer, J. V. Marins (2004), Measurement of the effect of Amazon smoke on inhibition of cloud formation. *Science,* **303**, 1342 – 1345

Lau, K.-M., M.-K. Kim, and K.-M. Kim (2006), Aerosol induced anomalies in the Asian summer monsoon – the role of the Tibetan Plateau. *Climate Dynamics*, in press.

Lin, J.C., T. Matsui, R.A. Pielke Sr., and C. Kummerow, (2006), Effects of biomass burning-derived aerosols on precipitation and clouds in the Amazon Basin: A satellite-based empirical study. *J. Geophys. Res.* (In press)

McClatchey, R.A., W. Fenn, J.E.A. Selby, F.E. Volz, J.S. Garing (1972), Optical Properties of the Atmosphere, AFCRL Environ. Res. Papers, 411, 108 pp.

Matsui, T. H. Masunaga, S.M. Kreidenweis, R.A. Pielke Sr., W.-K. Tao, M. Chin, Y. Kaufman (2006), Satellite-based assessment of global warm cloud properties associated with aerosols, atmospheric stability, and diurnal cycle, *J. Geophys. Res.*, (In press).

Menon, S., J.E. Hansen, L. Nazarenko, and Y. Luo (2002), Climate effects of black carbon aerosols in China and India. *Science,* 297, 2250-2253.

National Research Council (2005), *Radiative forcing of climate change: Expanding the concept and addressing uncertainties.* The National Academies Press, Washington, D.C., http://www.nap.edu/openbook/0309095069/html/

Sekiguchi, M., T. Nakajima, K. Suzuki, K. Kawamoto, A. Higurashi, D. Rosenfeld, I. Sano, and S. Mukai (2003), A study of the direct and indirect effects of aerosols using global satellite data sets of aerosol and cloud parameters, *J. Geophys. Res.*, 108, 4699, doi:10.1029/2002JD003359.

Takemura, T., T. Nozawa, S. Emori, T. Y. Nakajima, and T. Nakajima (2005), Simulation of climate response to aerosol direct and indirect effects with aerosol transport-radiation model. *J. Geophys. Res.*, 110, D02202, doi:10.1029/2004JD005029.

Yu, H., R.E. Dickinson, M. Chin, Y.J. Kaufman, M. Zhou, L. Zhou, Y. Tian, O. Dubovik, and B.N. Holben (2004), The direct radiative effect of aerosols as determined from a combination of MODIS retrievals and GOCART simulations, *J. Geophys. Res.*, 109, D03206, doi:10.1029/2003JD003914.

Yu, H., et al. (2005), A review of measurement-based assessment of aerosol direct radiative effect and forcing. *Atmos. Chem . Phys. Discuss.*, 5, 7647-7768.

Chapter 5

REGIONAL COMPARISON AND ASSIMILATION OF GOCART AND MODIS AEROSOL OPTICAL DEPTH ACROSS THE EASTERN U.S.

5.1. Introduction

Recent developments of satellite remote sensing and chemical-transport models improve the characterization of regional/global distributions of aerosol concentrations [*Kaufman et al.* 1997; *Chin et al.* 2002]. Assimilation technique is also developed to maximize the utility of the existing aerosol products [*Yu et al. 2003*]. Those developments have significantly improved the understanding of the global aerosol radiative forcing.

This work compares the AOD from current versions of the Terra Moderate-Resolution Imaging Spectroradiometer (MODIS) retrievals, the Goddard Chemistry Aerosol Radiation and Transport (GOCART) model, and the MODIS-GOCART assimilated products across the eastern U.S. This region features high concentrations of anthropogenic hygroscopic aerosols accompanied by high relative humidity (RH) [*Malm et al.* 2004], the existence of an extensive ground-based aerosol monitoring network [*Malm et al.* 2004; *Holben et al.,* 1998], and the reported positive bias of the MODIS AOD during ACE-Asia field experiment in April 2001 [*Chin et al.* 2004]. Therefore, the

regional intercomparison is critical for further evaluation and improvement of existing products.

5.2. Data

5.2.1. Ground-based measurements

The following ground-based *column AOD* and near-surface light extinction index (*Bext*) are used to evaluate the aerosol products in this chapter.

- Aerosol Robotic Network (AERONET/AEROCAN) is the ground-based remotely sensed aerosol measurement network equipped with well-calibrated CIMEL Sunphotometers [*Holben et al.,* 1998]. The 10 rural sites in the eastern U.S. (including Cartel, GSFC, Cove, Egbert, Chequamegon, Bondville, Walker Branch, Stennis, Cart site, and Konza EDC) were carefully chosen to assure adequate data coverage and homogeneous spatial distribution. This study uses the Angstrom exponent coefficient derived from the *Level-2 quality assured daily mean (during daytime)* column AOD at 0.5 μm and 0.67 μm for deriving the AOD at 0.55 μm.
- The IMPROVE (Interagency Monitoring of Protected Visual Environments) monitoring network measures fine and coarse aerosols in mostly rural areas throughout the United States [*Malm et al.,* 2004]. The network collects *24-hour* PM2.5 and PM10 samples every third day. The PM2.5 samples are analyzed for mass, elemental composition, ions, and organic and elemental carbon, while the PM10 filters are analyzed for mass. The data are sufficient to reconstruct the major aerosol components ammonium sulfate and nitrate, organics, light absorbing carbon and soil, which account for most of the measure fine mass. A near-surface *Bext*

(visible broad band) is also calculated from these data using the aerosol components, assumed component mass extinction efficiencies, and component water growth estimates based on climatological values of RH [*US EPA* 2003].

5.2.2. Aerosol Products: MODIS, GOCART, and Assimilation

The MODIS instrument aboard the EOS Terra satellite has been providing *instantaneous aerosol measurements* over land and ocean since March 2000 with local overpass time around 10:30 A.M. (see details in *Kaufman et al.* [1997]). AOD is determined by fitting lookup tables of assumed aerosol optical properties to the observed radiance. Validation with AERONET measurements showed that averaged errors of MODIS Level-2 products are generally within the estimated uncertainties, $\pm 0.05 \pm 0.20\tau$ over land [*Chu et al.* 2002]. This study uses the Terra MODIS Level-3 (collection 4) column AOD at 0.55 μm, which are archived on a global 1°×1° latitude-longitude grid.

GOCART is a global chemical-aerosol-transport model, driven by the Goddard Earth Observing System Data Assimilation System (GEOS DAS) global analysis (2°×2.5° grid space), including RH fields. It prognoses a global distribution of sulfate and its precursors, organic carbon, black carbon, mineral dusts and sea salt. AOD is determined from the dry mass concentrations and the mass extinction coefficients, which are functions of the size distributions, refractive indices, and RH-dependent hygroscopic growth of individual aerosol types (see details in *Chin et al.* [2002]). Note that the aerosol optical properties could be different between the GOCART and MODIS retrievals. This study uses daily column AOD from *Chin et al.* [2004], which updated the emission inventory of aerosols and their precursors from the earlier version.

MODIS-GOCART has been integrated (denoted as ASSIM) through the optimal interpolation (OI) following the method in *Yu et al.* [2003]. The absolute errors, derived from the comparisons with the daily AERONET measurements over 22-month period across the eastern U.S. (see a next section), are used to derive the fractional error (f) and the minimum root-mean square (RMS) uncertainties (ε) for GOCART and MODIS that determine the weight of interpolation (f_{MODIS} =0.41, ε_{MODIS} =0.01, f_{GOCART} =0.35, ε_{MODIS}=0.05). The errors in the satellite retrievals are assumed to be uncorrelated at the horizontal length scale (L = 0 km), while the errors in the model are assumed to be horizontally correlated (L = 200 km) (see discussions in *Yu et al.* [2003]).

5.3. Regional intercomparison

The regional comparison extends from March 1, 2000 to December 31 ,2001 at AERONET and IMPROVE sites, located apart from the emission source. This comprises 22-month daily values promising enough data for a robust statistical analysis. The sampling is conducted only when the MODIS, GOCART, and AERONET/IMPROVE are simultaneously available. The focused area is the eastern U.S. (24°N-49°N, 100°W-70°W), which is approximately the same region with smoke/urban/dust aerosols defined in the MODIS retrievals [*Kaufman et al.* 1997].

5.3.1. Daily and Long-term Analysis

Figure 5.1 shows the 22-month averaged AOD from the three products. All three AOD data reproduce a gradient from highest values in the mid-east to the western edge of the domain, but they also have considerably different distributions of AOD across the

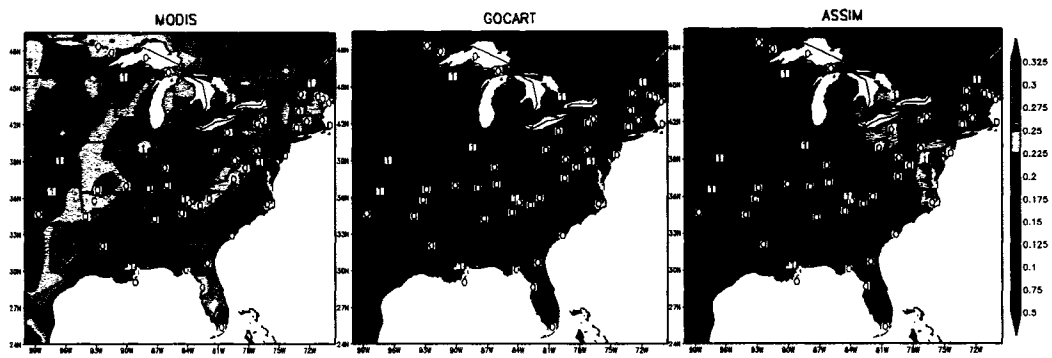

Figure 5.1. 22-month (Mar 1, 2000– Dec 31, 2001) averaged AOD at 0.55 μm from the MODIS retrievals, the GOCART simulation, and the MODIS-GOCART assimilation (ASSIM). AERONET and IMPROVE sites are represented with 1 and 0 in white box, respectively.

eastern part of the domain. The MODIS retrievals and ASSIM are spatially heterogeneous, and high AOD peaks exist (red regions: AOD > 0.3) along the coastal zones and over the Ohio River valley. The GOCART simulations appear to be more homogeneous and lower AOD than those in the MODIS retrievals.

Figure 5.2a compares the three AOD products with the ground-based measurements at 10 AERONET sites for a daily (black) and 22-month averaged case (red). For a daily case, the GOCART contains large scatters due to a combination of errors in the model simulation and the sampling volume difference (point versus grid), with a severe underestimation (more than factor of 2) at many high AOD. The temporal averaging most likely removed the point-versus-grid errors, and GOCART AOD (red) becomes comparable to the AERONET measurements (RMSE = 0.028). The characteristics of the errors were consistent with those in *Chin et al.* [2002]. The MODIS retrievals have high correlation, but overestimate the AOD for both a daily (RMSE = 0.152) and 22-month averaged case (RMSE = 0.091). These high biases are consistent to

the results as shown in *Chin et al.* [2004]. The ASSIM generate the best daily-scale RMSE (0.112). However, correlation and a 22-month averaged RMSE are values between those in GOCART and MODIS.

The IMPROVE data is utilized to evaluate the comparison furthermore, since the distribution of the AERONET network would be coarse for a regional evaluation. Regardless the intrinsic difference between the IMPROVE-measured near-surface *Bext* and the AERONET-measured column AOD, the scatters of the daily values in Figure 5.2b appear quite similar to those in Figure 5.2a. This indicates that the vertical distribution of AOD is not a dominant factor during the study period (22-month), although the AOD in the free troposphere would be important in the biomass burning events. Therefore, only the 22-month averaged case is discussed here. Under the assumption of the uniform aerosol mixing in the boundary layer (i.e., zero intercept) for long-term integration, the regressed slopes approximately represent the mixing depth (Figure 5.2b). Direct conversion from the IMPROVE *Bext* to the corresponding column AOD products result in the mean depths of the aerosol mixing layers: 3.4, 2.1, and 2.4 (km) for MODIS, GOCART and ASSIM, respectively. The observed typical mixing depths across the eastern U.S. (~ 2 km) [*Holzworth* 1967] also indicate the overestimation of the MODIS retrievals and good agreement of the GOCART simulation found in the Figure 5.2a.

5.3.2. Warm and Cold Season Analysis

The analysis is separated into warm (April – September) and cold (October – March) seasons (Figure 5.3a). The MODIS retrievals capture the strong seasonality in

warm and cold seasons with consistent positive biases, while the GOCART simulation shows a weak overestimation (underestimation) of the AOD in the cold (warm) season. Because of the overestimated AOD of the MODIS retrievals and underestimated AOD of the GOCART simulations in the warm season, the ASSIM becomes less biased with the best RMSE (0.040). Yet, the cold-season positive biases in both the GOCART simulation and the MODIS retrievals result in an overestimation in the ASSIM.

The IMPROVE *Bext* is also utilized to evaluate seasonality of the estimated AOD furthermore (Figure 5.3b). Slopes obtained from the MODIS and the ASSIM versus IMPROVE are larger in the warm season (converted mixing depth 3.8 km and 2.5 km, respectively) than those in the cold season (converted mixing depth 2.7 km and 2.1 km, respectively), although both mixing depths are overestimated than the typical values in the warm (~2 km) and cold season (~1.5 km) [*Holzworth* 1967]. The converted mixing depth of the GOCART for the cold season (2 km) is higher than the typical observed depth (less than 1.5 km) [*Holzworth* 1967]. This support the weak overestimation of the GOCART simulation in the cold season found in Figure 5.3a.

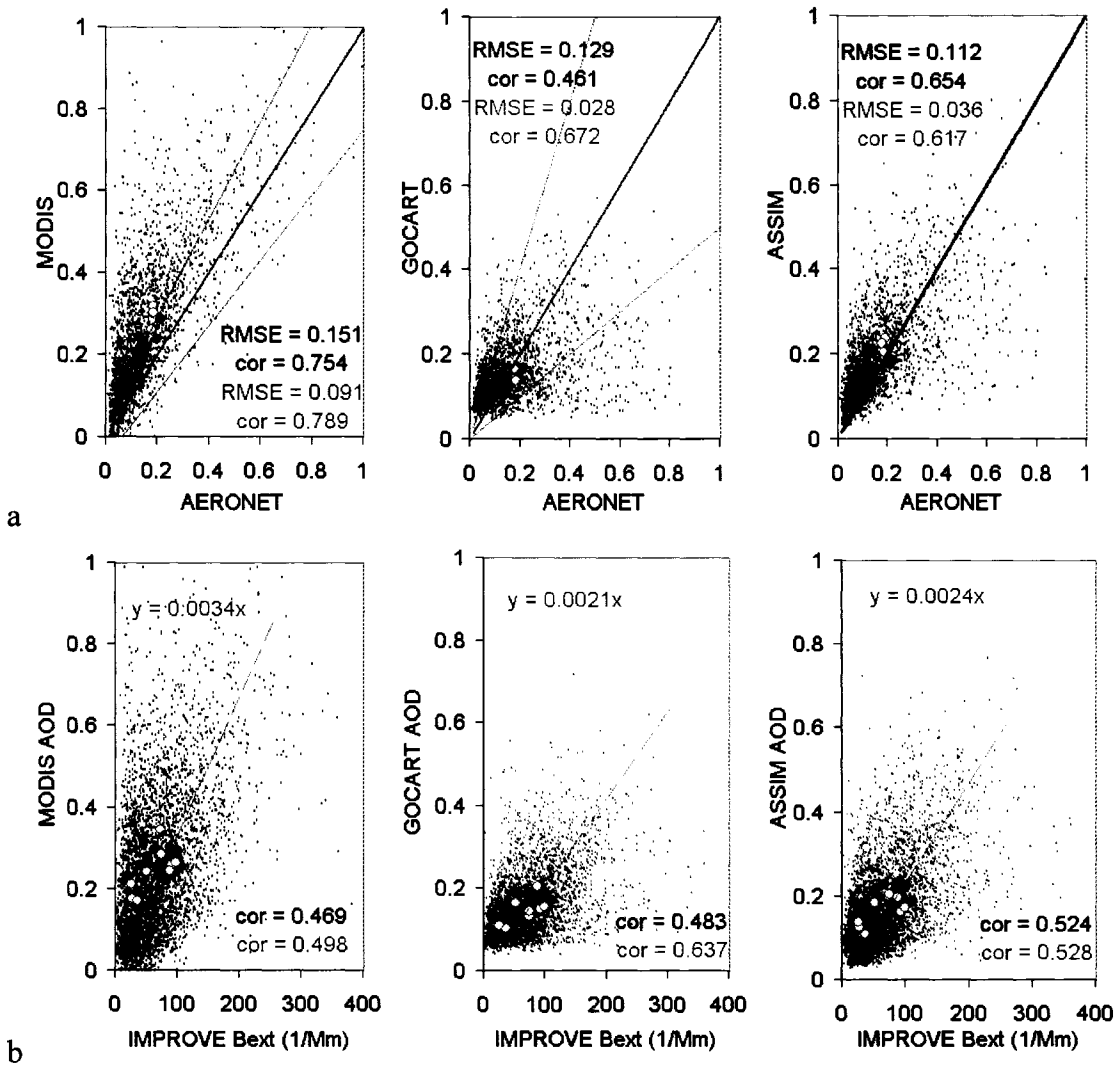

Figure 5.2.

a) Daily (black dots) and 22-month averaged (red dots) comparison between corresponding gridded AOD and AERONET measurements. (# of sample = 2627, # of site = 10)

b) Daily (black dots) and 22-month averaged (red dots) comparison between corresponding gridded AOD and IMPROVE measurements. (# of sample = 4328, # of site = 48)

Note that red open circles represent the sites in the coastal zone; the thick gray line represents a 1:1 ratio; and thin gray line represents estimated errors of the corresponding aerosol products [*Chu et al.* 2002; *Chin et al.* 2002].

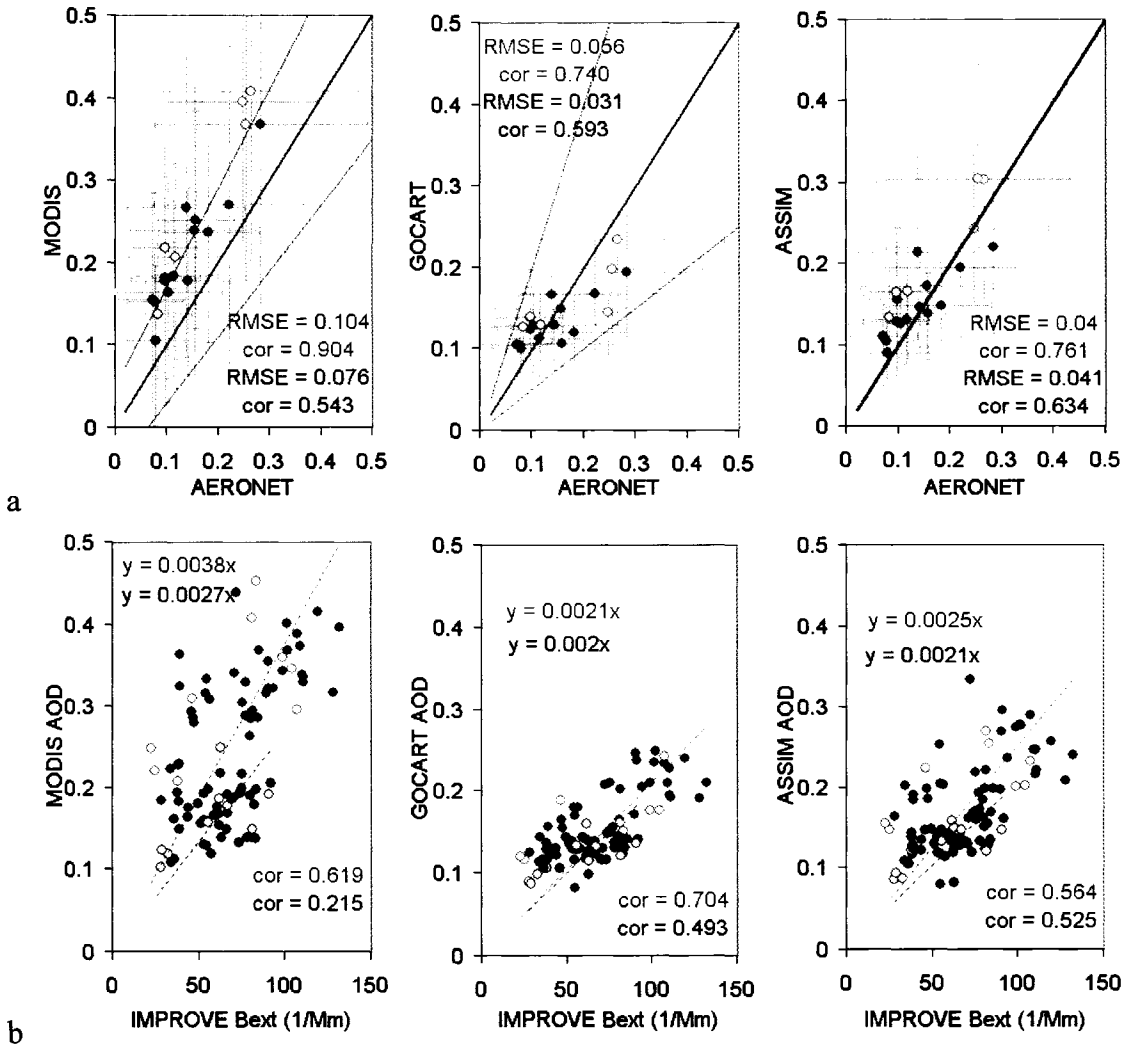

Figure 5.3.

a) Same as 2a, but integrated for warm and cold season. Warm Season (Red, April – September, # of sample = 1609, # of site = 10). Cold Season (Blue, October – March, # of sample = 1018, # of site = 10). Vertical and horizontal bars represent the standard deviation at each site.

b) Same as 2b, but integrated for warm and cold season. Warm Season (Red, April – September, # of sample = 2322, # of site = 47). Cold Season (Blue, October – March, # of sample = 2006, # of site = 48). Dotted line is the regression with zero intercept.

5.4. Probability Distribution

To illustrate the overall characteristics of the ground-based versus three AOD products, the probability distribution function (PDF) is examined in Figure 5.4. The PDF of the AERONET AOD is lognormally distributed. With respect to the central limit theorem, the PDF of the horizontally or temporally integrated values befalls narrower distribution with a peak at higher AOD. The running mean average of the AERONET measurements are performed in order to approximate a scale transformation from a point to the grid scale, since the direct horizontal average of the AERONET measurements cannot be conducted. Three-day running meaning (± one day) were conducted for representing the horizontal average with respect to the similar values of spatial autocorrelation (0.4~0.6) at hundreds-km horizontal scale (100~250 km) to the one-day temporal autocorrelation based on the result in *Anderson et al.* [2003]. The PDF resulted from the corrected AERONET measurements are shifted toward the higher AOD. A comparison with the shifted AERONET PDF suggests that the slight underestimation of the GOCART in the warm season is due to its narrower PDF associated with its large grid size, whereas slight overestimation of the GOCART in the cold season is due to the model bias. Those support the discussion in Figure 5.3b. The PDF of the MODIS retrievals is more broadly distributed, overestimating the frequency of large AOD. For the warm season, a combination of the high and low biases results in the appropriate PDF for the ASSIM. For the cold season, the ASSIM poorly represent the PDF due to a combination of the high biases of the MODIS and GOCART. These confirm the results; the quality of the ASSIM depends on the biases of the original products, which must be removed as much as possible before the assimilation.

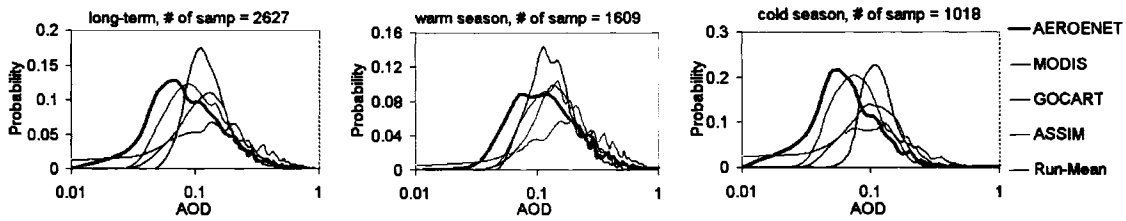

Figure 5.4. Probability distribution function of MODIS, GOCART, ASSIM, and the AERONET measurements. 3-day running means (Run-Mean) are performed for the AERONET measurements to represent the approximate grid-volume transformation.

5.5. Summary and Discussion

This study compared the spatio-temporal AOD of the instantaneous satellite (MODIS) retrievals, daily mean of chemical-transport model (GOCART) simulation, and assimilated (MODIS-GOCART) products with daily mean ground measurements at AERONET and IMPROVE sites across the eastern U.S. at a daily, seasonal, and 22-month average scale. The three AOD products exhibit significantly different distribution of AOD in the study area, and would result in the considerably different estimation of the aerosol effect on regional climate.

Overestimations of the MODIS Level-3 (collection 4) AOD at 0.55 μm are confirmed in comparison with the daily and time-integrated values in the AERONET measurements and IMPROVE *Bext* across the eastern U.S., although it has high correlations with AERONET measurements. The overestimation could be due to a) the erroneous estimation of the surface reflectance related to unresolved surface water contamination [*Chu et al.* 2002], b) the incorrect choice of the aerosol dynamic model and assumptions of aerosol optical properties [*Kaufman et al.* 1997], or c) a comparison between the instantaneous MODIS retrievals and the daily AERONET data [*Kaufman et al.* 2000]. Those issues should be included in future MODIS aerosol retrievals over land.

For a 22-month averaged case, the GOCART AOD are in the best agreement with AERONET measurements, whereas this agreement was deteriorated when the long-term integration was replaced by integration over a seasonal and daily scale. The coarse grid size and temporally smooth emission rate result in the characteristics of the histogram and the scatter plots of the GOCART. Careful examination revealed that GOCART has slight positive biases for the cold season. Biases could be corrected by improving the model processes for boundary layer depth estimates, including realistic seasonal variation of anthropogenic emission, incorporating precipitation-assimilated meteorological fields for wet deposition, or better handling the aerosol microphysics.

The optimal interpolation reduced the temporal RMSE of both the MODIS retrievals and the GOCART simulations. Because of the different systematic biases in the MODIS retrievals and the GOCART simulation, the assimilation (optimal interpolation) does not necessarily provide the best estimation. Developments of unbiased products are critical for better assimilation of regional AOD. These results can be utilized for future improvement of the aerosol estimation and assimilation from the GOCART and the MODIS.

References

Anderson, T.L., R.J.Charlson, D.M. Winker, J.A. Ogren, K. Holmen, 2003: Mesoscale Variations of Tropospheric Aerosols, *J. Atmos. Sci.,* **60,** 119 – 136.

Chin, M., P. Ginoux, S. Kinne, O. Torres, B.N. Holben, B.N. Duncan, R.V. Martin, J.A. Logan, A. Higurashi, and T. Nakajima, 2002: Tropospheric aerosol optical thickness from the GOCART Model and comparison with satellite and sun photometer measurements, *J. Atmos. Sci.,* **59,** 461 – 483.

Chin, M., D.A. Chu, R. Levy, L. Remer, Y. Kaufman, B. Hoben, T. Eck, and Paul Ginoux, 2004: Aerosol distribution in the northern hemisphere during ACE-Asia Results from global model, satellite observations, and Sunphotometer measurements. *Submitted to J. Geophys. Res.*

Chu, D.A., Y.J. Kaufman, C. Ichoku, L.A. Remer, D. Tanre, and B.N Holben, 2002: Validation of MODIS aerosol optical depth retrieval over land. *Geophys. Res. Lett.*, **29** (12).

Holben, B.N., T.F. Eck, I. Slutsker, D. Tanré, J.P. Buis, A. Setzer, E.F. Vermote, J.A. Reagan, Y.J. Kaufman, T. Nakajima, F. Lavenu, I. Jankowiak, and A. Smirnov, 1998: AERONET - A federated instrument network and data archive for aerosol characterization. *Remote Sens. Environ.*, **66**, 1-16.

Kaufman, Y.J., D. Tanré, L. Remer, E.F. Vermote, A. Chu, and B.N. Holben, 1997: Operational remote sensing of tropospheric aerosol over the land from EOS-MODIS. *J. Geophys. Res.*, **102**, 17051-17068.

Kaufman, Y.J., B.N. Holben, D. Tanré, I. Slutsker, A. Smirnovand T. F. Eck, 2000: Will aerosol measurements from *Terra* and *Aqua* polar orbiting satellites represent daily aerosol abundance and properties? *Geosphys. Res. Lett.*, **27**, 386-3864.

Malm, W.C., B.A. Schichtel, M.L. Pitchford, L.L. Ashbaugh and R.A. Eldred, 2004: Spatial and monthly trends in speciated fine particle concentration in the United States, *J. Geophys. Res.,* 109, D03306, doi: 10.1029/2003JD003739, 2004.

Holzworth, G.C. 1967: Mixing Depths, Wind Speeds and Air Pollution Potential for Selected Locations in the United States. *J. of Appl. Meteo.* **6(6)**, 1039–1044.

United States Environmental Protection Agency, Regional Haze: Tracking Progress Under the Regional Haze Rule: Guidance Document, **EPA Document No.** EPA-454/B-03-004, *Fed. Regist.*, 2003.

Yu, H., R.E. Dickinson, M. Chin, Y.J. Kaufman, B.N. Holben, I.V. Geogdzhayev, and M.I. Mishchenko, 2003: Annual cycle of global distributions of aerosol optical depth from integration of MODIS retrievals and GOCART model simulations. *J. Geophys. Res.*, **108,** D34128, doi:10.1029/2002JD002717, 2003.

Chapter 6

CONTINENTAL-SCALE MULTI-OBSERVATION CALIBRATION AND ASSESSMENT OF COLORADO STATE UNIVERSITY UNIFIED LAND MODEL BY APPLICATION OF MODIS SURFACE ALBEDO

6.1. Introduction

Land surface models (LSM) diagnose terrestrial mass and energy flux and biogeochemical processes, which are critical for applications in numerical weather forecasting and climate diagnostics. In the last several decades, hydrology and climate communities have developed a number of different types of LSMs for their research applications [*Pitman*, 2003]. Many LSMs participated in the Project for Intercomparison of Land-Surface Parameterization Schemes (PILPS) [*Henderson-Sellers et al.,* 2002]. PILPS' Phase 1 and Phase 2 experiments found a significant diversity in the performances of different LSMs [*Pitman et al.,* 1999]. This is because each LSM contain a number of different functional equations that represent soil-vegetation-atmosphere-transfer (SVAT) processes, and each function consists of different tunable parameters that usually cannot be measured directly or extensively in time and space.

The agreement between model output and observations can be improved by modifying tunable parameters. This process is called *model calibration.* Model

calibration can be accomplished manually (i.e. by-hand) for the simply structured LSM. However, as the structures of LSMs become more complicated, a manual calibration becomes difficult even for the experienced modeler. This is because parameterizations within LSMs are nonlinear and coupled; e.g., a change in the surface albedo results in the modification of turbulent heat flux, radiative temperature, photosynthesis, and root-zone soil moisture [*Niyogi et al.,* 1999]. Therefore, the hydrology community has been developing an automatic calibration framework that tunes a LSM via non-linear inversion model [*Gupta et al.,* 1999]. The automatic calibration more effectively improves an LSM with a simpler structure than one with a more complex structure [*Wood et al.,* 1998].

The calibration of an LSM generally requires two types of data: i) meteorological forcing, and ii) ground-truth observations of surface flux and state. The meteorological forcing data is the weather input that drives the LSM to calculate the energy and mass exchange (e.g., turbulent energy flux, runoff) and terrestrial state (e.g., biomass, soil moisture, temperature, and albedo), while surface observational data are used to examine the gaps between observations and model output. Most of the LSMs are usually calibrated or tested at a limited number of sites due to a lack of datasets required for the calibration. Calibrated tunable parameters at the specific site are not the universal answer, however. It is one possible combination of feasible parameters that satisfies the given calibration period and watershed; i.e., a calibration improves the performances of the LSM for a given calibrated time-scale and a given calibrated watershed [*Wood et al.,* 1998; *Lee et al.,* 1995].

LSMs create the spatial and temporal heterogeneity of the land surface energy and mass flux by assuming specific values of tunable parameters for each land-use/land-cover

(LULC) type and the geographical feature (e.g., topography, soil type, or leaf area). Because accurate spatial prediction of surface energy and mass flux is critical for the prediction of summertime deep cumulus convection and climate sensitivity [*Pielke,* 2001], the performance of an LSM should be assessed at every single numerical grid point within the model domain. Limited site calibration leads to uncertainty in the performance of an LSM, when the LSM has been applied to a region that features different combinations of soils, plants, and geology [*Niyogi et al.,* 1999; *Matsui et al.,* 2005].

Accuracy and horizontal coverage of datasets required for the calibration have been improved and extended in the past several years. Continental-scale high-resolution meteorological forcing has been developed by the Land Data Assimilation System (LDAS) project [*Cosgrove et al.,* 2003]. High-quality satellite datasets (LULC, leaf area index, surface temperature, and albedo) have been operationally derived from the Moderate Resolution Imaging Spectroradiometer (MODIS) aboard the Earth Observation Satellite (EOS) Terra and Aqua, which has provided global coverage since March 2000 [*Justice et al.,* 2002]. A network of ground eddy covariance tower measurements provides fluxes of CO_2, sensible and latent heat, and soil moisture, which are not directly available from satellite remote sensing [*Baldocchi et al.,* 2001]. A framework is needed that makes best use of the newly available datasets to calibrate and enhance the performance of LSMs. Otherwise it is becoming very difficult to evaluate an actual improvement of the LSM.

This chapter attempts to establish the continental-scale multi-observation calibration and assessment of an LSM over the conterminous U.S. (CONUS). This regional calibration framework uses the Colorado State University Unified Land Model

(CSU ULM) within the Land Information System (LIS) [*Peters-Lidard et al.,* 2004] coupled with the Parameter Estimation (PEST) model [*Watermark Numerical Computing,* 2004]. The continental-scale calibration process has three objectives. The first objective is to directly improve the performance of an LSM at a continental scale by tuning (or generalizing) the LULC- and geography-dependent parameters by minimizing the model-observation discrepancy for all the grid points within the model domain. The second objective is to determine the extent to which improvement in the performance of the LSM can be achieved by adjusting tunable parameters (obtained from a literature review) versus changing model structure. The third objective is to assess the performance between a limited-site calibration and a new large-scale calibration.

This study consists of a two-part series. Part I (this chapter) describes the calibration methodology and surface albedo calibration. Part II (Chapter 7) describes calibration of the land surface temperatures and turbulent heat fluxes. Surface albedo and associated net shortwave radiation are critical components of the surface energy and mass flux in an LSM [*Dickinson,* 1983], and the surface net radiation modulate the performance of the surface turbulent flux and land surface temperature, which are examined as a function of diffuse radiation in the next chapter. Although the ULM initialization uses a consistent set of the MODIS LAI and LULC data, the ULM does not produce surface spectral albedos that are consistent with the MODIS radiances, because of differences in the sophistication and assumptions of the canopy radiative transfer algorithms and soil albedo configurations. This discrepancy has been reported in a number of previous studies [*Oleson et al.,* 2003; *Zhou et al.,* 2003; *Tian et al.,* 2004;

Wang et al., 2004]. Thus, surface albedo must be estimated and its representation calibrated before the land-surface temperature calibration takes place.

6.2. Parameter Estimation (PEST) Model: Gauss-Marquardt-Levenberg algorithm

Parameter Estimation (PEST) model is a freely distributed optimization software, which uses a robust Gauss-Marquhardt-Levenberg (GML) algorithm. The LSM consists of numerous combinations of linear and nonlinear equations that represent energy and mass flux in the soil-plant-atmosphere system. The relationship between parameters and LSM output is represented as

$$\bar{c}_o = L(\bar{p}_o) \qquad \text{(eq. 6.3.1)}$$

L is a non-linear operator that transforms the n-dimensional tunable parameter vector ($\bar{p}_o$) into the m-dimensional LSM output vector ($\bar{c}_o$). Using the first order accuracy in Taylor's theorem, equation 1 is linearized to predict a new m-dimensional model output vector ($\bar{c}$),

$$\bar{c} = \bar{c}_o + \bar{J}(\bar{p} - \bar{p}_o) \qquad \text{(eq. 6.3.2)}$$

where $\bar{p}$ is the n-dimensional parameter vector which is slightly different from $\bar{p}_o$, $\bar{J}$ is the Jacobian matrix comprised of the m rows and n element of each row:

$$\bar{J} = \begin{bmatrix} \frac{\partial c_1}{\partial p_1} & \cdots & \frac{\partial c_1}{\partial p_n} \\ \vdots & \ddots & \vdots \\ \frac{\partial c_m}{\partial p_1} & \cdots & \frac{\partial c_m}{\partial p_n} \end{bmatrix} \qquad \text{(eq. 6.3.3)}$$

The numerical derivation of Jacobian matrix requires *n*- (forward differentiation) or 2×*n*-time (central differentiation) model evaluations.

The comparison between ground-truth or satellite observations ($\bar{o}$, *m* dimensions) and LSM output is defined by the weighted sums of squared deviations (Ψ: objective function):

$$\Psi = \left(\bar{o} - \bar{c}_o - \bar{J}(\bar{p} - \bar{p}_o)\right)^t \bar{Q} \left(\bar{o} - \bar{c}_o - \bar{J}(\bar{p} - \bar{p}_o)\right) \qquad \text{(eq. 6.3.4)}$$

,where $\bar{Q}$ is an *m*-dimensional square, diagonal matrix comprised of the squares of the weights in the diagonal elements. The optimal parameter upgrade vector ($\bar{u} = \bar{p} - \bar{p}_o$) is the vector that minimizes Ψ, i.e.

$$\frac{\partial \Psi}{\partial \bar{u}} = 0 \qquad \text{(eq. 6.3.5)}$$

The solution of the above equation is the Best Linear Unbiased Estimator (BLUE):

$$\bar{u} = \left(\bar{J}^t \bar{Q} \bar{J}\right)^{-1} \bar{J}^t \bar{Q} \left(\bar{o} - \bar{c}_o\right) \qquad \text{(eq. 6.3.6)}$$

Because the non-linear functions in LSM are linearized via the first order accuracy of Taylor's theorem, the above estimation requires several iterations to converge on the optimal parameter vector.

This approach is called the Gauss-Newton method. However, using this convergence scheme often becomes unreliable when the initial values of parameters are much different from the optimal values. In this case, the upgrade vector could lead to a stationary value of Ψ (zero gradient of Ψ), while Ψ is increasing. This is because the zero-gradient of Ψ could be either the local minimum or the maximum of Ψ. Most of non-linear parameter estimation methods benefit from adjusting $\bar{u}$ by taking advantage of both the Gauss-Newton method and steepest descent method:

$$\bar{u} = \left(\bar{J}^t \bar{Q} \bar{J} + \alpha \bar{I}\right)^{-1} \bar{J}^t \bar{Q} \left(\bar{o} - \bar{c}_o\right) \qquad \text{(eq. 6.3.7)}$$

where α is the adjusting Marquhardt-Levenberg parameter, and $\bar{I}$ is the n × n identity matrix [*Watermark Numerical Computing,* 2004]. The GML algorithm combines the advantages of the Gauss-Newton method and the steep descent method and therefore provides faster and more efficient convergence toward the minima of Ψ. The best set of parameter is selected from within reasonable ranges by adjusting the values until Ψ are reduced to a minimum in the weighted least squares sense [*Watermark Numerical Computing,* 2004]. PEST has been used in other non-linear inversion problems: e.g., a surface energy and carbon exchange model [*Wang et al.,* 2001], a distributed watershed model [*Liu et al.,* 2005], and a nutrient transportation model [*Baginska et al.,* 2003].

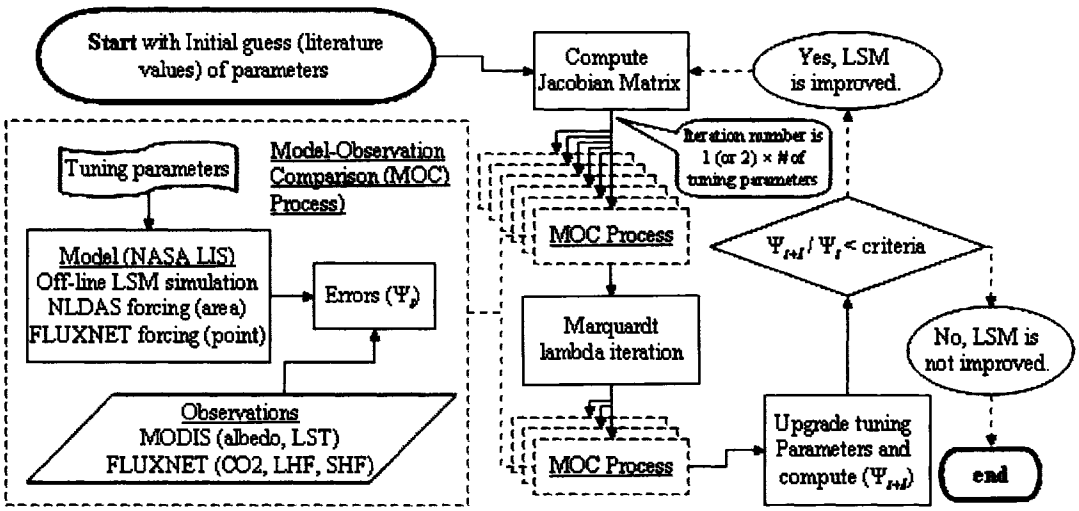

Figure 6.1. Flow chart of the calibration system. Model-Observation Comparison (MOC) processes are distributed in the parallel computing environment.

Figure 6.1 depicts the calibration process in the PEST. While continental-scale calibration requires significant machine time especially for computing the Jacobian matrix (the partial derivative of error as a function of each parameter), the parallel mode of PEST allows use of multiple CPUs for ensemble simulations and significantly reduces the required time (by nearly 30 times) [*Watermark Numerical Computing,* 2004]. This study used a Mac Xserve G5, consisting of 15 servers with dual 64-bit Mac G5 processors. Thus the maximum operating speed reaches to 135 gigaflops, enabling the completion of the calibration process in several days.

It should be noted that the population-evolution-based global optimization method generally performs better than the pure local search algorithm, because the global optimization method can avoid becoming stuck at multiple local optima in the parameter space [*Duan et al.,* 1992]. A recent development of the global optimization method

enables an efficient calibration process [*Vrugt et al.,* 2003]. However, it generally requires a computational cost that is as much as ten times that of the local search algorithm, and is impractical to apply to the high-resolution continental simulation in this study. Thus, the GML local searching algorithm is used, and it effectively reduces the apparent biases by generalizing the tunable parameters that satisfy the entire grid in the focused domain. This can be achieved mostly after the initial few iterations of local searching. The importance of evaluating the functional errors based on the post-calibration biases should be emphasized, and this study does not aim to develop an effective calibration method. This study examines the performance of large-scale calibration in comparison with a traditional limited-site calibration.

6.3. Tools and Datasets

6.3.1. Colorado State University Unified Land Model and Initialization

The Colorado State University (CSU) Unified Land Model, hereafter denoted as ULM, is the numerical land-surface model used in this study. The basic numerical schemes and code are extracted from the Community Land Model (CLM) 2.0 [*Oleson et al.*, 2004], the General Energy and Mass Transfer Model (GEMTM) [*Chen and Coughenour*, 1994], and the Land Ecosystem-Atmosphere Feedback (LEAF) model [*Walko et al.,* 2000]. Detailed soil-vegetation-atmosphere transfer parameterizations are described in the next chapter. The model includes a ten-layer soil, a two-component (sunlit and shaded) vegetation canopy, and 1 to 13 subgrid tiles. ULM has been developed within the NASA GSFC's Land Information System (LIS) that contains

several different LSMs and a wide variety of surface boundary conditions and meteorological forcings. The off-line simulations of LSM can be tested anywhere on globe down to the urban-resolving scale [*Peters-Lidard et al.,* 2004].

6.3.2. North American Land Data Assimilation System

High-quality atmospheric forcing datasets are critical for an LSM calibration. This study uses the assimilated forcing datasets derived by the multi-institutional North American Land Data Assimilation System (NLDAS) project [*Cosgrove et al.,* 2003]. Hourly National Weather Service Doppler radar-based (WSR-88D0) precipitation analyses were used to disaggregate the daily National Center for Environmental Prediction (NCEP) Climate Prediction Center (CPC) gauge-based precipitation to produce an hourly observation-based precipitation data set. Surface downwelling solar and thermal radiation is derived from Geostationary Operational Environmental Satellite (GOES) radiation data. Surface air temperatures, water vapor mixing ratios, horizontal winds, and surface pressures are derived from NCEP Eta Data Assimilation System (EDAS) output fields. These comprehensive forcing datasets are archived on a 0.125° grid box at every one-hour across the conterminous U.S. [see details in *Cosgrove et al.,* 2003]. The NLDAS meteorological field is used to force the CSU ULM on a one-hour time step.

6.3.3. Satellite-based Surface Observation: Initialization for the CSU ULM

A 0.25-degree subgrid LULC map was compiled from the MODIS-based University of Maryland (UMD) 1km-LULC data [*Hansen et al.,* 2000]. The UMD LULC

map contains 13 LULC classes. This study arranged the minimum tile fraction of 0.13% in the 0.25° grid in order to fully utilize the 1km information of the MODIS LULC data. Figure 6.2 shows the fractional coverage of UMD LULC classes in the study area. Vegetation amount is represented by a combination of green leaf-area index (LAI), dead LAI, and stem-area index (SAI), all of them derived from monthly composites of the MODIS 1km LAI from Boston University (hereafter denoted as BU LAI) [*Myneni et al.,* 2002]. The BU LAI product is exceptional in terms of the sophisticated algorithm used and the extensive validation work [*Knyazikhin et al.,* 1998; *Yang et al.,* 2004]. For LAI retrievals, the BU LAI uses a six-biome classification aggregated from the UMD LULC classes. Thus, BU LAI can be directly reassigned to the LAI in one of the 13 UMD LULC classes. The 1km LAI data are aggregated for each UMD LULC classes on the 0.25° grid map for the initialization of the ULM. Dead LAI is derived from the subtraction of green LAI in a previous month to a current month, assuming that dead foliage falls within a month (Dorman and Sellers 1989). SAI is computed as 20% of maximum LAI (L_{max}) of each UMD LULC class, whereas for grasslands SAI is computed from the difference between the L_{max} and green LAI. An L_{max} map was derived from 2000-2005 datasets of monthly BU LAI for each LULC type on each grid. Because ULM uses the 1-dimensional canopy radiative transfer model, vegetation fraction is defined as the canopy transmittance computed from the two-stream canopy radiative transfer model (TCRT). This configuration can avoid double counting of the surface reflectance ratio for vegetation fraction and LAI retrievals [*Matsui et al.,* 2005].

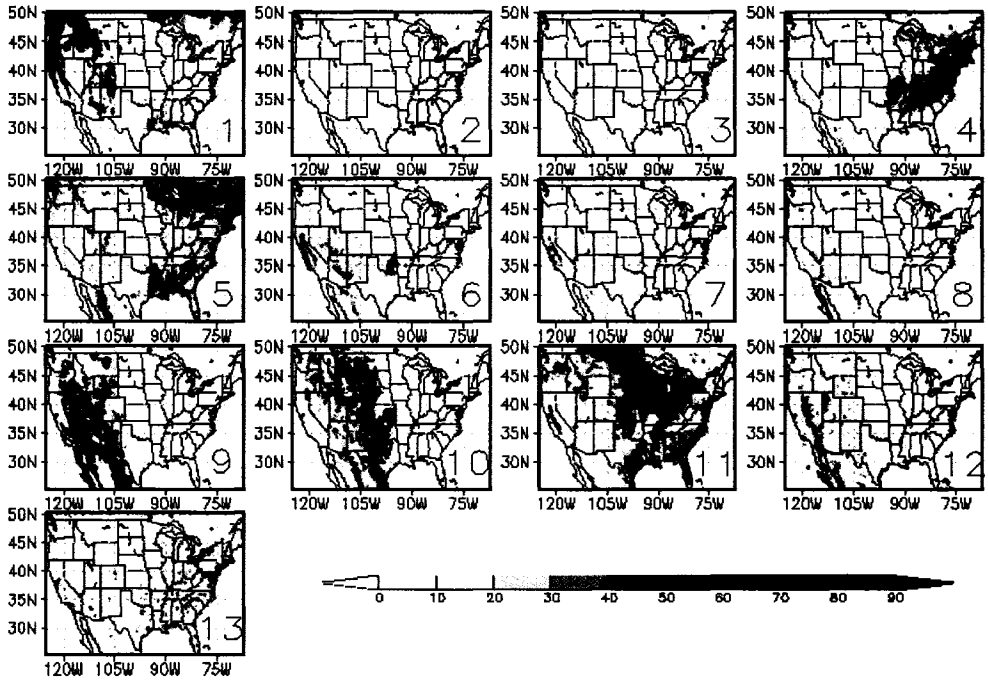

Figure 6.2. Distribution of fractional coverage of UMD LULC classes. 1. evergreen needleleaf forests, 2. evergreen broadleaf forests, 3. deciduous needleleaf forests, 4. deciduous broadleaf forests, 5. mixed forests, 6. woodlands, 7. wooded grasslands, 8. closed, shrublands, 9. open shrublands, 10. grasslands, 11. croplands, 12. barren, 13. urban

6.3.4. Satellite-based Surface Observation: MODIS spectral albedo

The MODIS instrument aboard the EOS Terra satellite has been providing important information for land surface properties with local overpass times around 10:30 AM/PM [*Justice et al.,* 2002]. Data quality of the MODIS land product is significantly better than those of the Advanced Very High Resolution Radiometer (AVHRR), because of the sensor on-orbit calibration [*Xiong et al.,* 2003], quality flags, and validation projects [*Morisette et al.,* 2002]. In addition to the MODIS LULC and BU LAI map for ULM's initialization, this study uses the MODIS spatially complete spectral surface albedo [*Moody et al.,* 2005] in Part I and land-surface temperature (LST) in Part II [*Wan*

et al., 2002] for calibration and evaluation of the performance of the off-line ULM. This study does not utilize other MODIS land products, such as surface evaporation fraction and net primary production, since they are derived from the surface spectral albedo, LAI, LULC and LST data using their own assumed relationships. In other words, the spectral albedo and LST are considered to be the data more directly related to the MODIS-observed radiance.

The spatially complete snow-free MODIS albedo datasets are used to calibrate leaf and soil optical properties in ULM (see section 4). The MODIS albedo was generated through a semi-empirical, kernel-driven linear bidirectional reflectance distribution function (BRDF). This BRDF relies on the 16-day composite of the atmospherically corrected MODIS surface reflectance. The product of MODIS albedo consists of local noon black-sky (for direct radiation) and white-sky (for diffuse radiation) albedo [*Schaaf et al.,* 2002]. A comparison with field measurement from the Surface Radiation Budget Network (SURFRAD) show that the MODIS surface albedo generally meets an absolute accuracy requirement of 0.02, with the root mean square errors less than 0.018 [*Jin et al.,* 2003]. In this study, this uncertainty of MODIS albedo is not taken into account for optimization process, but for the analysis of post- and pre-calibrated model albedo biases. Since this study intends to calibrate the vegetation and soil optical parameters, snow-free filled MODIS albedo products are used. The filled albedo product is a value-added product derived from MODIS spectral albedo by filling the missing values (including snow covered pixels) or low quality values [*Moody et al.,* 2005]. A temporal interpolation technique imposes pixel-level and local regional ecosystem-dependent phenological behavior onto retrieved pixel temporal data, while regional

unique pixel-level information is well maintained. The resulting snow-free spatially complete white- and black-sky surface spectral albedo maps are archived onto one-minute global map [*Moody et al.,* 2005]. For calibration work, one-minute MODIS data were aggregated onto the 0.25°-grid map, if more than 95% of land pixels are available in a 0.25°-grid cell.

This study uses the four different types of albedo: surface black- and white-sky albedo at visible (VIS) and near-infrared (NIR) bands, which corresponds to the direct and diffuse albedo at the VIS and NIR bands computed from the two-stream canopy radiative transfer model (TCRT) [*Dickinson,* 1983; *Sellers,* 1985]. The calibration of both black- and white-sky albedo is necessary for the ULM, because their accuracies are directly linked to the performance of sunlit- and shaded-canopy photosynthesis and net radiation in the ULM (and is described in next chapter). The effect of snow on the surface albedo was mechanically removed (snow component in the albedo was set to be zero in the numerical code) in this study, because this study aims to calibrate plant and soil optical properties against the snow-free MODIS surface albedo. Snow albedo will be calibrated in a future study.

6.4. Tunable Parameters and Calibration Periods

6.4.1. Two-stream Canopy Radiative Transfer (TCRT)

Surface spectral albedo is parameterized by the two-stream canopy radiative transfer model (TCRT) [*Dickinson,* 1983; *Sellers,* 1985] and empirical soil albedo model [*Idso et al.* 1975]. Soil albedo is used for the lower boundary condition of TCRT for vegetated tiles, while it represents the surface albedo for non-vegetated tiles (urban and

baregrounds class). Albedos in all subgrid tiles are averaged based on the fraction of subgrid tile coverage (0~1) to represent the total grid albedo.

The TCRT model has been widely used in different LSMs [e.g., *Xue et al.,* 1991; *Dickinson et al.,* 1993; *Sellers et al.,* 1996; *Oleson et al.,* 2004], because of its accuracy and computational efficiency in comparison with multi-stream or three-dimensional canopy radiative transfer [*Dickinson et al.,* 1987]. The TCRT model also plays an important role in computing the extinction coefficient of within-canopy sunlight penetration that is used for the sunlit- and shaded-components of canopy, photosynthetic capacity, and actually photosynthesis rates in the ULM.

Dickinson [1983] originally proposed to solve the canopy radiative transfer via the two-stream approximation,

$$-\bar{\mu}\frac{dI^{\uparrow}}{dL}+\left[1-\omega+\omega\beta\right]I^{\uparrow}-\omega\beta I^{\downarrow}=\omega\bar{\mu}K(\mu)\beta_o\exp(-K(\mu)L) \qquad \text{(eq. 6.4.1)}$$

$$-\bar{\mu}\frac{dI^{\downarrow}}{dL}+\left[1-\omega+\omega\beta\right]I^{\downarrow}-\omega\beta I^{\uparrow}=\omega\bar{\mu}K(\mu)(1-\beta_o)\exp(-K(\mu)L) \qquad \text{(eq. 6.4.2)}$$

where $I^{\uparrow}$ and $I^{\downarrow}$ are the upward and downward diffuse radiative flux normalized by the incident flux; μ is the cosine of the solar zenith angle; $K(\mu)$ is the optical depth of direct beam per unit leaf (or stem) area, and $K(\mu)=G(\mu)/\mu$; $G(\mu)$ is the relative projected area of leaf (or stem) in the direction of $\cos^{-1}\mu$, and $G(\mu)=\phi_1+\phi_2\mu$ (where $\phi_1=0.5-0.633\chi_L-0.33\chi_L^2$ and $\phi_2=0.877(1-2\phi_1)$); χ_L is departure of leaf angles

from a random distribution; $\overline{\mu}$ is the average inverse diffuse optical depth per unit leaf (or stem) area, and $\overline{\mu} = \int_0^1 [\mu'/G(\mu')]d\mu' = \frac{1}{\phi_2}\left[1 - \frac{\phi_1}{\phi_2}\ln\left(\frac{\phi_1+\phi_2}{\phi_1}\right)\right]$ (where μ' is the direction of scattered flux); ω is the scattering coefficient, and $\omega = \rho + \tau$; ρ is leaf-stem albedo; τ is the leaf-stem transmittance; L is the cumulative leaf-stem area index; β and β_o are upscattering fraction for diffuse and direct radiation, respectively. The upscattering parameter for diffuse radiation is inferred from the analysis of *Norman and Jarvis* [1975],

$$\omega\beta = 0.5 \cdot \left[\rho + \tau + (\rho + \tau)\left(\frac{1+\chi_l}{2}\right)^2\right] \qquad \text{(eq. 6.4.3)}$$

The upscattering fraction for direct radiation can be analytically derived from equation (6.4.1) and (6.4.2) with the assumption of single scattering ($\omega \to 0$) and semi-infinite canopy ($L \to \infty$) [*Dickinson,* 1983],

$$\omega\beta_o = \frac{1+\overline{\mu}K(\mu)}{\overline{\mu}K(\mu)}a(\mu) \qquad \text{(eq. 6.4.4)}$$

, where $a(\mu)$ is single scattering albedo

$$a(\mu) = \frac{\omega}{2}\frac{G(\mu)}{\mu\phi_2 + G(\mu)}\left[1 - \frac{\mu\phi_1}{\mu\phi_2 + G(\mu)}\ln\left(\frac{\mu\phi_1 + \mu\phi_2 + G(\mu)}{\mu\phi_1}\right)\right]. \qquad \text{(eq. 6.4.5)}$$

The analytic solution requires the inputs of the scattering coefficients of leaf and stem ($\omega = \rho + \tau$), soil albedo (α_{soi}, see the next section), total LAI and SAI, departure of leaf angles from a random distribution (χ_L), and the angle of the solar radiation (μ) (see the detailed analytic solution in *Sellers* [1985] and *Oleson et al.* [2004]).

In this study, tunable parameters include leaf reflectance at the VIS and NIR bands (ρ_{leaf}^{VIS} and ρ_{leaf}^{NIR}, respectively), dead leaf and stem reflectance for the VIS and NIR bands (ρ_{stem}^{VIS} and ρ_{stem}^{NIR}, respectively), and the departure of leaf angles from a random distribution (χ_L). The leaf-stem element reflectaince (ρ) are computed from the average of leaf and stem reflectances based on the weight of LAI and SAI. The equations applied to the VIS and NIR leaf and stem transmittance (τ) are kept the same as the ratio between the initial set of leaf reflectance and transmission in order to prevent an unrealistic ratio between leaf reflectance and transmittance due to an over-fitting in the calibration process.

6.4.2. Soil albedo

Initial model experiment uses the global soil color map, which contains 9 classes of soil color type that have values of dry and saturated (50% of dry value) soil albedo [*Reynolds et al.,* 1999]. This global soil map is not tunable, and the footprint size is too large (2.5°×2.5° grid size) to represent the spatial variability of soil albedo on the grid size used in this study. Thus, a tunable soil albedo map is introduced as a function of the log-normalized difference of maximum leaf area index (L_{max}) (see section 3.3) (*LND*).

$$LND = \frac{\ln(L_{\max}) - \ln(0.2)}{\ln(7) - \ln(0.2)} \qquad \text{(eq. 6.4.8)}$$

LND is closely related to the Normalized Difference Vegetation Index (NDVI), because LAI is derived as an exponential function of NDVI [*Myneni et al.,* 2002]. The values 0.2 and 7 are assigned as the minimum and maximum LAI within the domain. The *LND* should have a relationship with the topsoil organic fraction, because the maximum LAI is a good indicator of plant production rate and standardized soil respiration rate [*Reichstein et al.* 2003]. It is also well known that higher topsoil organic fraction tends to lower the soil albedo [e.g., *Jensen* 2000, Figure 13-8]. Thus, an empirical function is introduced to relate *LND* to dry soil VIS and NIR albedo:

$$\alpha_{dry}^{VIS} = \frac{0.01}{a^{VIS} + b^{VIS} LND} \qquad \text{(eq. 6.4.9)}$$

$$\alpha_{dry}^{NIR} = \frac{0.01}{a^{NIR} + b^{NIR} LND} \qquad \text{(eq. 6.4.10)}$$

where a^{VIS}, b^{VIS}, a^{NIR}, b^{NIR} are tunable parameters, and "*dry*" and "*sat*" refer to the dry and saturated (defined by the wetness fraction) soil moisture conditions. The proposed equations and tunable parameters can fit any possible pattern of expected relationship between the soil albedo and *LND*. Saturated soil albedo (α_{sat}^{VIS} and α_{sat}^{NIR}) is assumed to be 50% of the dry albedo [*Reynolds et al.,* 1999].

Temporally varying soil albedo is derived from dry and saturated soil albedo, wetness fraction (Δ) in top-soil moisture [$\Delta = \eta / \eta_{\max}$ where η is volumetric soil moisture (m^3m^{-3}) and $\eta_{\max}$ is porosity (m^3m^{-3})], and solar zenith angle [*Idso et al.,* 1975]. For dry soil (Δ<0.3), soil albedo is a sum of dry soil albedo and a correction factor of solar zenith angle A_ϕ [For direct radiation: $A_\phi = \left\{\exp\left[0.003286 \cdot \phi^{1.5}\right] - 1\right\}/100$. For diffuse radiation, A_ϕ is integrated for all solar zenith angles for direct radiation (= 0.034).],

$$\alpha_{soi}^{VIS} = \alpha_{dry}^{VIS} + A_\phi \qquad \text{(eq. 6.4.11)}$$

$$\alpha_{soi}^{NIR} = \alpha_{dry}^{NIR} + 0.5A_\phi \qquad \text{(eq. 6.4.12)}$$

For wet soil (Δ<0.5), soil albedo is a sum of saturated soil albedo and a correction factor of solar zenith angle

$$\alpha_{soi}^{VIS} = \alpha_{sat}^{VIS} + A_\phi \qquad \text{(eq. 6.4.13)}$$

$$\alpha_{soi}^{NIR} = \alpha_{sat}^{NIR} + 0.5A_\phi \qquad \text{(eq. 6.4.14)}$$

For intermediate soil, (0.3< Δ <0.5), soil albedo is linearly interpolated from values between saturated and dry albedo (Eq. 6.4.11 ~ 6.4.14),

$$\alpha_{soi}^{VIS} = \alpha_{dry}^{VIS} - \frac{(\Delta - 0.3)(\alpha_{dry}^{VIS} - \alpha_{sat}^{VIS})}{0.2} \qquad \text{(eq. 6.4.15)}$$

$$\alpha_{soi}^{NIR} = \alpha_{dry}^{NIR} - \frac{(\Delta - 0.3)(\alpha_{dry}^{NIR} - \alpha_{sat}^{NIR})}{0.2} \qquad \text{(eq. 6.4.16)}$$

6.4.3. Calibration domain and period

The domain size covers approximately the conterminous U.S. and northern Mexico (latitude of 25N to 50N, longitude of 125W to 65W) and a grid size of 0.25°×0.25° (Figure 6.3). The domain and grid size are configured close to those of NLDAS meteorological forcing. The simulation domain comprises of 16,648 land grid cells and total 61,883 subgrid tiles. The number of subgrid tiles per grid cell is close to one over the croplands in the Midwest, whereas it ranges up to 11 over the southeast and western portion of the domain (Figure 6.3).

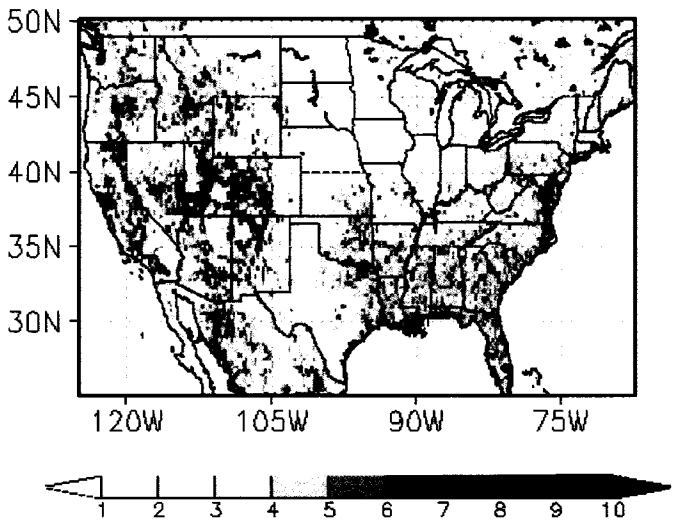

Figure 6.3. The number of subgrid tiles per modeled grid-cell.

While the MODIS spatially complete surface spectral albedo dataset is available from March 2000 to December 2004, three months from 2000, March, July and November are selected for the calibration due to computational time-constraints. These three months characterize the early development, maturity and senescence, respectively, of the vegetation over U.S. (Figure 6.4). The sensitivity of soil albedo (a^{VIS}, b^{VIS}, a^{NIR}, b^{NIR}) to the surface albedo can be relatively large in March, since both LAI and SAI are small over most the regions including the broadleaf and mixed forested areas. The contribution of soil albedo is almost negligible when the sum of LAI and SAI becomes greater than three [*Goudriaan,* 1977]. Thus, the contribution of leaf reflectance (ρ_{leaf}^{VIS} and ρ_{leaf}^{NIR}) becomes large in July over the eastern portion of domain and coastal regions in the western U.S. Because of the senescence of the vegetation in November, the contribution of the stem/dead leaf reflectance (ρ_{stem}^{VIS} and ρ_{stem}^{NIR}) becomes large over the deciduous forests. Over the central U.S., due to small LAI, soil albedo is the key parameter that controls the spectral albedo throughout the seasons. Top-layer (0~2cm) soil moisture has different spatial distributions between March, July, and November so that the parameterized soil albedo could be calibrated as a function of soil moisture. Thus, multi-month albedo calibration is designed to balance the calibrating weight of the optical properties between leaf, stem/dead leaf, and soil surface. The total number of calibrating points in the three-month period is 175,800, including black and white-sky albedo at the VIS and NIR bands. The large number and variations of simulation points enables a more robust calibration process than a limited-site calibration does. Each monthly simulation is separately performed for March, July, and November.

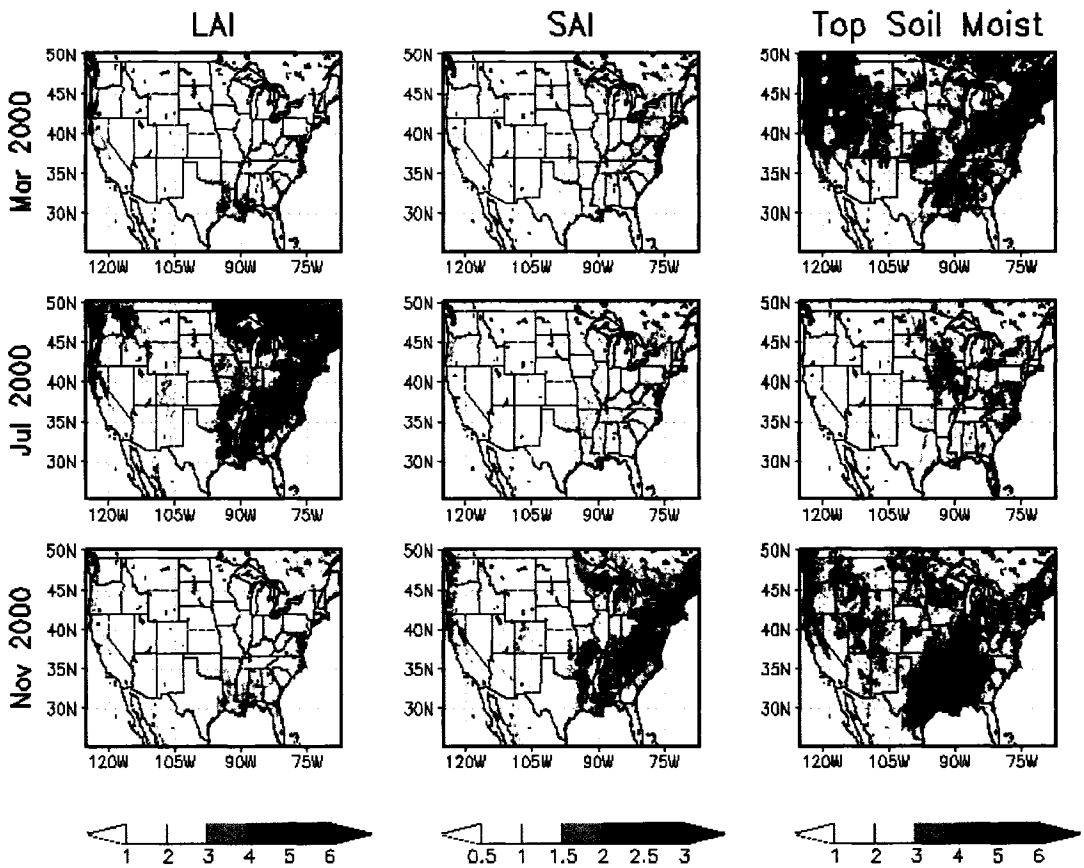

Figure 6.4. Monthly mean of leaf area index (LAI), dead leaf- and stem- area index (SAI), top-layer (0~2cm) soil moisture (kg m^{-2}).

6.5. Results

6.5.1 Experiments before Calibration

Table 6.1 shows the initial set of tunable parameters for each UMD LULC class. According to the correspondence between UMD LULC and BU LAI vegetation classes, the tunable parameters for surface albedo are the same between evergreen needleleaf and deciduous needleleaf forests, evergreen broadleaf and deciduous broadleaf forests,

woodland and wooded grasslands, closed and open shrublands (Table 6.1). In order to avoid unrealistic convergence, upper and lower bounds are assigned for tunable parameters for forests and savannas classes, respectively: ρ_{leaf}^{VIS} (0.08, 0.2), ρ_{leaf}^{NIR} (0.3, 0.6), ρ_{stem}^{VIS} (0.08, 0.3) and ρ_{stem}^{NIR} (0.25, 0.7). Values for the pre-calibration tunable parameters correspond to those that are commonly used in the community [*Bonan et al.,* 2002; *Dorman and Sellers,* 1989], and are displayed in Table 6.1. χ_L of savannas, crops and shrubs are set to be zero (random distribution). The pre-calibration ULM simulation used the existing global soil color map [*Reynolds et al.,* 1999].

Figure 6.5a shows the spatial map of differences in local-noon surface spectral albedo between the MODIS observations and the pre-calibration ULM (i.e., MODIS – ULM). In March and November, ULM overestimates the VIS albedo over the central U.S., where LAI is small. These biases are similar between black and white VIS albedo, but appear to be slightly larger in white albedo. Large errors appear at the NIR band. The largest overestimation of ULM exists in the central U.S. for all the months. In July, ULM underestimates the black NIR albedo across the Appalachian Mountains, Midwest, and

UMD	BU LAI	ρ_{leaf}^{VIS}	ρ_{leaf}^{NIR}	ρ_{stem}^{VIS}	ρ_{stem}^{NIR}	χ_L
1. evergreen needleleaf forests 3. deciduous needleleaf forests	needleleaf forests	0.070	0.350	0.160	0.380	0.00
2. evergreen broadleaf forests 4. deciduous broadleaf forests	broadleaf forests	0.100	0.450	0.160	0.380	0.250
5. mixed forests	-	0.100	0.450	0.160	0.380	0.250
6. woodlands 7. wooded grasslands	Savannas	0.070	0.350	0.160	0.380	0.00
8. closed shrublands 9. open shrublands	Shrubs	0.100	0.450	0.160	0.380	0.00
10. grasslands	grasses / cereal crops	0.110	0.580	0.360	0.580	-0.30
11. croplands	broadleaf crops	0.110	0.580	0.160	0.380	0.00

Table 6.1. Tunable parameters of each LULC class before the calibration. Pre-calibration soil albedo uses the global soil albedo map (Reynolds et al. 1999).

the western edge of U.S. ULM overestimates the white NIR albedo over the most of the domain in all the months.

Figure 6.5b shows descriptive statistics (*m*: mean, *s*: standard deviation, and *rmse*: root-mean-square error) and scatter plots of the errors (MODIS – ULM) in the local-noon albedo (×100) for the tile fraction (0.8 ~ 1.0) of each LULC type. Black and white sky VIS albedos show small scatter ($s < 2.0$) and biases ($m < 2.0$) of errors in all forest classes, savannas, and croplands, while large variations and biases are observed in shrublands, grasslands, bare ground, and urban. The ULM overestimates the black and white VIS albedo in shrublands, grasslands and urban. The overestimation of VIS albedo in shrublands and grasslands corresponds to the blue-shaded regions over the central U.S in March and November 2000 (Figure 6.5a). The ULM also slightly overestimates the white VIS albedo in needleleaf forests, broadleaf forests, and mixed forests, but this is almost within the uncertainty ranges (< 2.0) in the operational MODIS albedo product (Jin 2003). Strong variations and biases exist in all the LULC classes for NIR albedo. The ULM tends to underestimate the black NIR albedo in needleleaf forests, broadleaf forests and savannas, which corresponds to the red regions of black NIR albedo in July (Figure 6.5a). The ULM strongly overestimates ($m < -5.0$) NIR albedos in mixed forests, grasslands, croplands and urban classes. Those overestimations characterize the extensive blue area of white NIR albedo in Figure 6.5a. An interesting pattern of albedo bias in the ULM is that biases in white sky albedo are larger than those in black sky albedo. This is consistent with the finding from *Wang et al.* [2004], and can be explained by the fact that a difference between black- and white-sky albedo in the ULM (i.e., TCRT) is larger than that in the MODIS albedo. This will be further discussed in the following section.

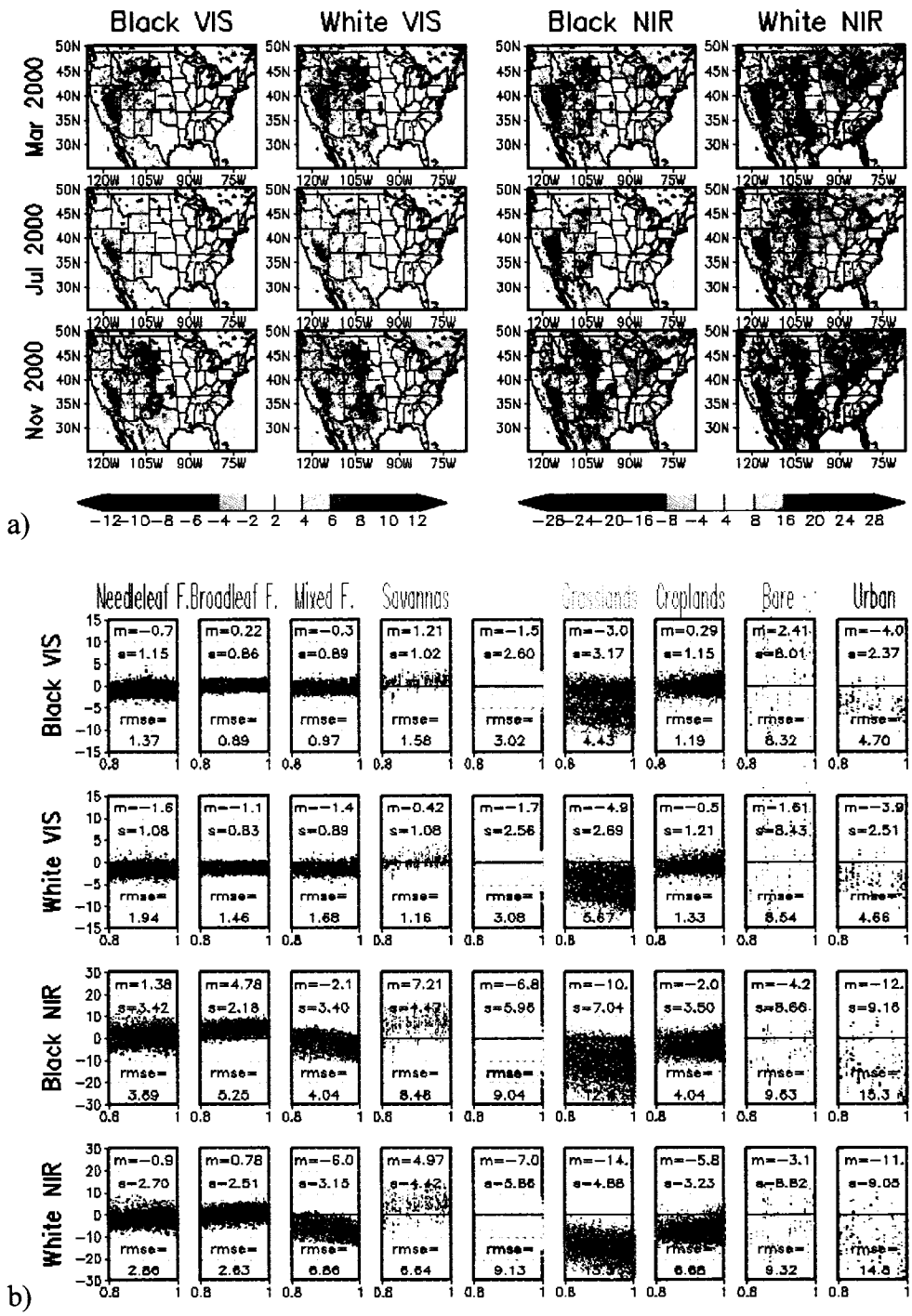

Figure 6.5. a) Spatial map of pre-calibration differences (MODIS – ULM) in spectral surface black and white albedos (×100). Note VIS and NIR albedo use different scales. b) Scatter plots and statistics (*m*: mean, *s*: standard deviation, and *rmse*: root mean square error) of the pre-calibration difference (MODIS– ULM) in spectral surface black and white albedo (×100). X-axis represents the fraction (0.8~1.0) of each land-cover class. VIS and NIR albedo use different scales in y-axis.

6.5.2. First Calibration Experiment

The calibration process takes approximately 5 iterations to achieve the convergence (approximately 300 model runs). Most of the errors were reduced after the first and second iterations. The entire calibration process results in the final Ψ of 1.12×10^6, which is 18.3% of Ψ in the experiment before the calibration ($\Psi = 6.12\times10^6$). Table 6.2 shows the resultant parameters for each LULC class and soil albedo parameterization. Maximum relative changes of VIS leaf reflectance (ρ_{leaf}^{VIS}) occur in broadleaf and mixed forest. Broadleaf forest increased about 50% of the initial ρ_{leaf}^{VIS} until at the high bound (0.15), while mixed forest decreased about half of the initial ρ_{leaf}^{VIS}. In NIR leaf reflectance the absolute changes are quite large (~0.14), although the relative changes are small. ρ_{leaf}^{NIR} was decreased in the mixed forests, shrublands, grasslands, and croplands, while it was increased in the needleleaf forests, broadleaf forests, and savannas. VIS stem reflectance (ρ_{stem}^{VIS}) shows a quite variety of changes. All the forest

UMD	BU LAI	ρ_{leaf}^{VIS}	ρ_{leaf}^{NIR}	ρ_{stem}^{VIS}	ρ_{stem}^{NIR}	χ_L
1. evergreen needleleaf forests 3. deciduous needleleaf forests	needleleaf forests	0.047	0.376	0.094	0.342	-0.208
2. evergreen broadleaf forests 4. deciduous broadleaf forests	broadleaf forests	**0.15**	0.516	0.096	0.426	**-0.400**
5. mixed forests	-	0.054	0.338	**0.080**	0.292	**0.600**
6. woodlands 7. wooded grasslands	Savannas	0.074	0.420	0.234	0.551	-0.017
8. closed shrublands 9. open shrublands	Shrubs	0.081	0.329	0.327	0.622	-0.240
10. grasslands	grasses / cereal crops	0.132	0.44	0.158	0.364	**0.600**
11. croplands	broadleaf crops	0.095	0.477	0.149	0.321	**0.600**
-		a^{VIS}	b^{VIS}	a^{NIR}	b^{NIR}	-
Soil Parameters		0.0524	0.070	0.0285	0.0263	-

Table 6.2. Tunable parameters of each LULC class after the initial calibration. In bold are the parameters that reach the upper or lower boundaries.

classes decrease the ρ_{stem}^{VIS} near the low bound (0.08). Shrublands increased by about 50% of the initial ρ_{stem}^{VIS}, while grasslands decreased by half of the initial ρ_{stem}^{VIS}. NIR stem reflectance (ρ_{stem}^{NIR}) substantially increased in the broadleaf forest (~63%), savannas, and shrublands, while it decreased in the grasslands considerably (38.3%). The convergence of the departure of leaf angles from a random distribution (χ_L) appears to be unusual in some classes. Broadleaf forests were expected to range from the random to the horizontally oriented distribution; however, it decreased χ_L to the lower bound (-0.4: vertically oriented leaf). Grasslands were expected to range from the random to the vertically oriented distribution; however, it increased χ_L to the higher bound (0.6: horizontal leaf). The mixed forests and croplands also increased χ_L to the higher bound (0.6: horizontal leaf). This unrealistic χ_L causes a problem in predicting the daytime diurnal cycle of within-canopy sunlight penetration and consequently the sunlit- and shaded-components of photosynthesis and net radiation. For example, a canopy with completely horizontally-oriented leaves has a constant rate of sunlight penetration during daytime. This tends to overestimate the sunlight penetration (sunlit-component of canopy) for local morning/evening time, while underestimating the sunlight penetration around local noon.

Figure 6.6a shows the spatial map of differences (MODIS - ULM) in surface spectral albedo between the post-calibration ULM and the MODIS. The calibration process significantly reduced the biases of ULM albedo over the central U.S. in the VIS band, and also reduced the biases of NIR albedo in most of the domain. In the VIS band,

the underestimations of the ULM albedo (red spots) appear to be in the area near the Great Salt Lake in Utah and barren land in central Mexico.

Figure 6.6b shows the statistics and scatter plots of biases after calibration for each LULC class. In shrublands and grasslands, the mean values of the errors in VIS albedo range within the uncertainty level of the MODIS product [*Jin et al.*, 2003]. In addition, the spread (standard deviation) of errors in grasslands becomes about 50% smaller than those of the pre-calibration: 1.41 vs. 3.17 for black-sky albedo and 1.46 vs. 2.69 for white-sky albedo (Figure 6.5b). This means that the new adjustable soil albedo parameterization together with tuned vegetation optical parameters improved the spatial representation of surface albedo in the ULM. On the other hand, errors in bare and urban-buildup classes have not been improved in terms of the RMSE, because the total grid number of these classes in the domain is too small to account for in the objective function. In addition, in urban regions, LAI is arbitrarily fixed to zero in the ULM. This might be unrealistic in the urban and suburban regions, where urban buildup and sidewalk trees coexist. Therefore, a manual calibration is currently needed for the urban pixels.

In the NIR band, biases (absolute values of mean error) in black-sky and white-sky albedo are decreased after the calibration for all LULC classes. However, black-sky NIR albedo in ULM appears to be slightly underestimated, because the biases of all the classes (excepting urban) of the albedo are positive, while the white NIR albedo in the ULM appears to be less biased. This means that the difference between black and white albedo in the ULM is still slightly larger than that in the MODIS albedo even after the calibration. This bias cannot be fixed by modulating the tunable parameters; it appears to be a functional bias, which will be investigated in the following section.

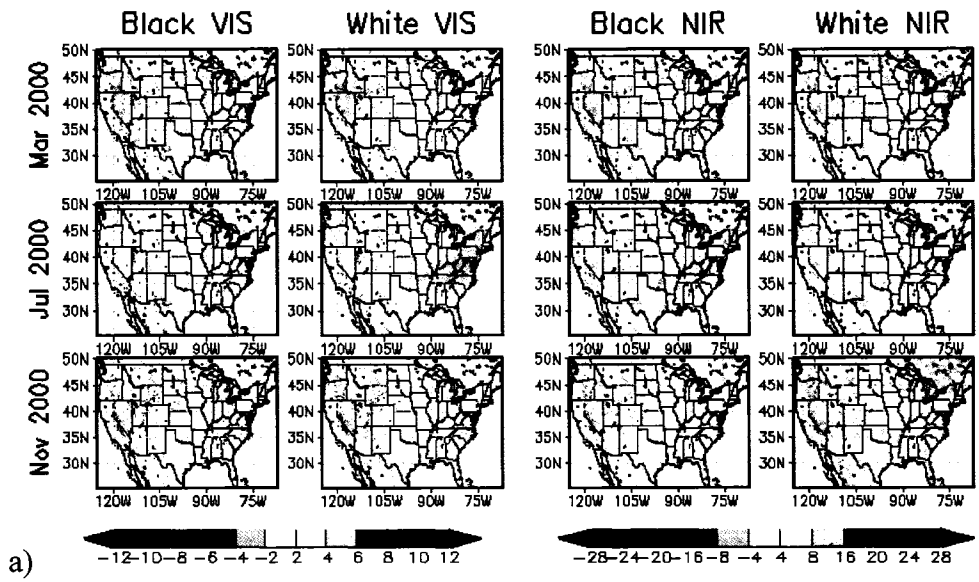

a)

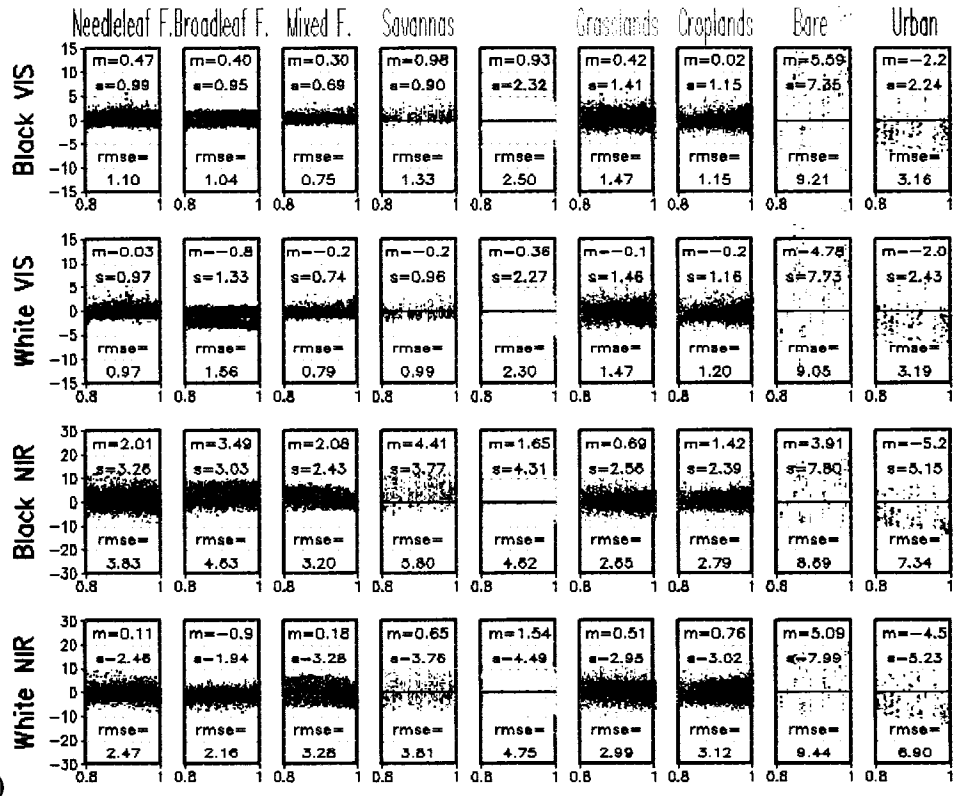

b)

Figure 6.6. a) Same as Figure 6.5a, but after the initial calibration. b) Same as Figure 6.5b, but after the initial calibration.

6.5.3 Second Calibration Experiment

In order to investigate the functional bias of the TRCT function, the diffuse- and direct-radiation upscattering fraction ($\omega\beta$ and $\omega\beta_0$ defined in eq. 6.4.3 and 6.4.4) for three different values of χ_L (-0.4, 0.0, and 0.6) are plotted as a function of cosine of solar zenith angle in Figure 6.7a. The diffuse-radiation upscattering fractions are larger than the direct-radiation upscattering parameter for any solar zenith angle. This is not possible, because the diffuse radiation is an integration of all angles of the direct radiation; i.e., diffuse-radiation upscattering fraction should be within the range of the direct-radiation upscattering fraction. This is due to the fact that the definitions of the upscattering

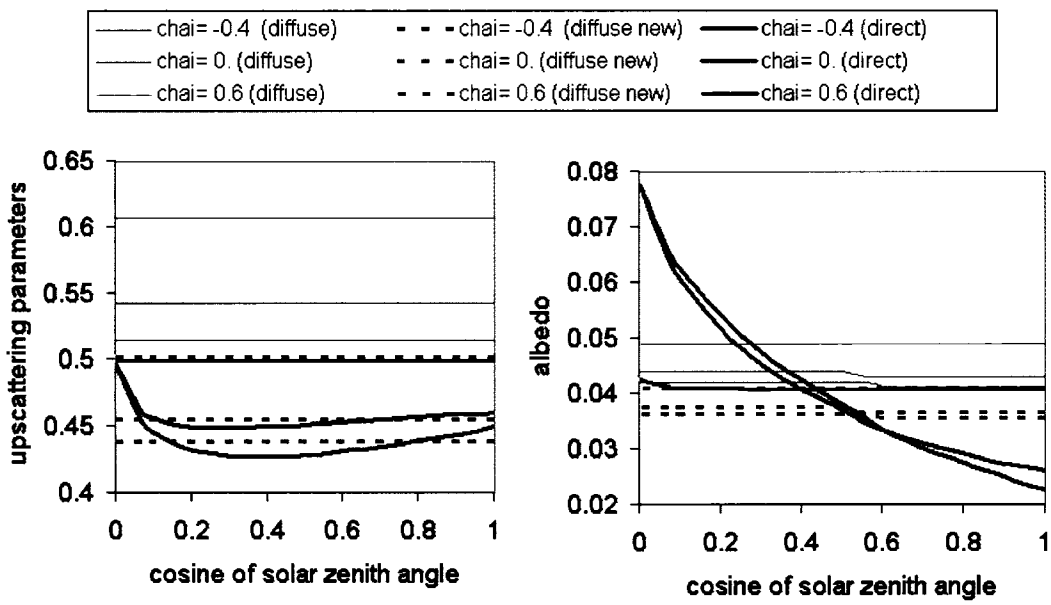

a) b)

Figure 6.7. Upscattering fractions and albedo computed from TCRT (LAI = 3, ρ = 0.1, τ = 0.05, α_{soi} = 0.1)

a) Up-scattering fraction for diffuse-radiation (solid thin), direct radiation (solid thick), and modified version of diffuse radiation (dash).
b) Surface albedo for diffuse-radiation (solid thin), direct radiation (solid thick), and modified version of diffuse radiation (dash).

fractions in equation 4.3 and 4.4 are taken from different sources. $\omega\beta$ is acquired from the analysis of *Norman and Jarvis* [1975], while $\omega\beta_o$ is derived from the analytic solution with the assumption of single scattering and semi-infinite canopy [*Dickinson,* 1983].

Thus, the definition of upscattering fraction for diffuse radiation is modified so as to be consistent with that for direct radiation. Numerically, the direct-radiation upscattering fractions are averaged over nine sky angles similar to the canopy model in *Goudriaan* [1977],

$$\omega\beta = \frac{\sum_{i=1}^{9} \frac{1+\bar{\mu}K(\mu_i)}{\bar{\mu}K(\mu_i)} a(\mu_i)}{9}, \quad where \quad \mu_i = \cos\left[(i-1)\cdot 10 + 5\right] \qquad (6.5.1)$$

Figure 6.7a shows that a new diffuse-radiation upscattering function together with the original value. It is now within the ranges of the direct-radiation upscattering function, and it is physically reasonable. the albedo for diffuse radiation is computed by using the original formula (eq. 6.4.3) and the new formula (eq. 6.5.1) (LAI = 3, ρ = 0.1, τ = 0.05, α_{soi} = 0.1). The new function reduces the white albedo from the original formulae (Figure 6.7b). For a cosine of solar zenith angle close to the unity, the differences between black and white sky albedos become smaller with the new functions. This new function does not slow down the computational time of the TCRT model for a long-term integration, because the modified diffuse-radiation upscattering fraction (eq. 6.5.1) needs to be computed once a day, and it is kept in the computer memory.

A second calibration was implemented from the lessons learned from the first calibration: i) fixed the functional error in diffuse-radiation upscattering fraction, and ii) manually fixed the surface albedo for the urban class (0.06 (VIS) and 0.20 (NIR) based on the mean albedo of the urban pixels from the MODIS, and iii) χ_L is fixed as the initial value (not calibrated) to prevent the unrealistic diurnal cycle of within-canopy sunlight penetration. The calibration process is completed with these conditions, and it takes approximately the same number of time steps to reach the final Ψ of 1.24×10^6, which is comparable to that of the initial calibration (1.12×10^6), and 20.2% of Ψ in the experiment before the calibration ($\Psi = 6.12\times10^6$).

Table 6.3 shows the final set of the tuned parameters. VIS leaf and stem reflectance (ρ_{leaf}^{VIS} and ρ_{stem}^{VIS}) do not diverge from the initial value in comparison with the first calibration results in Table 6.2. NIR leaf and stem reflectance (ρ_{leaf}^{NIR} and ρ_{stem}^{NIR}) are changed notably from the initial set of values in Table 6.1. The highest NIR leaf

UMD	BU LAI	ρ_{leaf}^{VIS}	ρ_{leaf}^{NIR}	ρ_{stem}^{VIS}	ρ_{stem}^{NIR}	χ_L
1. evergreen needleleaf forests 3. deciduous needleleaf forests	needleleaf forests	0.061	0.418	0.135	0.357	0.00
2. evergreen broadleaf forests 4. deciduous broadleaf forests	broadleaf forests	0.113	0.517	0.150	0.457	0.250
5. mixed forests	-	0.070	0.388	0.131	0.386	0.250
6. woodlands 7. wooded grasslands	Savannas	0.088	0.494	0.217	0.588	0.00
8. closed shrublands 9. open shrublands	Shrubs	0.107	0.355	0.182	0.667	0.00
10. grasslands	grasses / cereal crops	0.124	0.539	0.193	0.380	-0.30
11. croplands	broadleaf crops	0.116	0.566	0.156	0.320	0.00
-		a^{VIS}	b^{VIS}	a^{NIR}	b^{NIR}	-
Soil Parameters		0.0543	0.0529	0.0279	0.0236	-

Table 6.3. Tunable parameters of each LULC class after the second calibration. In gray are the parameters that are invariant during the calibration.

reflectance is cropland (0.566), and the lowest is shrubland (0.355). The highest NIR stem reflectance is shrubland (0.667), while the lowest is cropland (0.320). It seams that values between the stem and leaf reflectance in shrubland and cropland compensated each other during the calibration process.

Figure 6.8a shows the spatial map of differences (MODIS - ULM) in surface spectral albedo between the second calibrated ULM and MODIS. Similar to the map after the initial calibration, the additional calibration process and manual correction of the function in the TCRT model considerably reduced the biases of ULM albedo. Again, in the VIS band, the underestimation of the ULM albedo (red spots) appears in the same places as before.

Figure 6.8b shows the statistics and scatter plots of biases for each LULC class. VIS black- and white-sky albedo in the three forest classes virtually have no biases, and two standard deviations are mostly within the uncertainty ranges (< 2.) of the operational MODIS albedo product [*Jin et al.,* 2003]. Characteristics of biases of VIS black- and white albedo for the other LULC classes are quite similar to those in the first calibration experiments. Although standard deviations are slightly high, the mean biases of the NIR black- and white-sky albedo are also improved (< 2.) from the pre-calibration and the first calibration experiments, except for bare ground. By manually fixing the albedo, the biases and standard deviation of all types of albedo, including the urban class, are improved in comparison with the pre-calibration and first calibration experiments.

Finally, Figure 6.9 shows the fitted soil albedo values as a function of *LND* with a set of tuned parameters (a^{VIS}=0.0543, b^{VIS}=0.0529, a^{NIR}= 0.0279, b^{NIR}=0.0236). Both VIS and NIR albedos gradually decrease as *LND* decreases. The calibrated soil VIS

albedo ranges from 0.18 to 0.09, whereas the Reynolds' soil color map ranges from 0.24 to 0.10. The calibrated soil NIR albedo ranges from 0.36 to 0.19, whereas the Reynolds' soil color map ranges from 0.48 to 0.20. For both VIS and NIR band, the lowest values of albedo are very similar between the calibrated soil albedo and Reynolds' map. Soil VIS albedo is 50% of the NIR albedo, which is exactly the same ratio that Reynolds' soil albedo map specifies. Overall, the tunable albedo ranges are within realistic values compared to Reynolds' map, while minimizing the difference between the simulated and observed albedo.

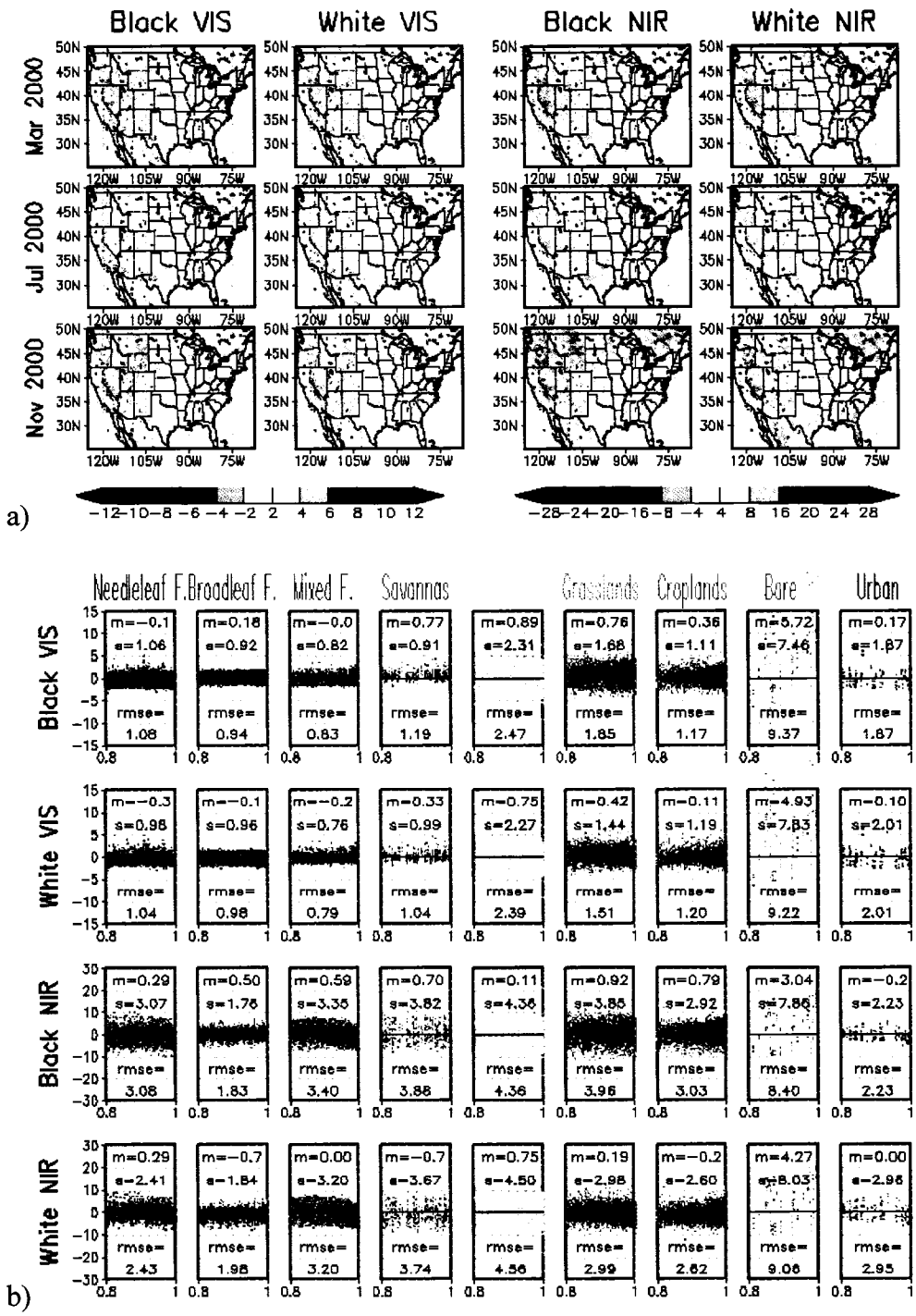

Figure 6.8. a) Same as Figure 6.5a, but after the manual correction and second calibration. B) Same as Figure 6.5b, but the manual correction and second calibration.

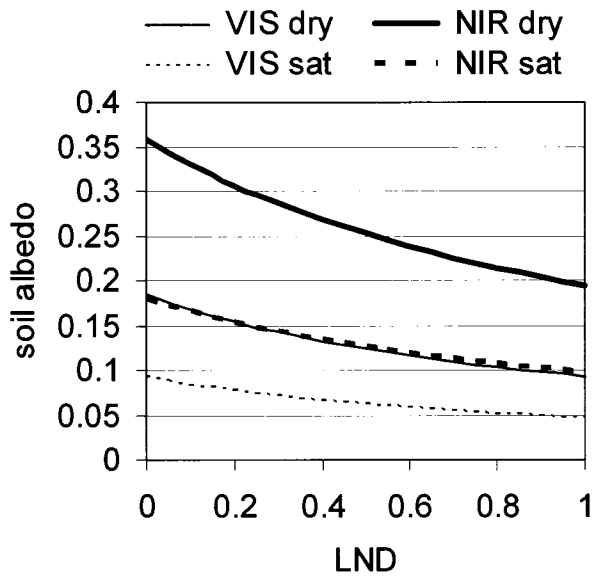

Figure 6.9. Dry and saturated soil albedo as a function of *LND* (see definition in section 4.2) with a set of tuned parameters (a^{VIS}=0.0543, b^{VIS}=0.0529, a^{NIR} = 0.0279, b^{NIR}=0.0236)

6.5.4. Validation of Calibrated Albedo in Different Years and Seasons

This section validates the tuned surface albedo in the ULM for March, July, and November of 2001 to 2004, using pre- and post-calibrated optical parameters (Table 6.1 and Table 6.3). The pre- and post-calibrated albedos are compared in terms of the objective function (Ψ) - the sum of squared errors between model and observations.

Figure 6.10a shows the objective functions for black- and white-sky VIS and NIR albedo. Pre-calibration has far greater values of total objective function in all years than those of the post-calibrated experiments. The largest component of the errors is attributed to the white-sky NIR albedo in the pre-calibration experiments [cf. *Wang et al.*, 2004]. It is clear that the manual correction of the functional error and the calibration process significantly reduced the objective function not only in the calibrated year (2000) but also

in the non-calibrated years (2001~2004). For all years, Ψ of the post-calibration experiments are approximately 20% of that of pre-calibration experiment.

In addition, ULM was applied in the three seasons between the calibrated months in 2000: April-May-June (AMJ), August-September-October (ASO), and December-January-February (DJF), with pre- and post-calibration parameters (Table 6.1 and Table 6.3). Figure 6.10b exhibits the corresponding objective functions for pre- and post-calibration experiments. Pre-calibration experiments show again high values of the objective function in all seasons, with highest values in DJF, an indication of the errors in the stem and soil optical parameters. The post-calibration experiments show small values of the objective functions, particularly in warm seasons, AMJ and ASO. Similar to the pre-calibration experiments, the objective function in DJF appears to be larger than those in AMJ and ASO. This study used the spatially continuous snow-free albedo, which interpolate the missing or snow-covered pixel [*Moody et al.,* 2005]. In DJF, the snow cover is often extensive in the northern portion of U.S., and the effect on surface albedo was unnaturally removed during the calibration process. However, the soil moisture is usually saturated beneath the snow in ULM, and it increases the discrepancy from the interpolated MODIS albedo in DJF (not shown here).

While the calibrations are conducted in three separate months in 2000, the set of calibrated parameters also improved the representation of albedo in ULM for the non-calibrated period at the same level. This suggests that i) interannual variability of albedo is lower than seasonal variability [*Wang et al.,* 2004] and ii) multi-season calibration successfully generalize the set of tunable coefficients, while avoiding the over-fitting of particular components of the optical parameters.

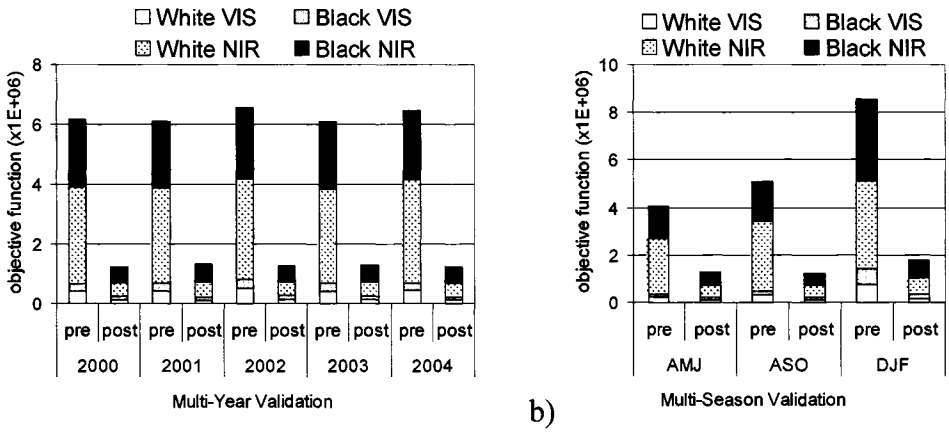

Figure 6.10.

a) Objective Function (Ψ) of spectral surface albedo for pre- and post-calibration simulations for March, July, November in 2000 (calibrated year), and 2001 ~ 2004 (validation years).

b) Objective Function (Ψ) of spectral surface albedo for pre- and post-calibration simulations for AMJ (April-May-June), ASO (August-September-October), and DJF (December-January-February) in 2000. January and February correspond to 2001.

6.5.5 Local- and Large-scale Calibration

This section compares the post-calibrated albedo with those calibrated in the limited-time period as well as for limited grid points. The different methods used for calibrating albedos are compared in terms of the objective function (Ψ). Four additional calibrations were conducted. The first experiment is to calibrate a set of tunable parameters only in July, which represent the limited-time calibration (denoted as *July*). The second, third, and forth experiments use the model grid of only every 2, 4, and 8 degrees in latitude and longitude direction (denoted as *2deg*, *4deg*, and *8deg*, respectively). For example, because this study uses a 0.25° grid, *2deg* experiment uses

approximately $(.25\ /2)^2 = 1/64$ of the total grid points that are in the *post* experiment (=175,800). Thus, the *8deg* experiment uses the least grid points $[(.25°\ /8°)^2 = 1/1024]$.

These experiments derived four different sets of tunable parameters for the given number of grid points and periods. These derived sets of tunable parameters are tested for the entire domain (every grid point for a total of 175,800 grid points) in a similar manner as in section 5.4. Figure 6.11 shows the objective functions of the limited-time and limited-site calibrations. The *July* experiment has the higher Ψ (1.93×10^6) than that of the *post* experiment (1.24×10^6) in a March-June-November period of 2000. The *July* experiment shows a nearly identical Ψ in the AMJ period, a slightly higher Ψ in the ASO period, and is twice higher in the DJF period in comparison with that of the *post* experiment. This clearly shows that the limited-time calibration tends to localize a set of tunable parameters for the limited calibration period. The *2deg*, *4deg*, and *8deg* experiments show the trend of Ψ, which are gradually increased from the *2deg* to *8deg* experiments. This suggests that a fewer number of the calibrated grid points tends to localize the tunable parameters for the calibrated points.

Although the localizing tendency is shown, the limited-site calibration even reduces the Ψ significantly from the *post* experiment (Figure 6.10) and it reduces the wall-clock time of calibration time linearly with respect to the grid number. Thus, there could be an optimal grid-volume reduction method for the continental calibration. For example, the EOF technique can be used to derive the grids and periods with the most representative combination of LAI, SAI and top-soil moisture for the large-scale domain. Together with a parallel simulation environment, this could considerably reduce the wall-

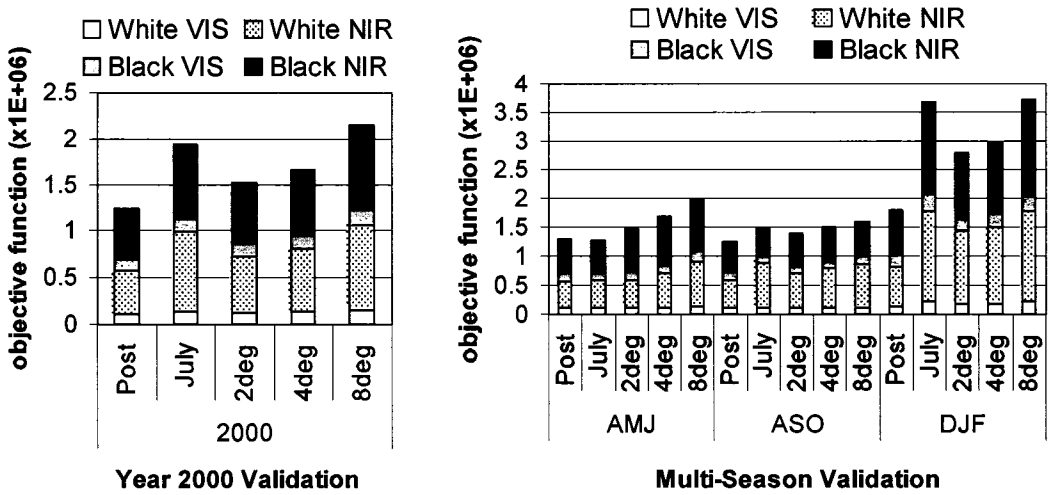

Figure 6.11. The objective functions of limited-site and limited-time calibrations are compared with continental-scale calibration.

clock time of the continental-scale calibration process, while the detailed method can be examined for future study.

6.5.6. Sensitivity of Albedo Calibration to the Surface Heat Flux and Temperature

The sensitivity of the simulated surface energy budget to the albedo calibration was addressed using pre- and post-calibrated surface albedo for the June-July-August period in 2000. The initial conditions and meteorological forcings are set identically between the experiments. Figure 6.12 shows the difference (post-calibration - pre-calibration) at 18:00Z (around local-noon time) of net shortwave radiation, available energy (sensible heat flux + latent heat flux), and radiative temperature averaged over the simulated period. Overall, the simulated surface energy budget has been changed significantly over the less-vegetated regions after the calibration. The largest difference exists over southwest U.S. and Mexico, particularly over Great Basin, Chihuahuan Desert

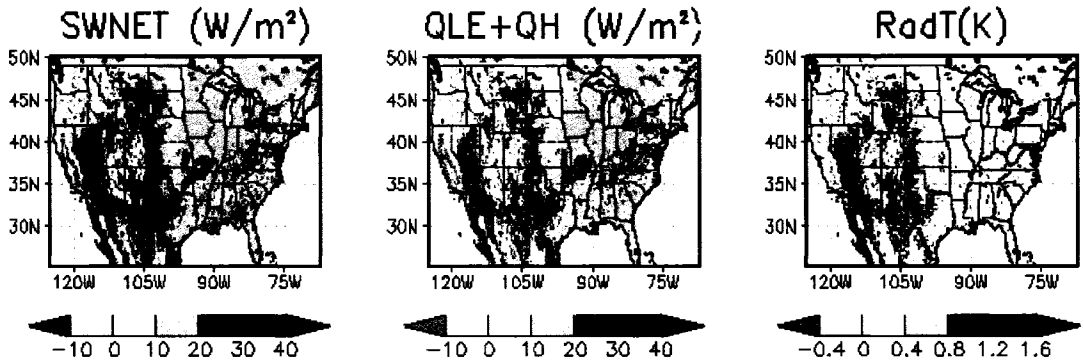

Figure 12. Sensitivity to albedo calibration (POST-EXP – PRE-EXP) of net shortwave radiation (SWNET), available energy (QLE+QH), and radiative temperature (RadT) averaged over June-July-August 2000.

and Baja California. In those regions, net shortwave radiation and available energy increased by more than 40 Wm^{-2} and radiative temperature by more than 1.6 K in the post-calibration experiments. On the other hand, net shortwave radiation, available energy, and radiative temperature were slightly decreased over the Appalachian Mountains, where the dominant LULC class is the broadleaf forest. The post-calibration simulation tends to improve the performance of the model LST in comparison with MODIS LST (also discussed in Part II [*Matsui et al.* 2006]). However, this improvement simultaneously depends on other parameters related to the function of surface heat flux in the ULM. Thus, the improvement of simulated albedo might not improve overall performance for different LSMs.

6.6. Summaries and Discussions

The continental-scale multi-observation calibration system is established for Colorado State University (CSU) unified land model (ULM) in the Land Information

System (LIS) coupled with the Parameter Estimation (PEST) model. The simulation domain was comprised of 16,648 land grid points and a total 61,883 subgrid tiles over the conterminous U.S. (CONUS), which enabled a more robust calibration process than a limited-site calibration does. This chapter (part I) aimed to calibrate the vegetation and soil optical properties by comparing model- and satellite-derived surface spectral albedos. The four different types of MODIS surface albedo, including black- and white-sky albedo for the visible (VIS) and near-infrared (NIR) bands were compared with the corresponding direct- and diffuse-radiation albedos for the VIS and NIR bands from the two-stream canopy radiative transfer (TCRT) and soil albedo model. Leaf and stem reflectances (ρ_{leaf}^{VIS}, ρ_{leaf}^{NIR}, ρ_{stem}^{VIS}, and ρ_{stem}^{NIR}), the departure of leaf angles from a random distribution (χ_L) for seven bundled LULC classes, in addition to the four parameters (a^{VIS}, b^{VIS}, a^{NIR}, and b^{NIR}) for new soil albedo parameterization were selected and calibrated via the Gauss-Marquardt-Levenberg (GML) algorithm. A new tunable soil albedo parameterization was developed as a function of log-normalized difference L_{max} (*LND*). Three months from 2000, March, July and November, were selected for the calibration, because these characterize the early development, maturity and senescence, respectively, of the vegetation over U.S.

Although the ULM initialization used a consistent set of the MODIS LAI and LULC, it was not guaranteed that the ULM would predict surface spectral albedos consistent with those observed from the MODIS radiances. This was due to the different sophistication and assumptions in the canopy radiative transfer algorithms and soil albedo configurations. In addition, the discrepancy of model albedo has been reported in previous studies [*Oleson et al.,* 2003; *Zhou et al.,* 2003; *Tian et al.,* 2004; *Wang et al.,*

2004]. ULM also showed that the experiment with the original set of parameters slightly overestimated the VIS black- and white-sky surface albedo in shrublands and grasslands over the central U.S., and strongly overestimated the NIR black- and white-sky albedo in the most of the LULC classes. The strong biases of VIS surface albedo in shrublands and grasslands are probably due to fact that the analytic solution of the original TCRT was derived under an assumption of semi-infinite canopy [*Dickinson,* 1983], which is an inappropriate assumption for less-vegetated LULC classes.

The GML calibration process takes approximately 5 iterations to achieve convergence. The entire calibration process reduced the Ψ (a weighted sum of squared deviation between model and observation) by 18.3% of Ψ before the calibration (Ψ = 6.12×10^{6}). After the initial calibration, ULM with a set of tuned optical parameters significantly reduced the biases in the VIS albedo for shrublands and grasslands over the central U.S. and the biases appeared in NIR albedo for most of the LULC classes. The lowered standard deviations of errors suggest that the new adjustable soil albedo parameterization together with the tuned vegetation optical parameters improved the spatial representation of surface albedo in ULM in comparison with MODIS albedo. However, there are several issues that cannot be fixed by tuning the calibration; i) errors in bare ground and urban-buildup classes were not improved effectively; ii) the difference between simulated black- and white-sky albedo is slightly larger than those of the MODIS albedo; and iii) leaf angle functions (χ_L) of some LULC classes were converged to high/low limits.

Multi-observation (black- and white-sky albedo) calibration revealed that the upscattering fraction for diffuse radiation was too high and out of the range of the direct-

radiation upscattering fraction. Thus, the direct-radiation upscattering fractions of 9-sky angles are integrated for the diffuse-radiation upscattering fraction, which solved the issue ii) raised after the initial calibration. A second calibration was implemented from the lessons learned from the first calibration: i) the functional error in diffuse-radiation upscattering fraction was fixed, ii) manually fixed the surface albedo for the urban class (0.06 for VIS and 0.20 for NIR based on the mean albedo of urban pixel from the MODIS), and iii) χ_L was retained as the initial value (not calibrated). This second calibration show an overall improvement of albedo from the pre- and initial calibration experiments, while retaining the set of more realistic values of parameters than those from after the initial calibration process.

Although the calibrations were conducted only in March, July and November in 2000, the set of calibrated parameters also improved the representation of albedo in ULM for non-calibrated periods at the same level. This demonstrates the robustness of the albedo calibration period designed in this study. On the other hand, another validation shows that the limited-time and limited-site calibration tends to localize sets of tunable parameters for a given calibrated periods and time. Some may inquire on the justification of tuned leaf/stem optical properties, which deviate from the literature-reviewed values [*Dorman and Sellers*, 1989; *Bonan et al.,* 2002]. This can be explained as follows. Usually optical properties are adjusted according to the simplification of a radiative transfer scheme. For example, atmospheric one-dimensional two-stream radiative transfer modifies the atmospheric optical properties through the delta-adjustment in order to account for the forward scattering peak [e.g., *Joseph* 1976]. Similarly, this calibration process can be judged as the adjustment of leaf/stem optical properties so as to account

for the several assumptions in the TCRT, including two-stream intensity, isotropic scattering, single-scattering assumption, plane-parallel canopy, semi-infinite canopy, and linear interpolation between the leaf and stem optical properties [*Dickinson,* 1983; *Sellers,* 1985]. The derived set of optical parameters can be applied to other models as the default values as long as they are using the same set of parameterizations and the MODIS products.

It is worthwhile to refer to the study described in *Tian et al.* [2004]. They reduced the biases of albedo in CLM2 with given vegetation optical properties by incorporating the new 500m MODIS Vegetation Continuous Fields (VCF) [*Hansen et al.,* 2002] and consistent MODIS BU LAI, and Plant Functional Types LULC maps. However, a note of caution about this approach needs to be mentioned here. BU LAI uses the specific LULC class (bundled UMD type LULC) to derive the 1km LAI map, while *Hansen et al.* uses their own algorithm to derive the fraction of forests and grasslands in the VCF. As *Myneni et al.* [2002] has shown LAI biases become large if the LULC category is misclassified between forests and grasslands. Therefore, the use of both BU LAI and VCF would be appropriate, only if the BU LAI algorithm consistently uses VCF for the derivation of LAI. The VCF and LANDSAT-level high-resolution LULC sets will be eventually required to correctly classify the LULC and to correctly derive the LAI and surface albedo.

The sensitivity of the simulated surface energy budget to albedo calibration was addressed using pre- and post-calibrated surface albedos for summer (June-July-August) 2000. After calibration, the simulated surface energy budget changed significantly over the less-vegetated regions. The largest difference occurred over southwest U.S. and

Mexico, particularly over Great Basin, Chihuahuan Desert and Baja California. In those regions, net shortwave radiation and available increased by more than 40 Wm^{-2} and radiative temperature by more than 1.6 K in the post-calibrated experiment. This suggests that these biases could have a prominent effect on the regional/global climate simulations.

Thus, in conclusion,

- Continental-scale calibration improved the model representation of surface albedo over the entire domain in comparison with the operational MODIS snow-free albedo, although the set of the tuned parameters might not be the global optima.
- Continental-scale calibration suggests the functional error in the model. There is the error in the formulation of diffuse-radiation upscattering fraction in the original TCRT model. The model must be corrected to reduce the overestimation of white-sky albedo. The suggested formula would be easy to incorporate into different models that use TCRT.
- The leaf angle distribution function cannot be calibrated probably because of the fundamental difference between the formulations used in the TCRT model the MODIS operational albedo products.
- The albedo in ULM was improved for not only the calibrated period but also non-calibrated years and seasons. The choice of calibration periods must be short for computational efficiency, but needs to have as large a variation in the calibrating parameters as possible for the representativeness of the tuning parameters. This enables an efficient, robust calibration process.
- Errors in the surface albedo directly control the surface energy and mass flux in the land surface model (LSM). Because all LSMs use a different set of parameterizations

and datasets, albedo calibration over the simulated domain must occur first.

References

Baldocchi, DD, and coauthors (2001), FLUXNET: A New Tool to Study the Temporal and Spatial Variability of Ecosystem-Scale Carbon Dioxide, Water Vapor and Energy Flux Densities, *Bull. Amer. Meteorol. Soc.*, **82**, 2415-2434.

Baginska, B., W. M.-H. and P. S. Cornish, (2003), Modelling nutrient transport in Currency Creek, NSW with AnnAGNPS and PEST, *Environmental Modelling & Software,* **18**, 801-808

Bonan, G. B., K. W. Oleson, M. Vertenstein, and S. Levis (2002), The land surface climatology of the Community Land Model coupled to the NCAR Community Climate Model. *J. Climate,* **15**, 3123–3149

Chen, D.-X., and M.B. Coughenour (1994), GEMTM: A general model for energy and mass transfer of land surfaces and its application at the FIFE sites. *Agric. For. Meteor.* **68**, 145-171.

Cosgrove, B. A., D. Lohmann, K. E. Mitchell, P. R. Houser, E. F. Wood, J. Schaake, A. Robock, C. Marshall, J. Sheffield, L. Luo, Q. Duan, R. T. Pinker, J. D. Tarpley, R. W. Higgins, and J. Meng (2003), Real-time and retrospective forcing in the North American Land Data Assimilation System (NLDAS) project, *J. Geophys. Res.*, **108**, 8842, doi:10.1029/2002JD003118.

Dickinson, R. E. (1983), Land surface processes and climate-surface albedos and energy balance. *Adv. Geophys.,* 25, Academic Press, 305–353.

Dickinson, R. E., P. J. Sellers, and D. S. Kimes (1987), Albedo of homogeneous semi-infinite canopies: comparison of two-stream analytic and numerical solutions. *J. Geophys. Res.,* **92**, 4282-4286

Dickinson, R. E., A. Henderson-Sellers, and P. J. Kennedy (1993), *Biosphere Atmosphere Transfer Scheme (BATS) Version le as Coupled to the NCAR Community Climate Model.* NCAR Technical Note, NCAR, 72 pp

Watermark Numerical Computing (2004), PEST Model-Independent Parameter Estimation User Manual: 5th Edition, http://www.sspa.com/pest/pestsoft.html

Dorman, J. L., and P. J. Sellers (1989), A global climatology of albedo, roughness length and stomatal resistance for atmospheric general circulation models as represented by the Simple Biosphere Model (SiB). *J. Appl. Meteor.,* **28,** 833–855.

Duan, Q., V. K. Gupta, and S. Sorooshian (1993), Shuffled complex evolution approach for effective and efficient global minimization. *J. Optimization Theory Appl.,* 76, 501–521.

Goudriaan, J. (1977), *Crop Micrometeorology: A Simulation Study*. Center for Agricultural Publication and Documents, Wageningen, 249 pp.

Gupta, H. V., L. A. Bastidas, S. Sorooshian, W. J. Shuttleworth, and Z. L. Yang (1999), Parameter estimation of a land surface scheme using multi-criteria methods. *J. Geophys. Res.*, **104**, 19491–19504.

Hansen, M. C., R. S. DeFries, J. R. G. Townshend, and R. Sohlberg (2000), Global land cover classification at 1km spatial resolution using a classification tree approach. *Int. J. Remote Sens.*, **21**, 1331–1364.

Henderson-Sellers, A., A. J. Pitman, P. Irannejad, and K. McGuffie (2002), Land surface simulations improve atmospheric modeling. *Eos, Trans. Amer. Geophys. Union*, 83, 145, 152.

Idso, S. B., R. D. Jackson, R. J. Reginato, B. A. Kimball, and F. S. Nakayama (1975), The dependence of bare soil albedo on soil water content. *J. Appl. Meteor,* **14**, 109–113.

Jensen, J. R. (2000), *Remote Sensing of the Environment: An Earth Resource Perspective*, Upper Saddle River, NJ: Prentice Hall, 544 pages.

Jin, Y., C. B. Schaaf, F. Gai, X. Li, A. Strahler, W. Lucht, and S. Liang (2003), Consistency of MODIS surface BRDF/Albedo retrievals: 2. Validation. *J. Geophys. Res.*, **108**, 4159, doi:1029/2002JD002804.

Joseph, J. H., W. J. Wiscombe, and J. A. Weinman (1976), The delta- Eddington approximation for radiative transfer. *J. Atmos. Sci.*, **33**, 2452–2459.

Justice, C. O., J. R. G. Townshend, E. F. Vermote, E. Masuoka, R. E. Wolfe, N. Saleous, D. P. Roy, and J. T. Morisette (2002), An overview of MODIS land data processing and product status. *Remote Sens. Environ.*, **83**, 3–15.

Knyazikhin, Y., J.V.Martonchik , R. B. Myneni, M. Verstraete, B. Pinty, and N. Gobron (1998), Synergistic algorithm for estimating vegetation canopy leaf area index and fraction of absorbed photosynthetically active radiation from MODIS and MISR data. *J. Geophys. Res.*, 103, 32257-32274.

Lee, T.J., R.A. Pielke, and P.W. Mielke, Jr. (1995), Modeling the clear-sky surface energy budget during FIFE87. *J. Geophys. Res.*, **100**, 25585-25593.

Liu, Y.B., O. Batelaan, F. D. Smedt, J. Poórová, L. Velcická, (2005), Automated calibration applied to a GIS-based flood simulatin model using PEST, in Van Alphen, van Beek & Taal (eds.), Floods, from Defense to Management, Taylor & Francis Group, London, 317-326.

Matsui, T., V. Lakshmi, and E. E. Small (2005), The Effects of Satellite-Derived Vegetation Cover Variability on Simulated Land–Atmosphere Interactions in the NAMS. *J. Climate.,* **18**, 21–40

Moody, E. G., M. D. King, S. Platnick, C. B. Schaaf, and F. Gao (2005), Spatially complete global spectral surface albedos: Value-added datasets derived from Terra MODIS land products. *IEEE Trans. Geosci. Remote Sens.,* 43, 144-158.

Morisette J.T., J. L. Privette, C. O. Justice (2002), A framework for the validation of MODIS land products, *Remote Sensing of Environment,* **83**, 77-96.

Myneni, R.B., and co-authors (2002), Global products of vegetation leaf area and fraction absorbed PAR from year one of MODIS data. *Remote Sens. Environ.,* **83**, 214-231.

Norman, J. M., and P. G. Jarvis (1975), Photosynthesis in Sitka spruce. Radiation penetration theory and a test case. *J. Appl. Ecol.,* **12**, 839–878.

Niyogi D., S. Raman, and K. Alapaty (1999), Uncertainty in specification of surface characteristics, Part 2- Hierarchy of interaction explicit statistical analysis, *Bound. Lay. Meteorol.*, **91**, 341-366.

Oleson, K. W., G. Bonan, M. Bosilovich, R. Dickinson, P. Dirmeyer, F. Hoffman, P. Houser, S. Levis, G.-Y. Niu, Peter Thornton, M. Vertenstein, S.-L. Yang, X. Zeng (2004), *Technical Description of the Community Land Model (CLM),* NCART Technical Note, NCAR/TN-461+STR.

Oleson, K. W., G. B. Bonan, C. Schaaf, F. Gao, Y. Jin, and A. Strahler (2003), Assessment of global climate model land surface albedo using MODIS data. *Geophys. Res. Lett.,* **30**, 1443, doi:10.1029/2002GL016749.

Pielke, R. A. Sr. (2001), Influence of the spatial distribution of vegetation and soils on the prediction of cumulus convective rainfall. *Rev. Geophys.,* **39**, 151–177

Pitman, A. J., and co-authors (1999), Key results and implications from Phase 1(c) of the Project for Intercomparison of Land-surface Parameterization Schemes. *Clim. Dynamics*, **15**, 673-684.

Pitman, A. J. (2003), The evolution of, and revolution in, land surface schemes designed for climate models. *Int. J. Climatol.,* **23**, 479–510.

Peters-Lidard, C. D., S. Kumar, Y. Tian, J. L. Eastman, and P. Houser (2004), Global Urban-Scale Land-Atmosphere Modeling with the Land Information System, Symposium on Planning, Nowcasting, and Forecasting in the Urban Zone, 84th AMS Annual Meeting 11-15 January 2004 Seattle, WA, U.S.A.

Reichstein, M. and co-authors (2003), Modeling temporal and large-scale spatial variability of soil respiration from soil water availability, temperature and vegetation productivity indices, *Global Biogeochemical Cycles,* **17**, 1104, doi:10.1029/2003GB002035.

Reynolds, C.A., T. J. Jackson, and W.J. Rawls (1999), Estimating Available Water Content by Linking the FAO Soil Map of the World with Global Soil Profile Databases and Pedo-transfer Functions. Proceedings of the AGU 1999 Spring Conference, Boston, MA. May31-June 4, 1999.

Schaaf, C. B. and co-authors (2002), First Operational BRDF, Albedo and Nadir Reflectance Products from MODIS. *Remote Sens. Environ.,* **83**, 135-148.

Sellers, P.J. (1985), Canopy reflectance, photosynthesis and transpiration, *J. of Remote. Sens.,* **6**, 1335-1372.

Tian, Y., R. E. Dickinson, L. Zhou, R. B. Myneni, M. Friedl, C. B. Schaaf, M. Carroll, and F. Gao (2004), Land boundary conditions from MODIS data and consequences for the albedo of a climate model, *Geophys. Res. Lett.,* **31**, doi:10.1029/2003GL019104.

Liang X.-Z., M. Xu, W. Gao, K. Kunkel, J. Slusser, Y. Dai, Q. Min, P. R. Houser, M. Rodell, C. B. Schaaf, F. Gao (2005), Development of land surface albedo parameterization based on Moderate Resolution Imaging Spectroradiometer (MODIS) data, *J. Geophys. Res.*, **110**, D11107, doi:10.1029/2004JD005579.

Vrugt, J. A, H. V Gupta, L. A Bastidas, W Bouten, and S Sorooshian (2003), Effective and efficient algorithm for multiobjective optimization of hydrologic models. *Wat. Resour. Res.*, **39**, 1214, doi:10.1029/2002WR001746.

Walko, R.L., L.E. Band, J. Baron, T.G.F. Kittel, R. Lammers, T.J. Lee, D.S. Ojima, R.A. Pielke, C. Taylor, C. Tague, C.J. Tremback, and P.L. Vidale (2000), Coupled atmosphere-biophysics-hydrology models for environmental modeling. . *Appl. Meteor.*, **39**, 931-944.

Wan, Z., Y. Zhang, Q. Zhang, and Z.-L. Li (2002), Validation of the land-surface temperature products retrieved from Terra Moderate Resolution Imaging Spectroradiometer data, *Remote Sens. Environ.*, **83**, 163-180.

Wang, Z., X. Zeng, M. Barlage, R.E.Dickinson, F. Gao, and C.B.Schaaf (2004), Using MODIS BRDF and albedo data to evaluate global model land surface albedo, *J. Hydrometeo.*, 5, 3-14.

Wang, Y.-P., R. Leuning, H. A. Cleugh, and P. A. Coppin, (2001), Parameter estimation in surface exchange models using nonlinear inversion: how many parameter can we estimate and which measurements are most useful?, *Global Change Biology*, **7**, 495-510.

Wood, E.F., and co-authors (1998), The project for Intercomparison of land-surface parameterization schemes (PILPS) Phase 2C Red-Arkansas River basin experiment: 1. Experiment description and summary Intercomparison, *Glob. Planet. Change*, **19**, 115-135.

Xiong, X., K. Chiang, J. Esposito, B. Guenther, and W. Barnes (2003), MODIS on-orbit calibration and characterization, *Metrologia* 40, S89-S92, PII: S0026-1394(03)56883-9.

Sellers, P. J., D. A. Randall, G. J. Collatz, J. A. Berry, C. B. Field, D. A. Dazlich, C. Zhang, G. D. Collelo, and L. Bounoua (1996), A revised land surface parameterization (SiB2) for atmospheric GCMs. Part I: Model formulation. *J. Clim.*, **9**, 676–705.

Xue, Y., P. J. Sellers, J. L. Kinter, and J. Shukla (1991), A Simplified Biosphere model for global climate studies. *J. Clim.*, **4**, 345–364.

Yang, W., and coauthors (2004), Validation of Collections 3 and 4 Terra MODIS Leaf Area Index and Fraction Vegetation Absorbed Photosynthetically Active Radiation Products. *IEEE Trans. Geosci. Remote Sens.* (submitted).

Zhou, L., and coauthors (2003), Comparison of seasonal and spatial variations of albedos from Moderate-Resolution Imaging Spectroradiometer (MODIS) and Common Land Model. *J. Geophys. Res.*, **108**, 4488, doi:10.1029/2002JD003326.

Chapter 7

MECHANISTIC RESPONSE OF TERRESTRIAL PLANT PRODUCTIVITY AND SURFACE ENERGY BUDGET TO ROUTINE AEROSOL LOADING OVER THE EASTERN U.S.

7.1. Introduction

Atmospheric aerosols are proposed to modify the atmospheric radiation by i) directly scattering and absorbing the solar radiation (denoted as *aerosol direct effect* [e.g., *Harshvardhan* 1993]) and by ii) modifying cloud properties via serving as cloud condensation nuclei (denoted as *aerosol indirect effect* [e.g., *Hobbs* 1993]). These aerosol effects can enhance multiple scattering of downwelling shortwave radiation that generally reduces net-absorbed shortwave radiation on the earth by increasing the planetary albedo, while increasing the ratio of diffuse-to-direct radiation.

The probability of multiple scattering processes depends on the optical thickness and properties in the atmosphere. Boundary- and mid-layer clouds tend to have optical depths much greater than unity that often cause an overcast sky, which has a nearly 100% of fraction of diffuse radiation and significantly reduced amounts of total global irradiance [*Hahn et al.* 2001]. On the other hand, atmospheric aerosols and cirrus clouds usually have optical depths less than unity, and most of them have larger forward than

backward scattering, with the exception of highly absorbing black carbon aerosols [*Liou* 2002]. This indicates that the aerosols and thin clouds can increase the fraction of diffuse solar radiation without significantly reducing the surface global irradiance.

Diffuse solar radiation is more advantageous for plant productivity than the direct radiation [e.g., *Goudriaan* 1977; *Gu et al.* 2002; *Low et al.* 2002; *Rocha et al.* 2004]. This is because diffuse solar radiation is absorbed on the plant canopy more homogeneously than direct radiation is, and is efficiently utilized in the photosynthesis process without exceeding the plant photosynthesis capacity. On the other hand, direct solar radiation is absorbed by the sunlit canopy and usually exceeds the plant photosynthesis capacity around noon [*Goudriaan* 1977; *Gu et al.* 2002].

Recently, the effects of aerosols on photosynthesis have been addressed [*Roderick et al.* 2001; *Cohan et al.* 2002; *Gu et al.* 2003; *Niyogi et al.* 2004; *Chang* 2004; *Misson et al.* 2005; *Kanniah et al.* 2006]. Following the massive eruption of Mt. Pinatubo in 1991, abnormal carbon sinks were observed on the global scale in the following year. *Roderick et al.* [2001] and *Gu et al.* [2003] proposed that the globally distributed sulphate aerosols in the upper troposphere enhanced solar radiation scattering which increased the terrestrial carbon sink by increasing the plant productivity and they show theoretical and observational evidence through their analysis of ground-based observation data. *Niyogi et al.* [2004] and *Chang* [2004] provided the first observational evidence of links between variability of routine aerosol optical depths (AODs), diffuse solar radiation, and terrestrial carbon fluxes for different landscapes over eastern U.S., and the statistical results indicated that routine aerosols tend to increase the daytime carbon sink at forests and croplands sites under clear-sky (no-cloud) conditions. *Misson et al.* [2005] also

reported that the aerosol-driven diffuse radiation contributed to the abnormal increase in the late-afternoon carbon sink at the Blodgett Forest (young ponderosa pine plantation) site. This is denoted as the aerosol diffuse-radiation effect (ADE).

Several studies have shown a negative impact of aerosols on plant productivity. While productivity has been increased in croplands and forest sites, *Niyogi et al.* [2004] and *Chang* [2004] showed that the carbon sink at C4 and C3 grass sites is not enhanced for high AODs. *Kanniah et al.* [2006] showed that regional smoke loading tends to depress the carbon sink at a savanna site with C4 grass understory in northern Australia. These two studies agree that high aerosol loadings are not advantageous for landscapes dominated by grasslands. *Chameides et al.* [1999] reported that the regional aerosols over China decrease by up to 30% the net surface solar radiation, with similar decreases in crop yields. *Krakauer and Randerson* [2003] investigated tree rings in North America, Europe and Northern Eurasia, and found that plant productivity in the boreal regions was decreased after the eruption of Mt Pinatubo. These previous studies have indicated that ADE varies depending on canopy structure and environmental conditions.

The previous works also confirmed that ADE plays an important role for plant photosynthesis and terrestrial carbon sink. At present, the ADE has been tested by statistical analysis at different sites with surface eddy covariance observations [*Gu et al.* 2002 & 2003; *Niyogi et al.* 2004; *Chang* 2004; *Misson et al.* 2005; *Kanniah et al.* 2006] and by local-scale simulation [*Cohan et al.* 2002]. The next step is to develop a reliable canopy parameterization in a land-surface model (LSM) in order to investigate a spatio-temporal distribution of ADE on the large scale, rather than using a point-observation approach. Therefore, this study aims i) to incorporate the ADE in a land surface model by

developing and calibrating a sun-shade canopy model for different landscapes with extensive datasets of satellite and eddy covariance measurements on the regional scale, and ii) to examine sensitivity of terrestrial plant productivity and surface energy fluxes to variability of aerosol loading, using a well-calibrated sun-shade canopy model.

The first part of this study (section 2 and 3) addresses parameterizations and tuning parameters in a developed sun-shade canopy model (section 2) and the continental-scale multi-observations model calibration process (section 3), which corresponds to a follow-up of *Matsui et al.* [2006]. In order to examine the ADE in the land surface model, the model's canopy must separately treat sunlit and shaded components, and the surface downwelling solar radiation must be separated for diffuse and direct components [*Gu et al.* 2002]. A sun-shade canopy model, however, contains more parameters than those in one-big leaf models [*Dai et al.* 2004]. At present, sun-shade canopy models, and most of the land-surface models (LSM) in general, have been tested at limited sites [*De Pury and Farquhar* 1997, *Wang and Leuning* 1998, *Dai et al.* 2004], and their potential performance remains uncertain in different landscapes and over larger scales. In this study, both accuracy and completeness of ground-based observations as well as extensive spatial coverage of satellite observations are simultaneously utilized in order to improve the surface carbon sink, turbulent heat flux, and land-surface temperature (LST) in the sun-shade canopy model on the regional scale.

The second part of this study examines the mechanical response of plant productivity and surface carbon/heat fluxes to the routine aerosol loading over the eastern U.S., using a well-calibrated sun-shade canopy model and satellite-model assimilated daily AOD map via off-line simulation. Although off-line simulations cannot investigate

dynamical land-atmosphere interactions [*Pielke* 2001], they can i) enhance the understanding of the canopy-level interactions of coupled carbon-energy fluxes and spatial distribution due to ADE without nonlinear feedback of the regional-scale atmosphere and resultant cloud-precipitation processes, and ii) remove the unavoidable misrepresentations of cloud-precipitation processes that typically occur in atmospheric models [*Tao et al.* 2002].

7.2. Basic Structure of CSU ULM within LIS

This study uses the Colorado State University (CSU) Unified Land Model (ULM) within the NASA GSFC Land Information System (LIS) [*Kumar et al.* 2006; *Matsui et al.* 2006]. CSU ULM includes a ten-layer soil and 1 to 13 subgrid tiles. The numerical schemes and codes in CSU ULM are based on the Community Land Model (CLM) [*Oleson et al.* 2004], LEAF2 [*Walko et al.* 2000] and GEMTM [*Chen and Coughenour* 1994]. There are also many miscellaneous modifications in parameterizations from these schemes. CSU ULM will incorporate the subgrid-snow model (SSNOD) in the near future [*Liston* 2004].

A subgrid land-use land-cover (LULC) map was compiled from the MODIS University of Maryland (UMD)-type 1km LULC data [*Hansen et al.* 2000]. A subgrid LAI and stem/dead leaf area index (SAI) are initialized and updated from monthly composites of the 1km MODIS LAI from Boston University [*Myneni et al.*, 2002] (see the detailed set of the initial conditions in *Matsui et al.* [2006]). In this study, ULM is run at 0.25° grid spacing and is driven by the North American Land Data Assimilation System (NLDAS) meteorological forcing with a 15-minute model time step [*Cosgrove et*

al. 2003]. Diffuse radiation is estimated from the broadband solar radiation as a function of global irradiance and extraterrestrial global irradiance (See Appendix A).

In order to examine the ADE, ULM needs to incorporate a sun-shade canopy scheme. *De Pury and Farquhar* [1997] developed the first integrated sun-shade canopy model by scaling up the leaf-level photosynthesis to bulk sunlit- and shaded-canopy photosynthesis according to the vertical profile of sunlit canopy fraction and nitrogen. *Wang and Leuning* [1998] further developed a more comprehensive sun-shade canopy model that separately prognoses the sunlit- and shaded-canopy energy budgets. *Dai et al.* [2004] has incorporated these schemes into the Common Land Model for application to climate studies. This study uses a similar set of equations proposed in the previous studies, to incorporate the sun-shade canopy model in ULM, and identifies and optimizes critical tuning parameters that control canopy energy and CO_2 fluxes.

7.2.1. Energy Balance Equations in A Sun-Shade Canopy Model

Energy budgets are diagnosed separately for sunlit and shaded canopy. Canopy air is assumed to have zero heat capacity; i.e., net shortwave radiation (SW) equals to the sum of net longwave radiation (LW), turbulent sensible (H) and latent heat (E) fluxes.

$$R_{sun} = SW_{sun} - LW_{sun} - H_{sun} - E_{sun} = 0 \qquad (2.1.1a)$$

$$R_{sha} = SW_{sha} - LW_{sha} - H_{sha} - E_{sha} = 0 \qquad (2.1.1b)$$

where subscript *sun* and *sha* represent the sunlit and shaded canopy, respectively. Both equations are solved with respect to the change in the sunlit and shaded vegetation temperature (T_{sun} and T_{sha}) via the Newton-Raphson iteration method [*Dai et al.* 2004].

Net solar radiation is separated into direct and diffuse radiation via an empirical relationship (see Appendix A). Net solar radiation and photosynthetically active radiation (PAR) on the canopy are computed by the two stream canopy radiative transfer (TCRT) scheme [*Sellers* 1985; *Matsui et al.* 2006]. Sunlit vegetation receives both direct and diffuse radiation, while shaded vegetation receives only diffuse radiation [*Norman* 1979]. The net absorbed PAR is computed in similar manner, but using visible-band radiation only. Sunlit fraction of canopy (f_{sun}) is derived by the integration of within-canopy extinction coefficient (k_b) of sunfleck penetration over total leaf (L) and stem (S) area index [*Norman* 1979]. k_b is derived from the TCRT for every model time step during daytime. Sunlit fraction (f_{sun}) becomes zero during night, and only the shaded component of energy budget equation is used (i.e. one-big leaf scheme). Canopy with vertically (or randomly) oriented leaf (such as grasslands and needleleaf forest) decrease the value of k_b toward noon, which means that sunlit fraction of the canopy becomes large around noon. On the other hand, canopy with horizontally oriented leaves tends to have constant k_b, i.e., constant sunlit fraction of canopy, throughout a daytime diurnal cycle. Net longwave radiation account for the emitted from, and received on vegetation, and it is divided by the same fraction of sunlit and shaded vegetation derived for the shortwave band [*Dai et al.* 2004].

Sensible heat flux from canopy air to atmosphere (H) equal to the sum of heat flux from sunlit and shaded vegetation to canopy air (H_{sun} and H_{sha}), and heat flux from

ground to canopy air (H_g) (see Table 7.1 for the complete set of equations). The heat capacity of air within the canopy space is assumed to be zero. Similarly, latent heat flux (E) from canopy air to atmosphere is equal to the sum of latent heat flux from sunlit and shaded vegetation to canopy air (E_{v_sun} and E_{v_sha}), and latent heat flux from ground to canopy air (E_g). The moisture capacity of air within the canopy space is assumed to be zero. CO_2 flux (A) from canopy air to atmosphere is equal to the sum of CO_2 flux from sunlit and shaded canopy to air within the canopy (A_{sun} *and* A_{sha}, respectively) and soil respiration (A_g), similar to the sensible and latent heat flux scheme. Thus, CO_2 capacity of air within the canopy space is assumed to be zero.

Although it is assumed that the canopy air heat, moisture and CO_2 capacity is zero, the values of variables in the canopy air space differ from those at the atmosphere 10m above the canopy height due to the canopy aerodynamic resistance (Table 7.1).

7.2.2. Tuning Parameters in Resistance Terms

This section explains the functions and tuning parameters selected in this study. It should be noted that i) details about the calibration of surface albedo in ULM can be found in *Matsui et al.* [2006]; ii) net longwave radiation is the physically based black body emission (note that uncertainties of vegetation emissivity affect only up to 0.5K of surface temperature over North America [*Jin and Liang* 2006]); and iii) NLDAS meteorological forcing is an unbiased product [*Cosgrove et al.* 2003]. Therefore, uncertainties of energy budget equations remain in the terms of resistance parameters in H, E, and A. In particular, tuning parameters were found in aerodynamic resistance and photosynthesis capacity. Tuning parameters were selected from preliminary sensitivity

Sensible heat flux	Latent heat flux	CO2 flux
$H = -\rho_{atm} C_p \frac{(T_{atm} - T_{air})}{r_{ah}}$	$E = -\lambda\rho_{atm} \frac{(q_{atm} - q_{air})}{r_{aw}}$	$A = -\frac{(c_{atm} - c_{air})}{1.36\, r_{aw}}$
$H_{sun} = -\rho_{atm} C_p (T_{air} - T_{sun}) \cdot \frac{f_{sun}(L+S)\cdot 2}{r_{b\_sun}}$	$E_{sun} = -\lambda\rho_{atm} (q_{air} - q_{sat}^{T_{sun}}) \cdot \left\{ \frac{f_{wet} f_{sun} (L+S)}{r_{b\_sun}} + \frac{f_{dry} f_{sun} L}{r_{b\_sun} + r_{s\_sun}} \right\}$	$A_{sun} = -(A_{leaf\_sun} - A_{d\_sun}) f_{sun} L$
$H_{sha} = -\rho_{atm} C_p (T_{air} - T_{sha}) \cdot \frac{f_{sha}(L+S)\cdot 2}{r_{b\_sha}}$	$E_{sha} = -\lambda\rho_{atm} (q_{air} - q_{sat}^{T_{sha}}) \cdot \left\{ \frac{f_{wet} f_{sha} (L+S)}{r_{b\_sha}} + \frac{f_{dry} f_{sha} L}{r_{b\_sha} + r_{s\_sha}} \right\}$	$A_{sha} = -(A_{leaf\_sha} - A_{d\_sha}) f_{sha} L$
$H_g = -\rho_{atm} C_p \frac{(T_{air} - T_g)}{r_{b\_soil}}$	$E_g = -\rho_{atm} \frac{(q_{air} - q_g)}{r_{b\_soil}}$	$A_g = A_{g\_ref} f(\Theta_g) f(T_g)$

Table 7.1. Set of equations for each component of sensible (H), latent (E), and CO_2 (A) fluxes. T represents temperature; q represents vapor mixing ratio; c represents CO_2 concentration; Subscript *atm* represents the atmosphere 10m above the canopy top; subscript *air* represents the air within the canopy space; subscript g represents the ground; ρ_{atm} is the dry air density at surface level; C_p is the specific heat of dry air at surface level; q_{sat} is saturated vapor mixing ration; f_{sun} and f_{sha} are sunlit and shaded fraction of vegetation; f_{wet} is wetted fraction of vegetation, and $f_{dry} = 1.- f_{wet}$; A_{l_sun} and A_{l_sha} are sunlit- and shaded-leaf photosynthesis; A_{d_sun} and A_{d_sha} are sunlit- and shaded-leaf dark (maintenance and growth) respiration (); A_{g_ref} is reference soil respiration rate; r_{ah} and r_{aw} are dry air and moisture resistance between the canopy air and atmosphere 10m above the canopy top height, which is derived from Monin-Obkhov similarity theory; r_{b_sun} and r_{b_sha} are resistance between sunlit, shaded leaves and canopy air, respectively; r_{b_sun} is resistance between soil and canopy air.

$\frac{1}{r_s} = a\left(\frac{A_{leaf} e_{leaf} P_{atm}}{c_{leaf} e_i}\right) + b$	(1)
$A_{leaf} = \min\langle W_V, W_J, W_E \rangle$	(2)
$W_V = \begin{cases} V_m \left\{\frac{c_{leaf} - \Gamma^*}{c_{leaf} + k_c(1 + o_{leaf}/k_o)}\right\}, & for\ C_3 \\ V_m, & for\ C_4 \end{cases}$	(3)
$W_J = \begin{cases} q_e\ \phi_{PAR} \left\{\frac{c_{leaf} - \Gamma^*}{c_{leaf} - 2\Gamma^*}\right\}, & for\ C_3 \\ q_e\ \phi_{PAR}, & for\ C_4 \end{cases}$	(4)
$W_E = \begin{cases} 0.5\, V_m, & for\ C_3 \\ 20000 V_m c_{leaf}/p, & for\ C_4 \end{cases}$	(5)
$A_d = \begin{cases} 0.015\, V_m, & for\ C_3 \\ 0.025\, V_m, & for\ C_4 \end{cases}$	(6)

Table 7.2. Set of equations for empirical stomatal conductance and photosynthesis model. T represents temperature; q represents vapor mixing ratio; e represents partial pressure of water vapor, c represents CO_2 concentration; o presents O_2 concentration; subscript leaf represent leaf-level process; subscript *atm* represents the atmosphere 10m above the canopy top; subscript *air* represents the air within the canopy space; Γ^* is CO_2 compensation point, k_c is rubisco Michaels-Menten constant for CO_2, k_c is rubisco inhibition constant for oxygen, q_e is the quantum yield of electron transport that depends on the LULC class, ϕ_{PAR} is absorbed PAR derived for unit sunlit and shaded LAI, V_m is temperature- and water-limited maximum rate of rubisco-limited assimilation rate. Note that the stomatal conductance is separately derived for sunlit and shaded leaf; thus, e_{leaf}, V_m, ϕ_{PAR} are also separately derived for sunlit and shaded components.

studies (not shown here) as well as the mechanical relationship in the surface energy budget equations. These are categorized as either 1) *a soil tuning parameter* that are common for all LULC types or 2) *LULC-dependent tuning parameters* that are specific for each LULC types.

The flux gradient and resistances are derived based on the Monin-Obukhov length for very unstable, unstable, stable, and very stable condition of universal similarity functions [*Zeng et al.* 1998]. In these functions, the most important tuning parameter is the canopy roughness length (z_{can}), which is a *LULC-dependent tuning parameter*. Particularly, a reduction (increase) in z_{can} can suppress (enhance) surface turbulent energy flux, thereby increasing (decreasing) daytime canopy and soil temperature. Leaf-level and soil-surface roughness length are also important (see Appendix B). However, they are not optimized for simplicity, because the calibration process becomes much more complex and time-consuming as the number of the tuning parameters increases.

During daytime, surface sensible and latent heat fluxes and radiative temperature are strongly controlled by the soil evaporation rate over less-vegetated ground. Soil evaporation (E_g) is a function of vapor mixing ratio between canopy air (q_{air}) and soil surface (q_g), which is a function of relative humidity for air within top-soil pore space (RH_{soil}).

$$q_g = RH_{soil} \cdot q_{sat}^{Tg} \qquad (7.2.2.1)$$

There are a number of different formulations for RH_{soil}. *Mahfouf and Noilhan* [1991] and concluded that the formulation strongly depends on the depth of the top soil layer. Initially, ULM used the formula from *Philip* [1957], but this study formulated a tuning-oriented equation for estimating RH_{soil} (Figure 7.1a).

$$RH_{soil} = 1 \Big/ \left(1 + \exp\left[-a_{soi} (2 \cdot b_{soi} \frac{\Theta_{top}}{\Theta_{sat}} - 1 \right] \right) \qquad (7.2.2.2)$$

where Θ_{sat} is saturated volumetric soil moisture, Θ_{top} is top-soil volumetric soil moisture; a_{soi} (fixed as 6.0 in this study) and b_{soi} are *soil tuning parameters* that can fit most of the different formulations compared by *Mahfouf and Noilhan* [1991]. For example, b_{soi} of 3 is close to the *Phillip* [1957], while b_{soi} of 0.9 is close to *Lee and Pielke* [1992]. Higher (lower) b_{soi} enhances (suppresses) daytime bare soil evaporation. Initial values were set to 3, close to the original formula.

Soil respiration parameterization (Ag) is a function of soil temperature, soil water status and a reference soil respiration rate (A_{g_ref}) following *Norman et al.* [1992]. *Reichstein et al.* [2003] investigated in-situ soil respiration rates from 17 different forest and shrublands sites in Europe and North America, and found that the A_{g_ref} is explained by the seasonal maximum LAI better than other factors, including leaf litter fall, leaf production, peak leaf biomass, mean annual precipitation, and annual average air temperature. Following to *Reichstein et al.* [2003], this study formulated A_{g_ref} as a function of MODIS-derived maximum LAI (L_{max}) for each site.

$$A_{g\_ref} = s_1 (1 - \exp[-s_2 L_{\max}]) \qquad (7.2.2.3)$$

where s_1 and s_2 are *soil tuning parameters* that can fit from linear to non-linear relationship between A_{g_ref} and L_{max} proposed in *Reichstein et al.* [2003].

Daytime surface energy fluxes and canopy temperature are strongly coupled with the stomatal conductance associated with photosynthesis rate over dense vegetation area. Sunlit- and shaded-canopy stomatal conductance are coupled with photosynthesis rate based on semi-empirical formulations in *Ball et al.* [1987] and *Collatz et al.* [1991] (Table 7.2). Carbon assimilation rate is the minimum among rubisco-limited rate (W_V), light-limited assimilation rate (W_J), and carbon compound export limitation (W_E). Because W_V and W_J dominantly control the photosynthesis in this model, tuning parameters are related to these two photosynthesis rates.

First, W_J is particularly important for shaded-leaf photosynthesis, since it is generally light-limited environment (i.e., $A_{l\_sha} = W_j$). W_J linearly depends on the quantum yield of electron transport (q_e) (*LULC-dependent tuning parameters*) (Table 7.2), which could be diagnosed from the light-use efficiency under a 100% diffuse-radiation environment.

Second, W_V is particularly important for sunlit-leaf photosynthesis, since it is generally light-saturated, rubisco-limited environment (i.e., $A_{l\_sun} = W_V$). W_V linearly depends on sunlit- and shaded-component of rubisco-limited photosynthetic capacity (V_m^{sun} and V_m^{sha}) (Table 7.2), which are functions f_T of bulk sunlit- or shaded-canopy temperature (T_{sun} or T_{sha}), water stress function (f_Ψ), and scaled sunlit- or shaded-vegetation reference photosynthetic capacity (V_{ref}^{sun} or V_{ref}^{sha}).

$$V_m^{sun} = V_{ref}^{sun} \; f_{T_{sun}} \; f_\Psi \qquad (7.2.2.4a)$$

$$V_m^{sha} = V_{ref}^{sha} \; f_{T_{sha}} \; f_\Psi \qquad (7.2.2.4b)$$

The temperature-stress function is the combination of Q_{10} function for the reference temperature (25°C) and the thermal breakdown of metabolic processes.

$$f_{T_{sun}} = \frac{a_{Q10}^{(T_{sun}-298.16)/10}}{1+\exp[(0.02a_{Q10}+0.1)(T_{sun}-T_{opt})]} \qquad (7.2.2.5)$$

where a_{Q10} is the *LULC-dependent tuning parameters* that controls the shape of temperature function; T_{opt} is an optimum temperature. The same function is applied for the shaded component, using shaded canopy temperature (T_{sha}). Variability of a_{Q10} is found to be much more important than variability of T_{opt}, for fitting surface CO_2 flux against the observation. In addition, noon-time temperature depression in photosynthesis is captured only at limited sites. Thus, T_{opt} is not optimized. Higher (lower) a_{Q10} tends to generate a sharp (moderate) rise in temperature function and resultant photosynthesis capacity (Figure 7.1b).

The water-stress function is formulated as

$$f_\Psi = \sum_{i=1}^{10}\left(\frac{\Psi_{wilt}-\Psi_{soil}^i}{\Psi_{wilt}+\Psi_{sat}}\right)\cdot f_{root}^i \qquad (7.2.2.6)$$

where Ψ_{wilt} is plant water potential at wilting point (~ -2 to -3Mpa), Ψ_{sat} is saturated soil water potential (close to 0Mpa), Ψ_{soil}^i is soil water potential in the ith soil layer, f_{root}^i is

root fraction in the *i*th soil layer [*Zeng* 2001]. f_Ψ ranges from 0 (wilting point) to 1 (optimal point). In this study, there are no clear drought signals at all Fluxnet observations sites and initial model experiment in 2000 and 2001. Thus, Ψ_{wilt} is not optimized in this study.

V_{ref}^{sun} and V_{ref}^{sha} are analytically scaled from the canopy-top photosynthesis capacity (V_{ref}^{top} : *LULC-dependent tuning parameter*) and within-canopy vertical profile of sunfleck penetration and photosynthesis capacity [*de Pury and Farquhar* 1997].

$$V_{ref}^{sun} = \frac{\int_0^L V_{ref}^{top}\, e^{-k_n x}\, e^{-kx}\, dx}{\int_0^L e^{-kx}\, dx} \qquad (7.2.2.7a)$$

$$V_{ref}^{sha} = \frac{\int_0^L V_{ref}^{top}\, e^{-k_n x} (1 - e^{-kx})\, dx}{\int_0^L (1 - e^{-kx})\, dx} \qquad (7.2.2.7b)$$

where x is cumulative leaf area index, k_n is a within-canopy extinction coefficient of V_{ref}. ($= V_{ref}^{top}\, e^{-k_n x}$). Observational studies have shown that photosynthesis capacity (e.g., nitrogen content) is positively correlated with the within-canopy profile of absorbed solar radiation; i.e., plants intend to allocate more V_{ref} toward the canopy top to utilize the greater amount of absorbed photon in leaves [*Field* 1983; *Hirose and Werger* 1987]. Thus, k_n is usually related to the extinction of diffuse light for total canopy and tuning parameter.

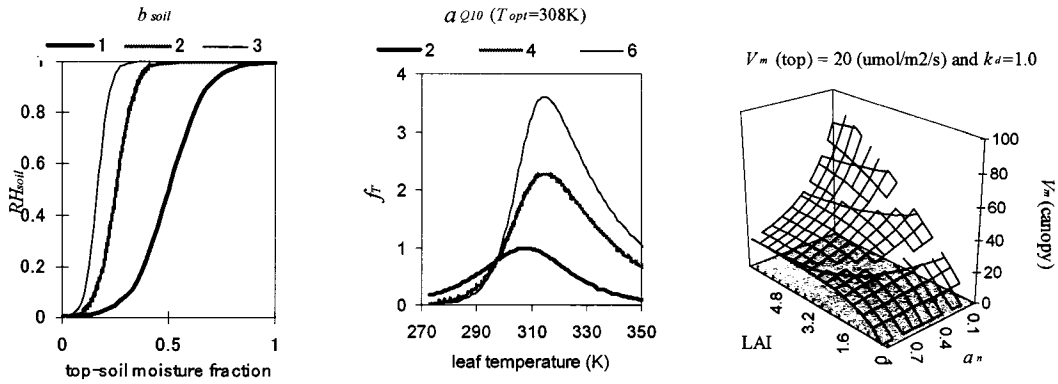

a) b) c)

Figures 7.1. a) Top-soil RH_{soil} as a function of b_{sol}. b) Temperature weight of V_m (μmol /m^2 /s) as a function of a_{Q10}. c) Reference canopy photosynthesis capacity (V_{ref}) as a function of LAI and k_n.

$$k_n = a_n k_d, \qquad (7.2.2.8)$$

where k_d is the within-canopy diffuse light extinction, and a_n is *an LULC-dependent tuning parameter*. For large a_n (~1), canopy-scale photosynthesis capacity is nearly invariant for the range of LAI between 3 and 6, while small a_n (~0.1) can linearly increase the photosynthesis capacity within the same range of LAI (Figure 7.1c). Initial values of a_n are set to be 1, similar to the optimal light-use assumption in *Field* [1983], *Hirose and Werger* [1987] and *Sellers et al.* [1996].

7.3. Continental-Scale Multi-Observation Calibration and Assessment of CSU ULM

7.3.1. Method

Similar to the previous calibration study [*Matsui et al.* 2006], this study uses Parameter Estimation (PEST) model. PEST uses a robust Gauss-Marquhardt-Levenberg (GML) algorithm, which combines the advantages of the Gauss-Newton method and the

steep descent method and therefore provides faster and more efficient convergence toward the objective function minima [*Watermark Numerical Computing* 2004] (see the details in Chapter 6). The best set of parameter is selected from within reasonable ranges by adjusting the values until the discrepancies between the model generated values and those measured in the field is reduce to a minimum in the weighted least squares sense.

The calibration will be performed over a domain that covers approximately the eastern U.S. (latitude of 25°N to 50°N, longitude of 100°W to 70°W). The calibration period is May to September in 2000. This period experiences vegetation growth and senescence as well as intra-seasonal shift in synoptic weather conditions. A time period from May to September in 2001 is used for the model validation. Each simulation starts from April, this month being considered a spin-up period.

This study uses MODIS V4 land-surface temperature (LST) 0.05° CMG product [*Wan et al.* 2002]. This product significantly reduces uncertainties associated with the cloud contamination, and it has been validated with in-situ measurements in field campaigns that confirmed that the LST accuracy is better than 1K in almost all clear-sky cases [*Wan et al.* 2002, 2004; *Coll et al.* 2005]. MODIS LST 0.05° is aggregated into 0.25° datasets, only if more than 95% of 0.05° pixels are available within a 0.25° grid. LST in all subgrid tiles are averaged based on the fraction of subgrid tile coverage (0~1) to represent the total 0.25° grid LST in the ULM. The model- and satellite-derived monthly LST are compared for the calibration process in a consistent manner (see Appendix C).

Although a combination of satellite-derived daytime LST potentially estimates the status of surface energy flux, uncertainties remain in the surface turbulent heat and CO_2 fluxes. Therefore, measurements of CO_2 flux and turbulent sensible and latent heat fluxes are required to reduce the uncertainties in the energy budget equations. This study also uses these measurements from the network of surface eddy covariance measurements Fluxnet [*Baldocchi et al.* 2001]. In addition to these fluxes, light use efficiency (*LUE*) for the cosine of solar zenith angle greater than 0.5 is also computed and compared with the model output, since *LUE* is critical for examining the ADE [*Niyogi et al.* 2004; *Chang* 2004].

ID	Site	Species	UMD LULC class	Lat Lon (°)
Niwt	Niwot Ridge Forest, Colorado	subalpine fir, engelmann spruce, and lodgepole pine	evergreen needleleaf forests	40.033, -105.546
Meto	Metolius, Oregon	ponderosa pine, antelope bitterbrush, and greenleaf manzanita	evergreen needleleaf forests	44.437, -121.567
Wind	Wind River Crane Site, Washington	douglas –fir, western hemlock, and etc.	evergreen needleleaf forests	45.821, -121.952
Morg	Morgan Monroe State Forest, Indiana	sugar maple, tulip popla, sassafras, white oak, black oak and etc.	deciduous broadleaf forests	39.321, -86.413
Umic	U. of Michigan Biological Station, Michigan	bigtooth aspen, quaking aspen, eastern white pine, and northern red oak	deciduous broadleaf forests	45.560, -84.714
Gret	Great Mountain Forest, Norfolk, Connecticut	red maple, eastern white pine, and hemlock	mixed forests	41.967, -73.233
Harv	Harvard Forest, Massachusetts, USA	oak, red maple, black birch, white pine, hemlock, white oak, black oak, and hickory	mixed forests	42.536, -72.172
Duke	Duke Forest, Pine, North Carolina	loblolly pine with red maple, sweetgum, and white oak in the understory.	mixed forests	35.978, -79.094
Will	Willow Creek, Wisconsin	white ash, sugar maple, basswood, green ash, and red oak with sugar maple and ironwood saplings, leatherwood, maidenhair, bracken ferns, and blue cohosh in the understory.	mixed forests	45.906, -90.080
Bond	Bondville, Illinois	annual rotation between Corn (C4) - 2001, Soybeans (C3) - 2000	croplands	40.006, -88.292
Fort	Fort Peck, Montana	C3 grass	grasslands	48.308, -105.101

Table 7.3. A list of the FLUXNET observation sites

Monthly composites of the instantaneous MODIS LST, monthly composites of the hourly sensible/latent/CO_2 fluxes and LUE with respect to diffuse-radiation fraction are compared with the corresponding model outputs in order to compute the objective function ($\Psi_{tot} = \Psi_{LST} + \Psi_{SHF} + \Psi_{LHF} + \Psi_{CO2} + \Psi_{LUE}$). Since the sub-components of the objective functions (Ψ_{LST}, Ψ_{SHF}, Ψ_{LHF}, Ψ_{CO2}, Ψ_{LUE}) belong to the different variables that have different variances and observational points, the weight of the each objective function (see eq. 6.2.4 in Chapter 6) is set to have the following relationships in the initial-step objective functions.

$0.5\Psi_{LST} = \Psi_{SHF} = \Psi_{LHF} = \Psi_{CO2} = \Psi_{LUE}$.

ULM is run on the local scale for comparing the ground *in-situ* observations within the LIS. The local-scale simulations are forced by the Fluxnet-observed meteorological variables whenever they are available and the soil boundary conditions use co-located 1km STATSGO soil data [*Miller and White* 1998]. The eleven Fluxnet sites were chosen depending on the data availability and LULC types over North America, which is composed of three sites for evergreen needleleaf forests, two for deciduous broadleaf forests, three for mixed forests, and one site for croplands and grasslands (Table 7.3). Because there are no Fluxnet sites for deciduous needleleaf forests, evergreen broadleaf forests, savannas, and shrublands, tuning parameters in these land-cover classes are not optimized. However, it should not exacerbate quality of the calibration, because the five LULC classes that have Fluxnet sites cover the most of the fractional area in the domain (Figure 7.2). Croplands are located mainly in the

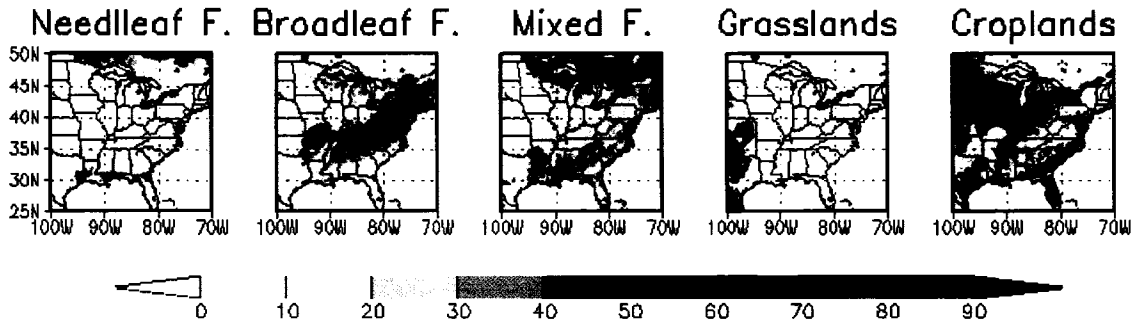

Figure 7.2. Distributions of fractional coverage of UMD LULC classes over eastern U.S.

Midwestern U.S. and some portions close to coast in the southeast U.S. Grasslands cover mostly the southwestern edge of the domain. Mixed forests are located in two regions, including southern U.S. and Canadian boreal region (at northern edge of the domain). Broadleaf forests exist in the middle to the eastern portions of the domain. Croplands, mixed forest, and deciduous broadleaf forest are the three dominant LULC classes that cover the study area (Figure 7.2).

7.3.2. Results

7.3.2.1 Pre-calibration experiment

Figure 7.3a shows spatial maps of pre-calibration model biases (MODIS – ULM) in daytime LST. ULM consistently underestimates daytime LST over most of the domain throughout the season, up to 15K. There are small fractions of less-biased areas over the Midwest U.S. in July and August. The large underestimations exist in the southwestern corner of the domain in August and September. Figure 7.3b shows descriptive statistics (*m*: mean, *s*: standard deviation, and *rmse*: root-mean-square error) and scatter plots of the errors (MODIS – ULM) in the daytime LST for the tile fraction (0.8 ~ 1.0) of each LULC type. ULM consistently underestimates the daytime LST in all LULC types

(Figure 7.3a). Among LULC classes, the largest underestimation in LST appears to be in grasslands (9.34K). Grasslands and croplands show the large spread of scatters (s=3.87 and s=3.24, respectively). The forest classes also show underestimated LST (m: 4.13 ~ 5.82K), while the spreads of scatter are relatively smaller (s = 1.73 ~ 2.32K) than those of grasslands and croplands.

Figure 7.4 shows the monthly composite of diurnal cycles of CO_2 sink (A: note that negative values are defined to be a sink), latent heat flux (E), and sensible heat flux (H) as well as light use efficiency (LUE: defined as A normalized by PAR) observed at eleven Fluxnet sites (black closed circles) and predicted by pre-calibrated ULM (red closed circles). Fluxnet sites for the evergreen needleleaf forest class (*Niwt*, *Meto*, and *Wind*) show reasonable agreement between the observations and the model. *Niwt* shows a good agreement in A and LUE between the observation and the model ($RMSE$=2.085 and 0.090), while *Meto* and *Wind* shows that ULM overpredicts A in the morning. Pre-calibrated ULM tends to overestimate the sensible heat flux in *Wind* site.

Fluxnet sites for the deciduous broadleaf forest class (*Morg* and *Meto*) show large disagreements in all fluxes between the observations and the model. Pre-calibrated ULM consistently overestimates CO_2 sink (A) and LUE. ULM predicts bell-shaped patterns of daytime diurnal cycles in A, while the observations shows sharp rises and descends in A in morning and afternoon, respectively. ULM also fails to create seasonal patterns in A. Noon-time peak values in A tend to be constant throughout the seasons, which result in large overestimations in May and September. Nocturnal H in ULM is consistently negatively biased (excepting *Morg* in May). Features of the ULM biases in the mixed forest class (*Gret*, *Harv*, *Duke*, and *Will*) are quite similar to those in the deciduous

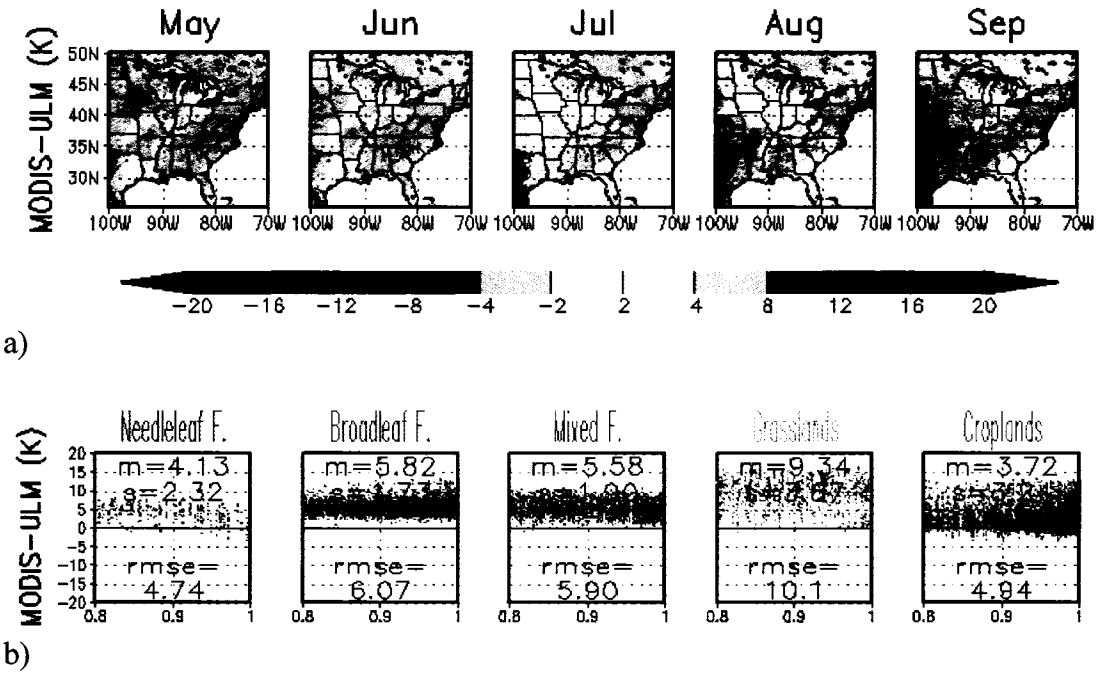

Figure 7.3. a) Spatial map of the errors (MODIS – ULM) in the daytime LST. b) Scatter plots and statistics (*m*: mean, *s*: standard deviation, and *rmse*: root mean square error) of the pre-calibration difference (MODIS– ULM) in daytime LST. X-axis represents the fraction (0.8~1.0) of each land-cover class.

broadleaf forest class. Simulated *A* has a bell-shaped daytime diurnal cycle while the observations have a triangular-shaped one. ULM has less seasonal variability in *A*, while the observations show an increase and decrease trend in *A* in early and late summer season, respectively (especially, *Gret*, *Harv*, and *Will*). ULM has consistent negative biases in nocturnal *H*. A Fluxnet site for the croplands class (*Bond*) shows the disagreements in seasonable variability between the observations and the model. The observation shows nearly zero in *A* in May and June and positive daytime *A* in September. ULM overpredicts daytime *A* in May, June, and September. Consequently, ULM overestimates daytime *A* and *LUE*, and underestimates daytime *H* in the corresponding months. A Fluxnet site for the grasslands class (*Fort*) shows that ULM significantly

overestimates the daytime E, and underestimates daytime H throughout the seasons. These are the largest errors in ULM (RMSE = 63.77 for E and RMSE = 55.59 for H) among all Fluxnet sites.

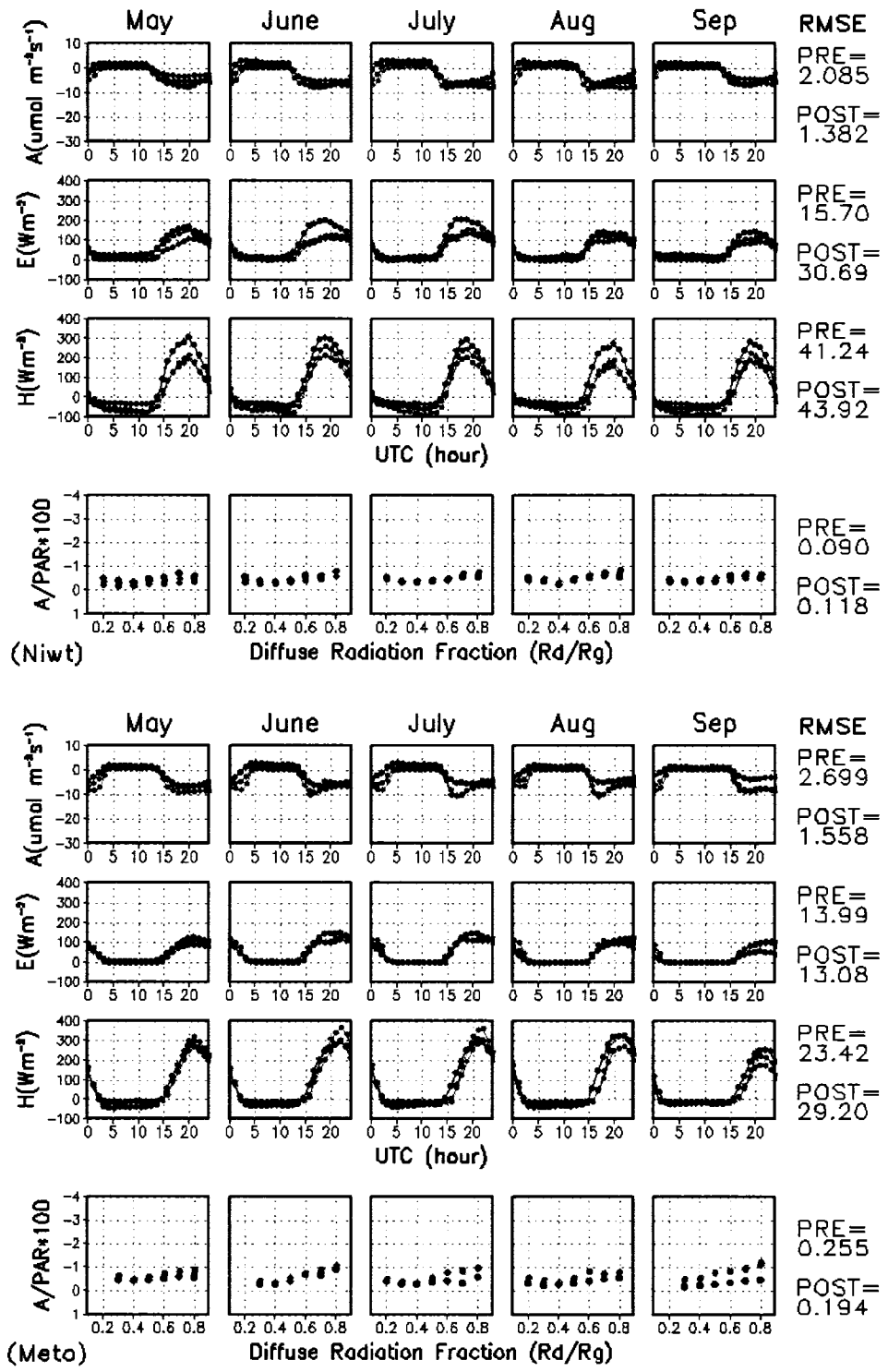

Figure 7.4. Mean diurnal cycle of surface sensible heat flux, latent heat flux, CO_2 flux and light-use efficiency (A/PAR) from Fluxnet observations (black), ULM pre-calibration experiment (red), and ULM post-calibration experiment (green). Root-mean squared errors (RMSE) are also computed.

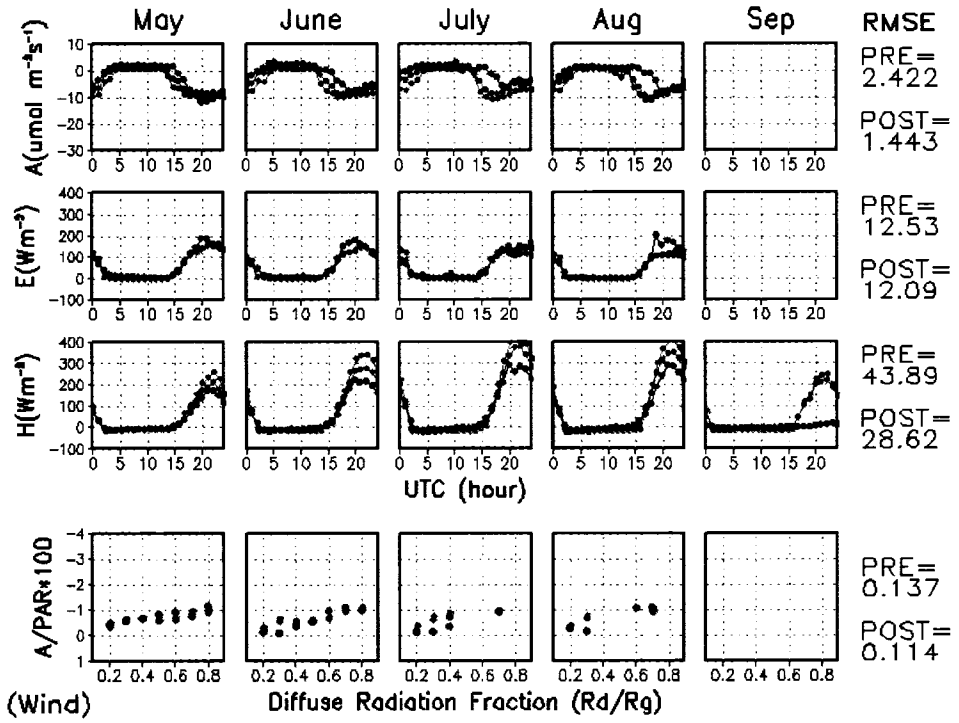

Figure 7.4. Continued.

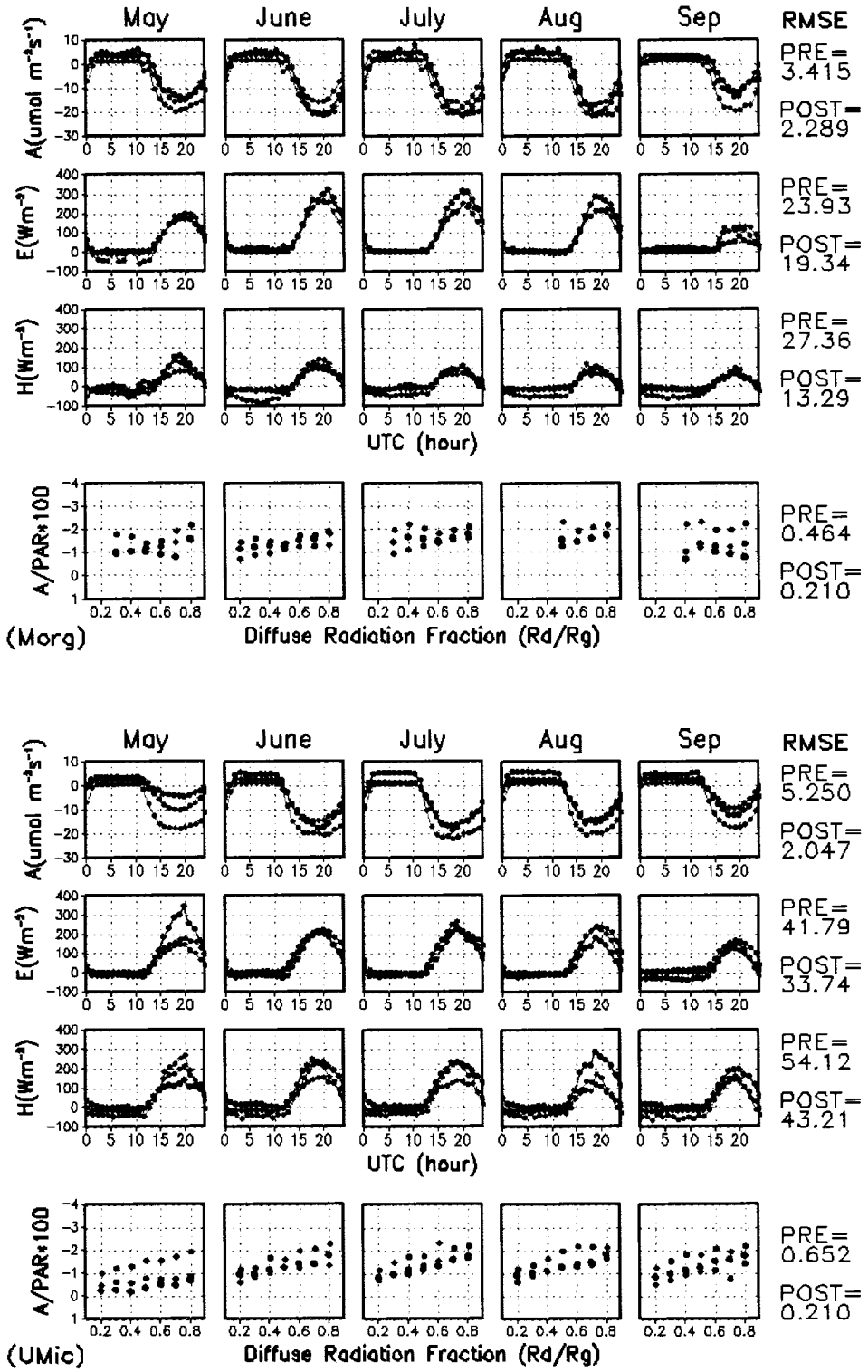

Figure 7.4. Continued.

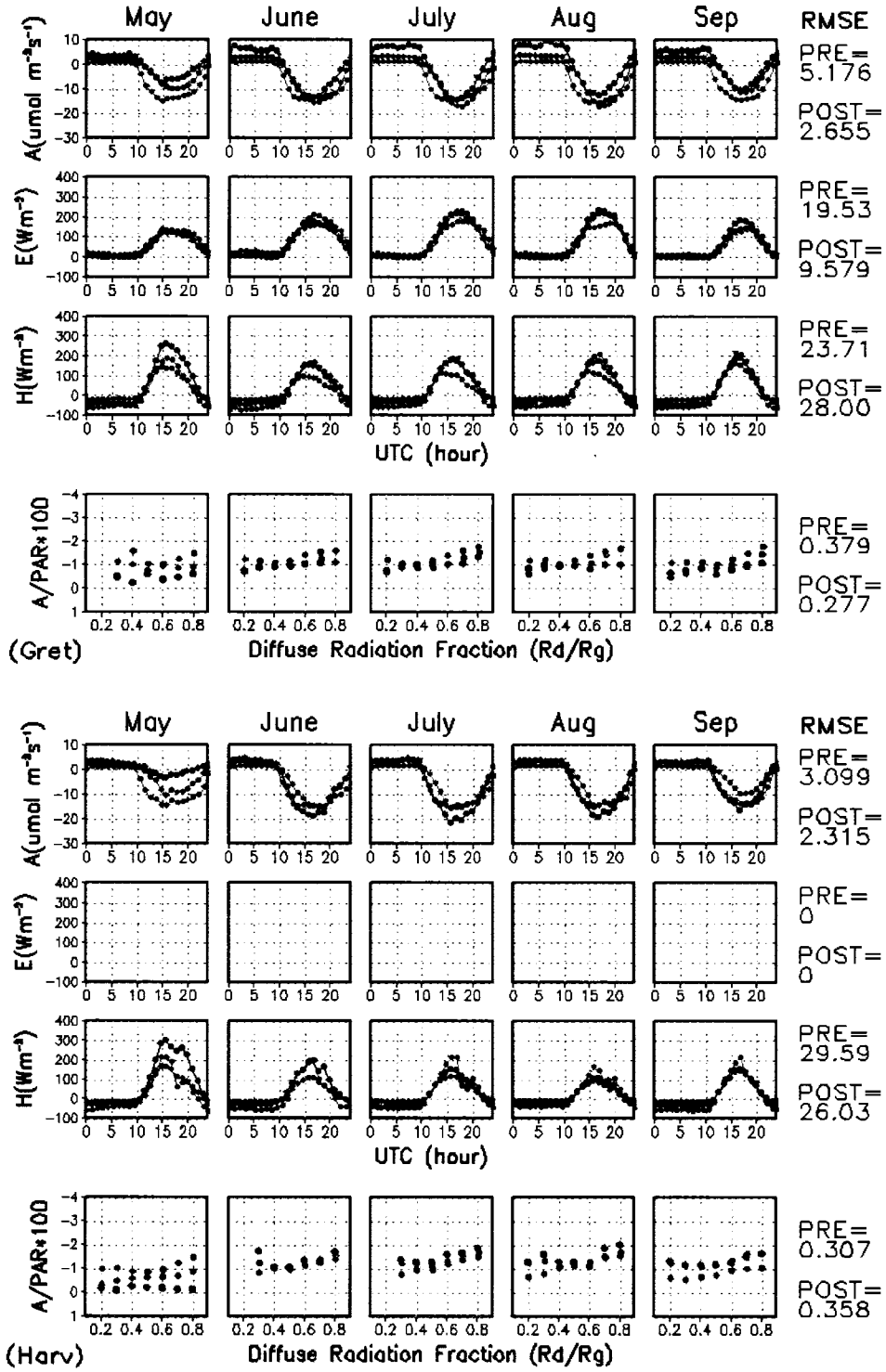

Figure 7.4. Continued.

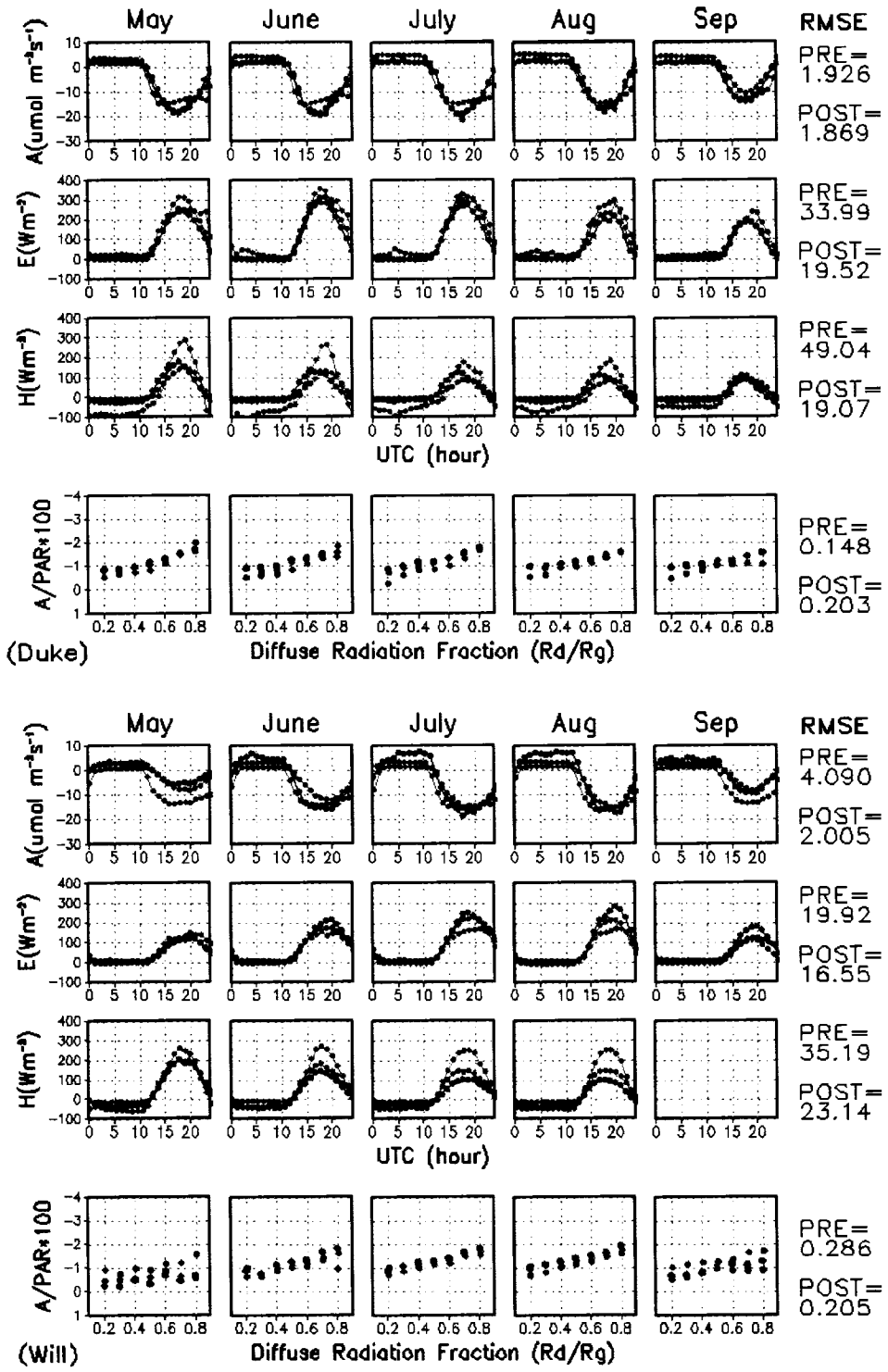

Figure 7.4. Continued.

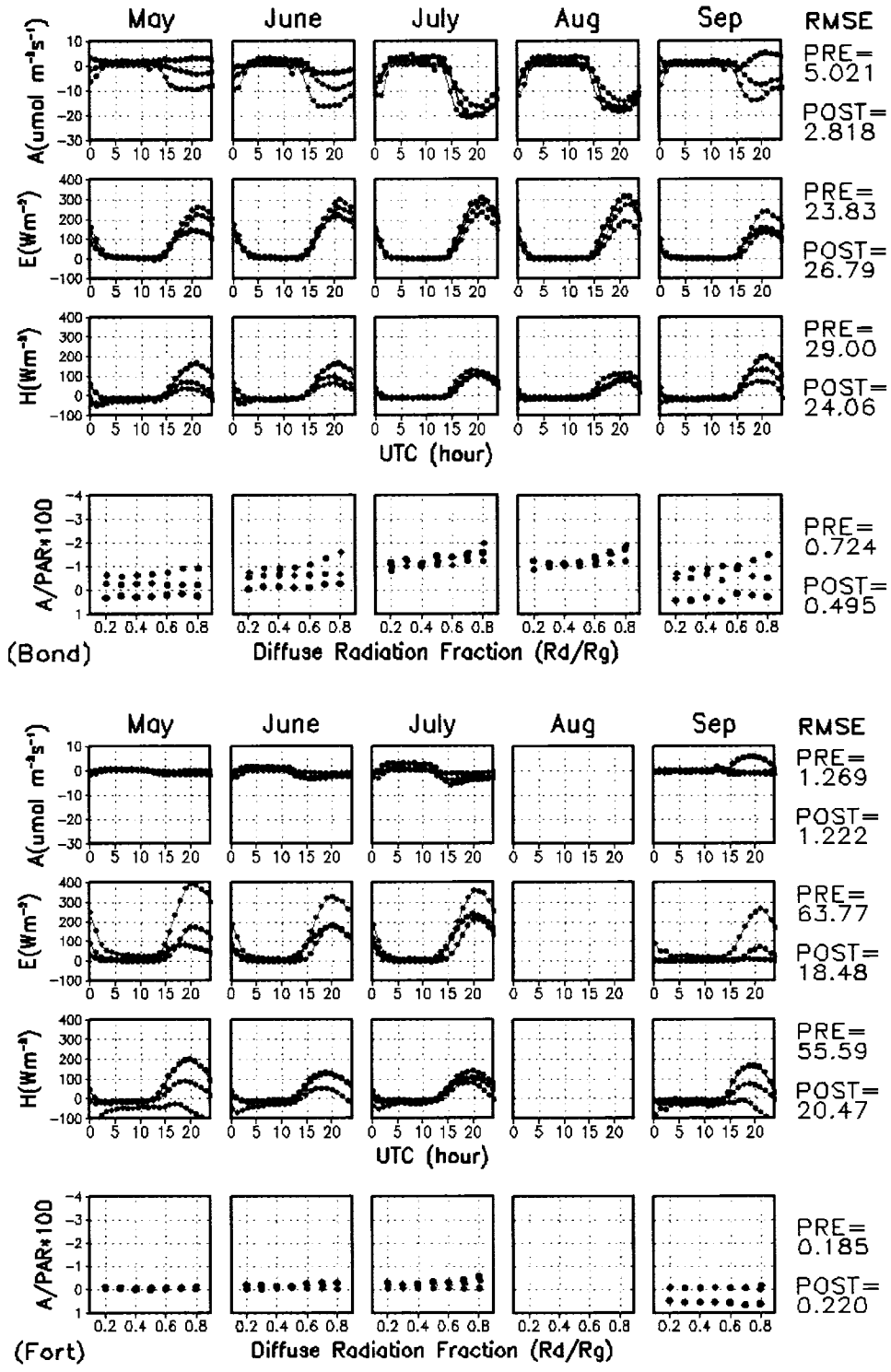

Figure 7.4. Continued.

7.3.2.2. Post-calibration experiment

Tuning parameters in ULM are optimized through the GML algorithm by minimizing the errors shown in the previous sections. Table 7.4 shows the set of tuning parameters in the pre- and post-calibration experiments. Main results of the calibration are that; i) the canopy roughness lengths (z_{can}) have been considerably reduced in all LULC classes that suppress turbulent heat fluxes; ii) the parameter for the unsaturated-soil RH (b_{soil}) has been reduced from 3 (corresponding to *Phillip* [1957]) to 1 (close to the formulation in *Lee and Pielke* [1992]) that reduced the bare-soil evaporation; iii) the parameters for the temperature control on photosynthesis capacity (a_{Q10}) in the broadleaf forest, mixed forest, and croplands have been largely increased in order to represent the sharp descends and rises in daytime diurnal cycle and realistic seasonal patterns in CO_2 flux.

Note that the parameters that control vertical profiles in photosynthesis (a_n) cannot be estimated together with canopy-top photosynthesis capacity (V_{ref}^{top}), because

LULC-dependent parameter	z_{can}(m)		V_{ref}^{top}(μmol/ m^2/s)		a_n(-)		a_{Q10}(-)		q_e(-)	
	pre	*post*	*pre*	*post*	*pre*	*post*	*pre*	*post*	*pre*	*post*
evergreen needleleaf forests	.935	.028	60.	38.3	1.0	0.5	2.1	2.9	0.06	0.04
deciduous broadleaf forests	1.925	.006	100.	19.0	1.0	0.1	2.1	4.5	0.06	0.04
mixed forests	1.925	.019	80.	17.6	1.0	0.1	2.1	7.0	0.06	0.04
grasslands	.06	.006	30.	10.8	1.0	0.5	2.1	2.8	0.04	0.04
croplands	.06	.062	100.	24.6	1.0	0.5	2.1	8.4	0.06	0.04

Soil parameter	a_{soi}(-)		b_{soi}(-)		s_1(-)		s_2(-)	
-	*pre*	*post*	*pre*	*post*	*pre*	*post*	*pre*	*post*
-	6.0	6.0	3.0	1.0	5.0	19.1	0.1	.06

Table 7.4. The set of tuning parameters in a pre- and post-calibration experiment. a_{soi} is not optimized. a_n and q_e are manually calibrated.

variability of canopy-scale photosynthesis capacity was found to be more sensitive to changes in a_n than to changes in V_{ref}^{top}. Thus, a_n have been manually changed and fixed based on the literature survey. For the deciduous broadleaf forest and mixed forest classes, a_n is set to 0.1, close to observed profiles in the boreal mixed forest [*Dang et al.* 1997] and in temperate broadleaf forest [*Koike et al.* 2004]. It is found that the seasonal variability of noon-time peak carbon sink is effectively correlated with variability of LAI (3~6). Using the initial value of a_n equal to 1, variability of LAI essentially does not affect the canopy-scale photosynthesis. On the other hand, the new a_n (0.1) linearly changes the photosynthesis capacity for the ranges of LAI variability (Figure 7.1c), and helped to improve the seasonal variability of A and LUE. *Yin et al.* [2003] found that within-canopy nitrogen extinctions for different crop species are linearly correlated with approximately 50% of within-canopy PAR extinctions. Thus, a_n is set to be 0.5 for croplands. For other classes, a_n is also set to be 0.5, since i) within-canopy nitrogen profile is known to be less efficient than the optimal light-use theory [*Terashima and Hikosaka* 1995]; ii) as surveyed by the authors, there are not enough literature that describe nitrogen (or photosynthesis capacity) profile for evergreen needleleaf forest and grasslands classes.

Similarly, quantum efficiency of electron transport (q_e) could not be effectively calibrated with parameters associated with photosynthesis capacity. Initial attempts (not shown here) indicated that initial values of q_e were so high that they often created light-saturated shaded-canopy photosynthesis, and also caused overestimation of photosynthesis in early morning and late afternoon. Therefore, q_e were set to be 0.04 for all LULC classes.

The post-calibration experiment extensively decreased the orange-shaded (underestimated) regions throughout the season (compared Figure 7.3a and Figure 7.5a), which is a vital improvement by reducing z_{can}. Yet, small fractions of underestimated regions exist in May and September elsewhere in the domain. On the other hand, overestimated (blue-shaded) regions appeared in watershed area along the lower Mississippi River in July and August and Florida throughout the seasons. Figure 7.5b shows the post-calibration errors in daytime LST for different LULC composite. The calibration process clearly improved mean model biases of LST for all LULC class, and slightly improved spread of model errors. Mean biases of three forest and croplands classes became close to the uncertainty level (~1K) in the MODIS LST product [*Wan et al.* 2004]. However, spreads of errors in grasslands (s=3.24K) and croplands (s=3.18K) remain relatively large. Mean biases in grasslands (m=2.47K) also continues to be high, although it has been largely decreased from the pre-calibration experiment (m=9.37K).

Results from the post-calibration experiment are shown in Figure 7.4 (green closed circle) together with the observations and the results from the pre-calibration experiment. The evergreen needleleaf forest class sites (*Niwt*, *Meto*, and *Wind*) show small improvements in A and LUE. In fact, E and H are not effectively improved by the calibration process, excepting daytime H in *Wind* site. The calibration process appears to be effective for the deciduous broadleaf forest sites (*Morg* and *Meto*). RMSE of all model variables has been improved from the pre-calibration experiment. Post-calibration experiment captures the seasonal and diurnal cycles in A due to changes in a_n (from 1.925 to 0.06) and a_{Q10} (from 2.1 to 4.5). Largely decreased z_{can} also suppresses the negative biases in nocturnal H. Improvements in daytime H and E from the post-calibration

experiment are relatively small. Similar improvements are found in the mixed forest sites (*Gret*, *Harv*, *Duke*, and *Will*). The post-calibration experiment effectively predicts triangular-shaped daytime diurnal cycle of A and E, similar to the observations. This improvement is discernible in *Duke* site. The post-calibration experiment has improved the prediction of the seasonal variability in noon-time peak value in A, in comparison with the rather constant values from the pre-calibration experiment. Overestimated daytime H in the pre-calibration experiment has been suppressed due to the largely decreased z_{can} (from 1.925 to 0.019). *LUE* in the post-calibration experiment appears to be slightly steeper in the gradient of *LUE* per DRF (Rd/Rg) for all the sites. The

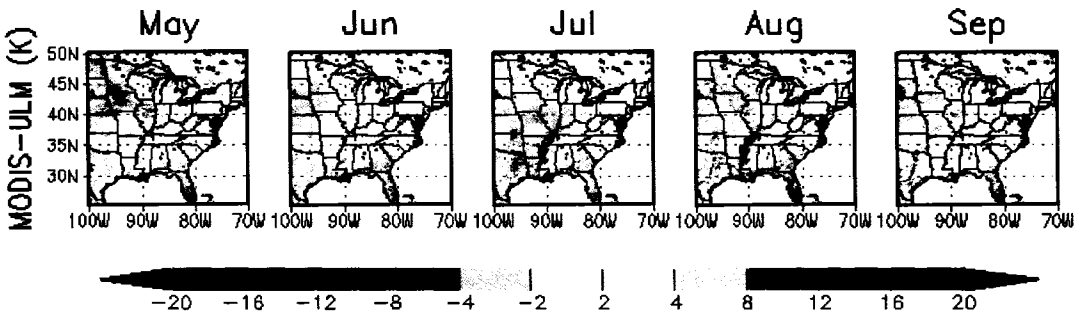

a)

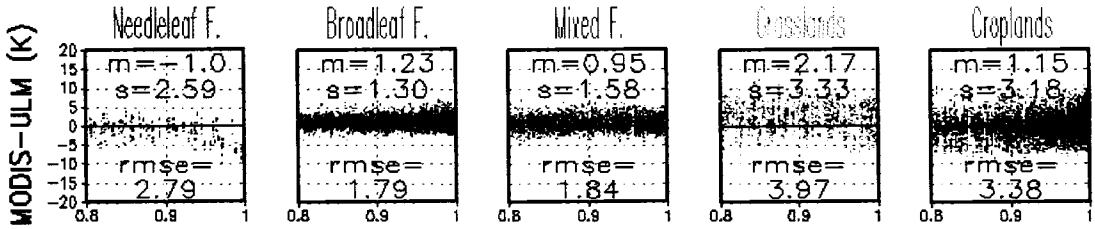

b)

Figure 7.5. Same as 7.3a and 7.3b, but for the post-calibration difference (MODIS–ULM) in daytime LST. X-axis represents the subgrid fraction (0.8~1.0) of each land-cover class.

croplands site (*Bond*) shows an effective improvement in A, H and LUE. Largely raised value in a_{Q10} (from 2.1 to 8.4) improved the seasonal cycle of A, although the post-calibration experiment yet underestimates A and E to some extent in July and August. Reduction in b_{soil} (from 3.0 to 1.0) improved E and H in the grasslands site (*Fort*). RMSE of post-calibration experiments (18.48 and 20.47 for E and H, respectively) are merely less than half of the pre-calibration experiment (63.77 and 55.59), which were the largest errors in the pre-calibration experiment among all sites.

7.3.3. Discussion

In order to examine the sensitivity of simulated terrestrial plant productivity and energy budget to routine aerosol loadings, the sun-shade canopy model has been developed and calibrated in the CSU ULM. One may concern the validity of tuned parameters after the calibration, especially the parameters that control vertical profiles in photosynthesis (a_n), and the parameters that control the shape of temperature function of photosynthesis capacity (a_{Q10}), and canopy roughness length (z_{can}) (Table 7.4).

While a_n is set as unity for all LULC classes in the pre-calibration experiment, a_n is manually corrected to 0.1 for broadleaf and mixed forests and 0.5 for other LULC classes according to findings in recent studies. A value of unity of a_n means that photosynthesis capacity declines from the canopy top toward the bottom at the same rate as solar radiation within the canopy. This assumes that plant allocates photosynthesis capacity to fully take advantage of the light environment in the canopy [*Field* 1983; *Hirose and Werger* 1987; *Sellers et al.* 1996].

Low (less than unity) a_n values mean that that within-canopy profile of

photosynthesis capacity is more homogeneous than that of the optimal light-use assumption [*Terashima and Hikosaka* 1995]. Forest trees, especially, tend to have a much more homogeneous gradient of within-canopy photosynthesis capacity [*Dang et al.* 1997; *Koike et al.* 2004]. *Dang et al.* [1997] speculated that vertical profile of photosynthesis capacity is controlled by resource (nutrient and water) availability. Optimum allocation of photosynthesis capacities requires a high demand of resources and plant structure (e.g., tissues) toward the canopy top. In order to fully utilize the solar radiation, resource allocations and plant tissues need to be modified for the changes in seasonal shifts of the light environment. *Dang et al.* [1997] hypothesized that the upper canopy of boreal forest trees does not have the genetic capability to take advantage of the light levels during the summer months. *Koike et al.* [2004] found that late or mid successional species tends to have a more homogeneous gradient of vertical profiles in photosynthesis capacity than early successional species. Thus, plant resource allocation appears to be linked to different survival strategies. As surveyed in the literature, there is no convincing theory, however, that adequately explains the observed vertical profiles of photosynthesis capacity and solar radiations.

The parameters that control the shape of temperature function of photosynthesis capacity (a_{Q10}) are mostly increased to represent the steeper diurnal cycles of photosynthesis. The function of temperature dependency of photosynthetic capacity mimics the Q10 function and thermal breakdown of metabolic processes [*Collatz et al.* 1991]. These kinetic properties significantly vary in different plant species, and they have been subject to much study [*Woodrow and Berry* 1988]. The intrinsic difficulty in any LSM is to deal with the bulk representation of plant physiology, including the over- and

under-story of different plant species. Thus, the bulk plant kinetic properties, and other uncertain parameters, must be estimated through nonlinear inversion theory.

Canopy roughness lengths (z_{can}) are largely reduced after the calibration in order to remove the sensible/latent heat flux and LST biases in the ULM. There are three aerodynamic resistances that control surface energy fluxes; including z_{can}, soil-surface roughness length, and leaf-surface roughness length (see Appendix B). Although simultaneous optimization of these three aerodynamic resistances could ease the extreme reduction in z_{can}, soil- and leaf-surface aerodynamic roughness lengths were not calibrated for the sake of simplicity in the optimization process. Indeed, uncertainties in canopy roughness length and canopy heat capacity still remained in the post calibration experiment. For example, in the evergreen needleleaf forest sites (*Niwt*, *Meto*, and *Wind*), the ULM-predicted daytime available heat flux ($E+H$) is underestimated at *Niwt*, overestimated at *Wind* site, and very close to the observations at *Meto* site (Figure 7.4). The tendency of biases is anti-correlated to the canopy height (*Niwt*=11.5m, *Meto*=34m, and *Wind*=60m), which indicates that the canopy heat capacity should be parameterized as a function of canopy height. However, at present, there are no large-scale canopy-height and canopy-density maps available for boundary conditions of LSMs. The cancellation of the Vegetation Canopy Lidar (VCL) mission [*Dubayah et al.* 1997] prevented the community of this valuable observation, including a global-scale 5km map of canopy structure, height and density. Canopy height and density are also essential for the modeling of highly heterogeneous landscapes, such as croplands and grasslands. The large spreads of scatter of LST biases in these two classes (Figures 7.3b and 7.5b) are mostly due to the subgrid heterogeneity; i.e., those classes contain some small portions of

tree and other plant species [*Hansen et al.* 2000]. While the continental-scale calibration can remove the basic biases in surface energy and flux, further reductions in grid-by-grid energy flux errors require the large-scale high-resolution map of canopy structure, height and density [*Dubayah et al.* 1997].

Although there are some aforementioned uncertainties in the performance of ULM, the overall result is a significant reduction in errors. The total error (weighted sum of squared error: Ψ) has been reduced by about 57% from the pre-calibration experiment ($\Psi=5.97\times10^6$) in the calibrated period. When the same set of experiment are applied for May-September 2001 period by using pre- and post-calibrated tuning parameters, the post-calibration experiment reduced Ψ by about 53% from the pre-calibration experiment ($\Psi=5.96\times10^6$). Thus, the approximately same order of improvement was achieved for the non-calibrated period. This robust improvement is similar to the previous continental-scale albedo-calibration study in *Matsui et al.* [2006].

7.4. Sensitivity of Sunlit-Shaded Model to Aerosol Loading

7.4.1 Methods

Using the improved confidence in and accuracy of the sun-shade canopy model (ULM), this section examines sensitivity experiments for aerosol diffuse-radiation effects (ADE) on the regional scale. Simulation periods and study area are consistent with the calibration study (section 3), which extended from May 1 to September 30 in 2000 and 2001 over the eastern U.S. Figure 7.6 shows seasonally averaged satellite-model assimilated daily aerosol optical depth (AOD) [*Matsui et al.* 2004]. Highest AODs

(~0.32) appear around Lake Erie and Chesapeake Bay, and gradually decrease toward the outside of the domain down to 0.1. Distribution patterns and magnitude of AODs appear to be quite similar in 2000 (m=0.191) and in 2001 (m=0.190). Figure 7.6 also shows seasonally averaged daily cloud optical depth (COD), which is inversely derived from NLDAS shortwave radiation (see Appendix D). CODs become larger toward the northeastern portion of the domain, and the domain-averaged value is nearly twice as high in 2000 (m=10.82) as in 2001 (m=5.995).

Solar radiation is computed from inversely derived cloud optical depth (COD), vertical profiles of pressure, temperature, humidity, and ozone concentrations from sounding climatology [*McClatchey et al.* 1972] and NCEP/NCAR reanalysis [*Kalnay et al.,* 1996] with and without the assimilated daily AODs via NASA-Langley Fu-Liou radiative transfer model [*Fu and Liou* 1993, *Charlock et al.* 2004]. AODs are vertically profiled according to measurements in *Spinhirne et al.* [1980], which confine the aerosol extinction mostly to the boundary layer. Aerosol compositions are estimated from the chemical-transport model [*Chin et al.* 2004], and aerosol optical properties are based on the Optical Properties of Aerosol and Cloud (OPAC) values [*Hess et al.* 1998].

Sensitivity experiments with CSU ULM are conducted for shortwave radiation with (a control experiment: CTL) and without aerosol loading (a potential experiment: POT). Except for perturbation of shortwave radiation, CTL and POT experiments have the identical meteorological forcings, and boundary conditions (soil texture and LAI). Seasonally averaged differences (CTL-POT) in surface downwelling solar radiation (dSW) ranges from -22 to -13W/m^2 (Figure 7.6). The domain-averaged dSW is -14.9W/m^2 in 2000 and -16W/m^2 in 2001. Spatial patterns of dSW appear to be somewhat

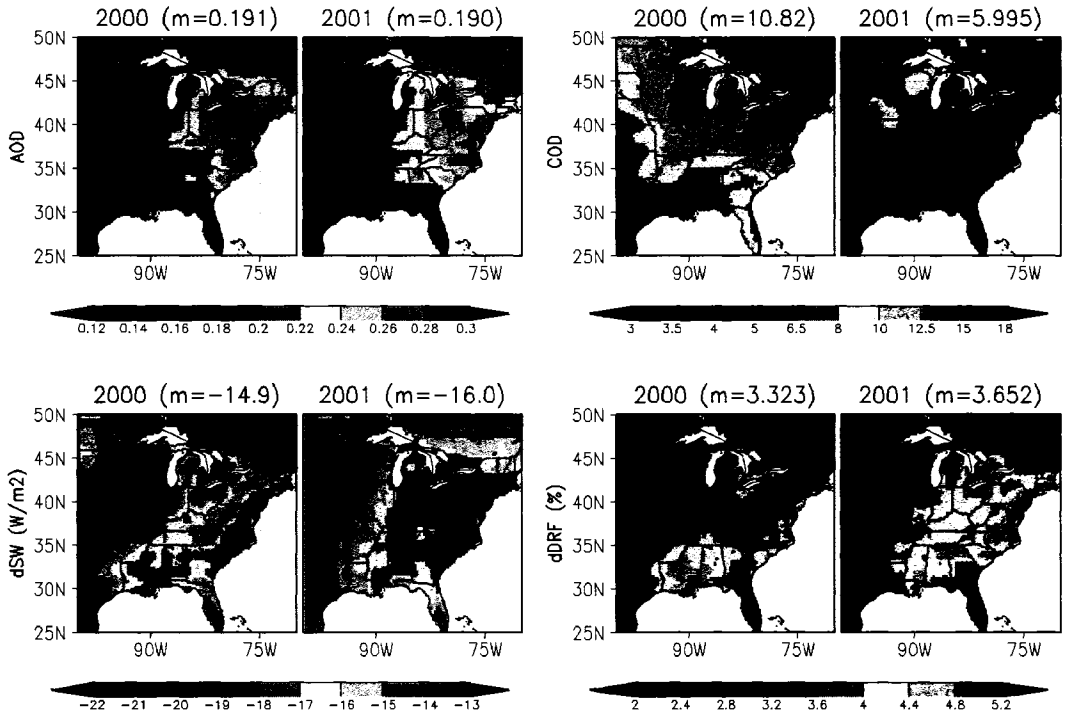

Figure 7.6. Seasonally averaged MODIS-GOCART assimilated aerosol optical depth AOD (0.55μm), inversely derived cloud optical depth (COD), differences (CTL-POT) in shortwave radiation (dSW), differences (CTL-POT) in diffuse radiation fraction (dDRF). *m* represents a domain-averaged value.

different from those of AODs. This is mostly due to distribution of COD and partly due to latitudinal trend in solar zenith angle. For example, dSW becomes smaller under thicker clouds due to the significantly reduced incoming solar radiation in the boundary layer. The increase in dSW simultaneously increases the diffuse radiation fraction (dDRF) according to the empirical separation of direct and diffuse radiation (see Appendix A). dDRF appears to be up to 5% around Lake Erie and Chesapeake Bay in 2001. Because of a combination of the high CODs and the small AODs, dDRF and dSW are suppressed over the northern portion of the domain, especially, in 2000. On the other hand, diffuse radiation is enhanced about 4% over the southeast U.S. in 2001 due to low

COD. For the whole domain, DRF has been increased approximately 3.5% by the routine aerosol loading (Figure 7.6).

7.4.2. Results

Figure 7.7 shows the spatial map of seasonal (May-September) net primary production ($NPP = \int A_{tot} dt$, where $A_{tot} = A_{tot} + A_{tot}$ (see Table 7.1)), seasonally-averaged daily (integrated over daytime diurnal cycle) surface latent heat flux (E), sensible heat flux (H), and land-surface temperature (LST) in the CTL experiments and the sensitivity experiments (CTL-POT).

The CTL experiment shows that the largest NPP (~1200g C/m^2) appeared over the deciduous broadleaf and mixed forests in U.S., while the smallest NPP exits in urban regions, which are scattered in the domain as tiny spots (the first row in Figure 7.7). NPP is also small in the western edge of the domain. Domain-averaged NPP is larger in 2000 (873.5g C/m^2) than in 2000 (787.0g C/m^2). This high NPP in 2001 is discernible over Canadian boreal forests regions. The sensitivity experiments (CTL-POT) show that aerosol loading increases the NPP up to +35 g C/m^2 (about 3% increases from the CTL experiment) in the southeast U.S. in 2000 and 2001. dNPP in Canadian boreal regions appear to be slightly positive (up to +14g C/m^2) in 2001, but slightly negative (down to -14g C/m^2) in 2000. dNPP appears to be negligible or slightly negative over the croplands and grasslands regions down to -14g C/m^2. Overall, plant productivity tends to be increased in forest regions of southeast U.S., while it has been slightly decreased in crop regions by the aerosol loading. Domain-averaged dNPP are -0.71gC/m^2 in 2000 and

+4.972gC/m^2 in 2001, which correspond to about -0.1% and +0.5% increases from the CTL experiment, respectively (the first row in Figure 7.7).

The CTL experiment shows large E (>160W/m^2) over the southern portion of the domain, while smallest E (down to 40 W/m^2) exists over Canadian boreal region, and is loosely coupled with the spatial distribution of seasonal NPP (the second row in Figure 7.7); i.e., the plant productivity and the transpiration are closely coupled via the equation (1) in Table 7.3 [*Ball et al.* 1987; *Collatz et al.* 1991]. The sensitivity experiments show that E is mostly decreased by aerosol loading over the croplands and grasslands down to -6W/m^2. This is due to the contribution of bare-soil evaporation, which represents a high fraction of total evaporation in low LAI LULC classes, such as grasslands and croplands. On the other hand, dE is mostly negligible over the mixed forests and deciduous broadleaf forests in the southeast U.S. and the Canadian boreal region. Domain-averaged dE are slightly negative in 2000 (-3.10W/m^2) and in 2001 (-3.12W/m^2) (the second row in Figure 7.7).

The CTL experiment shows that H is highest over the mixed and needleleaf forest in Canadian boreal region and deep-south of U.S. (the third row in Figure 7.7). Domain-averaged H (58.69W/m^2 in 2001 and 73.78W/m^2 in 2001) are approximately 50% of E. There are low-H regions in the vicinity of these two highest H regions. Domain-averaged total available energy (H+E) is greater in 2001 (218.9W/m^2) than that in 2000 (191.5W/m^2) due to less cloud cover in 2001 (Figure 7.6). Sensitivity of H to the aerosol loading (dH) is almost negative over the whole domain down to -12W/m^2, and domain-averaged dH is -7.57 W/m^2 in 2000 and -8.36W/m^2 in 2001, all of which are much greater than those of dE. This means that the aerosol loading tends to reduce surface

sensible heat flux more than latent heat flux due to the increased photosynthesis in some regions. Spatial patterns in lowest dH (dark purple regions) is coherent to the regions that have near-zero (white regions) dE, including the mixed and deciduous broadleaf forest in the southeast U.S. and Canadian boreal region (the third row in Figure 7.7).

The CTL experiment shows that LST peaks in the southwest edge of the domains (up to 308K), and is decreased toward the northern edge of the domain (down to 290K) (the forth row in Figure 7.7). Northern boreal regions have lower LST in 2000 than in 2001 probably due to the thick cloud cover in 2000 (Figure 7.6). Similar to the dH, dLST are almost negative over the entire domain. The highest sensitivity (i.e., the lowest value in dLST) appears to be in the east coast down to -0.5K. The extensive negative dLST explains why dE appears to be neutral over some forest regions, in spite of increase in NPP. Reductions in leaf temperature due to reduced surface downwelling solar radiation

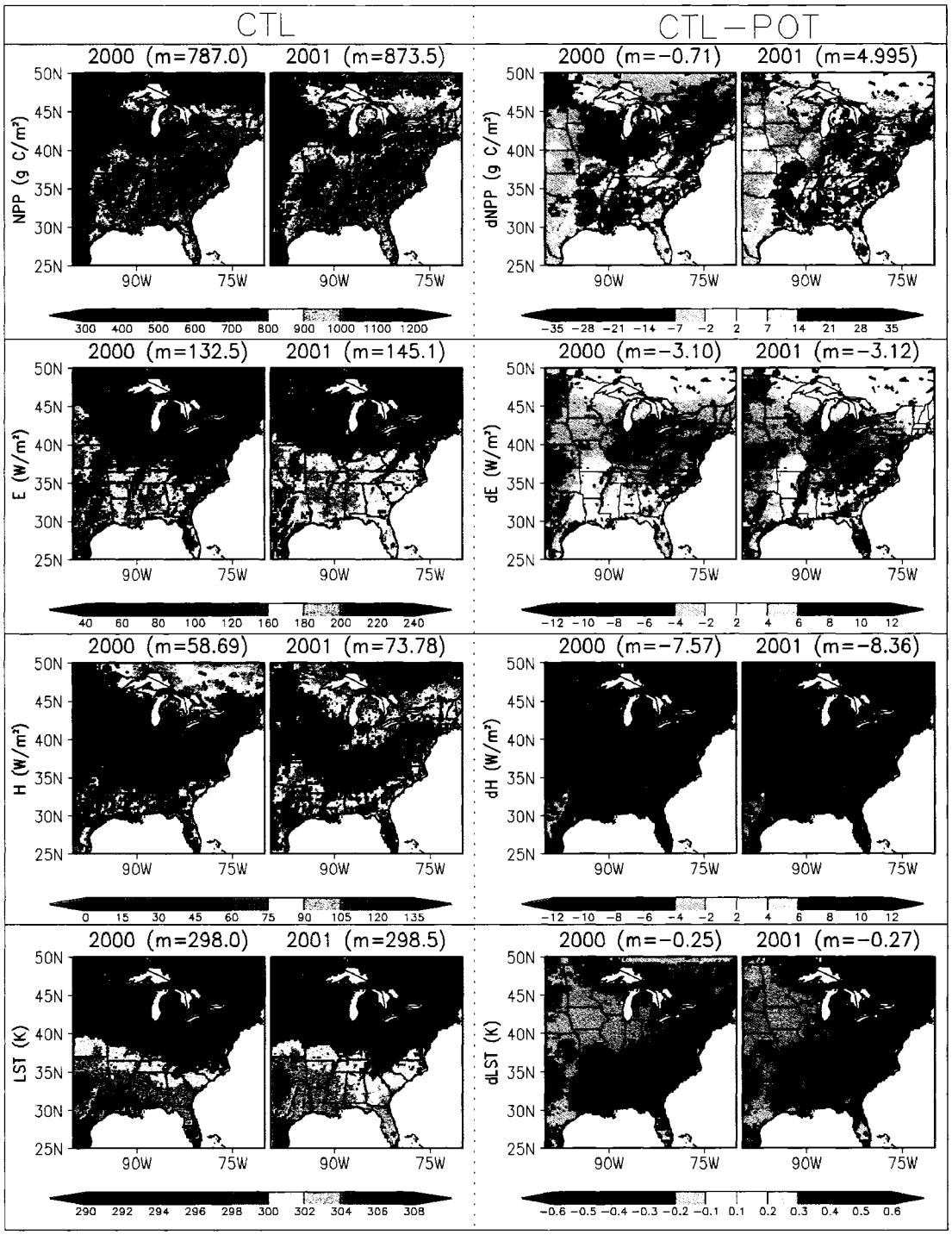

Figure 7.7. Seasonally averaged control (CTL) and sensitivity (CTL-POT) values of net primary production (NPP), latent heat flux (*E*), sensible heat flux (*H*), and land-surface temperature (LST). Note that LST, *H* and E are values integrated over daytime diurnal cycle. *m* represents a domain-averaged value.

decrease within-leaf vapor mixing ratio, which reduces the gradient in vapor mixing ratio between leaf and canopy air. However, canopy photosynthesis and resultant stomatal conductance has been increased by aerosol loading. Thus, increased stomatal conductance and decreased gradient in vapor mixing ratio compensate each other, resulting in the neutral dE (the forth row in Figure 7.7).

Figure 7.8a shows the seasonal cycles of monthly dNPP averaged over the entire domain, deciduous broadleaf forests, mixed forests, and croplands. Domain-averaged dNPP are negative in May 2000 and 2001; they are gradually increased and peaked in July to August; and are decreased in September. The seasonal cycle of dNPP in 2001 is much greater than in 2000. Especially, deciduous broadleaf forests and mixed forests have much larger values of dNPP in August 2001 (+7.135g C/m^2 and +5.049g C/m^2, respectively) than in August 2000 (+1.483g C/m^2 and +1.701g C/m^2, respectively). Croplands consistently have negative dNPP throughout the seasons, except in August 2001 (+1.184g C/m^2).

Figure 7.8b shows the daytime diurnal cycle of sensitivity of total (sunlit plus shaded) canopy photosynthesis (dA_{tot}) to aerosol loading averaged over the entire domain, deciduous broadleaf forests, mixed forest, and croplands. Diurnal cycles of domain-averaged dA_{tot} peaked at 18Z (+0.156μmol/m^2/s in 2000 and +0.297μmol/m^2/s in 2001), and have the lowest values in early morning (at 12Z) and late afternoon (at 24Z), namely when the solar zenith angle is close to 90°. Although all three LULC classes have similar diurnal cycles, their magnitudes, especially noon-time peak values, are quite different each other. Deciduous broadleaf forests have the largest noon-time peak values of dA_{tot} (+0.306μmol/m^2/s in 2000 and +0.659μmol/m^2/s in 2001), and most of dA_{tot} are positive

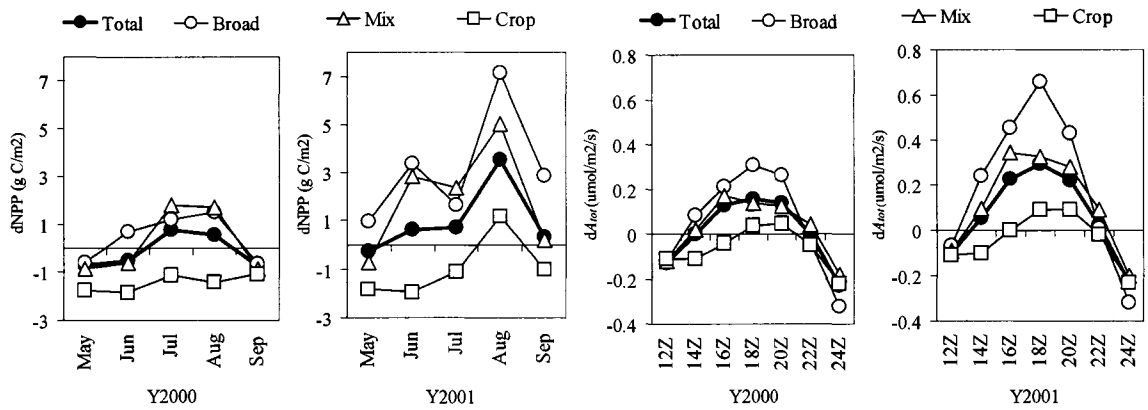

a) b)

Figure 7.8. a) Seasonal cycles of sensitivity of NPP (dNPP) to the aerosol loading. b) Daytime diurnal cycles of sensitivity of total-canopy photosynthesis (dA_{tot}) to the aerosol loading. Values are averaged over the entire domains, deciduous broadleaf forests, mixed forests, and croplands.

throughout the daytime diurnal cycle. The diurnal cycle of mixed forests is quite similar to the domain-averaged one. On the other hand, croplands have the smallest noon-time peak values of dA_{tot} (+0.046μmol/m^2/s in 2000 and +0.091μmol/m^2/s in 2001), and dA_{tot} values are almost negative throughout the daytime diurnal cycle. As a result, it causes seasonal reductions in NPP over croplands are seen in Figures 7.8a and 7.7. There are one-hour differences in the timing of the peak dA_{tot} among three LULC classes. This is simply explained by the longitudinal locations of these LULC classes; e.g., most of the croplands are located in the western portion of the domain, while most of the mixed forests are located in the middle-to-eastern portion of the domain. Thus, the croplands have the one-hour-late diurnal peak, while the mixed forests have the one-hour-early diurnal peak.

The first row in Figure 7.9 shows responses of sunlit- and shaded-canopy photosynthesis (dA_{sun} and dA_{sha}) to aerosol loading at 18Z, when the ADE becomes most

productive (Figure 7.8b). Sunlit-canopy photosynthesis (A_{sun}) is increased in the southern portion of the domain, while it is decreased in the northern portion especially in 2000 (Figure 7.10). In comparison with dA_{sun} (0.019μmol/m^2/s in 2000 and 0.071μmol/m^2/s in 2001 for domain averaged values), the magnitude of increases in shaded-canopy photosynthesis (dA_{sha}) appears to be more extensive in the domain (0.133μmol/m^2/s in 2000 and 0.220μmol/m^2/s in 2001 for domain averaged values). Thus, it is concluded that aerosol loading mechanically enhances the shaded-canopy photosynthesis, which mostly lead to higher plant productivity over the forest regions in ULM.

The second row in Figure 7.9 also shows scatter plots of changes in sunlit- and shaded-canopy-scaled rubisco-limited carbon assimilation rate (dW_v) and light-limited carbon assimilation rate (dW_J), as linked to changes in sunlit- and shaded-canopy photosynthesis (dA_{sun} and dA_{sha}). In definitions (Table 7.2), light-limited (W_J) and rubisco-limited rates (W_v) are essential factors that control canopy photosynthesis rate. Generally, an increase in absorbed solar energy in canopy linearly elevates the W_J (equation 4 in Table 7.2). However, this linear increase of W_J can be impeded by the limitation of the photosynthesis capacity (W_v) (equation 3 in Table 7.3). The scatter plots demonstrate that the variability of dA_{sun} at 18Z is linearly correlated with variability of dW_v (r=0.983 in 2000 and r=0.988 in 2001), while the dW_J is less correlated with canopy photosynthesis; i.e., sunlit-canopy photosynthesis is in rubisco-limited environment. On the other hand, variability of dA_{sha} is strongly correlated with variability of dW_J (r=0.909 in 2000 and r=0.907 in 2001), while variability of dW_v does not explains the variability dA_{sh}; i.e., shaded-canopy photosynthesis is in a light-limited environment. This is the fundamental mechanism of how sunlit- and shaded-canopy photosynthesis responds to

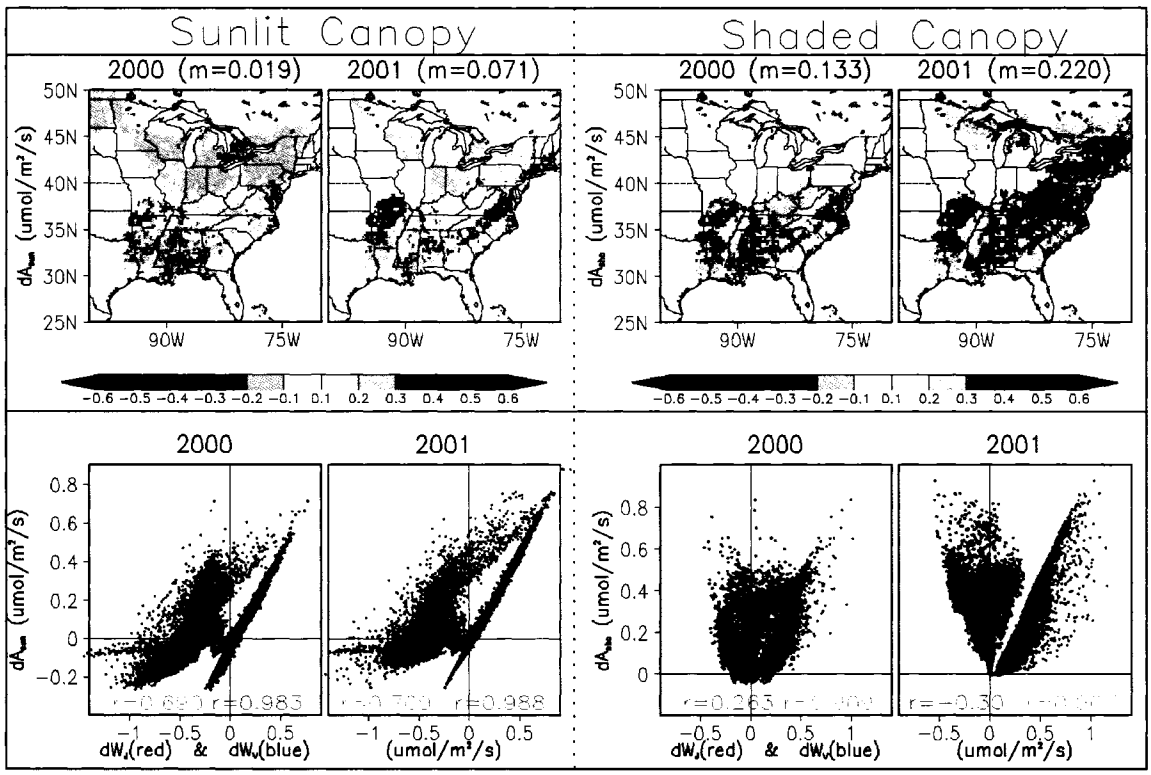

Figure 7.9. Sensitivity (CTL-POT) of sunlit- and shaded-canopy photosynthesis (dA_{sun} and dA_{sha}) to the aerosol loading at 18:00Z, and scatter plots between each canopy photosynthesis and corresponding light-limited carbon assimilation rate (dW_J) and rubisco-limited carbon assimilated rate (dW_V) . Note that W_J and W_V are scaled for sunlit- or shaded canopy. *m* represents a domain-averaged value. *r* represents a linear correlation coefficient.

the light environment around noon. Close to sunrise or sunset both sunlit- and shaded canopy are in light-limited environment (not shown).

With a given spatio-temporal heterogeneous distribution of ADE (Figures 7.7 and 7.8), the simulated variability of ADE is linked to the several factors. One is clearly the solar zenith angle that dominantly controls diurnal cycle of ADE (Figure 7.8b). However, the solar zenith angle does not explain the spatial, seasonal, and inter-annual variability of ADE as seen in Figures 7.7 and 7.8a. Figure 7.10 shows the scatter plots of normalized ADE (here, defined as a increase in total-canopy photosynthesis per unit

AOD ($dA_{tot}/dAOD$)) as linked to different factors, including cloud optical depth (COD), aerosol optical depth (AOD), leaf area index (LAI), and 10m-above-canopy atmospheric temperature (T_{atm}). Effects of COD and AOD on the ADE were demonstrated by the simulation study in *Cohan et al.* [2002]. Temperature effect was suggested by *Krakauer and Randerson* [2003]. Variability of LAI should be important to determine the amount of shaded-canopy LAI. The scatter plots are further clustered for deciduous broadleaf forests, mixed forests, and croplands in all-sky and clear-sky conditions. Linear correlation coefficients for all scatter plots in Figure 7.10 are depicted in Table 7.5.

First, the effects of COD are shown in all-sky conditions (the first row in Figure 7.10). For the entire domain, variability of normalized ADE declined from low COD to high COD, particularly in 2000 (r=-0.43). In 2001, the correlation between COD and ADE is very small (-0.04), because of the low variability of COD (<10). When clustered for different LULC classes, COD effects even better explain the ADE. Especially, COD effects in mixed forests have linear correlations of -0.93 in 2000 and -0.82 in 2001. Note that two separated clusters of scatter plots in mixed forest indicate separate locations of the mixed forests class, in Canadian boreal regions or southern U.S. (Figure 7.2). Overall, COD has consistent and strong negative effects on normalized ADE for individual LULC class.

Second, the effects of AOD are examined in clear-sky conditions, since they could be overwhelmed by the strong COD effects in all-sky conditions (the first row in Figure 7.10). Overall, AOD effects on the normalized ADE tend to be small and inconsistent for the whole domain and each LUCL class. Scatter plots and correlation coefficient values suggest positive correlations between normalized ADE and AOD, but

the relation does not hold for deciduous broadleaf forest (r=-0.37 in 2000 and r=-0.52 in 2001) and croplands (r=-0.11 in 2001). This is the examination for the normalized ADE. In clear-sky conditions, changes in total-canopy photosynthesis (dA_{tot}) have a linear correlation with the changes in AOD (dAOD) (not shown).

Third, the effects of LAI are examined in all-sky and clear-sky conditions (the second row in Figure 7.10). Scatter plots show the apparent positive correlations between LAI and normalized ADE for the entire domain in 2000 and 20001. The correlations are stronger in clear-sky conditions (r=0.703 in 2000 and r=0.832 in 2001) than those in all-sky conditions (r=0.487 in 2000 and r=0.756 in 2001), because the strong COD effects impede these correlations in all-sky conditions. Unlike for the entire domain, LAI does not well explain the variability of normalized ADE for the individual LULC class. The correlations tend to be relatively small, and often become negative (Table 7.5). The exception is the scatter plots of the mixed forests, which tend to have high correlations (0.496~0.761) for all years and all conditions.

Finally, the effects of T_{atm} are examined in all-sky and clear-sky conditions (the third row in Figure 7.10). For the entire domain, correlations appear to be low (excepting all-sky conditions in 2000), and the scatter plots appears to be triangular-shaped and clustered. For the individual LULC class, the T_{atm}-ADE correlations appear to be very high especially for all-sky conditions in 2000 (up to 0.937 for mixed forests). Correlations become slightly lower than all-sky conditions in 2000 for the rest of the cases, in particular with clear-sky conditions. This is due to a combination of positive and negative correlations depending on the ranges of T_{atm}, which can be clearly seen in the scatter plots of croplands in clear-sky conditions in 2000. In the range of T_{atm} from 290K

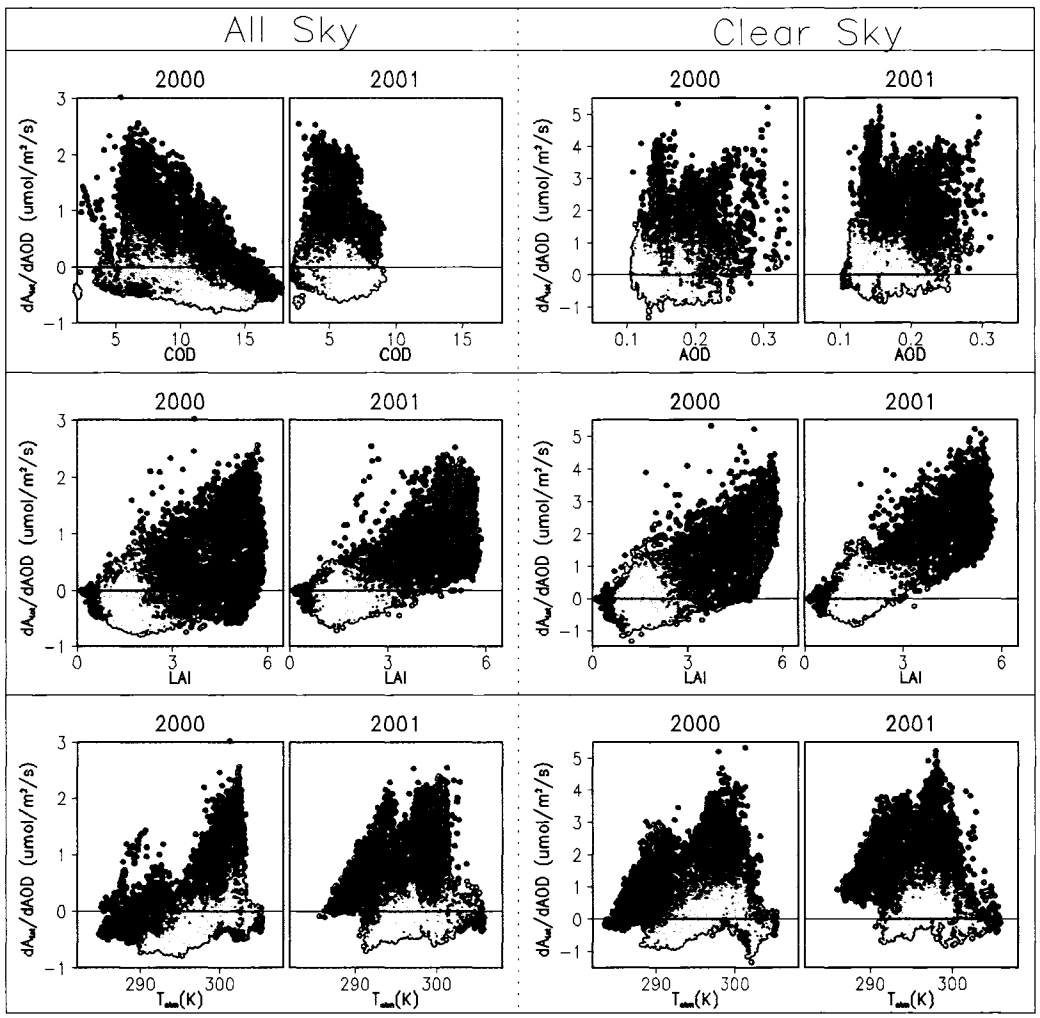

Figure 7.10. Scatter plots of seasonally averaged normalized aerosol diffuse-radiation effect (ADE, defined as $dA_{tot}/dAOD$) and different factors, including cloud optical depth (COD), aerosol optical depth (AOD), leaf area index (LAI), and 10m-above-canopy air temperature (T_{atm}). All variables are integrated over daytime diurnal cycle. The scatter plots are further clustered for deciduous broadleaf forests (green), mixed forests (red), and croplands (yellow) in all-sky and clear-sky conditions.

to 300K, normalized ADE is increased for higher T_{atm}. However, for T_{atm} higher than ~300K, additional increases in T_{atm} tend to decrease ADE. This relationship closely mimics the temperature function in photosynthetic capacity (equation 2.2.5 and Figure 7.1b).

conditions	all sky					
factor	COD		LAI		T_{atm}	
year	2000	2001	2000	2001	2000	2001
Total	-0.43	-0.04	0.487	0.756	0.47	0.062
Broad	-0.77	-0.64	0.241	-0.15	0.911	0.582
Mix	-0.93	-0.82	0.761	620	0.937	0.931
Crop	-0.73	-0.25	-0.24	0.045	0.752	0.392
conditions	clear sky					
factor	AOD		LAI		T_{atm}	
year	2000	2001	2000	2001	2000	2001
Total	0.384	0.353	0.703	0.832	0.117	0.19
Broad	-0.37	-0.52	0.422	-0.11	0.897	0.691
Mix	0.309	0.183	0.598	0.496	0.699	0.656
Crop	0.11	-0.11	0.033	0.317	0.427	0.215

Table 7.5. Linear correlation coefficients between the normalized aerosol diffuse-radiation effects (ADE) ($dA_{tot}/dAOD$) and different factors, corresponding to Figure 10.

To summarize, LAI is the most import factor that explains the whole-domain variability of normalized ADE, while the COD and T_{atm} are two critical factors that explain the variability of normalized ADE for the individual LUCL class. Although AOD is the basic driver for ADE, it appears to be an unimportant factor for the variability of normalized ADE.

7.4.3. Discussions

The sensitivity experiments shows that the plant productivity (measured as NPP) is increased by the aerosol loading over most of the forest regions, but is decreased over most of the croplands and grasslands (Figure 7.7). These results are consistent with the result for deciduous forests [*Gu et al.* 2002] and for croplands [*Chameides et al.* 1999]. The overall spatial distributions of the ADE are well explained by the variability of LAI (Figure 7.10 and Table 7.5); the LULC types with high LAI (such as forests) tend to have a large portion of shaded canopy, while the ones with low LAI (such as croplands and

grasslands) tends to have a small portion of the shaded canopy. Since the enhancement of shaded-canopy photosynthesis is the essential mechanism of the productive ADE (Figure 7.9), ADE became unproductive for low-LAI regions (Figure 7.7).

For the individual LULC class, variability of cloud optical depth (COD) appears to be the critical factor that controls the ADE. As the COD is increased, normalized ADE (defined as $dA_{tot}/dAOD$) is linearly decreased, and it becomes mostly negative for COD approximately higher than 15 (Figure 7.10). These relationships mostly explain the spatial variability of dNPP in Figure 7.7. Large differences exist in COD between 2000 and 2001 (Figure 7.6). The high COD in 2001 over the northern portion of the domain reduce the ADE down to -14g C/m^2 over the Canadian boreal forest, in comparison with positive ADE in 2001. This result is consistent with the findings in *Cohan et al.* [2002]; namely, NPP is increased by aerosol loading in clear-sky day, while it is decreased in cloudy days. In clear-sky days, aerosol loading clearly increased total canopy photosynthesis over most of the grid (Figure 7.10). Normalized ADE in clear-sky conditions is nearly twice (up to 5μmol/m^2/s per AOD) as high as that in cloud-sky conditions (Figure 7.10). As indicated in Figure 7.8b, if it is averaged only at 18:00Z, normalized ADE becomes even larger (up to 10μmol/m^2/s per AOD; not shown here), which are comparable to the observed normalized ADE at the Fluxnet sites over the eastern U.S. [*Niyogi et al.* 2004; *Chang* 2004].

Figure 7.10 shows that variability of 10m-above-canopy atmospheric temperature (T_{atm}) also explains the variability of the normalized ADE for individual LULC class. The normalized ADE increased from the lowest to an optimum temperature, and decreased from the optimum temperature to the highest temperature. Thus, the low temperature in

the northern portion of the domain, such as Canadian boreal regions, created the canopy-photosynthesis environment susceptible to be affected by a reduction in temperature. This result is nearly consistent with the findings and speculation in *Krakauer and Randerson* [2003]. Their detailed analysis shows that the tree-ring-estimated NPP is slightly increased in temperate forest (30°-45°N) and decreased in boreal forest (45°-60°N and >60°N) after the eruption of Mt. Pinatubo. They also speculated that the reduction in NPP in boreal forest is regulated to low-temperature environment. In this study, mixed forests are distributed in southern U.S. and Canadian boreal regions. Optimum temperature (T_{opt}) for photosynthesis capacity (equation 2.2.5) has been set at 307K for the mixed forests, which correspond to the seasonally-averaged daily LST in southern U.S. (Figure 7.7). On the other hand, seasonally averaged LST ranges from 294K to 300K in the Canadian boreal regions. Thus, the reductions in canopy temperature trigger equation 2.2.5 that reduces the canopy photosynthesis capacity. For gaining more confidence on the temperature functions, additional investigation is required for the regionally dependent T_{opt} map rather than the flat values for each LULC class. Although the details are not examined here, seasonal variability of dNPP in Figure 7.8a could be explained by variability of LAI, COD, and T_{atm}, in addition to the basic driver, AOD. Especially, AOD, LAI and T_{atm} are usually peaked in the middle of summer, which also corresponds to the seasonal peak of dNPP.

Figure 7.9 demonstrates the importance of the diurnal cycle, namely solar zenith angle, for the ADE. *Gu et al.* [2002], *Niyogi et al.* [2004], and *Chang* [2004] focused on their statistical sampling from local 10:00am to 2:00pm, which corresponded to 16Z to 20Z in this domain. During this period, ADE becomes most productive, because the light-

saturated sunlit-canopy photosynthesis is generally unaffected by aerosol-driven reductions in direct radiation (Figure 7.9). On the other hand, ADE impede plant productivity during other periods (before16Z and after 20Z), because both sunlit- and shaded-canopy photosynthesis are in light-limited environment. In addition, diurnal cycles of temperature also could accelerate the diurnal cycles; i.e., the noon-time peak of canopy temperature can enhance the normalized ADE, and vice versa in the early morning or evening. One remarkable finding is that the aerosol loading can increase the amplitude of daytime diurnal cycle of carbon sink. This may have important implications for the carbon cycle community.

Overall understandings of the mechanistic response of plant productivity to aerosol loading in the mechanistic sun-shade model are shown in the flow chart (Figure 7.11). It should be noted that changes in plant productivity (i.e., photosynthesis) can modify the latent heat flux and leaf temperature, which feedback to the light-

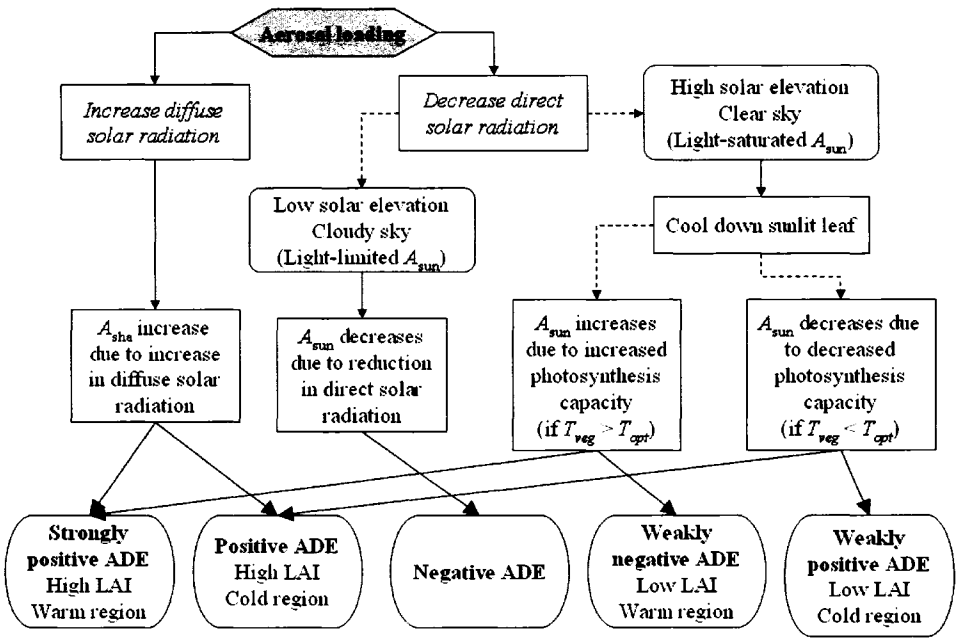

Figure 7.11. A flow chart of the mechanistic response of plant productivity to aerosol loading.

saturated photosynthesis rate. However, these feedback processes are secondary, and are omitted from the flowchart for simplicity.

7.5. Summary

This study developed and calibrated a sun-shade canopy model against the extensive datasets of satellite and eddy covariance measurements on the regional scale, and examined the sensitivity of plant productivity and surface energy to variability of diffuse radiation due to aerosol loading, using a well-calibrated sun-shade canopy model. The sun-shade canopy model was developed in the Colorado State University (CSU) Unified Land Model (ULM) within the NASA GSFC Land Information System (LIS) [*Matsui et al.* 2006, *Kumar et al.* 2006]. ULM is run at 0.25° grid space, and is driven by the North American Land Data Assimilation System (NLDAS) meteorological forcing with a 15-minute model time step [*Cosgrove et al.* 2003]. Diffuse radiation is estimated from the broadband solar radiation as a function of global irradiance and extraterrestrial global irradiance.

This study used a similar set of equations [*De Pury and Farquhar* 1997; *Wang and Leuning* 1998; *Dai et al.* 2004] to incorporate a sun-shade canopy model in ULM and critical tuning parameters are optimized against the MODIS land-surface temperature (LST) and data from eleven Fluxnet sites. These tuning parameters are essentially related to the aerodynamic and stomatal resistance terms. Before optimization, ULM extensively underestimates the LST up to 15K in comparison with MODIS product, and ULM poorly predicts the CO_2 and surface heat fluxes in comparison with the Fluxnet observations.

Manual tuning and Gauss-Maquardt-Levenberg automatic tuning are used to constrain the parameters values. Main results of the calibration are significant reductions in canopy roughness lengths (z_{can}) that suppress turbulent heat fluxes, a reduction in the parameter for the unsaturated-soil RH (b_{soil}) that reduces the bare-soil evaporation, the large adjustment of parameters for the temperature control on photosynthesis capacity (a_{Q10}) in the broadleaf forest, mixed forest, and croplands that improved the representation of the sharp descends and rises in daytime diurnal cycle and generated more realistic seasonal patterns in CO_2 flux.

After the calibration, ULM predicted the daytime LST very close to the uncertainty level of MODIS LST product [*Wan et al.* 2004], and diurnal as well as seasonal cycles of surface CO_2 and surface heat fluxes in ULM were in better agreement with those from the Fluxnet observations. This validation demonstrated the significant improvement of ULM for the non-calibrated period (May-September 2001). Light-use efficiency was also improved significantly, and this gives credibility to the use of the ULM to examine the aerosol diffuse-radiation effect (ADE) on terrestrial productivity and energy budget over the continental-scale.

With the well-calibrated sun-shade canopy model, ADE are examined over the eastern U.S. for May-September seasons in 2000 and 2001. All-sky aerosol direct radiative forcing (ADRF) was computed from the satellite-model assimilated daily AODs and inversely derived cloud optical depth (COD) via NASA-Langley Fu-Liou radiative transfer model [*Fu and Liou* 1993, *Charlock et al.* 2004]. Sensitivity experiments were conducted for all-sky conditions with and without the satellite-model assimilated AODs, which corresponds to a control (CTL) and potential (POT) experiment, respectively.

The sensitivity experiments (CTL-POT) showed that aerosol loading increases the NPP up to 35 g C/m^2 in the mixed forest and deciduous broadleaf in the southeast U.S. in 2000 and 2001. ADE on NPP appears to be negligible or slightly negative over the croplands and grasslands regions down to -14g C/m^2. For the whole domain, aerosol loading slightly decreased latent heat flux (-3.10W/m^2 in 2000 and -3.12W/m^2 in 2001), sensible heat flux (-7.57W/m^2 in 2000 and -8.36W/m^2 in 2001), and LST (-0.25K in 2000 and –0.27K). These reductions are spatially heterogeneous due to the irregular response of photosynthesis and stomatal conductance for different landscape.

Detailed examinations revealed that the spatial distribution of normalized ADE in the domain is well explained by the variability of LAI, because the amount of LAI mostly determines the shaded-fraction LAI. For the individual LULC class, COD and 10m-level atmospheric temperature (T_{atm}) appeared to be important factors that control the variability of normalized ADE. ADE becomes most productive around noon, because the light-saturated sunlit-canopy photosynthesis is generally unaffected by aerosol-driven reductions in direct radiation. On the other hand, ADE impedes plant productivity close to the period of sunrise and sunset, because both sunlit- and shaded-canopy photosynthesis are in light-limited environment. To summarize, aerosol loading is most productive for high LAI, optimum temperature, and high solar elevation in clear-sky conditions, and is least productive for low LAI, low temperature under cloud-sky conditions in early morning or late afternoon.

On the regional-scale estimate, plant productivity changed by only +0.5% in 2001 and –0.09% in 2000. As shown in Figure 7.8 and Figure 7.10, ADE becomes most productive around noon in clear-sky conditions. Previous observations studies [*Gu et al.*

2002; *Niyogi et al.* 2004; *Chang* 2004] focused on their statistical sampling namely in the most productive time period. However, when the effects were integrated over the diurnal cycle and cloudy-sky conditions, aerosol loading tends to have relatively weak effects on the terrestrial plant productivity [*Cohan et al.* 2002; *Krakauer and Randerson* 2003].

Uncertainties of regional estimate of ADE include the poor treatment of croplands in terms of the number of species. This issue must be improved not only for examination of ADE, but also for general coupled land-atmosphere models. At present, satellite-derived LULC map typically contains single croplands class, but there are extensive diversity of crop species and agricultural management in the real world. Thus, an up-to-date 1km-grid crop map is needed on the regional to global scale. An additional uncertainty is the spatial distribution of temperature functions of photosynthesis capacity. This study used eleven different Fluxnet sites for constraining the tuning parameters. More and more sites should be incorporated in a future study, particularly sites for LULC classes that were not calibrated in this study. A more comprehensive set of calibration sites should provide additional insight to the spatial distribution of temperature functions of photosynthesis capacity.

Appendix A: Estimation of Diffuse Radiation from Global Irradiance from ISIS observations

A sun-shade canopy scheme requires the proper separation of solar radiation into diffuse and beam components [*Gu et al.* 2002]. The NLDAS downwelling solar radiation is produced by the University of Maryland from NOAA's Geostational Operational

Environmental Satellites (GOES) [*Pinker et al.,* 2003]. Current products provide the broad-band (beam and diffuse) downwelling solar radiation at every 1-hour period.

Diffuse radiation fraction, DRF (R_d/R_g, where R_d is diffuse solar irradiance and R_g is total global irradiance at the surface), is often estimated from the transmittance (R_g/R_{ext}, where R_{ext} is extra-terrestrial global irradiance) [e.g., *Roderick* 1999]. *Roderick* [1999] used a step-wise linear function to fit the DRF and transmission with daily and monthly averaged insolation data. This study used the Integrated Surface Irradiance Study (ISIS): NOAA surface-based solar monitoring programs, which provides instantaneous surface radiation data, including direct and diffuse at broad band and PAR band with consistency, and accuracy based on reference standards maintained at levels better than 1% at nine different sites in the U.S. [*Hicks et al.* 1996]. Nine ISIS sites are chose from the conterminous U.S.

A total of 42,961 instantaneous radiation observations and binned averaged values from every site are compiled in the scatter plots (Figure A1a). Patterns of averaged DRF values appear to be close to the step-wise function in *Roderick* [1999]. Unlike the linear step-wise function, derived value shows the slight decrease in DRF for 0.05 ~ 0.3 of transmittance. On the other hand, lowest peak of DRF is at 0.8 of transmittance, which is consistent to the results in *Roderick* [1999]. The variability of DRF is further investigated as a function of cosine of solar zenith angle (u). Figure A1b clusters the relationship into the eight different class of u. There is smooth transition of DRF-transmission function from low to high class of u. For high u, DRF are constantly high for low transmittance range (~0.3), and DRF decrease rapidly for higher transmittance (0.4~0.8), and becomes the lowest DRF for 0.85 of transmittance. As the u_0 decrease, the lowest DRF values

slightly increases, being highest for $u = 0.05$. This unique solar-angle dependence could explain the slight difference of the DRF-transmittance relationships in different studies discussed in *Roderick* [1999]: i.e., latitudinal difference and u_0 tendencies between the sites results in the slightly different DRF-transmission relationship.

In practice, the values in Figure A1b are utilized as a look-up table, to separate NLDAS shortwave radiation into the diffuse and beam radiation as a function of transmittance and solar zenith angle in the LIS.

Appendix B: leaf-level turbulent heat flux for sun-shade canopy model

The aerodynamic resistances to heat and moisture transfer between leaves and

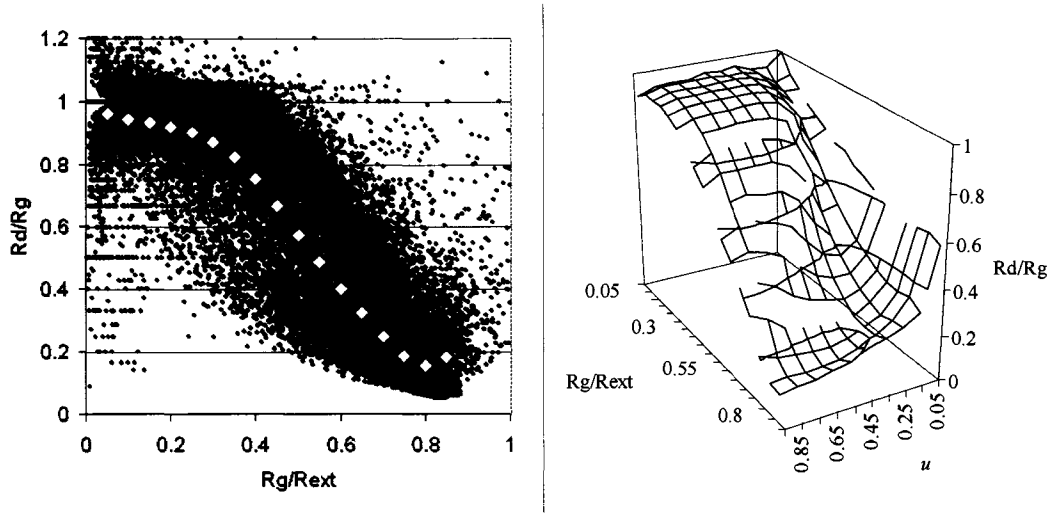

Figure A1. a) Diffuse radiation fraction (DRF: Rd/Rg) as a function of transmittance (Rg/Rext). Small black-filled dots are instantaneous observation. White diamond dots are averaged diffuse radiation fraction for bins of transmittance. b) Diffuse radiation fraction (Rd/Rg) as a function of transmittance (Rg/Rext) and cosine of solar zenith angle (u).

canopy air at reference height are separately derived for sunlit and shaded components. If the drag area density is constant in the canopy profile (i.e., uniform canopy), relative wind speed decreases exponentially in the vertical profile of canopy [*Albini* 1981]. A profile of within-canopy wind speed ($u(x)$) is expressed as functions of wind speed at canopy top (u_{can}^{top}) and the cumulative leaf and stem area index (x); i.e., $u(x) = u_{can}^{top} e^{-k_u x}$. Based on this relationship, the wind speed at the canopy top can be derived from the bulk canopy wind speed ($u_{can} = u^*$).

$$u_{can}^{top} = u_{can}(L+S)k_u \Big/ \left(1 - e^{-k_u(L+S)}\right) \qquad \text{(B.1)}$$

because u_{can} is defined as $u_{can} = \int_0^{L+S} u_{can}^{top} e^{-k_u x} dx \Big/ \int_0^{L+S} e^{-x} dx$. k_u is the extinction coefficient for within-canopy wind speed (= 1). Using u_{can}^{top}, bulk sunlit- and shaded-canopy wind speed (u_{sun} and u_{sha}, respectively) and can be scaled from the profile of sunlit (or shaded) leaf fraction and within-canopy wind.

$$u_{sun} = \frac{\int_0^{L+S} u_{can}^{top} e^{-k_u x} e^{-kx} dx}{\int_0^{L+S} e^{-kx} dx} = \frac{u_{can}^{top}\left(\dfrac{1 - e^{-(k_u+k)(L+S)}}{k_u + k}\right)}{f_{sun}(L+S)} \qquad \text{(B.2a)}$$

$$u_{sha} = \frac{\int_0^{L+S} u_{can}^{top} e^{-k_u x}(1 - e^{-kx})\, dx}{\int_0^{L+S} (1 - e^{-kx})\, dx} = \frac{u_{can}^{top}\left\{\left(\dfrac{1 - e^{-k_u(L+S)}}{k_u}\right) - \left(\dfrac{1 - e^{-(k_u+k)(L+S)}}{k_u + k}\right)\right\}}{f_{sha}(L+S)} \qquad \text{(B.2b)}$$

The aerodynamic resistances for sunlit (r_{b_sun}) and shaded (r_{b_sha}) vegetation are

$$r_{b\_sun} = 200\sqrt{d_{leaf}/u_{sun}} \tag{B.3a}$$

$$r_{b\_sha} = 200\sqrt{d_{leaf}/u_{sha}} \tag{B.3b}$$

where d_{leaf} is a characteristic leaf dimensionless length (*a common tuning parameter*).

The aerodynamic resistances to heat and moisture transfer between the ground and the canopy air at reference height depends on LAI and friction velocity (u^*) [*Zeng et al.* 2004].

$$r_{b\_soil} = 1/\left\{\left(D_{dense} + (D_{soil\_bare} - D_{dense})e^{-k_u(L+S)}\right)\cdot u^*\right\} \tag{B.4}$$

where k_u is an extinction coefficient of within-canopy turbulence (= 1, which is the same parameter in equation 2.2.1), D_{dense} is a drag coefficient for dense canopy (= 0.004), and D_{soil_bare} is a bare-soil drag coefficient given by

$$D_{soil\_bare} = \frac{k_{VK}}{a}\left(\frac{z_{soil}\,u^*}{c}\right)^{-0.45} \tag{B.5}$$

where k_{VK} is the Von-Karman constant (=0.4), a is 0.13, c is a kinematic viscosity ($=1.5\times10^{-5}$), z_{soil} is the roughness length for soil surface (*a common tuning parameter*) [*Zeng et al.* 2004].

Appendix C: Model LST consistent with Satellite-observed LST

Since the LSM calibration using the satellite-derived LST is a difficult task, the consistent LST in the ULM must be defined to the satellite-derived LST. Tera-MODIS sensor observes the LST within the wide viewing angle at around local 11:00 am. *Pinheiro et al.* [2005] showed that the Advanced Very High Resolution Radiometer (AVHRR) LST tends to observe canopy temperature for large satellite view angle, while it tends to observe both canopy and ground temperature on nadir view. This is because of the effect of clumping and 3-D structure of sparse canopy. Grid-scale LST is expressed as a weighted sum of vegetation (T_v) and ground (T_g) temperature.

$$LST_{sat} = f_{veg}(\varphi)T_v + (1 - f_{veg}(\varphi))T_g \qquad \text{(C.1)}$$

, where $f_{veg}(\varphi)$ is vegetation fraction that depends on satellite-view-angle. This study utilizes the extinction coefficient (k_φ) of within-canopy energy penetration in TCRT for quosi-black leaf and angle of energy penetration of φ. Thus, $f_{veg}(\varphi)$ depends on the total leaf and stem area index and LULC-dependent leaf angle distribution function that determines k_l.

$$f_{veg}(\varphi) = 1 - \exp(-k_\varphi (L+S)) \qquad \text{(C.2)}$$

In the above equation, the $f_{veg}(\varphi)$ become larger for dense canopy and higher k_{φ}, value (for large φ).

Furthermore, T_v must be defined consistent to the sun-shade canopy scheme. Vegetation temperature for a cumulative leaf area (x) is a weighted sum of the sunlit and shaded vegetation temperature.

$$T_v(x) = e^{-kx} T_{v\_sun} + (1 - e^{-kx}) T_{v\_sha} \qquad \text{(C.3)}$$

e.g., for a canopy top (x = 0), $T_v(x)$ is represented by the sunlit vegetation temperature only, while $T_v(x)$ is represented by the shaded-vegetation temperature for the bottom of semi-infinite canopy. Thereby, the within-canopy extinction coefficient of satellite viewing angle (k_{φ}) is used to scale the canopy temperature consistent to sun-shaded canopy scheme and satellite viewing angle.

$$T_v = \frac{\int_0^{L+S} T_v(x) e^{-k_{\varphi} x} dx}{\int_0^{L+S} e^{-k_{\varphi} x} dx} \qquad \text{(C.4)}$$

The above mathematical expression incorporates the idea that the satellite tends to observe the upper-canopy temperature, which comprises more fraction of sunlit-vegetation temperature.

Appendix D: A simple retrieval of cloud optical depth from the GOES-derived surface downwelling shortwave radiation

This appendix briefly explains a simple retrieval of cloud optical depth (COD) and cloud liquid water path (CLWP) from the NLDAS surface downwelling shortwave radiation (*SW*). NLDAS *SW* is derived from GOES radiance [*Pinker et al.* 2003]. Since GOES-derived cloud properties (effective radius, CLWP) are not available for this temporal resolution, cloud properties needs to be estimated from broadband NLDAS *SW*. The goal of the algorithm is to derive the cloud properties that reproduce the realistic all-sky (clear + cloudy) downwelling shortwave radiation with and without aerosol loading through a radiative transfer code.

This simple retrieval uses the NASA Langley-version of the Fu-Liou code (NFL), which updated several components of the original four-stream correlated-k radiative transfer code [*Fu and Liou* 1993, *Charlock et al.* 2004]. The vertical profile of atmospheric temperature, water vapor mixing ratio, and ozone mixing ratio are derived from a mid-latitude summer climatological sounding [*McClatchey et al.* 1972]. Surface broadband albedo is set to 0.1.

A relationship between top-of-atmosphere (TOA: S_{TOA}) and surface downwelling shortwave radiation in clear sky (SW_{clear}) is given by the simple Beer's law

$$SW_{clear} = SW_{TOA}\, e^{-k_{clear}/u} \qquad \text{(D.1)}$$

, where k_{clear} is extinction coefficient of clear sky (absorption and Rayleigh scattering of molecular), u is cosine of solar zenith angle. For a given climatological vertical profiles

and surface albedo, variation of k_{clear} (therefore SW_{clear}) is explained by the forth-order of polynomial fit as a function of u, using NFL code.

$$k_{clear} = -0.7284u^4 + 1.7952u^3 - 1.5967u^2 + 0.7747u + 0.0027 \qquad \text{(D.2)}$$

Cloud radiative forcing is defined as

$$\Delta SW = SW_{cloudy} - SW_{clear} \qquad \text{(D.3)}$$

, where SW_{cloudy} is cloudy-sky surface downwelling shortwave radiation. ΔSW is also a function of cloud properties, if SW_{clear} is known as a *priori*. Because of the one broad-band of NLDAS *SW*, cloud properties are constrained as follows: i) cloud is in liquid phase (not ice phase); ii) cloud is distributed from 600mb to 800mb; iii) cloud fraction is unity; iv) cloud effective radius is 8μm (assuming continental cloud). For a given constrains, a relationship between ΔSW and cloud optical depth (COD) is derived for different u via NFL code (Figure D1a).

For a given relationship in Figure D1a, COD is inversely derived for a given u and NLDAS *SW* as follows.

1. Derive the difference between NLDAS *SW* and estimated SW_{clear} (using the equation D.3) for a given u by using the relationship in equation B.2.
2. If ΔSW is greater than ΔSW of COD = 1, COD is estimated by the relationship in Figure D1a.

In this retrieval, ΔSW less than that of COD = 1 is not considered as cloud. Because NLDAS SW was derived with the specific assumptions of aerosol climatology and vertical profile of temperature, humidity, and ozone [*Pinker et al.* 2003], ΔSW in these low ranges can be the radiative forcing background aerosols or uncertainties of using sounding climatology in the algorithm (~10% of error). According to the probability density function of aerosol optical depth (AOD) over eastern U.S. [*Matsui et al.* 2004], 99.5% is distributed below an AOD of 0.65. For the radiative forcing of AOD of 0.65 (sulfate), ΔSW is less (67~84%) than ΔSW for COD = 1.

Finally CLWP is derived from the assumed cloud droplet effective radius (R_e = 8μm) and the derived COD via

$$CLWP = \frac{\rho_w \cdot COD \cdot R_e}{1.5} \qquad \text{(D.4)}$$

Thereby, derived cloud liquid water path and assumed effective radius (8μm) are used to drive the NFL code for computing SW in all sky conditions, with and without aerosol loading. Figure B1b shows a scatter plot that compare the seasonally averaged NLDAS SW and reconstructed NFL SW, and it clearly demonstrates that this simple algorithm successfully replicates the NLDAS SW (r=0.99).

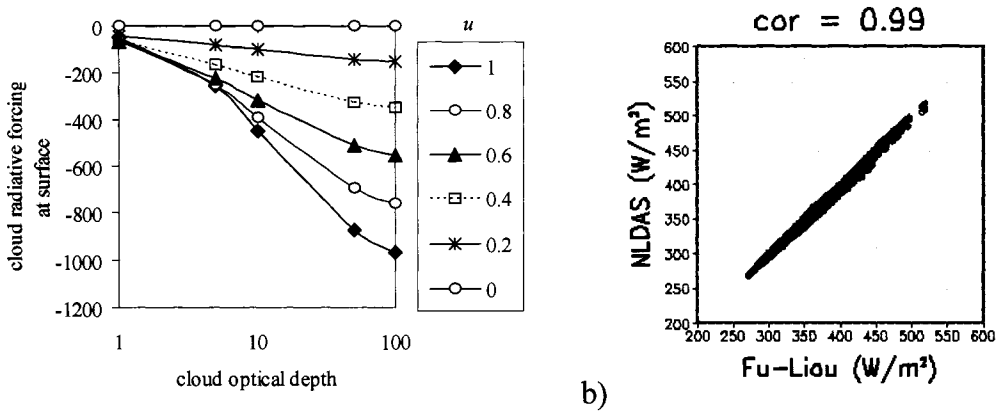

Figure B1. a) Variation of ΔSW as functions of cosine of solar zenith angle (u) and cloud optical depth (COD). b) Comparison between Fu-Liou-derived SW and NLDAS (GOES-derived) SW. Note that hourly SW are averaged from May 1st to Oct 1st in 2006. Green line represents 1:1 ratio.

References

Albini, F. A. (1981), A phenomenological model for wind speed and shear stress profiles in vegetation cover layers. *J. Appl. Meteor.,* **20,** 1325–1335.

Baldocchi, DD, and co-authors (2001), FLUXNET: A New Tool to Study the Temporal and Spatial Variability of Ecosystem-Scale Carbon Dioxide, Water Vapor and Energy Flux Densities, *Bull. Amer. Meteor. Soc.*, **82**, 2415-2434.

Ball, I. E. Woodrow, and J. A. Berry (1987), A model predicting stomatal conductance and its contribution to the control of photosynthesis under different environmental conditions. *Progress in Photosynthesis Research,* Vol. 1, J. Biggins, Ed., Martinus Nijhof, 221–234.

Chameides, W. L., H. Yu, S.C. Liu, M. Bergin, X. Zhou, L. Mearns, G. Wang, C.S. Kiang, R.D. Saylor, C. Luo, Y. Huang, A. Steiner and F. Giorgi (1999), Case study of the effects of atmospheric aerosols and regional haze on agriculture: An opportunity to enhance crop yields in China through emission controls? *Proc. Nat. Acad. Sci*, **96**, 13,626-633.

Chang, H. (2004), Direct observations of aerosol effects on carbon and latent heat fluxes. M.S. Thesis, Dept. of Marine, Earth, and Atmospheric Sciences, North Carolina State Univ., Raleigh, NC 27695.

Charlock, T.P., F.G. Rose, D.A. Rutan, D. Fillmore, and W. Collins (2004), All-sky aerosol direct forcing to SW and LW at TOA and surface using CERES Terra and the MATCH assimilation, International Radiation Symposium (IRS), Aug. 23-28 Busan, Korea.

Chen, D.-X., and M.B. Coughenour (1994), GEMTM: A general model for energy and mass transfer of land surfaces and its application at the FIFE sites. *Agric. For. Meteor.* **68**, 145-171.

Cohan, D.S., J. Xu, R. Greenwald, M.H. Bergin, and W.L. Chameides (2002), Impact of atmospheric aerosol light scattering and absorption on C-uptake by terrestrial plants. *Global Biogeochem. Cycles*, **16**: doi 10.1029/2001GB001441.

Coll, C., V. Caselles, J.M. Galve, E. Valor, R. Niclòs, J.M. Sánchez, and R. Rivas (2005), Ground measurements for the validation of land surface temperatures derived from AATSR and MODIS data, *Remote Sens. Environ.*, **97**, 288-300.

Collatz, G.J., J.T. Ball, C. Grivet and J.A. Berry, 1991, Physiological and environmental regulation of stomatal conductance, photosynthesis and transpiration: a model that includes a laminar boundary layer. *Agriculture and Forest Meteorology*, **54**, 107-136.

Cosgrove, B. A., D. Lohmann, K. E. Mitchell, P. R. Houser, E. F. Wood, J. Schaake, A. Robock, C. Marshall, J. Sheffield, L. Luo, Q. Duan, R. T. Pinker, J. D. Tarpley, R.

W. Higgins, and J. Meng (2003), Real-time and retrospective forcing in the North American Land Data Assimilation System (NLDAS) project, *J. Geophys. Res.*, 108(D22), 8842, doi:10.1029/2002JD003118.

Dai, Y., R. E. Dickinson, and Y.-P. Wang (2004), A two-big-leaf model for canopy temperature, photosynthesis, and stomatal conductance. *J. Climate*, **17**(12), 2281-2299.

Dang, Q.L., Margolis, H.A., Sy, M., Coyea, M.R., Collatz, G.J., Walthall, C.L. (1997), Profiles of photosynthetically active radiation, nitrogen and photosynthetic capacity in the boreal forest: implications for scaling from leaf to canopy. *J. Geophys. Res.*, **102**, 28,845–28,859.

de Pury, D.G.G., and G.D. Farquhar (1997). Simple scaling of photosynthesis from leaves to canopies without the errors of big-leaf models. *Plant, Cell, and Environment,* 20: 537-557

Dorman, J.L. and Sellers, P.J. (1989). A global climatology of albedo, roughness length and stomatal resistance for atmospheric general circulation models as represented by the Simple Biosphere Model (SiB). *J. Appl. Meteor.*, 833-855.

Dubayah, R., J. B. Blair, J. Bufton, D. Clark, J. JaJa, R. Knox, S. Luthcke, S. Prince, and J. Weishampel (1997), The Vegetation Canopy Lidar Mission. *Land Satellite*

Information in the Next Decade II: Sources and Applications. American Society for Photogrammetry and Remote Sensing, 100-112.

Field, C. (1983), Allocating leaf nitrogen for the maximization of carbon gain: leaf age as a control on the allocation program, *Oecologia*, 56, 341-347

Fu, Q., and K.-N. Liou (1993), Parameterization of the radiative properties of cirrus clouds. *J. Atmos. Sci.,* **50**, 2008-2025.

Goudriaan, J. (1977), *Crop Micrometeorology: A Simulation Study*. Center for Agricultural Publication and Documents, Wageningen, 249 pp.

Gu, L., D.D. Baldocchi, S. B. Verma, T. A. Black, T. Vesala, E. M. Falge, and P.R. Dowty (2002), Advantages of diffuse radiation for terrestrial ecosystem productivity. *J. Geophys. Res.*, **107**(D6), DOI 10.1029/2001JD001242.

Gu, L., Baldocchi, D.D., Wofsy, S.C., Munger, J.W., Michalsky, J.J., Urbanski, S.P. and Boden, T.A. (2003), Response of a deciduous forest to the Mount Pinatubo eruption: Enhanced photosynthesis. *Science,* **299**, 2035-2038.

Hahn, C.J., W.B. Rossow and S.G. Warren (2001), ISCCP cloud properties associated with standard cloud types identified in individual surface observations. *J. Climate*, **14**, 11-28.

Hansen M.C., Defries R.S., Townshend J.R.G., Sohlberg R., 2000: Global land cover classification at 1km spatial resolution using a classification tree approach. *Int. J. Remote Sens.*, **21**, 1331-1364.

Harshvardhan, R. (1993), Chapter 3: Aerosol-climate interactions. *Aerosol–Cloud–Climate Interactions,* P. V. Hobbs, Ed., Academic Press, 76–93.

Hess, M., P. Koepke, and I. Schult (1998), Optical Properties of Aerosols and clouds: The software package OPAC, *Bull. Amer. Meteor. Soc.,* **79**, 831-844.

Hicks, B.B., J.J. DeLuisi and D.R. Matt (1996), The NOAA integrated surface irradiance study (ISIS)—a new surface radiation monitoring program. *Bull. Amer. Meteor. Soc.* 77(12), 2857–2864.

Hirose, T. and Werger, M. J. A. (1987), Maximizing daily canopy photosynthesis with respect to the leaf nitrogen allocation pattern in the canopy. *Oecologia* **72**, 520-526.

Hobbs, P.V. (1993), Chapter 2: Aerosol-cloud interactions. Tropospheric aerosols. *Aerosol–Cloud–Climate Interactions,* P. V. Hobbs, Ed., Academic Press, 33–69.

Jin, M., and S. Liang (2006), An improved land surface emissivity parameter for land surface models using global remote sensing observations. *J. Climate*, **19**, 2867-2881.

Kalnay *et al.* (1996), The NCEP/NCAR 40-year reanalysis project. *Bull. Amer. Meteor. Soc.*, **77**, 437-471.

Kanniah K., N. Tapper, J. Beringer, X. Zhu, C. Long (2006), Preliminary investigations of the role of smoke aerosols on carbon uptake of a northern Australian tropical savanna, Atmospheric Radiation and Measurement (ARM) Science Team Meeting in Albuquerque, New Mexico, March 27 - 31, 2006.

Koike, T., Kitaoka, S., Ichie, T., Lei, T.T. and Kitao, M. (2004), Photosynthetic characteristics of mixed broadleaf forests from leaf to stand.,*In*: Shiomi, M. and Kawahata, H. eds. Global Environmental Change in the Ocean and on land. TerraPub, Tokyo, 453-472.

Krakauer, N. Y., and J. T. Randerson (2003), Do volcanic eruptions enhance or diminish net primary production? Evidence from tree rings, *Global BIogeochem.Cycles*, **17**(4), 1118, doi:10.1029/2003GB002076.

Kumar, S. V., C. D. Peters-Lidard, Y. Tian, P. R. Houser, J. Geiger, S. Olden, L. Lighty, J. L. Eastman, B. Doty, P. Dirmeyer, J. Adams, K. Mitchell, E. F. Wood and J. Sheffield (2006), Land Information System - an interoperable framework for high

resolution land surface modeling. *Environmental Modelling & Software,* **21**, 1402-1415.

Lee, T. J. and R. A. Pielke (1992), Estimating the soil surface specific humidity. *J. Appl. Meteor.,* **31,** 480–484.

Liou, K. N., 2002: *An Introduction to Atmospheric Radiation.* 2d ed. Academic Press, 583 pp.

Liston. G. E., 2004: Representing subgrid snow cover heterogeneities in regional and global models. *J. Climate*, **17**, 1381-1397.

Low, B.E., and Co-Authors (2002), Environmental controls over carbon dioxide and water vapor exchange of terrestrial vegetation, *Agriculture and Forest Meteorology,* **113**, 97-120.

Mahfouf J. F., J. Noilhan (1991), Comparative study of various formulations of evaporation from bare soil using in situ data. *J. Appl. Meteor.* **30**,1354–1365.

Matsui, T., S.M. Kreidenweis, R.A. Pielke Sr., B. Schichtel, H. Yu, M. Chin, D.A. Chu, and D. Niyogi (2004), Regional comparison and assimilation of GOCART and MODIS aerosol optical depth across the eastern U.S. *Geophys. Res. Lett.* **31**, L21101, doi:10.1029/2004GL021017.

Matsui, T., A. Beltrán-Przekurat, R. A. Pielke Sr., D. Niyogi, and M. B. Coughenour (2006), Continental-scale multi-observation calibration and assessment of Colorado State University Unified Land Mode: Part I. Surface albedo, *J. Geophys. Res.* (Accepted)

McClatchey, R.A., W. Fenn, J.E.A. Selby, F.E. Volz, J.S. Garing (1972), Optical properties of the atmosphere, *AFCRL Environ. Res. Papers*, **411**, 108 pp.

McNider, R. T., W. M. Lapenta, A. P. Biazar, G. J. Jedlovec, R. J. Suggs, J. Pleim (2005), Retrieval of model grid-scale heat capacity using geostationary satellite products. part I: first case-study application, *J. Applied Meteo.*, **44**, 1346–1360.

Miller, D. A., and R. A. White (1998), A conterminous United States multi-layer soil characteristics data set for regional climate and hydrology modeling. *Earth Interactions,* **2**.

Misson L., M. Lunden, M. Mc Kay, A. H. Goldstein (2005), Atmospheric aerosol light scattering and surface wetness influence the diurnal pattern of net ecosystem exchange in a semi-arid ponderosa pine plantation. *Agric. For. Meteor.*, **129**, 69-83.

Myneni, R.B., and co-authors, 2002: Global products of vegetation leaf area and fraction absorbed PAR from year one of modis data. *Remote Sens. of Environ.*, **83**(1-2), 214-231

Niyogi, D., H.-I. Chang, V.K. Saxena, T. Holt, K. Alapaty, F. Booker, F. Chen, K.J. Davis, B. Holben, T. Matsui, T. Meyers, W.C. Oechel, R.A. Pielke Sr., R. Wells, K. Wilson, and Y. Xue (2004), Direct observations of the effects of aerosol loading on the net ecosystem CO_2 exchanges over different landscapes. *Geophys. Res. Letts.*, **31**, L20506, doi:10.1029/2004GL020915.

Norman, J. M. (1979), Modeling the complete crop canopy. *Modification of the Aerial Environment of Crops*, B. J. Barfield and J. F. Gerber, Eds., *American Society of Agricultural Engineers*, 249–280.

Norman, J. M., Garcia, R. and Verma, S. B. (1992), Soil surface Co_2 fluxes and carbon budget of a grass land. *J. Geophys. Res.*, **97**(D17), 18845-18853.

Olson, K. W., G. Bonan, M. Bosilovich, R. Dickinson, P. Dirmeyer, F. Hoffman, P. Houser, S. Levis, G.-Y. Niu, Peter Thornton, M. Vertenstein, S.-L. Yang, X. Zeng, 2004: Technical Description of the Community Land Model (CLM), NCART TECHNICAL NOTE, NCAR/TN-461+STR,

Philip, J. R. (1957), Evaporation and moisture and heat field in the soil. *J. Meteror.* , **14**, 354-366.

Pielke Sr., R.A. (2001), Influence of the spatial distribution of vegetation and soils on the prediction of cumulus convective rainfall. *Rev. Geophys.*, **39**, 151-177.

Pinheiro, A. C., J. L. Privette, R. Mahoney, and C. J. Tucker. 2004. Directional effects in a daily AVHRR land surface temperature dataset over Africa. IEEE Trans. Geosci. Remote, 42(9): 1941-1954.

Reichstein, M. and co-authors (2003), Modeling temporal and large-scale spatial variability of soil respiration from soil water availability, temperature and vegetation productivity indices, *Global Biogeochemical Cycles,* **17**, 1104, doi:10.1029/2003GB002035.

Rocha, A.V., H.B. Su, C. Vogel, H.P. Schmid, and P.S. Curtis (2004), Photosynthetic and water use efficiency responses to diffuse radiation by an aspen-dominated northern hardwood forest. *Forest Science*. **50**(6), 793-801.

Roderick, M. L. (1999), Estimating the diffuse component from daily and monthly measurements of global radiation, *Agricultural and Forest Meteorology*, **95**, 169-185.

Roderick, M.L., Farquhar, G.D., Berry, S.L. and Noble, I.R. (2001), On the direct effect of clouds and atmospheric particles on the productivity and structure of vegetation. *Oecologia,* **129**, 21-30.

Sellers, P. J. (1985), Canopy reflectance, photosynthesis and transpiration. *Int. J. Remote Sens.*, **6,** 1335–1372.

Sellers, P. J., D. A. Randall, G. J. Collatz, J. A. Berry, C. B. Field, D. A. Dazlich, C. Zhang, G. D. Collelo, and L. Bounoua (1996), A revised land surface parameterization (SiB2) for atmospheric GCMs. Part I: Model formulation. *J. Clim.*, **9**, 676–705.

Spinhirne, J. D., J. A. Reagan, and B. M. Herman (1980), Vertical distribution of aerosol extinction cross section and inference of aerosol imaginary index in the troposphere by lidar technique, *J. Appl. Meteorol.*, **19**, 426–438.

Tao, W.-K., D. Starr, A. Hou, P. Newman, and Y. Sud (2003), A cumulus parameterization workshop, *Bull. Amer. Meteor. Soc.*, **84**(8), 1055–1062.

Terashima, I. and Inoue, Y. (1984), Comparative photosynthetic properties of palisade tissue chloroplasts and spongy tissue chloroplasts of *Camellia japonica* L.: Functional adjustment of the photosynthetic apparatus to light environment within a leaf. *Plant and Cell Physiology,* **25**, 555-563.

Walko, R.L., L.E. Band, J. Baron, T.G.F. Kittel, R. Lammers, T.J. Lee, D.S. Ojima, R.A. Pielke, C. Taylor, C. Tague, C.J. Tremback, and P.L. Vidale (2000), Coupled

atmosphere-biophysics-hydrology models for environmental modeling. . *Appl. Meteor.*, **39**, 931-944.

Wan, Z., Y. Zhang, Q. Zhang, and Z.-L. Li (2002), Validation of the land-surface temperature products retrieved from Terra Mode rate Resolution Imaging Spectroradiometer data, *Remote Sens. Environ.*, **83**, 163-180.

Wan, Z., Y. Zhang, Q. Zhang, and Z.-L. Li (2004), Quality assessment and validation of the global land surface temperature, *Int. J. Remote Sens.*, **25**, 261-274.

Wang, Y.P and R. Leuning (1998), A two-leaf model for canopy conductance, photosynthesis, and partitioning of available energy. I. Model description. *Agric. For. Meteo.*, **91**, 89-111.

Watermark Numerical Computing (2004), PEST Model-Independent Parameter Estimation User Manual: 5th Edition, http://www.sspa.com/pest/pestsoft.html

Yin, X., Lantinga, E.A., Schapendonk, A.H.C.M., and Zhong, X. (2003), Some quantitative relationships between leaf area index and canopy nitrogen content and distribution. *Annals. of Botany*, **91**, 893-903.

Zeng, X., M. Zhao, and R. E. Dickinson (1998), Intercomparison of bulk aerodynamic algorithms for the computation of sea surface fluxes using TOGA COARE and TAO data. *J. Climate.*, **11**, 2628–2644.

Zeng, X. (2001), Global vegetation root distribution for land modeling. *J. Hydrometeor*. 2, 525-530.

Zeng, X., R. E. Dickinson, M. Barlage, Y. Dai, G. Wang, and K. Oleson (2005), Treatment of undercanopy turbulence in land models. *J. Climate.,* **18**, 5

Chapter 8

Further Discussion and Future Direction

8.1 Further Discussion and Future Direction

Aerosol climate effects are investigated in chapters 2 through 7. This final chapter addresses further discussion and future direction suggested by each chapter from an integrated perspective.

Chapters 2 and 3 examined aerosol-cloud interactions for different thermodynamic environments [*Matsui et al.* 2004a and 2006b]. Marine low cloud properties are derived from TRMM TMI and VIRS sensors. Aerosol index (AI) is derived from MODIS and GOCART multi-spectrum AODs. Although satellite retrievals of aerosols do not distinguish the chemical properties, multi-channel MODIS sensors can use multi-spectral AODs to estimate the mean size of particles, which is more important than the composition for determining variations in the cloud-nucleating ability of aerosol particles [*Dusek et al.* 2006]. This satellite-based study supports the hypothesized aerosol indirect effects; namely, higher concentrations of aerosols tend to decrease the mean size of cloud droplets, suppress the warm rain process, and slightly increase the cloud fraction. However, this study does not support the hypothesis that cloud liquid water path is constant or increases with aerosol loading, which is similar to the finding of *Han et al.* [2002]. The reduction in cloud liquid water path with increased aerosol concentrations

can be physically explained by the modulation of boundary layer turbulence and entrainment rate for high concentrations of cloud droplets [*Jiang et al.* 2002, *Xue and Feingold* 2006]. However, the negative feedback of aerosols on cloud liquid water path is limited to boundary-layer clouds, which have low updraft speeds. For vigorous convective clouds, the presence of aerosols tends to increase cloud liquid water path [*Koren et al.* 2005, *Lin et al.* 2006, *Khain and Pokrovsky* 2004], as initially hypothesized by *Albrecht* [1989]. *Koren et al.* [2005] show that aerosols tend to invigorate the cloud structure and increase cloud fraction over the Atlantic Ocean. *Lin et al.* [2006] show that biomass burning-derived smoke tends to increase cloud-top height, liquid water path, ice fraction, cloud fraction, and precipitation rate over the Amazon forest. Because of the elevated cloud-top height and enhanced ice fraction, aerosols tend to increase the cloud-top effective radius in this case, as opposed to the cases of marine low clouds [*Matsui et al.* 2004a and 2006b, *Kaufman et al.* 2005]. Thus, future research must rationalize the various competitions between the turbulence feedback and updraft speed not only for liquid clouds, but also for mixed phase and ice cloud over land and ocean [*Y. Kaufman* 2006; Z. *Levin* 2006; *R. Wood* 2006; personal communications].

Chapter 4 presented estimations of the global mean and gradient of aerosol radiative forcing [*Matsui and Pielke* 2006]. Both aerosol direct and indirect radiative forcings are much more heterogeneous than the forcing due to greenhouse gases (GHGs) in terms of the proposed metric, *Normalized Gradient of Radiative Forcing (NGoRF)*. The strong gradient of aerosol radiative forcing could modulate the atmospheric heating and circulation on the various scales [e.g., *Gill* 1984; *Emanuel* 1995]. While using different modeling frameworks, *Rotstayn and Lohmann* [2002] and *Takemura et al.*

[2006] concluded that the aerosol dynamic effect can induce much greater perturbation on the regional climate than the local aerosol direct/indirect effect, and showed that the dynamic effect due to anthropogenic aerosols contributes to the reported 20th-century drought tendency over North Africa [*IPCC* 2001]. *Menon et al.* [2002] show that the aerosol direct effect redistributes lower-atmospheric stability (LTS) elsewhere on the globe. Chapter 3 also shows that LTS appears to be the first-order effect on the cloud fraction, which is linearly correlated with cloud radiative forcing [*Klein and Hartmann* 1992]. This indicates that the global thermodynamic field perturbed by the aerosol direct effect could overwhelm the local aerosol direct and indirect effects [*Matsui et al.* 2006b]. This strong dynamic feedback was also demonstrated by *Kim and Lee* [2006]. They used the global modeling to examine the aerosol direct effect, and found that global low cloud fields modulated by the aerosol dynamic effect have a greater radiative forcing than the local aerosol direct effect.

Satellite-based measurement studies have advantages for studies of aerosol-cloud interactions due to the facts that 1) the satellite data are observations; 2) the horizontal footprint size could be down to a few kilometers; 3) cloud processes can be observed nearly on the global scale. However, satellite-based measurement studies also have disadvantages, because 1) the measurement is instantaneous, and temporally discontinuous (excepting geostationary satellites); 2) dynamic and local effects cannot be separated. Satellites observe the current climate that includes all possible anthropogenic effects, including aerosols, GHGs, land-cover change, and etc. A global model can separate the dynamic and local effects via a sensitivity study [*Rotstayn and Lohmann* 2002; *Takemura et al.* 2006; *Kim and Lee* 2006]; therefore, models could be used to

examine *NGoRF*. However, a global model has the disadvantage of the intrinsic difficulty in subgrid parameterization of cloud-precipitation process [*Randall et al.* 2003]. *Matsui and Pielke* [2006], *Kaufman et al.* [2005], and *Kaufman and Koren* [2006] showed that the largest factor of aerosol indirect effect is the cloud fraction. Whereas the global-modeling community traditionally focuses on parameterizing the droplet size (or number) and cloud liquid water path as a function of aerosol concentrations [*Lohmann and Feichter* 2004; *Rotstayn and Lohmann* 2002; *Takemura et al.* 2006], the cloud fraction is poorly parameterized in global atmospheric models [*Randall et al.* 2003]. In order to explicitly represent cloud fraction, linked to moist convection and aerosol loading, microphysics must resolve the size distribution of hydrometeors, and the grid spacing of the simulation must be down to a few kilometers [*Khain and Pokrovsky* 2004]. Furthermore, a few tens to hundreds of meters of grid spacing must be used for explicit representation of the large eddy and turbulence feedback processes in stratocumulus clouds [*Jiang et al.* 2002, *Xue and Feingold* 2006]. Thus, further research must include *large-scale*, *fine-resolution*, and *long-term* integrations of the numerical simulation for better understanding of *NGoRF* and local- and large-scale aerosol effects simultaneously. For this, we need to reduce the parameterization costs using an alternative method that heavily utilizes look-up table [*Matsui et al.* 2004c], together with better use of parallel computing environments.

Chapter 5 evaluates three different estimates of aerosol optical depth (AOD) against ground-based observations over the eastern U.S. [*Matsui et al.* 2004b]. The three AOD products evaluated include one from a global chemical transport model (GOCART), one from satellite measurement (MODIS), and one assimilated (MODIS-GOCART)

product. The study revealed that the assimilated AOD is a superior estimate in the warm season, but not in the cold season due to the slight overestimation of both the MODIS and GOCART products in comparison with ground-truth data. Thus, both products must remove the intrinsic biases as much as possible before the assimilation.

The biases in the MODIS AOD over land are much greater than those in GOCART, and mostly related to the uncertainties in spatio-temporal heterogeneity of land surface albedo in comparison with ocean albedo. The MODIS algorithm takes advantages of the fact that wavelengths in the mid-IR are 1) long enough to penetrate most of the aerosol particles; 2) well correlated with the reflectance in the shortwave (0.47μm and 0.66μm), and 3) insensitive to the ~300K earth surface emission, unlike the 3.75μm wavelength [*Kaufman et al.,* 1997]. Based on results from a variety of surface covers and regions using atmospherically corrected LANDSAT TM and AVIRIS aircraft images, the surface reflectances at 0.47μm and 0.66μm over various land covers can be estimated from that at 2.1μm, using mean values of $\alpha_{0.47\,\mu m} / \alpha_{2.1\,\mu m} = 0.25$ and $\alpha_{0.66\,\mu m} / \alpha_{2.1\,\mu m} = 0.5$. Based on the estimated spectral surface albedo, an inversion of the radiative transfer model is applied to derive the column AOD over land. However, the estimation of surface albedo does not account for the 1) correlations for different land-cover types and 2) the bi-directional reflectance distribution function (BRDF). Other issues includes the treatment of sub-pixel cloud, snow/ice and water contamination, uncertainties in heterogeneous surface reflectance, aerosol properties beyond the scope of the assumption of aerosol models, and the sub-grid water content [*Chu et al.* 2002]. Most of these issues will be resolved in the next version of MODIS AOD products [*Levy et al.* 2006]. A new algorithm improves the assumptions for surface reflectance and for

regional aerosol optical properties, and implements a simultaneous inversion of three channels of MODIS radiances (0.47, 0.66, and 2.12μm). The initial validation shows that most of the over-predictions found in the previous version of MODIS AOD are significantly reduced by using the new algorithm [*Levy et al.* 2006].

The quality of AOD estimates from global chemistry transport models depends on three components: aerosol and precursor emissions inventories, atmospheric objective analysis, and simulated aerosol optical and microphysical process [*Kinne et al.* 2003]. These three factors must be simultaneously improved for better prediction of AODs. It is yet difficult to estimate the exact amount of surface emissions of various aerosols and precursors in terms of space and time from literature review or historical records [e.g., *Streets et al.* 2002]. As long as a model uses an accurate objective reanalysis, an inversion technique can be used to estimate spatio-temporal emission [e.g., *Schichtel et al.* 2006]. The emergence of new aerosol datasets, including an extensive network of ground-truth measurements (AERONET [*Holben et al.,* 1998] and IMPROVE [*Malm et al.,* 2004]) and satellite-based measurements (MODIS [*Remer et al.* 2005], MISR [*Kahn et al.* 2005] and CALIPSO [*Kaufman et al.* 2003]), will provide us an opportunity for inversely estimating a global aerosol emission field [*AeroEarth*: http://aerocenter.gsfc.nasa.gov/ae/]. The accuracy of the objective analysis, i.e., the chemical transport process, is critical for this technique. First, because of the inability of models to accurately predict the cloud-precipitation processes, a model must assimilate the satellite-measured radiances of clouds and precipitation processes [e.g., *Hou et al.* 2004, *Vukicevic et al.* 2006], which are the critical sink process for aerosols and precursors. Second, model spatial resolution must be at least down to tens of kilometers

that can resolve mesoscale variations in aerosols [*Anderson et al.* 2003]. Present chemical transport models tend to employ a coarse-resolution objective analysis. This makes the predictions difficult to compare with ground-truth data, although the use of a probability density function (PDF) can help to examine scale differences [*Matsui et al.* 2004b, *Anderson et al.* 2003]. These developments are ongoing in different agencies and universities. Thus, collaborative work is essential to integrate available datasets and techniques for further improvement of chemical transport models.

Chapters 6 and 7 used the calibrated uncertain parameters in the Unified Land Model (ULM). Chapter 6 optimized plant and soil optical properties by comparing the model-derived surface spectrum albedo with the satellite-observed albedo, and ULM is significantly improved the representation in surface spectral albedo [*Matsui et al.* 2006b]. Chapter 7 further calibrates the model parameters related to radiative temperature, surface CO_2 fluxes, and turbulent sensible/latent heat fluxes by comparing with the corresponding observations from the MODIS product and the eddy-covariance flux measurements (Fluxnet) [*Matsui et al.* 2006b]. These works are the first attempt to establish the comprehensive, continental-scale calibration framework for a land surface model (LSM). Although the calibration successfully removed the tuning-parameter-related model biases, there is much work to be completed in future studies.

First, the calibration framework requires more ground-based and satellite-based datasets that are becoming available in this decade. In chapter 7, some of the LULC classes (shrublands, different types of croplands, grasslands, evergreen broadleaf forest, and deciduous needleleaf forest) lack surface observation sites for their calibration. Oklahoma MESONET (http://www.mesonet.ou.edu/public/current.html) and more sites

in FLUXNET are available for recent years. These surface flux and meteorological data can be readily incorporated into the calibration framework. A continental to global-scale river discharge database (http://www.sage.wisc.edu/riverdata/) can be used to constrain parameters related to surface infiltration and water budget in soil. For cold season simulations, ULM will include the subgrid snow distribution model (SSNOWD) in the near future [*Liston* 2004], and MODIS snow cover data are available to calibrate subgrid snow parameters that should be related to the topographic index, canopy height, and surface temperature climatology.

Second, the calibration algorithm requires further improvement. Chapters 6 and 7 use a simple Gauss-Marquardt-Levenberg (GML) algorithm in the PEST model. This is essentially the numerical, local-search algorithm that may be stuck in a local minima instead of reaching on the global minima. Ideally, the population-evolution global search algorithm should be used for the continental calibration. Yet, the global search algorithm requires a large amount of computational time and CPUs. Therefore, some new techniques are required to reduce the number of land grid points by limiting to the least number of most representative land-grid points.

Chapter 7 examines the aerosol diffuse-radiation effect via the off-line ULM simulations. Although off-line simulation using NLDAS meteorological forcing can eliminate the errors of cloud-precipitation processes in a meteorological model, the off-line simulations lack the understanding of feedback mechanism of atmospheric dynamics and cloud-precipitation processes. NASA GSFC Land Information System is currently coupled with a meteorological model through the Earth System Modeling Framework [*S. Kumar* 2006; personal communication]. This will allow use of the calibrated ULM for

studies of land-atmosphere interactions in the near future. In addition, chapter 7 does not include the aerosol indirect effects in the sensitivity experiments. As discussed before, the aerosol indirect effect over land is currently at a low stage of scientific understanding. If the cloud cover is extensively increased due to the aerosol loading as observed in *Lin et al.* [2006], aerosol loading could deteriorate overall the plant productivity, as indicated by the numerical experiments.

References

Albrecht, B.A. (1989), Aerosols, cloud microphysics, and fractional cloudiness, *Science,* **245**, 1227-1230.

Anderson, T.L., R.J. Charlson, D.M. Winker, J.A. Ogren and K. Holmén (2003), Mesoscale variations of tropospheric aerosols, *J. Atmos. Sci.,* **60**(1), 119–136.

Chu, D.A., Y.J. Kaufman, C. Ichoku, L.A. Remer, D. Tanre, and B.N. Holben (2002), Validation of MODIS aerosol optical depth retrieval over land. *Geophys. Res. Lett.*, **29** (12).

Emanuel, K.A. (1995), On thermally direct circulations in moist atmospheres. *J. Atmos. Sci.*, **52**, 1529-1534.

Dusek, U., G. P. Frank, L. Hildebrandt, J. Curtius, J. Schneider, S. Walter, D. Chand, F. Drewnick, S. Hings, D. Jung, S. Borrmann, M. O. Andreae (2006), Size Matters More Than Chemistry for Cloud-Nucleating Ability of Aerosol Particles, Science, 312, 1375 – 1378, DOI: 10.1126/science.1125261

Gill, A. (1982), *Atmosphere-Ocean Dynamics*. Academic Press, New York, 662 pp.

Han, Q., W. B. Rossow, J. Zeng, and R. Welch (2002), Three different behaviors of liquid water path of water clouds in aerosol–cloud interactions. *J. Atmos. Sci.*, **59**, 726–735.

Holben, B.N., T.F. Eck, I. Slutsker, D. Tanré, J.P. Buis, A. Setzer, E.F. Vermote, J.A. Reagan, Y.J. Kaufman, T. Nakajima, F. Lavenu, I. Jankowiak, and A. Smirnov, 1998: AERONET - A federated instrument network and data archive for aerosol characterization. *Remote Sens. Environ.*, **66**, 1-16.

Hou, A. Y., S. Q. Zhang, and O. Reale (2004) Variational continuous assimilation of TMI and SSM/I rain rates: Impact on GEOS-3 hurricane analyses and forecasts. *Mon. Wea. Rev.*, **132**, 2094–2109

IPCC Third Assessment Report (2001), Climate change 2001: The scientific basis. J.T. Houghton et al., Eds.,Cambridge Univ. Press, Cambridge, 994 pp.

Jiang, H., G. Feingold, and W.R. Cotton (2002), Simulations of aerosol-cloud-dynamical feedbacks resulting from entrainment of aerosol into the marine boundary layer during the Atlantic Stratocumulus Transition Experiment. *J. Geophys. Res.* **107**, doi: 10.1029/200JD001502.

Kahn, R., B. Gaitley, J. Martonchik, D. Diner, K. Crean, and B. Holben (2005), MISR global aerosol optical depth validation based on two years of coincident

AERONET observations, *J. Geophys. Res.*, **110**, D10S04, doi:10.1029/2004JD004706.

Kaufman, Y. J., D. Tanre, L. A. Remer, E. F. Vermote, A. D. Chu, and B. N. Holben (1997), Operational remote sensing of tropospheric aerosol over the land from EOS-MODIS, *J. Geophys. Res.*, **102**, 17,051 – 17,061.

Kaufman, Y.J., D. Tanré, J.-F. Léon, and J. Pelon (2003), Retrievals of profiles of fine and coarse aerosols using lidar and radiometric space measurements. *IEEE Trans. Geosci. Remote Sens.*, **41** (8), 1743-1754.

Kaufman, Y. J., I. Koren, L. A. Remer, D. Rosenfeld, and Y. Rudich (2005), The effect of smoke, dust and pollution aerosol on shallow cloud development over the Atlantic Ocean. *Proceedings of the National Academy of Sciences*, **102**(32), 11207-11212.

Khain A. and A. Pokrovsky (2004), Simulation of effects of atmospheric aerosols on deep turbulent convective clouds using a spectral microphysics mixed-phase cumulus cloud model. Part II: Sensitivity Study. *J. of the Atmos. Sci.*, **61**(24), 2983–3001.

Kinne S. and co-authors (2003), Monthly averages of aerosol properties: A global comparison among models, satellite data, and AERONET ground data, *J. Geophys. Res.* **108**(D20), 4634, doi:10.029/2001JD001253, 2003.

Kim, M. K., and W. S. Lee (2006), Dynamic feedbacks of troposphere aerosols on marine low cloud during boreal spring, *Geophys. Res. Lett.*, **33**, L16704, doi:10.1029/2006GL026351.

Klein, B., S. A., and D. L. Hartmann (1993), The seasonal cycle of low stratiform clouds. *J. Climate,* **6**, 1587-1606.

Koren, I., Y. J. Kaufman, D. Rosenfeld, L. A. Remer, and Y. Rudich (2005), Aerosol invigoration and restructuring of Atlantic convective clouds. *Geophys. Res. Lett.*, **32**, doi: 10.1029/2005GL023187.

Levy, R. C., L. A. Remer, and O. Dubovik (2006), Global aerosol optical models and lookup tables for the new MODIS aerosol retrieval over land. *J. Geophys. Res.* (Submitted)

Lin, J.C., T. Matsui, R.A. Pielke Sr., and C. Kummerow (2006), Effects of biomass burning-derived aerosols on precipitation and clouds in the Amazon Basin: A satellite-based empirical study. *J. Geophys. Res.* 111, D19204, doi:10.1029/2005JD006884.

Lau, K.-M., M.-K. Kim, and K.-M. Kim (2006), Aerosol induced anomalies in the Asian summer monsoon – the role of the Tibetan Plateau. *Climate Dynamics*, in press.

Lohmann, U., and J. Feichter, 2005: Global indirect aerosol effects: A review. *Atmos. Chem. Phys.*, **5**, 715–737.

Remer, L. A., Y. J. Kaufman, D. Tanre, S. Mattoo, D. A. Chu, J. V. Martins, R.-R. Li, C. Ichoku, R. C. Levy, R. G. Kleidman, T. F. Eck, E. Vermote, and B. N. Holben (2005), The MODIS aerosol algorithm, products and validation. *J. Atmos. Sci.* **62**, 947–973.

Rotstayn, L. D., and U. Lohmann, 2002: Tropical rainfall trends and the indirect aerosol effect. *J. Climate.*, **15**, 2103–2116.

Malm, W.C., B.A. Schichtel, M.L. Pitchford, L.L. Ashbaugh and R.A. Eldred, 2004: Spatial and monthly trends in speciated fine particle concentration in the United States, *J. Geophys. Res.*, 109, D03306, doi: 10.1029/2003JD003739, 2004.

Matsui, T., H. Masunaga, R. A. Pielke Sr., and W.-K. Tao (2004a), Impact of aerosols and atmospheric thermodynamics on cloud properties within the climate system. *Geophys. Res. Lett.* **31**, L06109, 10.1029/2003GL019287.

Matsui, T., S. M. Kreidenweis, R.A. Pielke Sr., B. Schichtel, H. Yu, M. Chin, D.A. Chu, and D. Niyogi (2004b), Regional comparison and assimilation of GOCART and MODIS aerosol optical depth across the eastern U.S. *Geophys. Res. Letts.*, **31**, L21101, doi:10.1029/2004GL021017.

Matsui, T., G. Leoncini, R.A. Pielke Sr., and U.S. Nair (2004c), A new paradigm for parameterization in atmospheric models: Application to the new Fu-Liou radiation code. Atmospheric Science Paper No. 747, Colorado State University, Fort Collins, CO 80523, 32 pp

Matsui, T. H. Masunaga, S.M.Kreidenweis, R.A.Pielke, Sr, W.-K. Tao, M. Chin, Y. Kaufman (2006a), Satellite-based Assessment of Global Warm Cloud Properties Associated with Aerosols, Atmospheric Stability, and Diurnal Cycle, . *J. Geophys. Res.*, 111, D17204, doi:10.1029/2005JD006097.

Matsui, T. and R.A. Pielke Sr. (2006b), Satellite-based estimation of spatial gradient of aerosol radiative forcing, *Geophys. Res. Letts.* **33**, L11813, doi:10.1029/2006GL025974.

Matsui, T., A. Beltran-Przekurat, R.A. Pielke Sr., D. Niyogi, and M. Coughenour (2006c), Continental-scale multi-observation calibration and assessment of land surface model by application of MODIS surface albedo, *J. Geophys. Res.* (Accepted)

Matsui, T., et al. (2006d), Mechanical response of plant productivity and surface energy budget to routine aerosol loading, using a well-calibrated sun-shade model (in preparation).

Randall, D., M. Khairoutdinov, A. Arakawa, and W. Grabowski (2003), Breaking the cloud parameterizations deadlock. *Bull. Amer. Meteor. Soc.*, **84**, 1547–1564.

Schichtel, B. A., W.C. Malm, K.A. Gebhart, M. G. Barna, and E.M. Knipping (2006), A hybrid source apportionment model integrating measured data and air quality model results, *J. Geophys. Res.*, **111**, D07301, doi:10.1029/2005JD006238.

Stephens, G. L., et al. (2002), The CloudSat mission and the A-train: A new dimension of space-based observations of clouds and precipitation. *Bull. Amer. Meteor. Soc.*, **83**, 1771-1790, doi:10.1175/BAMS-83-12-1771.

Streets, D.G., T.C. Bond, G.R. Carmichael, S.D. Fernandes, Q. Fu, D. He, Z. Klimont, S.M. Nelson, N.Y. Tsai, M.Q. Wang, J.-H. Woo, and K.F. Yarber, An inventory of gaseous and primary aerosol emissions in Asia in the year 2000, *J. Geophys. Res.*, **108**, D21, doi:10.1029/2002JD003093.

Twomey, S., M. Piepgrass, and T. L. Wolfe (1984), An assessment of the impact of pollution on global cloud albedo. *Tellus,* **36B**, 356-366.

Vukicevic, T., M. Sengupta, A. S. Jones and T. Vonder Haar (2006), Cloud-resolving satellite data assimilation: information content of IR window observations and uncertainties in estimation. *J. of Atmos. Sci.*, **63**(3). 901–919.

Xue, H. and G. Feingold (2006), Large-eddy simulations of trade wind cumuli: investigation of aerosol indirect effects. *Journal of the Atmospheric Sciences*, **63**, 1605–1622.

Yu, H., et al. (2005), A review of measurement-based assessment of aerosol direct radiative effect and forcing. *Atmos. Chem . Phys. Discuss.*, 5, 7647-7768.